University of Southampton

FACULTY OF ENGINEERING, SCIENCE AND MATHEMATICS

SCHOOL OF ENGINEERING SCIENCES

LARGE-EDDY SIMULATION OF FLOW AROUND AN AIRFOIL AT LOW REYNOLDS NUMBER NEAR STALL

by

Jaber Hmoud Almutairi

Thesis for the degree of Doctor of Philosophy

May 2010

Abstract

The behaviour of flow at low Reynolds number around a NACA-0012 airfoil near stall has been studied using large eddy simulation (LES). An *a posteriori* study was carried out to compare direct numerical simulation (DNS) and LES, with and without a subgrid scale model. Good agreement was found with a noticeable improvement when incorporating a mixed-time-scale model with the LES. A simulation at a Reynolds number of 50,000 and incidence of 9.25° showed that a low-frequency flow oscillation phenomenon can be captured by LES but that this is sensitive to the computational domain width. A transient low-frequency mode was also observed at a Reynolds number of 130,000. Dynamic stall was studied for a flow at a Reynolds number of 50,000 and Mach number of 0.4 for the case of gusting flow past a stationary airfoil. The results show that the LES is capable of reproducing important aerodynamic characteristics, such as the hysteresis loops of lift, drag and pitching moment coefficients, which are found to compare favourably with experimental data. A comparison between the natural low-frequency flow oscillation and the forced low-frequency flow oscillation in the dynamic stall simulation shows that the latter has aerodynamic characteristics that are more regular. Simpler numerical methods were used to assess their ability to describe the flow at low-Reynolds number around the NACA-0012 airfoil. An unsteady viscous-inviscid interaction method gave realistic results for the low-frequency flow oscillation, for which the range of Reynolds numbers and the corresponding Strouhal numbers and incidences were determined. A periodic forcing technique showed high effectiveness in controlling flow separation, where the low-frequency flow oscillation near stall and the flapping of the flow at high Mach number (M = 0.8) and zero incidence were completely removed, with a noticeable increase in airfoil performance.

Table of contents

List of Figures

DECLARATION OF AUTHORSHIP

I, Jaber H Almutairi, declare that the thesis entitled Large-Eddy Simulation of Flow around an Airfoil at Low Reynolds Number near Stall and the work presented in the thesis are both my own, and have been generated by me as the result of my own original research. I confirm that:

- this work was done wholly or mainly while in candidature for a research degree at this University;
- where any part of this thesis has previously been submitted for a degree or any other qualification at this University or any other institution, this has been clearly stated;
- where I have consulted the published work of others, this is always clearly attributed;
- where I have quoted from the work of others, the source is always given. With the exception of such quotations, this thesis is entirely my own work;
- I have acknowledged all main sources of help;
- where the thesis is based on work done by myself jointly with others, I have made clear exactly what was done by others and what I have contributed myself;
- parts of this work have been published as:

Almutairi, J. H., Jones, L. E., and Sandham, N. D. (2010) 'Large eddy simulation of flow around an airfoil near stall', *Proceedings Direct and Large-Eddy Simulation VII.* 527-531, Springer Netherlands.

Almutairi, J. H., Jones, L. E., and Sandham, N. D. (2010) 'Intermittent bursting of a laminar separation bubble on an airfoil', *AIAA Journal.* **48** (2), 414-426.

Signed: ……..

Date: ……

Acknowledgment

I would like to thank Professor Neil Sandham who guided me honestly and sincerely from the beginning of my PhD study until I finished this thesis. I would like also to thank Dr. Lloyd Jones who provided me an excellent support in using the numerical code. I would like also to thank Dr. Zhiwei Hu who was encouraging me through out the course of this thesis. I am thankful for my mum for her moral support. I am very grateful to my wonderful wife and daughters (Danah, Renad, Nadeyah, Rawan and Al-Jouri) for their patience, encouragement and optimism during the years of study.

Nomenclature

a,b = filtering coefficients

A = pitch rate

c = airfoil chord

C_d , C_t = mixed time scale model parameters

C_D = drag coefficient

C_{df} = friction drag coefficient

C_{dp} = pressure drag coefficient

C_f = skin-friction coefficient

C_L = lift coefficient

C_p = pressure coefficient

E = energy cascade

f = frequency of the flow oscillation or van Driest's function

$\bar{F}$ = filtered inviscid flux vector

F_η = periodic forcing function in η direction

F_ξ = periodic forcing function in ξ direction

$\bar{G}$ = filtered viscous flux vector

H = shape factor $H = \delta^* / \theta$

i, j, k = tensor indices

k = wavenumber

K = turbulent kinetic energy

l = bubble length

l_m = pitching moment parameter

$l_\circ$ = length scale of the largest eddy

l_{SGS} = length scale for unresolved flow

L_z = domain length in spanwise direction

L_{ij} = Germano identity

m_{ij} = eddy viscosity for dynamic Smagorinsky model

M = reference Mach number

n = amplification factor

N = maximum wave number

N_t = total number of grid points

N_z = total number of grid points in spanwise direction

N_η = number of grid points in curvilinear direction η

N_ξ = number of grid points in curvilinear direction ξ

$\bar{p}$ = filtered pressure

Pr = Prandtl number

q_{SGS} = velocity scale for unresolved flow

q = flow variable

$\bar{q}$ = filtered flow variable

q' = small scale of the flow variable

$\tilde{q}$ = Favre filtered flow variable

Q = conservative flow variables or second invariant of the velocity gradient tensor

$\bar{Q}$ = filtered conservative flow variables vector

$R_{\delta_s^*}$ = Reynolds number based on displacement thickness and velocity at separation.

R_{θ_s} = Reynolds number based on momentum thickness and velocity at separation.

Re = Reynolds number based on the free-stream conditions and chord-length

R_{uu} = two-point velocity correlation function

$\bar{S}_{ij}$ = strain rate tensor

S_t = Strouhal number ($f\, c \sin\alpha$/U)

t = non-dimensional time

$\tilde{T}$ = filtered temperature

T_s = time scale

$u_\circ$ = velocity scale of the largest eddy

u,v,w = velocity components in Cartesian coordinates

u',v',w' = fluctuation velocity components in Cartesian coordinates

$\tilde{u}_1,\tilde{u}_2,\tilde{u}_3$ = filtered velocity components in Cartesian coordinates

u_τ = friction velocity

U = free stream velocity

U_H, U_E, U_n = convective velocities in viscous inviscid interaction modelling

x, y, z = Cartesian coordinates

x_s = stretched grid variable

y^+ = wall units in *y* direction $y^+ = \frac{yu_\tau}{\nu}$

α = angle of attack

$\bar{\alpha}$ = mean angle

$\dot{\alpha}$ = rate of change of incidence

δ^* = displacement thickness

δ_{ij} = Kronecker delta

ε = dissipation rate

ϕ = phase angle for phase-averaged measurement

ϕ = random number between 0 and 2π

γ = ratio of specific heats

$\bar{\Delta}$ = filter size

Δx^+ = wall units in *x* direction $\Delta x^+ = \frac{\Delta x u_\tau}{\nu}$

Δt = time step

Δz^+ = wall units in *z* direction $\Delta z^+ = \frac{\Delta z u_\tau}{\nu}$

$\Delta\alpha$ = amplitude of flow oscillation

η = Kolmogorov scale of length

η^+ = freestream boundary

μ = dynamic viscosity

θ = momentum thickness

ν = fluid kinematic viscosity

ν_s = surface transpiration velocity

ρ_∞ = free stream fluid density

$\bar{\rho}$ = filtered fluid density

τ = Kolmogorov scale of time

$\tau_\circ$ = time scale of the largest eddy

τ_{ij} = subgrid scale stress tensor

τ_{kk} = isotropic part of the SGS Reynolds stress tensor

τ_w = shear wall stress

υ_t = eddy viscosity

ω = circular frequency of flow oscillation

σ = filter coefficient

$\xi^{\pm}$ = exit boundary

$\psi(x)$ = one-dimensional field

$\langle\ \rangle$ = averaging over z

DNS = direct numerical simulation

DS = dynamic Smagorinsky model

FFT = fast Fourier transformation

LES = large eddy simulation

LES_narrow = large eddy simulation with narrow computational domain ($L_z = 0.2\ c$)

LES_wide = large eddy simulation with wide computational domain ($L_z = 0.5\ c$)

LSB = laminar separation bubble

MTS = mixed time scale

PIV = particle image velocimetry

RANS = Reynolds-averaged Navier-Stokes

RPV = remotely piloted vehicle

SGS = subgrid scale

SM = Smagorinsky model

TF = transfer function

UAV = unmanned air vehicle

VII = viscous-inviscid interaction

1. Introduction

This thesis is concerned with large eddy simulation of airfoil flows with Reynolds numbers of the order of 10^5, for which laminar-turbulent transition and boundary-layer separation control the performance. For example, the performance of the airfoil is markedly decreased when the flow fully detaches from an airfoil surface (airfoil stall) which may occur as a result of the bursting of the laminar separation bubble over the airfoil surface. The high level of unsteadiness of the laminar separation bubble just prior to stall, where low-frequency flow oscillation is sometimes observed, can also reduce the performance. Accurate prediction of the laminar-turbulent transition process and associated flow phenomena is possible using numerical tools such as direct numerical simulation and large eddy simulation. Low-Reynolds airfoil performance can be improved by controlling the boundary layer which also needs an efficient numerical tool that can predict the effect of flow control techniques on the performance of the low-Reynolds number airfoil.

This chapter presents a literature review of flow phenomena associated with low-Reynolds number aerodynamics and flow control, and begins in section 1.1 with a literature review of types of stall and the role of the laminar separation bubble. The mechanism of flow separation and structure of the laminar separation bubble including the important literature review is illustrated in section 1.2. Section 1.3 points out the mechanism and the importance of low-frequency flow oscillation phenomena. Section 1.4 presents a literature review of the dynamic stall phenomenon. Section 1.5 considers flow control techniques that can be used to modify the flow boundary layer in order to enhance the airfoil performance. Finally, the objectives and structure of the PhD thesis are given.

1.1 Types of airfoil stall and role laminar separation bubble

Stall of an airfoil is a critical phenomenon that limits the performance. Airfoil stall can be classified into three main types: leading-edge stall, thin-airfoil stall, and trailing-edge stall (McCullough and Gault, 1951). The leading-edge stall phenomenon occurs when the flow separates near the leading edge without any reattachment downstream of the separation. In thin-airfoil stall, the flow reattaches and becomes turbulent. The point

of reattachment shifts downstream as the angle of attack is increased. In trailing-edge stall, the separation of the turbulent boundary layer first occurs at a point near the trailing edge and then moves toward the leading edge as the angle of attack is increased.

Early studies of leading-edge stall and thin-airfoil stall, such as Crabtree (1959), Owen and Klanfer (1953), Gaster (1966), and Young & Horton (1966), made lasting contributions to understanding the phenomenon of laminar separation bubbles, which control both these types of stall. The laminar separation bubble (LSB) phenomenon is important in many applications involving low Reynolds numbers. Stall behaviour at low Reynolds numbers is currently of much interest due to applications to micro air vehicles and unmanned air vehicles (UAVs) where there may be laminar separation near the leading edge (Lissaman, 1983; Mueller and DeLaurier, 2003). Despite this importance, there is still only a limited capability to predict and control LSBs. Remotely piloted vehicles (RPVs) have recently been introduced for scientific and military purposes. These RPVs are small vehicles which are flying at high altitude (up to 30 km from sea level) where the kinematic viscosity is high due to the significant decrease of the ambient density. Therefore, these RPVs operate at Reynolds numbers lower than half a million and require specially-designed low-Reynolds-number airfoils (Lissaman, 1983).

Over the last half century, extensive research has been conducted concerning the stalling of airfoils at relatively high Reynolds numbers, i.e. Reynolds numbers that exceed one million (Lissaman, 1983). Low-Reynolds-number airfoils have not been studied as extensively, because until recently UAVs were not used widely for military or civilian purposes. In addition, there are some difficulties that have limited the study of the low-Reynolds-number airfoils, such as the lack of experimental techniques to capture the three-dimensional time-dependent nature of transition and LSB behaviour, which have significant effects on the performance of the airfoil. In spite of the fact that many experimental and analytical studies have been carried out, methods for predicting the development of LSBs are still limited. More extensive airfoil data are available for moderate to high Reynolds numbers, for which the turbulent boundary layer remains attached to the airfoil. Thus there is a need for continuing research on low-Reynolds-number airfoils, especially given the improved capacity and performance of computers to

perform calculations using highly-accurate numerical methods, such as direct numerical simulation (DNS) and large eddy simulation (LES), which can be used to study the characteristics of flows at low Reynolds numbers.

The laminar-to-turbulent transition process usually occurs near to the leading edge in the flow over an airfoil at high Reynolds ($Re > 10^6$) number, and thus the boundary layer is turbulent over a large part of the airfoil. A turbulent boundary layer is better able to resist separation than a laminar boundary layer due to the high rate of momentum transport in the normal direction. By contrast, if the Reynolds number is low ($10^4 < Re < 10^6$) the boundary layer will be laminar over a longer distance than for higher Reynolds number airfoils, and hence the flow may become fully separated, or else turbulent entrainment will lead the flow to reattach downstream of the transition point to form a laminar separation bubble. If the Reynolds number is lower than 10^4 the laminar boundary layer will likely separate without any subsequent reattachment (Gad-el-Hak, 1990). Accurate modelling of laminar separation bubbles is important for the prediction of lift and drag. Sometimes a bubble can be removed by imposing disturbances upstream of the separation point. However, the resulting turbulent boundary layer will dominate the flow field above the upper surface of the airfoil, causing increases in skin friction, which in turn results in increased drag. If the separated shear layer fails to reattach, the separation will cause stall (Haggmark, 2000). On the other hand, bubbles can be useful in fixing transition, and this is exploited in some high performance airfoils (e.g. Giguère and Selig, 1999).

The large effects of an LSB on airfoil performance are illustrated by Laitone (1997), who compared measurements of lift and drag for low-Reynolds-number, rectangular platform wings of the NACA 0012 profile with thin, flat, cambered plates. He found that there is a discontinuity of lift coefficient versus the increase of the angle of attack when a flow around the NACA 0012 airfoil is studied at a Reynolds number below 70,000. This discontinuity can be seen when the Reynolds number is 20,700 as illustrated in Figure 1.1, taken from Laitone (1997). He also showed that, as the Reynolds number increases, the discontinuity decreases, as shown in Figure 1.2 where the Reynolds number is increased to 42,100. The discontinuity disappeared as Reynolds number approaches

70,000, which is considered to be the critical Reynolds number above which performance is more consistent.

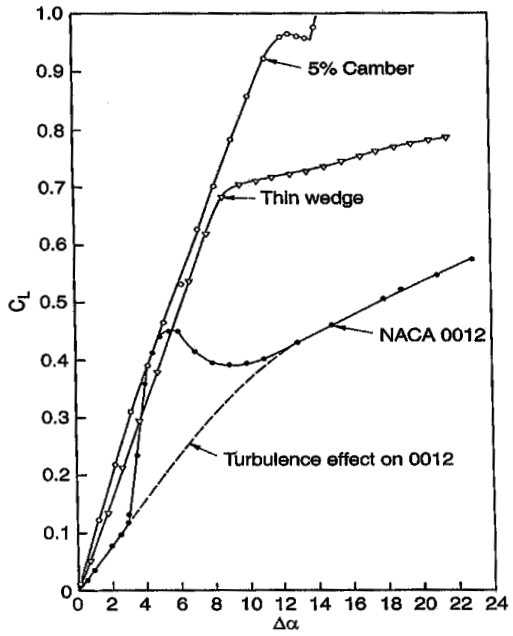

Figure 1.1 Variation of lift coefficient with the angle of attack of NACA 0012, thin, flat, and cambered plates (Laitone 1997)

1.2 Structure of a laminar separation bubble

1.2.1 Pre-1990 investigations

The behaviour of the flow at low Reynolds number is governed by two phenomena: laminar boundary layer separation and transition to turbulence. The laminar separation bubble typically occurs as a result of an adverse pressure gradient on the upper surface of the airfoil. The boundary layer is created when the fluid particles slow down by friction, to satisfy the no slip condition on the body surface. When the pressure increases in the direction of flow the velocity of fluid particles in the near wall region decreases, and if the resulting adverse pressure gradient is strong enough the fluid particles break away from the surface at a point called the separation point. The direction of the velocity becomes reversed behind this point. The thickness of the rotational flow is enlarged immediately after the boundary layer separation point accompanied by a pronounced increase of the normal velocity component. Transition to turbulence usually occurs downstream of the separation and allows the flow to reattach to the surface, hence creating a laminar separation bubble.

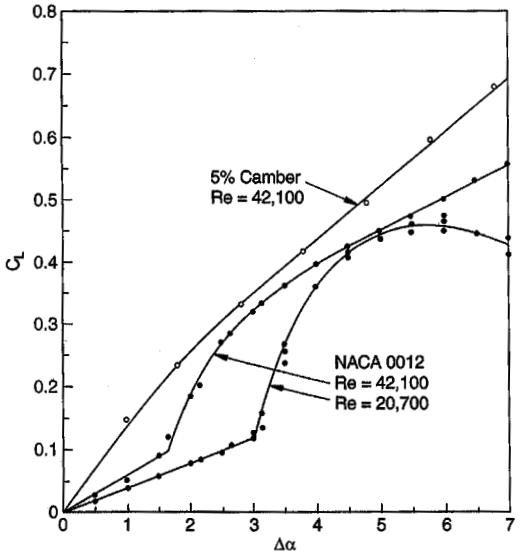

Figure 1.2 Behaviour of lift coefficient when increasing Reynolds number from 20,700 to 42,100 on NACA 0012 (Laitone 1997)

A useful sketch of a laminar separation bubble was given by Horton (1969) and developed by Roberts (1980) as shown on Figure 1.3, where S, R and T represent the separation point, the reattachment point and the transition point, respectively. In this figure, the laminar separation bubble is divided into two main sections: the first one is the separated shear layer which falls between the two lines, $S''T''R''$ and $ST'R$, whereas the second section is the area between STR line and $ST'R$ line. The second section contains the bubble and consists of the "reverse flow vortex" which lies downstream of the transition point T, and the "dead air region" which falls upstream of the transition point T. The dead air region has a constant surface pressure "plateau" as illustrated in Figure 1.4 (Roberts 1980).

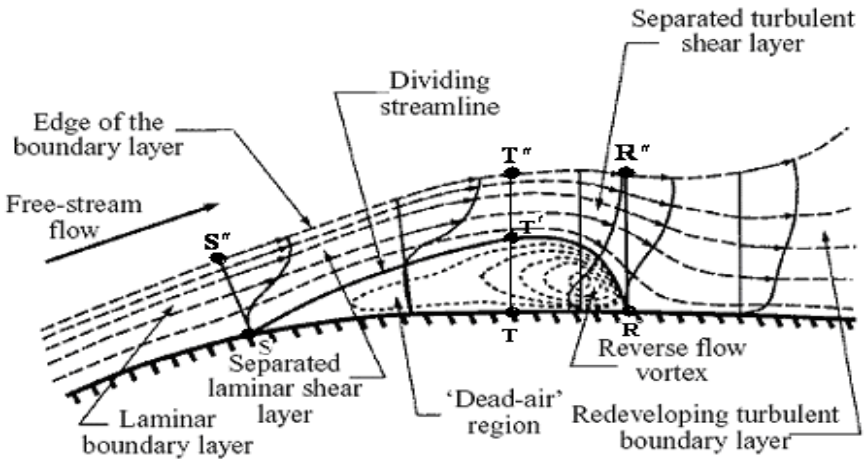

Figure 1.3 Short laminar separation bubble with expanding in z direction (Horton 1969)

The bubble behaviour strongly depends on the strength of the adverse pressure gradient, the angle of attack and the Reynolds number. If the Reynolds number is decreased or the angle of attack is increased then the flow may become unable to resist the adverse pressure gradient and the shear layer may fail to reattach causing a fully separated flow (Baragona 2004). It is also possible for the flow to reattach after long distance, causing a "long" bubble to be produced. The process of altering a "short" bubble, occupying a relatively small percentage of airfoil chord, to a long bubble or even to full separation, is called "bursting".

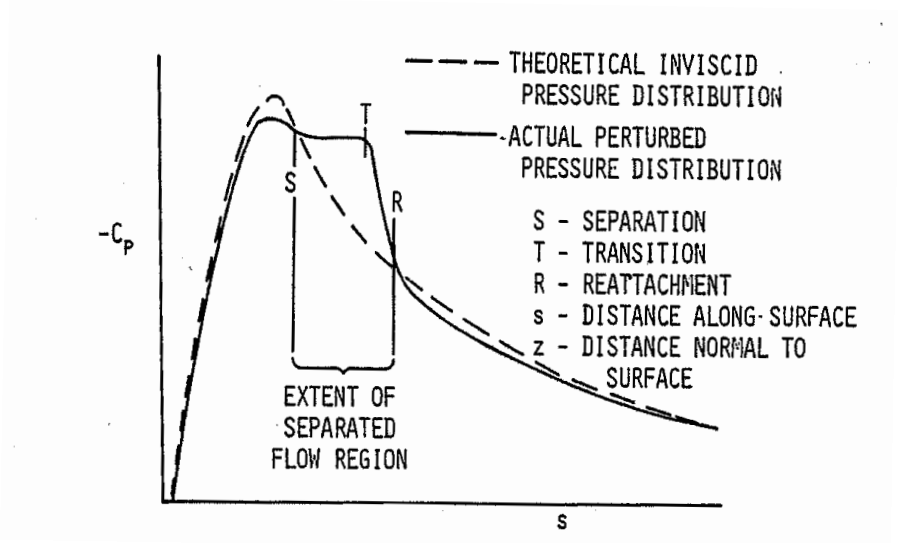

Figure 1.4 The surface pressure distribution as illustrated by Roberts (1980)

Crabtree (1959) investigated experimentally a two-dimensional straight wing with a 10 per cent thick RAE 101 section in a low-speed wind tunnel. His results supported the conclusion of Owen and Klanfer (1953) about the critical value of Reynolds number that distinguishes between short and long bubbles. This Reynolds number is based on the displacement thickness and the velocity of the boundary layer at the separation point $R_{\delta_s^*} = U\delta_s^*/\nu$. Owen and Klanfer (1953) found that if $R_{\delta_s^*}$ is greater than 550 the bubble can be classified as a short bubble while if $R_{\delta_s^*}$ is less than 450 it will be a long bubble. The range of 450 to 550 can result in either a short or long bubble. They suggested that if the ratio of bubble length to the displacement thickness at the separation point l/δ_s^* is of the order of 100 the bubble will be called short. On the other hand the long bubble has l/δ_s^* on the order of 10^2 to 10^3.

Gaster (1966) studied the behaviour of a large number of bubbles on a flat plate experimentally by putting an inverted airfoil above the flat surface. By changing the location and incidence angle of the airfoil he was able to measure the behaviour of many bubbles. A dimensionless pressure gradient $\left(\frac{\theta_s^2}{\nu}\frac{\Delta U}{\Delta x}\right)$ was found to be an important parameter that describes and controls the behaviour of the bubble. The momentum thickness was preferred since it changes more slowly than the displacement thickness near separation. Gaster found that when the normalized pressure gradient is equal to -0.09 separation occurred and the corresponding critical Reynolds number (R_{θ_s} = 125 or $R_{\delta_s^*}$ = 460) determines the onset of the bursting.

The classification into short and long bubbles can also be made based on their effects on pressure and velocity outside the separation bubble. Figure 1.5 (Gaster, 1966) shows the influence of decreasing the Reynolds number R_{θ_s}, on the behaviour of the pressure distribution around the laminar separation bubble. The extent of constant pressure increases as the Reynolds number is decreased, but after the reattachment point R the pressure distributions corresponding to the Reynolds numbers R_{θ_s} = 394, 347, 332 and 284 become almost the same as in the theoretical inviscid pressure distribution, only

with a small reduction in the suction peak. On other hand, when R_{θ_s} is decreased to 232 the suction peak decreases dramatically and as the extent of the constant pressure continues to increase, the circulation decreases. This significant change indicates that bursting has occurred and the separation bubble has changed to a long bubble. In conclusion, the short bubble has an insignificant effect on the pressure distribution in the outer region of the separation bubble while the long bubble has a significant effect.

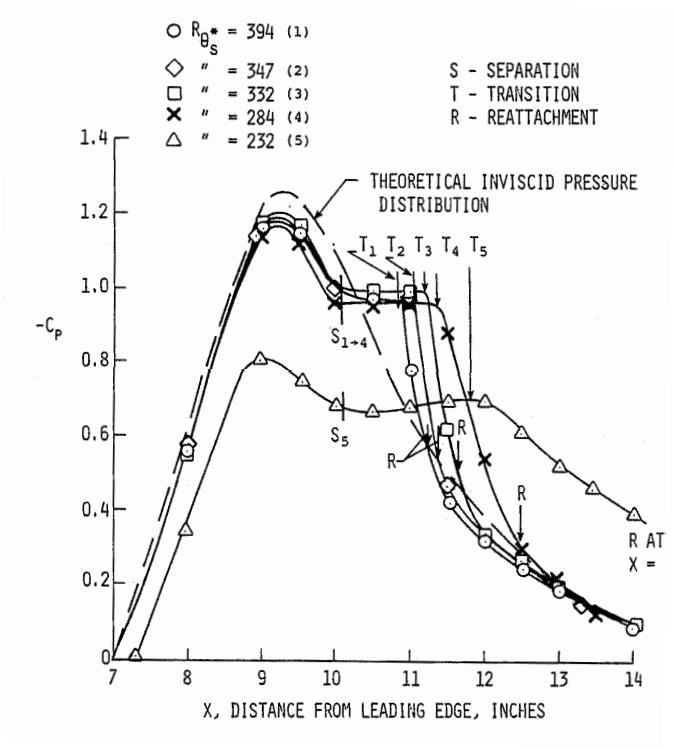

Figure 1.5 Pressure distribution on the surrounding area of the separation bubble

Horton (1969) used the experimental results for turbulent and laminar boundary layer separation from Gaster (1966) to develop a semi-empirical method for predicting the growth and bursting of laminar separation bubble. Horton found that bursting has occurred when the turbulent boundary layer fails to reattach, and when the theoretical pressure recovery does not intersect the inviscid pressure distribution.

Prediction of a laminar separation bubble was successively achieved by Drela and Giles (1987) who used a viscous-inviscid interaction (VII) computational method on low-Reynolds number airfoil flows. They used the steady Euler equations to describe the

inviscid flow and two integral equations for the boundary layer which are coupled by the displacement thickness to describe the viscous flow. The nonlinear set of equations was solved simultaneously by the Newton method.

1.2.2 Post 1990 investigations

The increasing capacity and performance of computers allows the study of LSB phenomena by high accuracy numerical methods, such as DNS and LES. The first two-dimensional simulation was presented by Pauley *et al.* (1990), who solved the incompressible unsteady Navier-Stokes equations to study the periodic shedding of vortices from an LSB in channel flow, by imposing an adverse pressure gradient obtained by a suction technique. Their time-averaged results show a favourable agreement with the experiment of Gaster (1966). They suggested that bursting might be the time-average of the periodic vortex shedding. They also found that there is no direct effect of the Reynolds number on some of the characteristics of flow separation, such as the Strouhal number based on the vortex shedding and boundary layer momentum thickness. The two-dimensional computations of Pauley *et al.* (1990) were extended to three-dimensions by Pauley (1994) who added random noise and sine wave perturbations at the inlet of the same computational domain. She showed that the behaviour of the separated flow is essentially the same as in the two-dimensional simulation when the streamlines are averaged across the span, in the case of the random noise disturbances. The length of the separated region was found to be longer with a lower vortex shedding frequency in the case of the sine wave perturbation. Ripley and Pauley (1993) investigated separation at low-Reynolds number by solving two-dimensional unsteady incompressible Navier-Stokes equations for a fluid with constant viscosity. Periodic vortex shedding was observed. They verified the inviscid pressure distribution of Gaster (1966) but with a spike in the pressure distribution at the end of pressure plateau. This spike was eliminated when three-dimensional large-eddy simulation (LES) was used (Wilson and Pauley, 1998). They also studied the influence of several parameters and models of LES such as constant and dynamic coefficient subgrid scale models.

Alam and Sandham (2000) studied the behaviour and structure of a short laminar separation bubble in both two- and three-dimensional flows. They produced an adverse

pressure gradient by applying a suction profile at the upper boundary condition. In the two-dimensional simulation, they found that the short laminar separation bubble was 40% longer than that produced by the three-dimensional simulation. In the same study, the forced transition process was shown to occur by oblique modes with subsequent Λ–vortex breakdown and reattachment as turbulent flow. Incompressible flow over a flat surface was also simulated in a DNS by Spalart and Strelets (2000). They used aspiration through the opposite boundary, thereby forcing the laminar boundary layer to separate. Their simulation showed the complete process of transition to turbulence for a flow in which they also observed a "wavering" of the shear layer within the transition region, followed by Kelvin-Helmholtz vortices that were amplified to produce a three-dimensional flow without pairing, which means that the cause of the transition is the growth of Kelvin-Helmholtz disturbances. Over the separated flow region, skin friction initially has small negative values, followed by a weak attempt to recover during which it approaches a value of zero, before developing to large negative values. This behaviour was used to identify a process of turbulent re-separation. A large eddy simulation on a flat plate with semicircular leading edge was carried out by Yang and Voke (2001), who demonstrated that the free shear layer of the laminar separation bubble becomes inviscidly unstable by means of the Kelvin-Helmholtz instability mechanism. The instability waves grow downstream until they are converted by secondary instability to three-dimensional motions. Streamwise vortices are formed in the vicinity of the reattachment point and roll-up further downstream of the laminar separation bubble, leading to a breakdown to turbulence.

The process was studied experimentally by Zhang *et al.* (2008), who applied a quasi-3D PIV technique on the SD7003 airfoil at Reynolds numbers of 20,000 and 60,000 and an incidence of 4°, to study vortex shedding in the transition of the LSB and the propagation of vortices in the turbulent boundary layer. They verified the DNS results of Spalart and Strelets (2000) and the LES results of Yang and Voke (2001) concerning the primary role of the Kelvin-Helmholtz mechanism on the vortex shedding of the vortices and the subsequent breakdown to turbulence.

One of the first attempts to simulate a three-dimensional flow over lifting body configuration was by Hoarau *et al.* (2003). They used DNS to simulate incompressible flow around a NACA 0012 airfoil at a very low Reynolds number (Re = 800) and an incidence of 20°. They used a second-order accurate, central finite-difference scheme to solve the space derivatives and a fractional time-stepping scheme with second-order accuracy. They used a domain with four chord lengths in the spanwise direction for a three-dimensional simulation for which the results of a two-dimensional simulation were used as an initial condition. The objectives of their study were to show the feasibility of the DNS to capture the 3D coherent structures in the early stages of turbulence and to show the onset of secondary instability. They identified the three-dimensional transition mechanism and observed that the lift and drag coefficients obtained from the three-dimensional simulation are significantly reduced compared to the two-dimensional simulation. They found vortex shedding from the upper surface of the airfoil as a result of the von Karman wake instability instead of the Kelvin-Helmholtz instability, because of the very low Reynolds number. They considered their simulation as a vital step toward a full transition to turbulence and higher Reynolds numbers.

The quasi-3D LES (only 4 points across span with spanwise domain width of 0.012 chord) of Yuan *et al*. (2006) on an SD7003 airfoil at a Reynolds number of 60,000 was able to capture some important physical behaviour, but the laminar separation bubble at high incidence (8°) was 50% larger than the experimental measurements of Nerger *et al*. (2003). They speculated that this difference was due to the 1% freestream turbulence intensity in the experiment which is consistent with Hall and Gibbings (1972) and Lian and Shyy (2007), who showed that the transition point of the boundary layer shifts forwards with an increase in the freestream turbulence intensity leading to a shorter and thinner LSB, but it may also be due to the effect of the inadequate spanwise width of the computational domain of their LES. More recently, laminar separation bubbles at different Reynolds numbers and incidences for a flow past an SD7003 airfoil were investigated by Windtle *et al*. (2006) who showed that two-dimensional unsteady Reynolds-Averaged Navier-Stokes (RANS) simulations can provide comparable results with the experiments in terms of the transition position and the size of the LSB.

A complete laminar-turbulent transition process was demonstrated numerically by Shan *et al.* (2005), who performed a two- and three-dimensional DNS study for a compressible flow over NACA 0012 with Mach number of M = 0.2, a Reynolds number of 100,000, and an incidence angle of 4^o. They captured the most important phenomena for a flow at UAV flight conditions, such as flow separation, vortex shedding, breakdown to turbulence, and boundary layer reattachment. In their two-dimensional simulation, they explained the early stages of the development of instability in the near-wake region, and how the disturbances grow and are carried upstream by the acoustic waves toward the separated shear layer near the airfoil leading edge.

Jones *et al.* (2008) presented the first resolved DNS of flow around a NACA-0012 airfoil at Reynolds number of 50,000 and $\alpha = 5°$. They triggered the transition to turbulence by adding volume forcing to the momentum equations and found that the turbulence self-sustains due to the absolute instability of the vortex shedding. They observed that the behaviour of the laminar separation bubble in the forced case was different to the unforced case, and that forcing is able to improve the aerodynamic performance of the airfoil. The interpretation of instability development was clarified and expanded by Jones *et al.* (2010), who provided contours of perturbations at successive times to illustrate an acoustic feedback instability mechanism.

1.3 Low-frequency flow oscillations of airfoil flows near stall

As the angle of incidence is increased a short bubble can burst and either fail to reattach or become much longer. Recent experiments have also seen an unusual switching between stalling and non-stalling for low-Reynolds-number airfoils, with unsteady separation bubbles exhibiting low-frequency oscillations. For example, Zaman *et al.* (1989) made some remarkable conclusions about the low-frequency phenomenon during an experimental and numerical study of flow around two-dimensional airfoils at low Reynolds numbers in the range of 0.15×10^5 – 3.0×10^5. They concluded that the flow oscillations corresponding to this phenomenon are different from other fluid mechanical phenomena, such as bluff-body shedding, flow over cavities, or supersonic jet screech. They also specified the types of airfoils where the low-frequency oscillations can occur, which are the airfoils that exhibit either ‘trailing-edge stall’ or ‘thin-airfoil stall’. The

fluctuations of the lift coefficient were found to be as much as 50% of the mean lift coefficient. Figure 1.6 is taken from Zaman *et al.* (1989) to provide insight into the behaviour of lift coefficient during the low-frequency oscillation phenomenon.

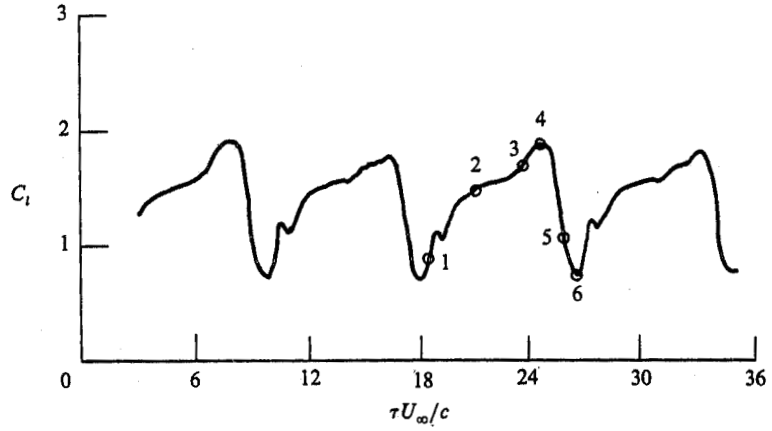

Figure 1.6 Computational results for time-dependent lift coefficient for the LRN airfoil at Re = 75,000 with 15° incidence taken from Zaman *et al.* (1989).

In a later study, Bragg *et al.* (1996) tested an LRN-1007 airfoil at Reynolds numbers between 0.3×10^6 and 1.25×10^6 and at incidences between 14.4° and 16.6°. The lift coefficient exhibited a low frequency oscillation and they found that as the incidence was increased, the Strouhal number (defined as $St = fc\sin\alpha/U_\infty$, where f is the frequency of the flow oscillation, c is the chord length, α is the incidence, and U_∞ is the free stream velocity) tended to increase. Strouhal numbers associated with the oscillation lay in the range of 0.017 to 0.03, which is around ten times lower than the Strouhal number for bluff body shedding. Broeren and Bragg (1999) performed another experiment using the same airfoil at Re = 3×10^5 and $\alpha = 15°$ for which phase averages on the upper surface of the airfoil clearly showed a growth of the leading edge separation bubble and trailing edge separation until they merged, causing full boundary layer separation and stall. Broeren and Bragg (2001) tested five different airfoil shapes (NACA 2414, NACA 64A010, LRN-1007, E374 and Ultra-Sport) measuring the wake velocity across the span and using mini-tufts for flow visualisation. They classified the cases according to the type of airfoil stall, which were 'leading-edge stall' for the NACA 2414 airfoil, 'trailing-edge stall' for the Ultra-Sport airfoil and 'thin airfoil stall' for the NACA 64A010. The LRN-1007 and E374 airfoils exhibited a combination of thin airfoil stall and

the trailing edge stall, i.e. the laminar separation bubble formed near the leading edge and grew in length as the incidence increased, but at the same time the flow separated near the trailing edge and the separation point moved forward until it merged with the laminar separation bubble. They found that the low frequency flow oscillation always occurs in the airfoils that exhibited thin airfoil stall or the combination of both the thin airfoil stall and the trailing edge stall. They noted that the low frequency flow oscillation is essentially a two-dimensional phenomenon.

Rinoie and Takemura (2004) performed a similar experimental study of a NACA 0012 airfoil at a Reynolds number of 130,000 and $\alpha = 10°$ and $11.5°$ that provided insight into the mechanism behind the low-frequency oscillation. At $\alpha = 10°$, they detected a steady, short laminar separation bubble near the leading edge with a length of approximately 10% chord. In the time-averaged flow they observed the formation of a long bubble with a length of 35% chord at $\alpha = 11.5°$. At this incidence the flow exhibited a regular low frequency oscillation in which it switched between a short laminar separation bubble of about 10% chord near the leading edge and a fully separated flow. Phase-averaged measurements indicated that the flow oscillations formed a short laminar separation bubble, similar to that at $\alpha = 10°$, at a phase angle $\phi = 0°$, and then the flow separated to form a long bubble between $\phi = 45°$ and $\phi = 90°$ with 30% and 50% chord, respectively. The flow separated completely without any reattachment between $\phi = 90°$ and $\phi = 270°$, and a short laminar separation bubble was formed again at $\phi = 315°$. Until the present project this phenomenon has not been studied by direct or large-eddy simulation.

The most recent research in the low-frequency flow oscillation was conducted by Sandham (2008), who used a time accurate viscous-inviscid interaction method for the coupled potential flow and integral boundary-layer equations to study several airfoils near stall. He modelled the laminar-turbulent transition by an absolute instability, which sustains the transition of the laminar bubble without using any upstream perturbations. The Strouhal number S_t for the low-frequency flow oscillations was found to be dependent on the shape of the airfoil. He concluded that the phenomenon of the low-

frequency oscillation can be captured by simple models of boundary layer transition and turbulence, because the bubble bursting occurred as a consequence of potential flow/boundary-layer interactions. However, such models need further development and calibration, for example against numerical simulations, which are becoming increasingly feasible (Jones *et al.* 2008).

1.4 Dynamic stall

In the previous section it was seen how a harmonic behaviour emerged naturally near stall. A related phenomenon occurs when the oscillations are imposed, for example by oscillating the airfoil in pitch. Dynamic stall is an unsteady phenomenon that is characterised by pitching the airfoil beyond the static stall angle, leading to a significant increase in the stall angle. In dynamic stall the aerodynamic forces such as the lift, drag and pitching moments are very different from those obtained in the static stall. Dynamic vortex shedding is often associated with dynamic stall, where a large eddy originates near the leading edge of the airfoil and then convects downstream during the oscillation cycle.

The first observation of the dynamic stall was in the helicopter blades where it was found that each blade was switching periodically between stalled and unstalled states which then produced large blade oscillations. Dynamic stall can also adversely affect the performance of the axial-flow compressor blades and large wind turbines (Akbari and Price, 2003).

An important study of the dynamic stall phenomenon was made by McCroskey *et al.* (1976) who experimentally investigated the origin of the boundary layer separation and the mechanism of the leading-edge vortex shedding for an incompressible flow with moderate to high Reynolds number. They tested a NACA-0012 airfoil over a wide range of Reynolds numbers with and without different leading edge modifications. They also applied boundary-layer trips to eliminate the leading-edge bubble to investigate whether the bursting of the leading-edge bubble is responsible for the dynamic stall as suggested by Johnson and Ham (1972). Instead, they found that the vortex shedding was fed by sudden turbulent boundary layer separation.

McCroskey *et al.* (1976) also studied the effect of different parameters such as the Reynolds number, the amplitude of the oscillation, the reduced frequency (defined as $k = \omega c / 2U_\infty$, where $\omega = 2\pi f$ is the circular frequency of the flow oscillation) and the airfoil geometry. They found that the Reynolds number, airfoil geometry and the type of the boundary layer have negligible effects on the dynamic vortex shedding, whereas there were major influences of the amplitude of oscillation, leading edge geometry and the reduced frequency on the time-dependent lift and pitching moment coefficients.

Dynamic stall of a NACA 0012 airfoil that oscillates in pitch at high Reynolds number (Re = 10^6) was studied by Tuncer *et al.* (1990) who carried out unsteady two-dimensional computations for turbulent flow based on a velocity-vorticity formulation of the incompressible Navier-Stokes equations incorporating the Baldwin-Lomax turbulence model. The NACA 0012 airfoil was oscillating sinusoidally with $\alpha(t) = 15^\circ + 10^\circ \sin(\omega t)$, with several different reduced frequencies (k = 0.1, 0.15 and 0.25). They found that their numerical method was capable of capturing the dominant characteristics of the dynamic stall, including the leading-edge vortex shedding, and their computational results were in good agreement with experiment. They described the mechanism of the dynamic stall process from observations of instantaneous streamlines and the lift, drag and pitching moment coefficient behaviour. During the upstroke motion, the flow on the upper surface exhibited a small trailing edge separation that started at $\alpha = 6°$ and was seen to move upstream rapidly at $\alpha = 20°$ where the boundary layer thickness was noticeably increased. It is important to mention that the flow was found to be still attached to the airfoil, which contrasts with the static airfoil simulation in which the flow detached from the airfoil completely at $\alpha = 12°$. The boundary layer continued to grow as the airfoil incidence increased until the trailing edge separation reached the leading-edge at $\alpha = 23°$. After that (at $\alpha = 23.9°$), a sudden flow separation near the leading-edge occurred with the formation of a large vortex that was shed downstream with a constant velocity. The speed of this dynamic stall vortex over an NACA0012 airfoil was measured experimentally by McCroskey *et al.* (1976) as 35-40% of the freestream velocity, whereas it was determined numerically by Ericsson and Reding (1980) as 40% of the freestream velocity over a cambered airfoil. Tuncer *et al.* (1990) also found that as the reduced frequency of

oscillation increases, the dynamic stall and the corresponding formation of the dynamic stall vortex shedding is delayed to a higher incidence. This conclusion was also found and highlighted in other publications such as McCroskey *et al.* (1976), Choudhuri and Knight (1996), Visbal and Shang (1989), Akbari and Price (2003) and Ducoin *et al.* (2009).

Lorber and Carta (1988) studied experimentally the effect of constant pitch rate ramps of a Sikorsky SSC-A09 airfoil at large Reynolds number ($2\times10^6 < \mathrm{Re} < 4\times10^6$). The magnitude of the pitch rate ramps (defined as $A = \dot{\alpha}c / 2U_\infty$, where A is the pitch rate, $\dot{\alpha}$ is the rate of change of incidence) were varied between A = 0.001 and A = 0.020, whereas the Mach number was between 0.2 and 0.4. They observed that the strength of the dynamic vortex increases as the pitch rate increases whereas it decreases as the Mach number increases. They noticed that there is a rapid increase of the lift coefficient at the birth of the dynamic vortex. They supported the conclusion of McCroskey *et al.* (1976) that the bursting of the leading-edge laminar separation bubble is not responsible for the dynamic stall phenomenon, since they observed that the flow near the leading edge was fully attached at incidences just beyond the dynamic stall whereas the flow was separated over the trailing edge portion.

A two-dimensional numerical study was performed by Akbari and Price (2003) who used a vortex method, with the assumptions that the flow is laminar, unsteady and incompressible, to investigate the effect of several parameters on the behaviour of the dynamic stall for a NACA-0012 airfoil with pitching oscillation. The parameters varied were the Reynolds number (Re = 3000 – 10,000), the reduced frequency of oscillation (k = 0.15, 0.25 and 0.5), the mean incidence ($\bar{\alpha}$ = 15° and 20°) and the location of the pitch axis (x/c = 0.25 and 0.5). The Reynolds number was found to have little influence on the characteristics of the dynamic stall, such as the force and pitching moment coefficients, which is in agreement with the observation of McCroskey *et al.* (1976). The reduced frequency was found to be a major factor that affects the flow separation, which was found to be delayed to a higher incidence as the reduced frequency increased. The maximum lift coefficient occurred at an incidence close to the maximum angle of the pitching oscillation. Increasing the mean incidence was found to advance the flow separation during the dynamic stall oscillation cycle, while it was found that moving the

location of the pitch axis backward had a small effect on the formation and shedding of the dynamic stall vortex. When the observations of Akbari and Price (2003) are compared with those of Tuncer *et al*. (1990), it is obvious that the parameters that affect the characteristics of the dynamic stall phenomenon for laminar flow are almost the same as for the flow.

Visbal and Shang (1989) performed a two-dimensional simulation to solve the Navier-Stokes equations for laminar flow around a rapidly pitched NACA 0015 airfoil at a Reynolds number of 10,000 and Mach number of 0.2. They investigated the effect of the pitch axis of the airfoil and also the constant pitch rate case, in which the airfoil was pitching constantly from $\alpha = 0°$ to $\alpha = 60°$. Their results were comparable with experiment even though they assumed that the flow was laminar. The flow exhibited a highly unsteady motion where the flow separation point moved upstream from the trailing-edge toward the leading edge, where the dynamic vortex formed and was shed downstream. They also found that as the pitch rate increased the dynamic stall angle was increased and as the pitch axis moved downstream the formation of the dynamic stall vortex was delayed, with an associated decrease of the aerodynamic forces such as the pressure and lift coefficients.

1.5 Control of flow separation

The ultimate objective of much of the research into separation bubbles is to understand how to control the flow. Boundary layer control can be defined as any process that can change the behaviour of the boundary layer in order to provide an enhancement of performance. There are different objectives for boundary layer control, such as delaying or advancing the transition (depending on the application), preventing or triggering separation, reducing the skin-friction drag, or enhancing the lift coefficient. Also, there are different routes or methods that may achieve these objectives whether actively or passively.

In most situations separation has a bad effect on performance, for example separation is usually responsible for a loss of lift and an increase of drag of airfoils. If the separation is delayed then the drag will decrease and the lift will be enhanced. Separation

can be avoided by designing a specific shape by, for example, enforcing the skin friction to be just above zero along the surface. This concept was developed by Stratford (1959a) who forced the turbulent boundary layer to remain at the onset of the separation condition but without separating. It was experimentally used by Stratford (1959b) to obtain a flow with low drag. An inverse design was used by Liebeck (1978), who calculated the pressure profile required to achieve the Stratford condition. He experimentally tested his airfoil shapes at several low-Reynolds numbers (5×10^5 to 2×10^6) and found that if the adverse pressure gradient is kept very close to the separation state the improved pressure recovery would result in higher lift-to-drag ratio. The main drawback of this technique, i.e. reducing the skin-friction to zero to enhance the performance of the airfoil, is that the flow may suddenly separate if the incidence is increased by a few degrees and thus the performance of the airfoil will sharply decrease.

The basic idea for most boundary layer control methods is to add momentum to the fluid particles that are very close to the wall. Examples of these methods include suction (Purohit, 1987), blowing (McLachlan, 1989) acoustic excitation (Zaman *et al*, 1987), periodic forcing excitation by imposing an oscillating wire or flap upstream of the separation (Roos and Kegelmant, 1986; Katz *et al.*, 1989; Bar-Sever, 1989), creating streamwise vortices via passive or active vortex generators (Shan *et al.*, 2008) and utilising magnetic field through plasma actuators (Post and Corke, 2004; Huang *et al.*, 2006). An extensive review of these boundary layer control methods is provided by Gad-el-Hak and Bushnell (1991). Flow separation control is currently used with very good impact in aeronautical applications such as the vortex generators on commercial aircraft wings, the flap with blowing on some supersonic fighters, and the passive bleeding at the entrance to the Concorde engine (Gad-el-Hak and Bushnell, 1991).

It is important to understand the basic principle of the behaviour of the velocity profile near the point of separation, which can be modified to postpone or advance the separation. At the separation point the gradient of velocity at the wall $\left(\partial u/\partial y\right)_o$ is zero while it is positive upstream of the separation point and negative downstream of the

separation point. A necessary condition for flow separation is $\left(\partial^2 u/\partial y^2\right)_o > 0$, so in order to allow the flow to remain attached this quantity should be changed to become negative.

Flow can be forced to be turbulent by promoting transition, either by placing mechanical roughness elements near the leading edge of the airfoil or by adding momentum to the flow in the near wall region. Roughness elements, which can be serrations, bumps or ridges (Gad-el-Hak, 1989), develop nonlinear disturbances in the boundary layer thus bypassing the linear stages of transition. The effect of roughness elements, which are also called "turbulators", is found to be more significant in low-Reynolds number airfoils. Lissaman (1983) found that the lift-to-drag ratio was increased by 25% when a roughness strip was placed at a distance of 25% chord from the leading edge of an airfoil at a Reynolds number of 40,000, while the improvement decreased to 10% when the Reynolds number was increased to 60,000 and no improvement was found at a Reynolds number of 100,000. Turbulators should be designed to produce a turbulent boundary layer as thin as possible, because a thick turbulent boundary layer suffers from high drag and is less resistant to separation than a thin one.

Greenblatt and Wygnanski (2000) emphasised that periodic forcing (or excitation) is an efficient tool to control flow separation compared to traditional methods. They mentioned two main disadvantages of using traditional methods for separation control, which are the complicated engineering design and weight of the plumbing system for continuous suction or blowing, and the need for auxiliary compressors or large amount of engine bleeding. In a recent paper, Shan *et al*. (2008) performed numerical simulations with active and passive vortex generators to study the feasibility of controlling flow separation over a NACA0012 airfoil at a Reynolds number of 10^5 and an incidence of 6°. Active vortex generators were capable of entirely eliminating the time- and span-averaged laminar separation bubble and were found to be more effective than passive vortex generators which could not eliminate the laminar separation bubble completely. It should be noted that, despite the elimination of the laminar separation bubble, the lift was not increased and the drag was not reduced. This result is surprising because the performance of the airfoil should be enhanced when the bubble size is reduced or

eliminated. In contrast, Gross and Fasel (2009) showed that the lift coefficient increased from 0.632 to 1.24 when they introduced pulsed vortex generator jets to control the flow separation over NACA 64-618 airfoil at a Reynolds number of 64,000 and incidence of 8.64°. Also, You and Moin (2008) showed that the turbulent separation over an NACA 0015 airfoil at a high Reynolds number (Re = 896,000) and incidence of 16.6°, can be delayed and the lift coefficient can be increased significantly by providing suction and blowing to the near wall flow. They performed large eddy simulations to implement the synthetic jet, which consists of a slot placed near the leading edge (12% chord from the leading edge) and extended across the span with a cavity inside the airfoil. They found that synthetic jet actuation was responsible for a 70% increase of lift coefficient and a 15-18% decrease of drag coefficient.

Perturbations can be used to initiate an earlier transition. For example, Jones (2007) introduced low amplitude disturbances by adding volume forcing to the momentum equations. The ability to initiate the instability by periodic disturbances means that it can be used to reduce the size of an LSB by advancing the transition. The perturbations can also be introduced in the form of sound waves. Collins and Zelenevitz (1975) showed that the sound waves can partially reattach the separated flow over a NACA 2412 airfoil at Reynolds number is 2.9×10^5 for two high angles of incidence α = 20.25° and 23.9°, above the static stall incidence which is about 12°. The lift coefficient was increased by more than 35% for the former angle and 53% for the latter angle. The drag reduction was 49% and 26% in the 20.25° and 23.9°cases, respectively.

The influence of acoustic excitation on low-Reynolds number applications was also investigated experimentally by Zaman *et al.* (1987). He studied a range of flows around the LRN-1007 airfoil with Reynolds numbers (4×10^4 to 1.4×10^5) and at different incidences where the airfoil is either unstalled, pre-stall with the low-frequency flow oscillation phenomenon, or fully stalled. He found that in the cases where the flow exhibited a laminar separation bubble without eventually stalling, the laminar separation bubble was entirely eliminated using low amplitude and frequency of the external acoustic excitation, but with a significant loss of lift coefficient, which was also found to continue to fall as the excitation frequency was decreased. He also observed that the low-

frequency flow oscillation, which was detected in the airfoil wake in the pre-stall cases, was entirely eliminated by a high frequency of excitation, but again with a pronounced loss of lift coefficient. He observed that in stall cases it is essential to introduce very high amplitude external acoustic waves, which then produce transverse velocity components with a corresponding enhancement of the lift and drag, and suggested that producing transverse velocity perturbations is more practical and effective than external acoustic excitation. Hsiao *et al.* (1990) explained that the effectiveness of their internal acoustic approach was due to the resulted improvement in the flow mixing and momentum transport, which produced suction peak at the leading edge of the NACA 63_3-018 airfoil and increased significantly the performance of the airfoil.

Periodic forcing was utilised for flow separation control by Bar-Server (1989) who inserted a 0.1 mm tungsten oscillating wire upstream and parallel to the LRN(1)-1010 airfoil to produce spanwise velocity perturbations. He studied the effect of periodic forcing over a wide frequency range for several incidences above the static stall angle. He observed that the stall angle, at a Reynolds number of 1.5×10^5, was increased from 11° to about 20°, with an associated increase in the maximum lift coefficient. Separation was delayed and moved from the leading edge to about 80% chord when he applied the forcing technique at the post stall incidence $\alpha = 20°$, with a 30% drag reduction and 11.9% lift increase.

Passive flow separation control was used by Rinoie *et al.* (2009) to suppress the NACA-0012 airfoil stall at a Reynolds number of 130,000. They successfully delayed the burst of the short laminar separation bubble by inserting a thin plate inclined to the surface and inside the separated shear layer at a higher incidence than the stall incidence. As a result, the maximum lift coefficient was increased by about 0.1 and the stall angle was increased from 11° to 13°. They found that the vortical structures that were generated at the trailing edge of the thin plate (which they called “burst control plate”) could affect the vortical structures inside the short laminar separation and this led to the burst delay. The study of Rinoie *et al.* (2009) did not mention the effect of the burst control plate on the performance of the airfoil in terms of lift to drag ratio.

To summarise, it appears that flow control can be used to delay separation and enhance the performance of airfoils, and in particular periodic forcing may be exploited as a flow control tool. The effect of periodic forcing on the airfoil performance is investigated in the present study and comparisons with other studies will be presented. In particular, the flow control technique will also be used to remove a "flapping" mode of the NACA-0012 airfoil at a Reynolds number of 50,000 and Mach number of 0.8.

1.6 Objectives of the PhD

The main objectives of this PhD project were:

1) To develop and validate a numerical tool for large eddy simulation of a low-Reynolds number flow around NACA 0012 airfoil, including the behaviour of the laminar separation bubble. This will allow simulations to be carried out near stall, focusing on bubble bursting phenomena.

2) To carry out simulations which capture the unusual switching between stalled and unstalled flow for an airfoil at low Reynolds number. The importance of the computational domain width on the phenomenon will be examined.

3) To study the laminar separation bubble under a condition of dynamic stall by both the large eddy simulation and a viscous-inviscid interaction method, and compare the results with the natural low-frequency flow oscillation.

4) To investigate the ability of simpler predictive methods such as the viscous-inviscid interaction methods to study the unsteadiness of the laminar separation bubble including the low-frequency flow oscillation phenomenon.

5) To investigate the feasibility of applying flow control, in the form of boundary layer disturbances introduced upstream of separation, for two purposes :

    a) to enhance the aerodynamics properties of a flow with low Reynolds number (Re = 50,000) near stall where the flow was found to switch between stalled and non-stalled conditions, and

b) to reduce or entirely eliminate the flapping oscillation on the two-dimensional simulation at incidence of 0° and Reynolds number of 5×10^4.

1.7 Structure of thesis

In Chapter 2, the numerical methods, governing equations and subgrid scale models are introduced and the filtering approach is discussed. In order to validate the developed numerical code, an "*a posteriori*" study between DNS and LES with and without a subgrid scale model is performed in Chapter 3. The developed LES code is utilised in Chapter 4 to attempt to capture the low-frequency flow oscillation for a flow around a NACA 0012 airfoil near stall at Reynolds numbers of 50,000 and 130,000. Additionally, the effect of the computational domain width on the low-frequency flow oscillation phenomenon is investigated. Chapter 5 considers the behaviour of a laminar separation bubble of flow under dynamic stall conditions by large eddy simulation and viscous-inviscid interaction method and compares the results with the natural low-frequency flow oscillation. Chapter 6 studies the low-frequency flow oscillation phenomenon for the NACA 0012 airfoil near stall, by viscous-inviscid interaction. Chapter 7 presents the effect of the flow separation control by performing LES with periodic forcing applied to the low-frequency flow oscillation and flapping phenomena.

2 Numerical simulation methods

The starting point for the present investigation was the direct numerical simulation code that was applied to airfoil flow by Jones (2007). In the present study this code is extended to large eddy simulation using filtering and sub-grid scale modelling.

In this chapter, two numerical approaches will be presented: direct numerical simulation and large eddy simulation. First of all, it is important to provide some background on the spatial and temporal scales of turbulence, so that the resolution requirements of the two approaches can be assessed. Then, governing equations for unsteady compressible flow including the subgrid scale (SGS) stress tensor are demonstrated. The procedure of modelling the subgrid scale by three types of models is explained, together with the low-pass filtering that is used for the simulations.

2.1 Turbulence scales and energy

Turbulent flow can be decomposed into a range of spatial and temporal scales. The largest scales are governed by the geometry of the flow while the smallest scales are governed by the fluid viscosity ν and the rate of energy dissipation ε. According to the Kolmogorov hypothesis the turbulent kinetic energy is transferred from large scales (also called large eddies) to small scales until it reaches smallest scales (known as the Kolmogorov scales). This energy cascade is calculated from

$$E = C\varepsilon^{2/3}k^{-5/3}, \tag{2.1}$$

where k is the wavenumber and C is a universal Kolmogorov constant which is taken from experimental data to be equal 1.5 (Pope 2000). The smallest scales in the turbulent flow are called the "Kolmogorov scales" of length, velocity and time, and are given respectively as

$$\eta = \left(\frac{\nu^3}{\varepsilon}\right)^{\frac{1}{4}}, \tag{2.2}$$

$$u = \left(\varepsilon\nu\right)^{\frac{1}{4}}, \tag{2.3}$$

$$\tau = \left(\frac{\nu}{\varepsilon}\right)^{\frac{1}{2}}, \tag{2.4}$$

On the assumption that the rate of dissipation, at equilibrium, is equal to the rate of production we have

$$\varepsilon \sim \frac{u_o^3}{l_o}, \tag{2.5}$$

where l_o is the length of the largest scale and u_o is corresponding scale for flow velocity. When ε is substituted into equation (2.2) we have

$$\eta = \left(\frac{\nu^3 l_o}{u_o^3} \cdot \frac{l_o^4}{l_o^4}\right)^{\frac{1}{4}} \Rightarrow \eta = \left(\frac{\nu^3}{u_o^3 l_o^3}\right)^{\frac{1}{4}} \cdot l_o. \tag{2.6}$$

The Reynolds number is defined as

$$\mathrm{Re} = \left(\frac{u_o l_o}{\nu}\right). \tag{2.7}$$

If we substitute (2.7) into (2.6) the following equation is obtained:

$$\frac{\eta}{l_o} \sim \mathrm{Re}^{-\frac{3}{4}}. \tag{2.8}$$

Following a similar procedure, the ratio of the other Kolmogorov scales to the largest scales can be easily obtained as follows

$$\frac{u}{u_o} \approx \mathrm{Re}^{-\frac{1}{4}}, \tag{2.9}$$

$$\frac{\tau}{\tau_o} \approx \mathrm{Re}^{-\frac{1}{2}}. \tag{2.10}$$

Here, τ_o is the timescale for the largest scale and Re is the Reynolds number. Thus the small scales of turbulence all get smaller compared to the large scales as Re increases.

2.2 Computational cost and direct numerical simulation (DNS)

The cost of resolving all turbulence scales by solving the three dimensional Navier-Stokes equations for isotropic turbulence is estimated to be around 4.4 $\mathrm{Re}^{9/4}$ (i.e. scaling with the cube of equation (2.8)) for total grid points required, and proportional to

Re^3 for computational time (Pope 2000). The numerical method dealing with fully resolved simulation is called direct numerical simulation (DNS). Obviously, applications of DNS are limited by the very fine mesh required to capture physical phenomena, so it is not applicable for designing aerodynamic devices at high Reynolds number. However, low Reynolds number aerodynamic applications such as micro air vehicles are likely to be feasible for DNS (Jones 2007).

2.3 Large eddy simulation

To avoid the high computational cost of DNS the approach of calculating the large scales of the turbulent flow and modelling the small ones, known as large eddy simulation (LES), has been developed. LES is playing an important role in the field of numerical computation of complex flows and is considered a powerful technique of solving the Navier-Stokes equations due to its ability to reproduce many time-dependent properties of turbulent flow.

Three steps are required to implement LES: the first step is the application of a filtering process to the Navier-Stokes equations, so that the small spatial scales are removed. As a result, the equations of motion for the "large eddy" portion of the flow will be produced. These equations include a subgrid scale stress tensor which describes the effect of the small unresolved scales on the resolved scales. The second step is constructing an expression from the resolved scale to create a "model" of the subgrid scale (SGS) stress tensor. The final step is to perform numerical simulations of the equations obtained from the first and second step. This numerical simulation should be applied on a fine enough grid so that the large eddies are resolved. As a comparison, the smallest scales of the large eddy simulation are much larger than the Kolmogorov scales which were mentioned in section 2.1.

One important advantage of using the LES for a flow calculation is its ability to resolve the large eddies directly. These are controlled by the geometry and boundary conditions of the flow and are largely responsible for much of the momentum, mass, and energy transport in the flow. LES models only the small eddies, which are less dependent on the geometry and are often taken to be more universal. However, LES still requires

fine meshes with relatively large numbers of grid points near the wall for high Reynolds number flows. LES also requires high numerical accuracy, which can be difficult to obtain. Compared to the Reynolds-averaged Navier Stokes (RANS) approach, LES needs a considerable computational time, which can be considered as another drawback of this method. However, the distinguishing feature of LES is its ability to capture important unsteady phenomena in a complex flow, such as the laminar separation bubble and vortex shedding in the present application. It is also useful in the study of control of turbulence by unsteady forcing.

2.4 Governing Equations

Any flow variable can be represented as a combination of large and small scales, i.e. if q is the flow variable, then $q = \overline{q} + q'$, where $\overline{q}$ is the large scale part, which can be resolved by LES, and q' is the small scale part of the flow, which must be modelled by a subgrid scale model (SGS). It is convenient to define $\overline{q}$ as a low-pass filtered flow variable. For compressible flow, it is appropriate to use $\tilde{q} = \dfrac{\overline{\rho q}}{\overline{\rho}}$ in the equations as a Favre (density weighted) filtered flow variable. The conservative and dimensionless form of the three-dimensional, unsteady, filtered Navier-Stokes equations for a viscous compressible flow can be written as:

$$\frac{\partial \overline{Q}}{\partial t} + \frac{\partial \overline{F}_j}{\partial x_j} = \frac{\partial \overline{G}_j}{\partial x_j} \tag{2.11}$$

where $\overline{Q}$ is a vector containing the filtered conservative flow variables, $\overline{F}$ is the filtered inviscid flux vector, and $\overline{G}$ is the filtered viscous flux vector. The variable and flux vectors can be written in dimensionless form (Mary and Sagaut, 2002) as

$$\overline{Q} = \begin{bmatrix} \overline{\rho} \\ \overline{\rho}\tilde{u}_1 \\ \overline{\rho}\tilde{u}_2 \\ \overline{\rho}\tilde{u}_3 \\ \overline{\rho}\left(\dfrac{\tilde{T}}{\gamma(\gamma-1)M_o^2} + \dfrac{\tilde{u}_1\tilde{u}_1 + \tilde{u}_2\tilde{u}_2 + \tilde{u}_3\tilde{u}_3}{2} \right) \end{bmatrix}, \overline{F}_j = \tilde{u}_j\overline{Q} + \begin{bmatrix} 0 \\ \delta_{1j}\overline{p} \\ \delta_{2j}\overline{p} \\ \delta_{3j}\overline{p} \\ \overline{p}\tilde{u}_j \end{bmatrix}, \overline{G}_j = \begin{bmatrix} 0 \\ \overline{\sigma}_{1j} - \tau_{1j} \\ \overline{\sigma}_{2j} - \tau_{2j} \\ \overline{\sigma}_{3j} - \tau_{3j} \\ \overline{\sigma}_{kj}\tilde{u}_k + \overline{b}_j \end{bmatrix}$$

where $\bar{\rho}$ refers to the filtered fluid density, $(\tilde{u}_1, \tilde{u}_2, \tilde{u}_3) = (\tilde{u}, \tilde{v}, \tilde{w})$ are the filtered velocity components vector in Cartesian coordinates, $\tilde{T}$ is the filtered temperature, γ is the ratio of specific heats, and M is the reference Mach number. The term b_j is defined as:

$$\bar{b}_j = \frac{\mu(\tilde{T})}{(\gamma-1)\,\mathrm{Re}\,\mathrm{Pr}\,M^2}\frac{\partial \tilde{T}}{\partial x_j}, \tag{2.12}$$

in which the dynamic viscosity of air μ can be calculated from a dimensionless form of Sutherland's law:

$$\mu(\tilde{T}) = \tilde{T}^{\frac{3}{2}}\frac{1+C}{\tilde{T}+C}, \tag{2.13}$$

where $C = 0.3686$ is used in the present study. The filtered temperature $\tilde{T}$ is related to the filtered density $\bar{\rho}$ and the filtered pressure $\bar{p}$ by the ideal gas law:

$$\tilde{T} = \gamma M^2 \frac{\bar{p}}{\bar{\rho}}. \tag{2.14}$$

All coordinate variables are non-dimensionalised by the airfoil chord c, while the velocity variables are non-dimensionalised by the inflow free-stream velocity U_∞ and time is normalized by c/U_∞. The density and temperature variables are normalized by their freestream conditions, whereas the pressure is normalized by $\rho_\infty U_\infty^2$. The viscous stress tensor $\bar{\sigma}_{ij}$ can be written as:

$$\bar{\sigma}_{ij} = \frac{\mu(\tilde{T})}{\mathrm{Re}}\left(\frac{\partial \tilde{u}_i}{\partial x_j} + \frac{\partial \tilde{u}_j}{\partial x_i} - \frac{2}{3}\delta_{ij}\frac{\partial \tilde{u}_k}{\partial x_k}\right) \tag{2.15}$$

where δ_{ij} is the Kronecker delta, and Re is the Reynolds number based on the free-stream conditions and chord-length

$$\mathrm{Re} = \frac{\rho_\infty u_\infty c}{\mu_\infty}, \tag{2.16}$$

The quantity τ_{ij} is the SGS stress tensor that expresses the effect of the small scales on the residual stress and should be modelled:

$$\tau_{ij} = \overline{\rho u_i u_j} - \overline{\rho u_i}\,\overline{\rho u_j}/\overline{\rho} \quad . \tag{2.17}$$

The models used in the present study are based on the concept of an eddy viscosity, so the stress tensor is written as

$$\tau_{ij} - \frac{1}{3}\delta_{ij}\tau_{kk} = 2\overline{\rho}\upsilon_t\left(\overline{\mathrm{S}}_{ij} - \frac{1}{3}\delta_{ij}\overline{\mathrm{S}}_{kk}\right), \tag{2.18}$$

where τ_{kk} is the isotropic part of the SGS stress tensor, υ_t refers to the eddy viscosity (which is given by the SGS model) and the strain rate tensor is defined as

$$\overline{S}_{ij} = \frac{1}{2}\left(\frac{\partial \tilde{u}_i}{\partial x_j} + \frac{\partial \tilde{u}_j}{\partial x_i}\right) \quad . \tag{2.19}$$

Applying dimensional analysis to the eddy viscosity υ_t gives:

$$\upsilon_t \;\; \alpha \;\; l_{SGS} \;\; u_{SGS} \tag{2.20}$$

where l_{SGS} and u_{SGS} are length and velocity scales for the unresolved motion, respectively. Modelling details will be given in section 2.6.

2.5 Spatial and temporal discretizations

The basic airfoil code (Jones, 2007) employs a fourth-order accurate central difference scheme for spatial discretization of the interior points and a Carpenter fourth-order accurate scheme (Carpenter *et al.*, 1999) to treat points near the boundary. The temporal discretization uses a fourth-order Runge-Kutta explicit scheme

$$q_i^{n+1} = q_i^n + \frac{1}{6}(k_1 + 2k_2 + 2k_3 + k_4) \tag{2.21}$$

$$k_1 = \left(\Delta t \frac{d(q_i^n)}{dt}\right)_{t=t_n} \tag{2.22}$$

$$k_2 = \left(\Delta t \frac{d(q_i^n + \frac{k_1}{2})}{dt}\right)_{t=t_n+\frac{\Delta t}{2}} \tag{2.23}$$

$$k_3 = \left(\Delta t \frac{d(q_i^n + \frac{k_2}{2})}{dt} \right)_{t=t_n+\frac{\Delta t}{2}} \tag{2.24}$$

$$k_4 = \left(\Delta t \frac{d(q_i^n + k_3)}{dt} \right)_{t=t_n+\Delta t} \tag{2.25}$$

The code implements the Runge-Kutta explicit scheme in a memory-efficient way, hence instead of using four arrays to store the 4 variables (k_1, k_2, k_3 and k_4), the code only uses 3 arrays (Q_{store} , Q_{old} and Q_{new}); Q_{old} stores the data from the previous time step which are fixed during the Runge-Kutta calculations whereas Q_{store} sums the four variables at each Runge-Kutta calculation step. The Q_{new} array is used to save the values of the four variables during the Runge-Kutta calculations until the last step when it is used to add the Q_{store} array to the value of the previous time-step data which are already stored in Q_{old}. Starting from $Q_{store} = 0$, the following procedure shows the time-stepping Runge-Kutta calculations.

$$\text{step1: } Q_{store} = Q_{store} + \frac{d(Q_{old})}{dt}, \text{ then } Q_{new} = Q_{old} + \frac{1}{2}\Delta t \frac{d(Q_{old})}{dt} \tag{2.26}$$

$$\text{step2: } Q_{store} = Q_{store} + 2\frac{d(Q_{new})}{dt}, \text{ then } Q_{new} = Q_{old} + \frac{1}{2}\Delta t \frac{d(Q_{new})}{dt} \tag{2.27}$$

$$\text{step3: } Q_{store} = Q_{store} + 2\frac{d(Q_{new})}{dt}, \text{ then } Q_{new} = Q_{old} + \Delta t \frac{d(Q_{new})}{dt} \tag{2.28}$$

$$\text{step4: } Q_{store} = Q_{store} + \frac{d(Q_{new})}{dt}, \text{ then } Q_{new} = Q_{old} + \frac{1}{6}\Delta t \frac{d(Q_{store})}{dt} \tag{2.29}$$

2.6 Subgrid-scale models

Several models have been developed to describe the effect of the SGS stress components. In general, an SGS model can be tested by comparing LES solutions with DNS solutions or with experimental results.

2.6.1 Smagorinsky model

The most widely-used SGS model, which exhibits good results for simple flows, is the Smagorinsky model (SM) (Smagorinsky, 1963). As with most other SGS models it employs the concept of eddy viscosity by relating the subgrid scale tensor to the strain rate of the resolved velocity field, as described mathematically in equation (2.18). The subgrid length scale l_{SGS} can be expressed by

$$l_{SGS} = C_s \overline{\Delta} \,, \tag{2.30}$$

where $\overline{\Delta}$ is the filter size, C_s is a constant and the velocity scale u_{SGS}

$$u_{SGS} = l\sqrt{2\overline{S}_{ij}\overline{S}_{ij}} \,. \tag{2.31}$$

Hence, the eddy viscosity can be expressed as

$$\upsilon_t = \left(\mathrm{C_s}\overline{\Delta}\right)^2 \sqrt{2\overline{S}_{ij}\overline{S}_{ij}} \,. \tag{2.32}$$

Several studies have been carried out to find the optimum value of $\mathrm{C_s}$. For example, Deardorff (1970) suggested that, for some flows such as wall-bounded flows, this value should be as low as 0.1 to avoid excessive damping, whereas Mason and Callen (1986) gave a role of thumb for finding an optimum value of C_s, saying that the higher its magnitude, the more accurate the finite-difference solution, but with a reduced range of scales resolved, whereas lower values of C_s indicate a wider range of scales resolved, but there is a higher possibility of numerical errors and a poor solution. They found also that C_s = 0.2 gives an optimum numerical solution, if it is applied with adequate resolution to homogeneous isotropic turbulence. Moin and Kim (1982) applied an exponential damping function to the near-wall region of plane channels so that the subgrid-scale stresses are reduced at this region. For this purpose, they used van Driest's function

$$f = 1 - \exp\left(\frac{-y^+}{25}\right) \tag{2.33}$$

as the wall-damping function, where y^+ is the distance to the nearest wall and the wall units are defined by

$$y^+ = \frac{yu_\tau}{\nu}, \tag{2.34}$$

where u_τ is the friction velocity which can be obtained from the following equation

$$u_\tau = \sqrt{\frac{\tau_w}{\rho}} \tag{2.35}$$

where τ_w is the wall shear stress. Therefore, the Smagorinsky model is modified for boundary layer flows to be of the following form:

$$\upsilon_t = \left(\mathrm{C_s}\bar{\Delta} f\right)^2 \sqrt{2\bar{S}_{ij}\bar{S}_{ij}} \tag{2.36}$$

As can be noticed from equation (2.33), in order to calculate the wall-damping function in an SGS model, the wall-unit coordinate y^+ must be used. The friction velocity near flow separation and reattachment points approaches zero, and thus the wall-damping function at this region will be almost zero, which gives a solution with low accuracy, hence using an SGS model free from a wall-damping function is important to obtain a more accurate solution. Another disadvantage of the SM for practical large-eddy simulation is the constant C_s, which should be regulated based on the type of flow. However, the most compelling advantage of the use of the SM is its simplicity.

Piomelli *et al.* (1990) proved that the Smagorinsky model is not appropriate to use for large-eddy simulation of transition to turbulence in plane channels, because it exhibits more dissipative characteristics, especially in the early stages of the transition where excessive damping of the resolved structures occurs. They found that the energy cascade is reversed in the early stages of the transition, i.e. energy is transferred from the small scales to the large scales, which is not observed in the fully turbulent flow. Piomelli *et al.*(1990) showed that the standard Smagorinsky model failed to predict the reversal of the energy cascade in the early stage of transitional flow. They postulated that this failure occurs because the model is constructed based on the large scale structures and always predicts nonzero residual stresses even in the laminar regions. Piomelli *et al.* (1990) overcame this defect by inserting the van Driest damping and shape factor functions into the subgrid length scale.

2.6.2 Dynamic Smagorinsky model

Germano *et al.* (1991) proposed an SGS model that overcame several defects of the basic Smagorinsky model using dynamic procedure in which the constant C_s varies in space and time during the calculation. He introduced a test filter $\tilde{G}$ with a test filter width $\tilde{\Delta}$, which should be greater than the length of the filter size $\bar{\Delta}$, which is normally the grid size and, if filtering is applied to the three spatial directions, can be calculated as $\left(\Delta_x \Delta_y \Delta_z\right)^{1/3}$. After applying the test filter to the filtered Navier-Stokes, equation (2.11) becomes

$$\frac{\partial \tilde{\bar{Q}}}{\partial t} + \frac{\partial \tilde{\bar{F}}_j}{\partial x_j} = \frac{\partial \tilde{\bar{G}}_j}{\partial x_j} \tag{2.37}$$

and the corresponding subgrid scale

$$T_{ij} = \widetilde{\overline{\rho u_i u_j}} - \widetilde{\overline{\rho u_i}}\,\widetilde{\overline{\rho u_j}}/\tilde{\bar{\rho}} . \tag{2.38}$$

Then, Germano found an algebraic relationship between T_{ij} and the filtered subgrid-scale by test filter $\tilde{\tau}_{ij}$, which is called the 'Germano identity'

$$L_{ij} = \tilde{\bar{\rho}} T_{ij} - \widetilde{\bar{\rho}\tau_{ij}} , \tag{2.39}$$

or

$$L_{ij} = \widetilde{\overline{\rho u_i}\,\overline{\rho u_j}/\bar{\rho}} - \widetilde{\overline{\rho u_i}}\,\widetilde{\overline{\rho u_j}}/\tilde{\bar{\rho}} . \tag{2.40}$$

Equation (2.40) is the resolved turbulent stress, and it can be solved explicitly by filtering. A Smagorinsky model is used for T_{ij} and $\tilde{\tau}_{ij}$, so that

$$\tilde{\tau}_{ij} = -\widetilde{C\bar{\Delta}^2 \left|\bar{S}\right| \bar{S}_{ij}} \tag{2.41}$$

and

$$T_{ij} = -C\tilde{\bar{\Delta}}^2 \left|\tilde{\bar{S}}\right| \tilde{\bar{S}}_{ij}, \tag{2.42}$$

where $\left|S\right| = \sqrt{2S_{ij}S_{ij}}$ is the magnitude of the strain rate tensor. Then, substituting equations (2.41) and (2.42) into equation (2.40) with multiplication of $\bar{S}_{ij}$ gives the following equation

$$\bar{S}_{ij} L_{ij} = -\tilde{\bar{\rho}} C \left(\tilde{\bar{\Delta}}^2 \left|\tilde{\bar{S}}\right| \tilde{\bar{S}}_{ij} \bar{S}_{ij} - \bar{\Delta}^2 \left|\tilde{\bar{S}}\right| \tilde{\bar{S}}_{ij} \bar{S}_{ij} \right). \tag{2.43}$$

Averaging over the spanwise direction for both sides of equation (2.43) produces the parameter C, which varies in spatial directions (x and y) and in time

$$C(x,y,t) = -\frac{\left\langle L_{kl} S_{kl} \right\rangle}{\tilde{\bar{\Delta}}^2 \left\langle \left|\tilde{\bar{S}}\right| \tilde{\bar{S}}_{mn} \bar{S}_{mn} \right\rangle - \bar{\Delta}^2 \left\langle \left|\tilde{\bar{S}}\right| \tilde{\bar{S}}_{pq} \bar{S}_{pq} \right\rangle}. \tag{2.44}$$

Hence, the dynamic eddy viscosity can be obtained and written as follows

$$m_{ij} = \frac{\left\langle L_{kl} \bar{S}_{kl} \right\rangle}{\left(\tilde{\bar{\Delta}}/\bar{\Delta}\right)^2 \left\langle \left|\tilde{\bar{S}}\right| \tilde{\bar{S}}_{mn} \bar{S}_{mn} \right\rangle - \left\langle \left|\tilde{\bar{S}}\right| \tilde{\bar{S}}_{pq} \bar{S}_{pq} \right\rangle} \left|\bar{S}\right| \bar{S}_{ij}. \tag{2.45}$$

An advantage of using the dynamic Smagorinsky (DS) model arises from the fact that it is not necessary to use an additional damping function near the solid boundaries and in laminar flow regions. Using the dynamic Smagorinsky model (DS) without averaging in a homogeneous plane will not guarantee a positive value of the eddy viscosity, which can lead to numerical instability, so the most important reason for averaging is to stabilize the solution. On the other hand, it is not always possible to find a homogeneous direction, especially for practical engineering flows. To rectify this limitation of the DS model, Ghosal *et al.* (1995) proposed a model based on 'dynamic localization' to determine the parameter C as a function of space and time, which is independent of the homogeneous direction and thus can be applied to any complex flow. The basic principle of their method is to constrain $C \geq 0$ before constructing an integral equation in a three-dimensional form that can be solved numerically at each time step to obtain C as a function of x, y, z, and t. They applied this model to isotropic turbulence and to flow over a backward-facing step, where a good agreement with experimental results was achieved. Furthermore, clipping, where negative values of C are changed to be zero, has been found to be useful for stabilizing the solution and preventing energy backscatter, thus ensuring that the energy is cascading from the large scales to small scales (Liu *et al.* 1994). Nevertheless, the DS model can suffer from computational instability which may require the use of a lower time step.

2.6.3 Mixed-Time-Scale model

The mixed-time-scale (MTS) model, which is constructed without using any explicit wall-damping function, was developed by Inagaki *et al.* (2005). In the MTS

model, the expression of the eddy viscosity mentioned in equation (2.20) is changed to be of the following form,

$$\upsilon_t \propto T_{SGS} \; u_{SGS}^2 \tag{2.46}$$

where T_{SGS} is a time scale, and u_{SGS} is a velocity scale, which can be calculated by explicitly filtering the velocity field using

$$u_{SGS}^2 = \left(\bar{u} - \tilde{\bar{u}}\right)^2. \tag{2.47}$$

When this expression for the velocity scale u_{SGS} is employed, the eddy viscosity υ_t in the laminar flow region will be guaranteed to approach zero, because the velocity scale approaches zero, as long as the flow is fully resolved and the velocity scale (u_{SGS}) approaches zero. This can be considered as an important benefit of using the MTS model, because it will not need supplementary damping functions. The time scale has been suggested by Inagaki *et al.* (2005) as $1/\left|\bar{S}\right|$. When they performed an *a priori* test in a channel flow, they found that the eddy viscosity $\upsilon_t \propto u_{SGS}^2/\left|\bar{S}\right|$ exhibited good agreement with other SGS models that have a wall-damping function, but it was not appropriate to implement this eddy viscosity in a region away from the wall where the problem of dividing by zero can arise. This problem was solved by adding another time scale $\bar{\Delta}/u_{SGS}$, which was proposed by Yoshizawa *et al.* (2000). Therefore, the eddy viscosity can be expressed as follows

$$\upsilon_t = \mathrm{C}_d T_s u_{SGS}^2 \tag{2.48}$$

where C_d is the fixed model parameter, and the time scale T_s can be obtained from the following equation

$$T_s^{-1} = \left(\frac{\bar{\Delta}}{u_{SGS}}\right)^{-1} + \left(\frac{C_t}{\left|\bar{S}\right|}\right)^{-1}. \tag{2.49}$$

The two model parameters C_d and C_t are set to be 0.03 and 10, respectively. These values were set from initial tests for turbulent channel flow with the currently used code and have since been left unchanged (Krishnan *et al.*, 2009).

2.7 Filtering approach

Grid-to-grid oscillations are not automatically removed by central finite difference schemes and may lead to numerical instabilities. To overcome this problem, artificial dissipation is often added to the Navier-Stokes equations. Another approach is to filter the flow field without disturbing the large scales. The latter technique will be used in the present work. The main aim of this section is to assess the effectiveness of various high order filters. The schemes are compared using spectral analysis for a one-dimensional test function.

2.7.1 Low-pass filter approach

Visbal and Rizzetta (2002) studied low-pass filtering and demonstrated its superior effects for compressible LES on a stretched, curvilinear grid, when it is incorporated into high-order, compact finite differencing schemes. They found that, in order to maintain numerical stability for a relatively coarse grid and thus suppress the numerical oscillations that arise from the unresolved scales, it is necessary to add a compact filter scheme with equal or higher order of accuracy than the spatial discretization. For example, the fourth order compact scheme should be combined with a filter of fourth order accuracy or greater.

Spatial filtering is carried out by applying explicit or implicit low-pass filters to the unfiltered field which produces an approximate solution. In order to understand the mechanism of the filtering operation the following equation will be studied:

$$\hat{q}_i + \beta\left(\hat{q}_{i-2} + \hat{q}_{i+2}\right) + \alpha\left(\hat{q}_{i-1} + \hat{q}_{i+1}\right) = aq_i + \frac{b}{2}\left(q_{i-1} + q_{i+1}\right) + \frac{c}{2}\left(q_{i-2} + q_{i+2}\right) + \frac{d}{2}\left(q_{i-3} + q_{i+3}\right) \tag{2.50}$$

where $\hat{q}_i$ represents the filtered value at point i, while the original (unfiltered) value is q_i at the same point i. This equation has been studied in detail, with more filter schemes than are presented here, in Lele (1992). The filter is called explicit if β and α are both zero. If one of them is not zero then the filter becomes implicit. Most of the necessary coefficients in equation (2.50) are derived by matching the coefficients of Taylor series

based on the order of accuracy order required for such a numerical scheme. The Taylor series derivation method is explained in Appendix A, where the fourth order tridiagonal filter scheme has been taken as an example. Table 2.1 illustrates several filter schemes, including coefficients and truncation errors. It should be noted that the superscript on the leading term of the truncation error represents the order of the filter.

The filter stencil is defined as the number of grid points required for one filtering process. For example if all of the coefficients on the right hand side of equation (2.50) (i.e. a, b, c and d) are non-zeros then the filter stencil will be 7 points wide. It is convenient to mention here the difference between a low-pass filter and a high-pass filter. A low-pass filter removes small scales, while a high-pass filter removes the large scales.

Table 2.1 Coefficients and truncation errors for several low-pass filters, applied to a grid with spacing *h*

Filter Scheme	β	α	a	b	c	d	***Truncation error***
4th order explicit (7-point stencil)	0	0	1/2	9/16	0	-1/16	$\frac{3}{16}h^4q^{IV}$
6th order explicit (7-point stencil)	0	0	11/16	15/32	-3/16	1/32	$\frac{1}{64}h^6q^{VI}$
4th order tridiagonal (5-point stencil)	0	0.475	7.85/8	7.8/8	-0.05/8	0	$\frac{0.05}{16}h^4q^{IV}$
4th order pentadiagonal (7-point stencil)	0.17029	0.65225	0.98919	1.3211	0.33335	0.00136	$\frac{-0.005}{16}h^4q^{IV}$
Top hat "A" (3-point stencil)	0	0	1/3	2/3	0	0	$-\frac{1}{3}h^2q^{II}$
Top hat "B" (3-point stencil)	0	0	1/2	1/2	0	0	$-\frac{1}{4}h^2q^{II}$

In the following sections, the filters presented in Table 2.1 will be compared using two methods: spectral analysis and filtering of random fields. Both of these methods produce a consistent prediction of the resolution characteristics of each of the filter schemes.

2.7.2 Spectral analysis:

Spectral analysis utilises the transfer function (TF) of equation (2.50)

$$TF(kh) = \frac{a + b\cos(kh) + c\cos(2kh) + d\cos(3kh)}{1 + 2\alpha\cos(kh) + 2\beta\cos(2kh)} \tag{2.51}$$

The derivation of this transfer function is described in Appendix A. Figure 2.1 shows the spectral behaviour of the selected filters schemes. The transfer function *TF* is equal to one if a wave passes through the filter unchanged. It is evident that the 4th order tridiagonal filter (α = 0.475) and the 4th order pentadiagonal filter maintains *TF* = 1 over the widest range of wavenumber compared to other filter schemes.

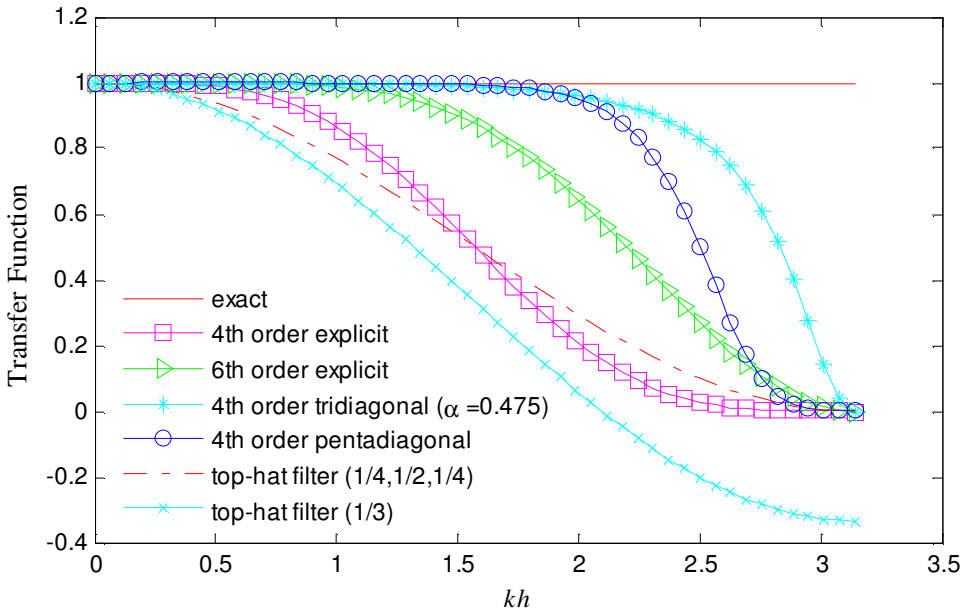

Figure 2.1 Filtering transfer function for different filter schemes.

Figure 2.2 shows the effect of increasing α towards 0.5 on the filtering transfer function. Setting the free parameter α of the fourth order tridiagonal filter as close as possible to 0.5 produces a spectral response with almost sharp cut-off characteristics.

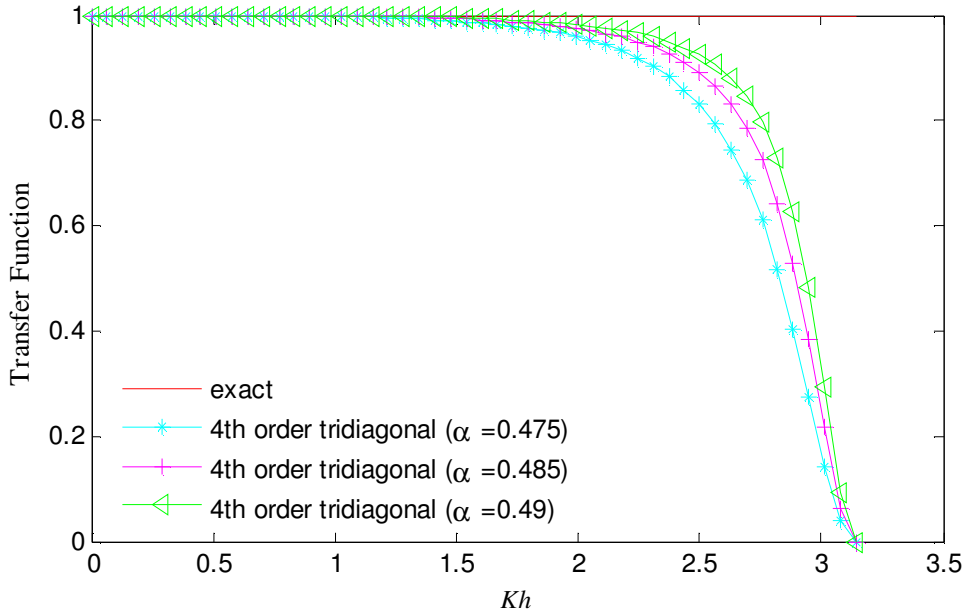

Figure 2.2 The response of filtering transfer function using different values of α.

2.7.3 Filtering of random fields

Another way of looking at the transfer function for different low-pass filters is by application of the Fast Fourier Transformation (FFT) to random fields. The FFT converts a discrete signal in the spatial domain to a discrete wavenumber domain faster than the discrete Fourier transformation. The FFT method implements the transform for a vector with length N by the following equation

$$\hat{u} = \sum_{j=1}^{N} u(j)\omega_N^{(j-1)(k-1)} , \tag{2.52}$$

where

$$\omega_N = e^{\frac{-2\pi i}{N}} . \tag{2.53}$$

In this technique, the filter is firstly applied to a one-dimensional test function with random noise. A test function is described according to the following equation:

$$u = \sum_{i=1}^{N} A\sin(2\pi i x + \phi),\ 0 \le x \le 1, \tag{2.54}$$

where A is the amplitude, x is the dimensionless length of the function, N is the maximum wave number, which has been chosen to be 1024 in the example, and ϕ is a

random number between 0 and 2π. Figure 2.3 shows this function before and after filtering by the six filter schemes (top hat filter A, top hat filter B, 4^{th} order explicit filter, 6^{th} order explicit filter, 4^{th} order tridiagonal and 4^{th} order pentadiagonal). Figure 2.4 shows energy spectra, and it can be seen that the shapes for the various filters are similar to those from Figure 2.1. One can observe that the 4^{th} order tridiagonal scheme (α = 0.475) preserves the largest energy at high k. In contrast, Figure 2.4 shows that the top-hat filter (A) is inadequate, with an accumulation of energy at the higher frequencies. If the filtering is continued for a few iterations this accumulation of energy is observed to be removed and the shape of the top-hat filter (A) will be changed as shown in Figure 2.5. All measures show that the 4^{th} order tridiagonal filter exhibits the best agreement with the unfiltered function.

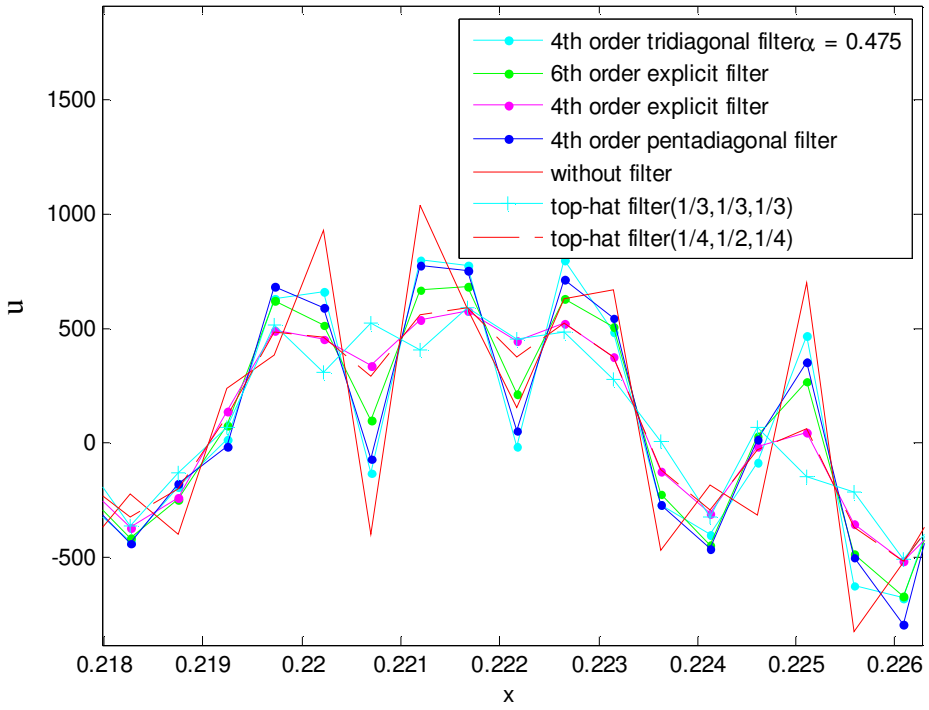

Figure 2.3 Subset of the test function with constant amplitude and its filtered functions by several filter schemes (exaggerated view).

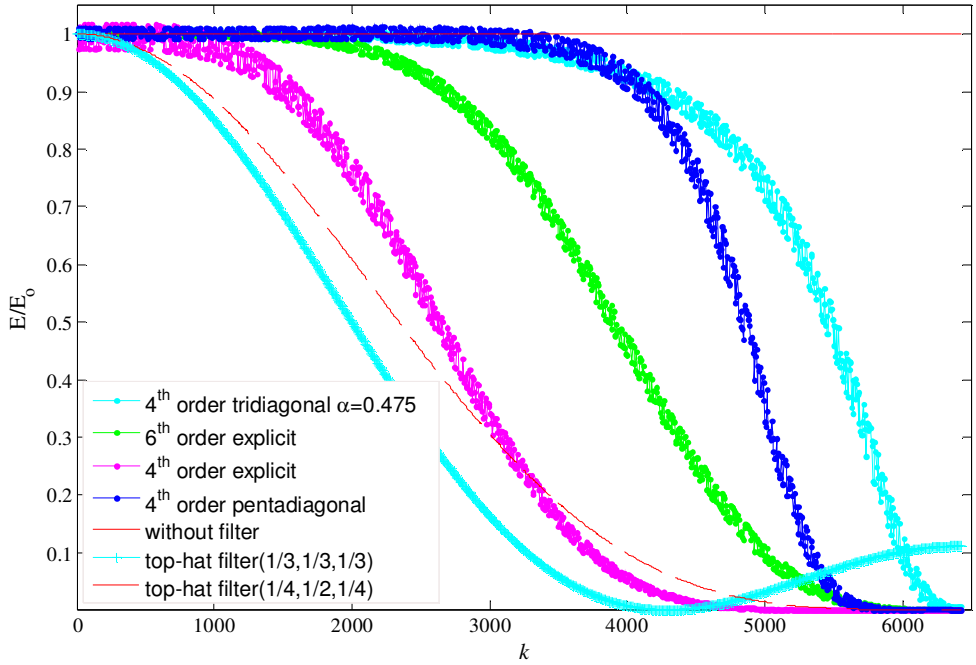

Figure 2.4 Energy spectra for different filter schemes (constant amplitude function).

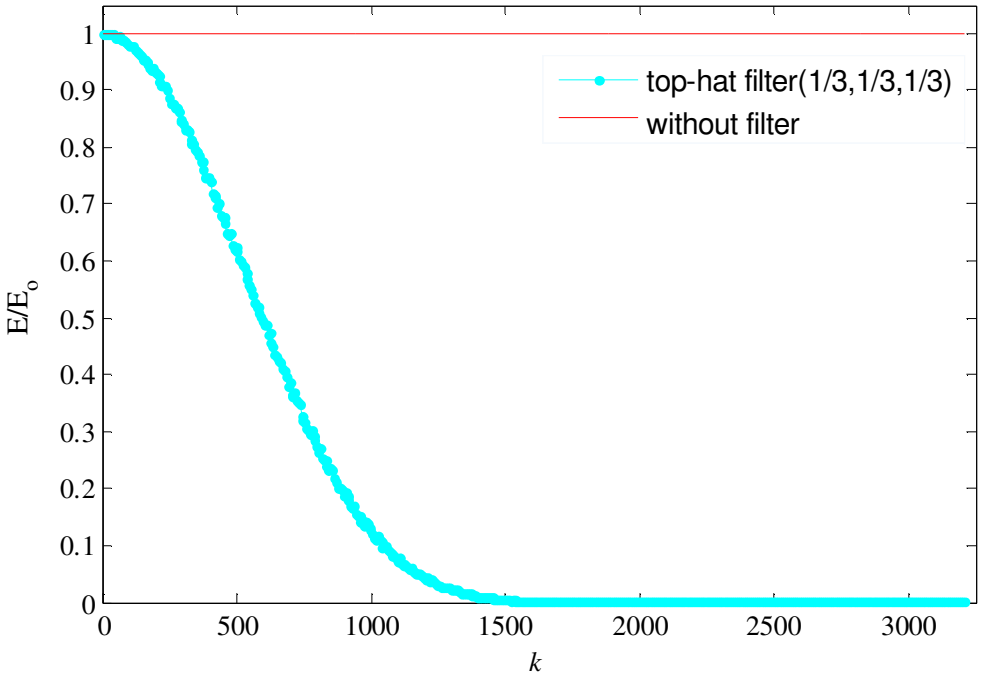

Figure 2.5 Energy spectra after 3 iterations for the top-hat filter (A).

2.7.4 Kolmogorov test function

A second test function was tested, using a spectrum with the Kolmogorov slope (-5/3), which is similar to the behaviour of the energy cascade for turbulent flow as discussed in section 2.1 and described in equation (2.10). This function is governed by the following equation:

$$u = \sum_{i=1}^{N} B(i)\sin(2\pi i x + \phi), 0 \le x \le 1, \tag{2.55}$$

where $B(i)$ is the decreasing amplitude of the test function, the amount of spectral roll-off is governed by the following equation:

$$B(i) = \sqrt{e^{(A-5/3\ln(2\pi i))}} \tag{2.56}$$

The other parameters: A, x, ϕ and N are the same as the constant amplitude test function. Figure 2.6 depict the unfiltered and filtered function with Kolmogorov slope.

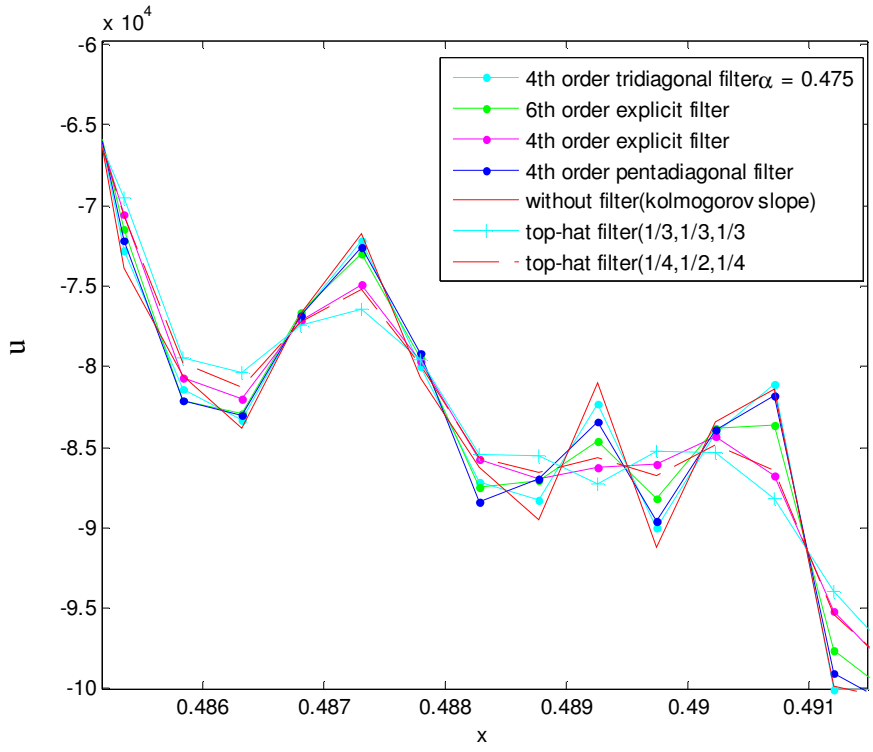

Figure 2.6 Subset of the test function with Kolmogorov slope amplitude and its filtered functions by various filter schemes (exaggerated view).

Repeated filtering of the test function is clearly useful to remove the oscillations as illustrated in Figure 2.7 where 400 applications of the filters have been made. The top-

hat filter schemes (A) and (B) and the 4th order explicit filter show the worst behaviour because they smooth the signal too much. The effect of the 6th order explicit filter is not too bad but the accuracy can be improved using implicit schemes such as the 4th order tridiagonal and the 4th order pentadiagonal. Overall, the best filter scheme appears to be the 4th order tridiagonal. Spectra on Figure 2.8 show the expected -5/3 slope at low wavenumbers and a rapid roll-off at high wavenumbers.

2.7.5 Filtering on stretched grid

So far, the filters have been applied over uniform grids for both test functions, but most practical flows have complex geometries and need non-uniform grids for numerical calculations. For example, a curvilinear stretched grid is typically used to simulate flow around an airfoil. Therefore, another test function with a non-uniform grid was constructed and six different filter schemes were tested. Equations 2.54 and 2.55 were used to construct two distinct functions. The only difference is the distribution of the grid points over the length of the variable x, which was changed to the stretched variable x_s over the same range (0 to 1). The grid points are stretched using the Eriksson function (Eriksson, 1982):

$$x_s = \frac{e^{\beta x} - 1}{e^{\beta} - 1}, \tag{2.57}$$

where β is any positive number. The Eriksson function provides a cluster of grid points near the domain boundary. Figure 2.9 shows a comparison between the uniform and the stretched grids, where the coefficient β is set to be 5, for which a larger concentration of grid points can be observed in the vicinity of $x = 0$.

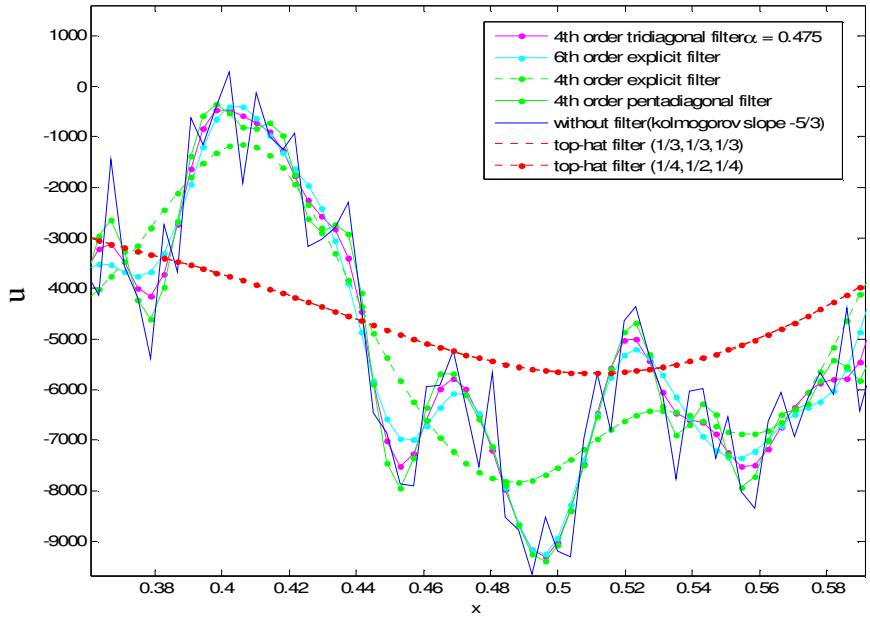

Figure 2.7 Filtered test function by repeating filtering (after 400 iterations).

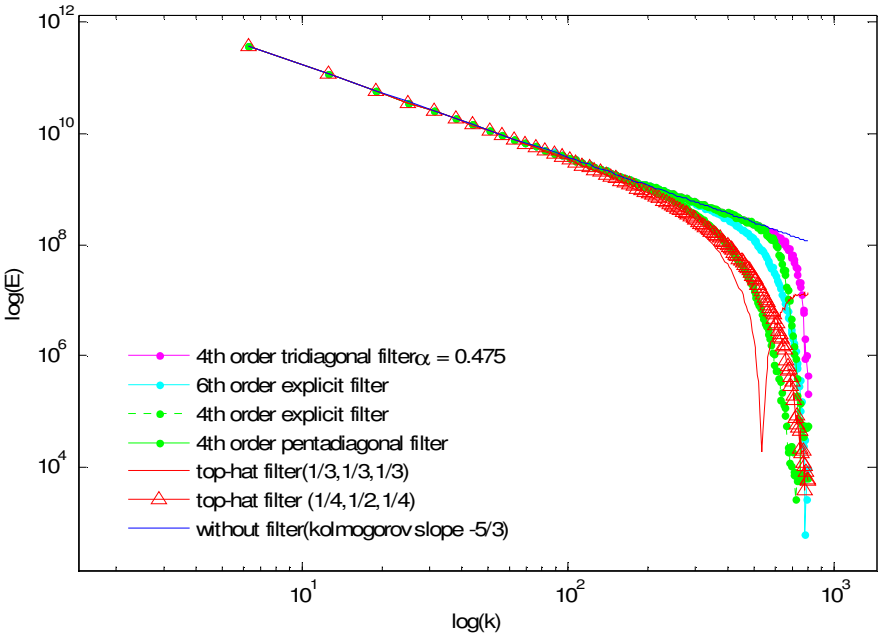

Figure 2.8 Energy spectra for Kolmogorov slope amplitude test function with different filter schemes (logarithmic scale).

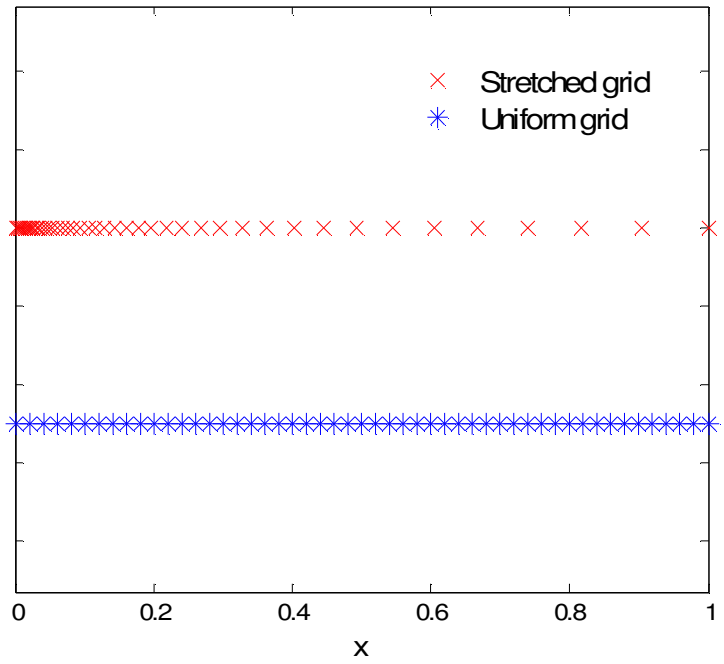

Figure 2.9 Comparison between uniform and stretched grids.

In order to assess the effect of the filters over a non-uniform grid, filtering has been incorporated in the Kolmogorov test function over the length of the variable x_s. There is a strong effect of filtering for all filter schemes in the fine grid (clustering) region, where a large number of grid points exist near the boundary ($x = 0$), whereas the 4th-order tridiagonal and the 4th-order pentadiagonal filters exhibit the best filtering in the coarse region and the top-hat filters have the worst effect. These filtering effects can be seen clearly by repeated filtering, as shown in Figures 2.10 and 2.11 for fine and coarse grids, respectively. From these figures, it is clear that the relative effectiveness of the filter schemes over a stretched grid in both fine and coarse regions is quite similar to a uniform grid. In conclusion, strong evidence has been presented supporting the high performance of the 4th-order tridiagonal and the 4th-order pentadiagonal filters, also on stretched grids.

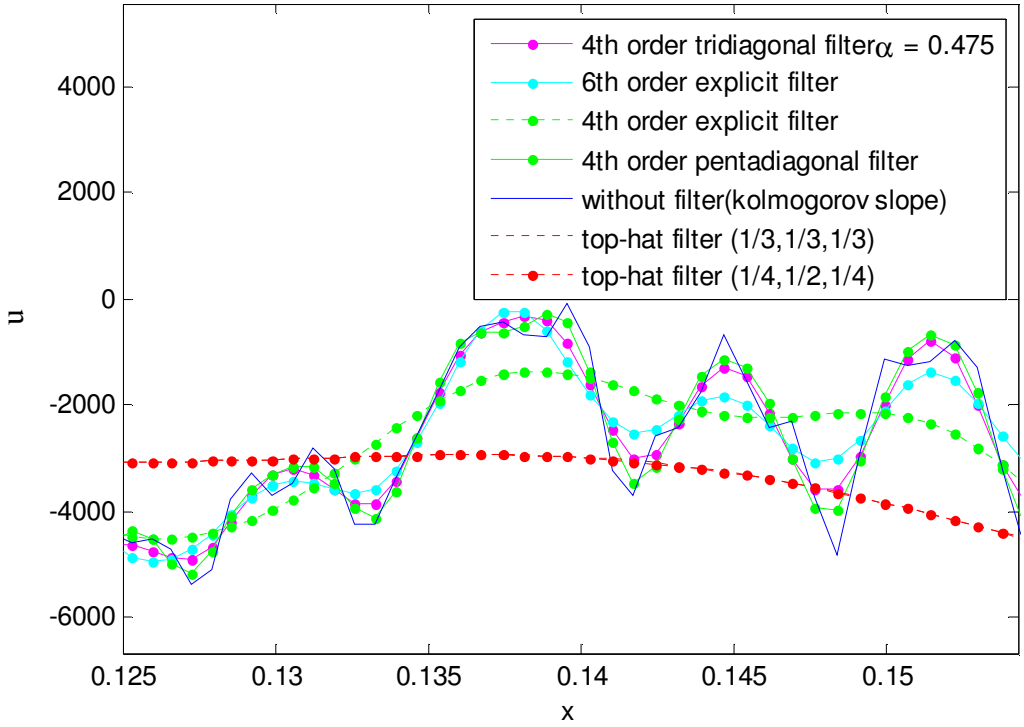

Figure 2.10 Effect of repeat filtering on Kolomogrov test function over the fine regions of the stretched grid (after 100 iterations).

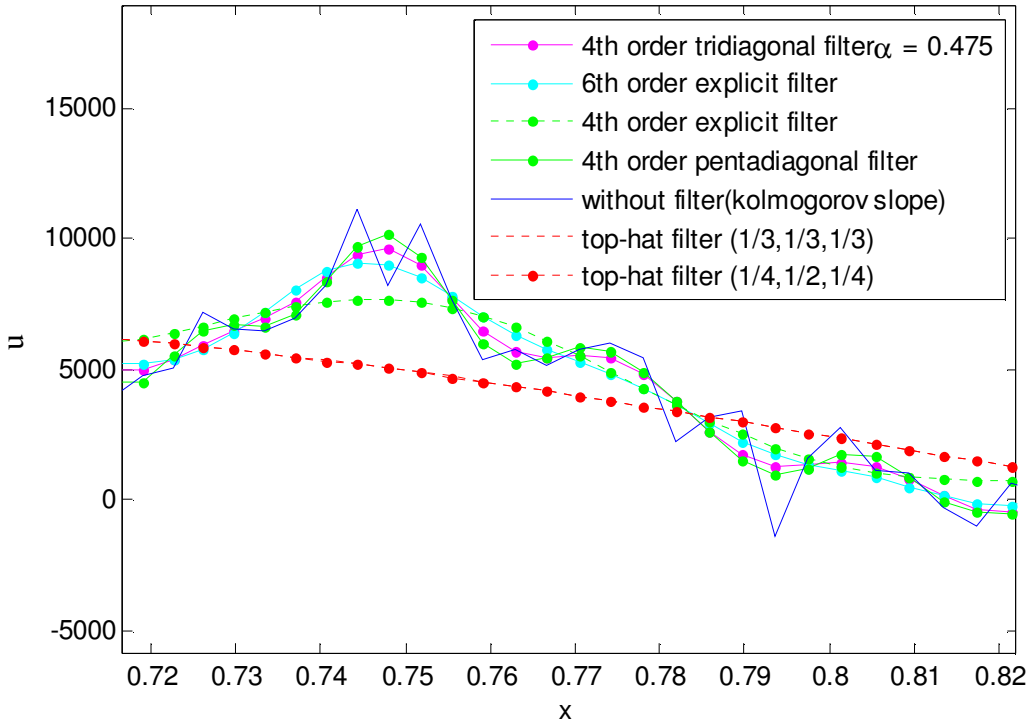

Figure 2.11 Effect of repeat filtering on Kolomogrov test function over the coarse regions of the stretched grid (after 100 iterations).

2.7.6 Discussion of commutation error for stretched grids

Differentiation and filtering operations do not commute when the filter has nonuniform width. The commutation error can be expressed as follows

$$\left[\frac{d\psi}{dx}\right] \equiv \overline{\frac{d\psi}{dx}} - \frac{d\bar{\psi}}{dx} \tag{2.58}$$

where $\psi(x)$ is a one-dimensional field and the over-bar denotes the filtering operation as before.

Ghosal and Moin (1995) developed new types of filters that have variable widths and second order accuracy. To apply these filters to high-order differential equations, extra terms must be added to the filtered Navier-Stokes equations, and this requirement is considered to be a drawback of these filters. This requirement was avoided by Van der Ven (1995), who constructed a family of LES filters of non-uniform width for which the commutation error is the same order as the differentiation operation. Vasilyev *et al.* (1998) presented a general class of commutative LES filters for nonhomogeneous turbulent flows without changing the widths of the filters. They studied the commutation error for continuous and discrete filters such as the Padé-type filter for homogeneous (periodic) and non-homogeneous (non-periodic) fields. They proved that the Padé filters, which are constructed much like the fourth-order tridiagonal filter scheme, are the best design for applications to nonuniform computational domains, because they are flexible in construction and close to the sharp cutoff filters. They also found that the order of the commutation error for the Padé filters is equal to the truncation error from the finite difference scheme, which means that the discrete filtering and differentiation operations commute up to any given order. In order to analyse the commutation error and to verify the practicality of using such filters, they mapped the nonuniform and uniform computational grids before any filter was used in any specific application. However, they mentioned that filtering in physical space is exactly the same as filtering in computational space, but it is much easier to use the latter. They also proved that using a discrete filter on homogeneous turbulent flow gives a solution with zero commutation error. In the present work we use the fourth-order tridiagonal scheme and apply the filter in *ijk* indices, as described in section 2.8.3

2.8 Filter implementation and boundary treatments

As mentioned earlier, the objective of applying the low-pass filter is to remove signals with higher spatial wavenumbers. The low-pass filter requires matrix multiplications to compute the filtered values from the unfiltered values as follows

$$\mathbf{B}\hat{\mathbf{Q}} = \mathbf{F}\mathbf{Q} \tag{2.59}$$

$\hat{\mathbf{Q}}$ and $\mathbf{Q}$ are filtered and unfiltered vectors; respectively. The size of these vectors is N_t, where N_t is the total number of grid points in a specific direction. $\mathbf{B}$ and $\mathbf{F}$ are square matrixes ($N_t \times N_t$) containing the boundary and the interior coefficients for the left hand side and the right hand side of equation (2.50), respectively. Non-periodic and periodic boundary conditions will be discussed in the following sections

2.8.1 Non-periodic boundary treatment

The boundary coefficients in non-periodic problems will be represented explicitly. Equation (2.59) of the 4th order tridiagonal can be presented in matrix form as follows:

$$\begin{pmatrix}
1 & 0 & \dots & \dots & \dots & \dots & \dots & \dots & \dots & 0 \\
0 & 1 & 0 & \dots & \dots & \dots & \dots & \dots & \dots & 0 \\
\beta & \alpha & 1 & \alpha & \beta & 0 & \dots & \dots & \dots & 0 \\
0 & \beta & \alpha & 1 & \alpha & \beta & 0 & \dots & \dots & 0 \\
0 & 0 & \beta & \alpha & 1 & \alpha & \beta & 0 & \dots & 0 \\
\dots & \dots & \dots & \dots & \dots & \dots & \dots & \dots & \dots & \dots \\
0 & \dots & \dots & 0 & \beta & \alpha & 1 & \alpha & \beta & 0 \\
0 & \dots & \dots & \dots & 0 & \beta & \alpha & 1 & \alpha & \beta \\
0 & \dots & \dots & \dots & \dots & \dots & \dots & 0 & 1 & 0 \\
0 & \dots & \dots & \dots & \dots & \dots & \dots & \dots & 0 & 1
\end{pmatrix}
\begin{bmatrix}
\overline{q}_1 \\ \overline{q}_2 \\ . \\ . \\ \overline{q}_{i-1} \\ \overline{q}_i \\ \overline{q}_{i+1} \\ . \\ \overline{q}_{N-1} \\ \overline{q}_N
\end{bmatrix}
=
\begin{pmatrix}
a_1 & b_1 & c_1 & d_1 & e_1 & 0 & \dots & \dots & \dots & 0 \\
a_2 & b_2 & c_2 & d_2 & e_2 & 0 & \dots & \dots & \dots & 0 \\
\frac{c}{2} & \frac{b}{2} & a & \frac{b}{2} & \frac{c}{2} & 0 & \dots & \dots & \dots & 0 \\
0 & \frac{c}{2} & \frac{b}{2} & a & \frac{b}{2} & \frac{c}{2} & 0 & \dots & \dots & 0 \\
0 & 0 & \frac{c}{2} & \frac{b}{2} & a & \frac{b}{2} & \frac{c}{2} & 0 & \dots & 0 \\
\dots & \dots & \dots & \dots & \dots & \dots & \dots & \dots & \dots & \dots \\
0 & \dots & \dots & 0 & \frac{c}{2} & \frac{b}{2} & a & \frac{b}{2} & \frac{c}{2} & 0 \\
0 & \dots & \dots & \dots & 0 & \frac{c}{2} & \frac{b}{2} & a & \frac{b}{2} & \frac{c}{2} \\
0 & \dots & \dots & \dots & 0 & e_2 & d_2 & c_2 & b_2 & a_2 \\
0 & \dots & \dots & \dots & 0 & e_1 & d_1 & c_1 & b_1 & a_1
\end{pmatrix}
\begin{bmatrix}
q_1 \\ q_2 \\ . \\ . \\ q_{i-1} \\ q_i \\ q_{i+1} \\ . \\ q_{N-1} \\ q_N
\end{bmatrix}
\tag{2.60}$$

Equation (2.60) is applicable for a 5 point filter stencil, like the 4th order tridiagonal filter with $\beta = 0$. In the case of wider filter stencils such as the 7 point filter stencil of the 4th order pentadiagonal filter, the boundary rows in equation (2.60) should be extended to be three rows rather than two rows and the equation is rearranged into the following form:

$$\begin{pmatrix} 1 & 0 & 0 & \dots & \dots & \dots & \dots & \dots & \dots & 0 \\ 0 & 1 & 0 & \dots & \dots & \dots & \dots & \dots & \dots & 0 \\ 0 & 0 & 1 & 0 & \dots & \dots & \dots & \dots & \dots & 0 \\ 0 & \beta & \alpha & 1 & \alpha & \beta & 0 & \dots & \dots & 0 \\ \dots & 0 & \beta & \alpha & 1 & \alpha & \beta & 0 & \dots & 0 \\ \dots & \dots & \dots & \dots & \dots & \dots & \dots & \dots & \dots & \dots \\ 0 & \dots & \dots & 0 & \beta & \alpha & 1 & \alpha & \beta & 0 \\ 0 & \dots & \dots & \dots & \dots & 0 & 0 & 1 & 0 & 0 \\ 0 & \dots & \dots & \dots & \dots & \dots & 0 & 0 & 1 & 0 \\ 0 & \dots & \dots & \dots & \dots & \dots & \dots & 0 & 0 & 1 \end{pmatrix} \begin{bmatrix} \bar{q}_1 \\ \bar{q}_2 \\ \bar{q}_3 \\ . \\ \bar{q}_{i-1} \\ \bar{q}_i \\ \bar{q}_{i+1} \\ \bar{q}_{N-2} \\ \bar{q}_{N-1} \\ \bar{q}_N \end{bmatrix} = \begin{pmatrix} a_1 & b_1 & c_1 & d_1 & e_1 & 0 & \dots & \dots & \dots & 0 \\ a_2 & b_2 & c_2 & d_2 & e_2 & 0 & \dots & \dots & \dots & 0 \\ a_3 & b_3 & c_3 & d_3 & e_3 & 0 & \dots & \dots & \dots & 0 \\ \frac{d}{2} & \frac{c}{2} & \frac{b}{2} & a & \frac{b}{2} & \frac{c}{2} & \frac{d}{2} & 0 & \dots & 0 \\ 0 & \frac{d}{2} & \frac{c}{2} & \frac{b}{2} & a & \frac{b}{2} & \frac{c}{2} & \frac{d}{2} & \dots & 0 \\ \dots & \dots & \dots & \dots & \dots & \dots & \dots & \dots & \dots & \dots \\ 0 & \dots & \dots & \frac{d}{2} & \frac{c}{2} & \frac{b}{2} & a & \frac{b}{2} & \frac{c}{2} & \frac{d}{2} \\ 0 & \dots & \dots & \dots & 0 & e_3 & d_3 & c_3 & b_3 & a_3 \\ 0 & \dots & \dots & \dots & 0 & e_2 & d_2 & c_2 & b_2 & a_2 \\ 0 & \dots & \dots & \dots & 0 & e_1 & d_1 & c_1 & b_1 & a_1 \end{pmatrix} \begin{bmatrix} q_1 \\ q_2 \\ q_3 \\ . \\ q_{i-1} \\ q_i \\ q_{i+1} \\ q_{N-2} \\ q_{N-1} \\ q_N \end{bmatrix} \tag{2.61}$$

It is necessary to know the coefficients of the boundary treatment. These coefficients are derived by matching the coefficients of a Taylor series. For fourth-order accuracy these coefficients are derived in Appendix B and are given as follows:

a_1 = 15/16, b_1 = 4/16, c_1 = -6/16, d_1 = 4/16, e_1 = -1/16, a_2 = 1/16, b_2 = 3/4, c_2 = 6/16, d_2 = -4/16, e_2 = -1/16, a_3 = -1/16, b_3 = 4/16, c_3 = 5/8, d_3 = 4/16, e_3 = -1/16,

The truncation errors for the first, second and third boundary point are $3/(2\times4!)\,h^4 q_1^{IV}$, $11/(8\times4!)\,h^4 q_2^{IV}$ and $-3/(2\times4!)\,h^4 q_3^{IV}$, respectively. The transfer functions for these boundary points are illustrated in Figure 2.12. It can be seen from this figure that the improvement of the approximation is increased gradually from the first boundary point to the third one, which exhibits nearly the same profile as the explicit 4^{th} order filter scheme at the interior points. The overshoot of the transfer function for the first and second boundary points is not desirable and hence the first two points near the boundary are kept without applying filtering in the present study.

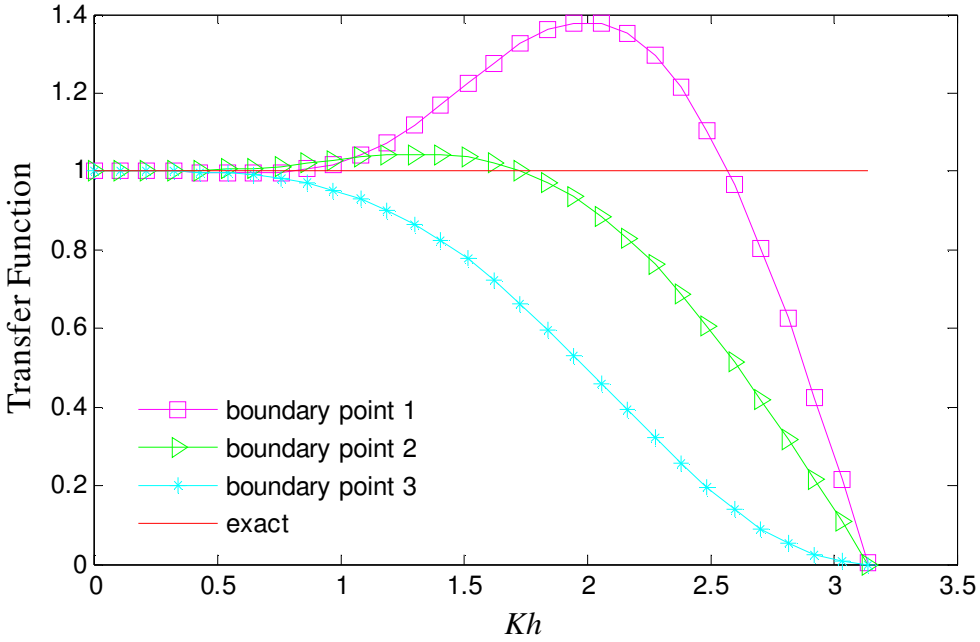

Figure 2.12 transfer functions of filtered boundary points (4th order accuracy)

Obviously equations (2.60) and (2.61) are sparse linear systems, with matrices containing only a relatively small number of matrix elements. If these sparse matrices are solved by normal linear algebra methods such as Gaussian elimination and Gauss-Jordan elimination they cost $O(N_t^2)$ operations in space , where N_t is the number of linear equations (or number of grid points). In this study, solvers for tridiagonal and pentadiagonal matrices for cyclic (periodic) and non-cyclic (non-periodic) are used from e.g. Press, Flannery, Teukolsky & Vetterling (1992). The main advantage of these methods is the reduction of the cost to be $O(N_t)$ operations.

2.8.2 Periodic boundary treatment

For periodic boundary conditions, the boundary points are treated as follows: $b_{1,N} = b_{i,i-1}$, $b_{1,N-1} = b_{i,i-2}$, $b_{2,N} = b_{i,i-2}$, where i is any interior point, similar treatment will be applied for the N_t^{th} row and $(N_t\text{-}1)^{\text{th}}$ row, and so on. In matrix form equation (2.60) is rearranged as follows:

$$\begin{pmatrix} 1 & \alpha & \beta & 0 & \dots & \dots & \dots & 0 & \beta & \alpha \\ \alpha & 1 & \alpha & \beta & 0 & \dots & \dots & \dots & 0 & \beta \\ \beta & \alpha & 1 & \alpha & \beta & 0 & \dots & \dots & \dots & 0 \\ 0 & \beta & \alpha & 1 & \alpha & \beta & 0 & \dots & \dots & 0 \\ 0 & 0 & \beta & \alpha & 1 & \alpha & \beta & 0 & \dots & 0 \\ \dots & \dots & \dots & \dots & \dots & \dots & \dots & \dots & \dots & \dots \\ 0 & \dots & \dots & 0 & \beta & \alpha & 1 & \alpha & \beta & 0 \\ 0 & \dots & \dots & \dots & 0 & \beta & \alpha & 1 & \alpha & \beta \\ \beta & 0 & \dots & \dots & \dots & 0 & \beta & \alpha & 1 & \alpha \\ \alpha & \beta & 0 & \dots & \dots & \dots & 0 & \beta & \alpha & 1 \end{pmatrix} \begin{bmatrix} \overline{q}_1 \\ \overline{q}_2 \\ . \\ . \\ \overline{q}_{i-1} \\ \overline{q}_i \\ \overline{q}_{i+1} \\ . \\ \overline{q}_{N-1} \\ \overline{q}_N \end{bmatrix} = \begin{pmatrix} a & \frac{b}{2} & \frac{c}{2} & 0 & 0 & \dots & \dots & 0 & \frac{c}{2} & \frac{b}{2} \\ \frac{b}{2} & a & \frac{b}{2} & \frac{c}{2} & 0 & \dots & \dots & \dots & \dots & \frac{c}{2} \\ \frac{c}{2} & \frac{b}{2} & a & \frac{b}{2} & \frac{c}{2} & 0 & \dots & \dots & \dots & 0 \\ 0 & \frac{c}{2} & \frac{b}{2} & a & \frac{b}{2} & \frac{c}{2} & 0 & \dots & \dots & 0 \\ 0 & 0 & \frac{c}{2} & \frac{b}{2} & a & \frac{b}{2} & \frac{c}{2} & 0 & \dots & 0 \\ \dots & \dots & \dots & \dots & \dots & \dots & \dots & \dots & \dots & \dots \\ 0 & \dots & \dots & 0 & \frac{c}{2} & \frac{b}{2} & a & \frac{b}{2} & \frac{c}{2} & 0 \\ 0 & \dots & \dots & \dots & 0 & \frac{c}{2} & \frac{b}{2} & a & \frac{b}{2} & \frac{c}{2} \\ \frac{c}{2} & 0 & \dots & \dots & \dots & 0 & \frac{c}{2} & \frac{b}{2} & a & \frac{b}{2} \\ \frac{b}{2} & \frac{c}{2} & 0 & \dots & \dots & 0 & 0 & \frac{c}{2} & \frac{b}{2} & a \end{pmatrix} \begin{bmatrix} q_1 \\ q_2 \\ . \\ . \\ q_{i-1} \\ q_i \\ q_{i+1} \\ . \\ q_{N-1} \\ q_N \end{bmatrix} \tag{2.62}$$

Equation (2.61) is rearranged in a similar fashion.

2.8.3 Implementation of filter schemes

In many practical applications, it is not necessary to use the whole filtered function but part of it according to the following equation:

$$\overline{u} = u - \sigma(u - \hat{u}) \tag{2.63}$$

where $\overline{u}$ represents the resulting filtered function, u is the unfiltered function and $\hat{u}$ is the filtered function using filters given by equations (2.60) or (2.61) or (2.62), depending on the type of boundary conditions and the order of accuracy, and σ is constant between 0 and 1. If σ is 0 that means there is no filtering and if it is 1 then the whole unfiltered function is filtered ($\overline{u} = \hat{u}$). Bogey and Bailly (2002) suggested setting σ between 0.1 and 0.2 in order to get a stable numerical solution.

In the present study, the conservative variables are first filtered in the *x* direction, and the resulting filtered variables are then filtered in *y* direction. If three-dimensional filtering is needed, the filtered variables in *y* direction are also filtered in the *z* direction. In order to evaluate the fourth order tridiagonal filter scheme, each processor of the computational domain is extended to include two grid points from the adjacent processors

which are called “halo” cells and they are used without filtering. Filtering of the interior points with halo cells is presented in matrix form in equation (2.64) where the subscript -1, 0, N+1 and N+2 represent the halo cells. The halo cells will be filtered later when they become part of the adjacent processor subdomain.

$$\begin{pmatrix} 1 & 0 & 0 & \dots & \dots & \dots & \dots & \dots & \dots & 0 \\ 0 & 1 & 0 & \dots & \dots & \dots & \dots & \dots & \dots & 0 \\ \beta & \alpha & 1 & \alpha & \beta & \dots & \dots & \dots & \dots & 0 \\ 0 & \beta & \alpha & 1 & \alpha & \beta & 0 & \dots & \dots & 0 \\ \dots & 0 & \beta & \alpha & 1 & \alpha & \beta & 0 & \dots & 0 \\ \dots & \dots & \dots & \dots & \dots & \dots & \dots & \dots & \dots & \dots \\ 0 & \dots & \dots & 0 & \beta & \alpha & 1 & \alpha & \beta & 0 \\ 0 & \dots & \dots & \dots & \dots & \beta & \alpha & 1 & \alpha & \beta \\ 0 & \dots & \dots & \dots & \dots & \dots & 0 & 0 & 1 & 0 \\ 0 & \dots & \dots & \dots & \dots & \dots & \dots & 0 & 0 & 1 \end{pmatrix} \begin{bmatrix} \overline{q}_{-1} \\ \overline{q}_0 \\ \overline{q}_1 \\ . \\ \overline{q}_{i-1} \\ \overline{q}_i \\ \overline{q}_{i+1} \\ . \\ \overline{q}_N \\ \overline{q}_{N+1} \\ \overline{q}_{N+2} \end{bmatrix} = \begin{pmatrix} 1 & 0 & 0 & 0 & 0 & 0 & \dots & \dots & \dots & 0 \\ 0 & 1 & 0 & 0 & 0 & 0 & \dots & \dots & \dots & 0 \\ \frac{c}{2} & \frac{b}{2} & a & \frac{b}{2} & \frac{c}{2} & 0 & \dots & \dots & \dots & 0 \\ 0 & \frac{c}{2} & \frac{b}{2} & a & \frac{b}{2} & \frac{c}{2} & 0 & 0 & \dots & 0 \\ 0 & 0 & \frac{c}{2} & \frac{b}{2} & a & \frac{b}{2} & \frac{c}{2} & 0 & \dots & 0 \\ \dots & \dots & \dots & \dots & \dots & \dots & \dots & \dots & \dots & \dots \\ 0 & \dots & \dots & 0 & \frac{c}{2} & \frac{b}{2} & a & \frac{b}{2} & \frac{c}{2} & 0 \\ 0 & \dots & \dots & \dots & 0 & \frac{c}{2} & \frac{b}{2} & a & \frac{b}{2} & \frac{c}{2} \\ 0 & \dots & \dots & \dots & 0 & 0 & 0 & 0 & 1 & 0 \\ 0 & \dots & \dots & \dots & 0 & 0 & 0 & 0 & 0 & 1 \end{pmatrix} \begin{bmatrix} q_{-1} \\ q_0 \\ q_1 \\ . \\ q_{i-1} \\ q_i \\ q_{i+1} \\ . \\ q_N \\ q_{N+1} \\ q_{N+2} \end{bmatrix} \tag{2.64}$$

This completes the overview of the numerical method. The parallel code used for the study was the same as that used by Jones (2007), with the addition of the SGS model and filtering and hence developed into an LES code. This is the main contribution of the current study, since the huge saving of computational cost compared with the DNS code allows the study of important phenomena such as low-frequency flow oscillations and dynamic stall. Validation of the code is considered in the next chapter.

3 Validation of the LES code

The main purpose of this chapter is to validate the LES code by performing an *a posteriori* study against the DNS results of flow around an NACA0012 airfoil at a Reynolds number of 50,000 and incidences of 0° and 5°. Firstly, in section 3.1 the two-dimensional filtered Navier-Stokes simulations are compared with the two-dimensional DNS to choose the optimum filter scheme. Secondly, in section 3.2 the validation is extended to cover a three-dimensional flow case.

3.1 2D filtered Navier-Stokes simulation results

DNS with a fine mesh will be considered as a reference solution and the next sections will be organized as follows: Firstly, some aerodynamic quantities will be presented from solution on the fine mesh DNS which consists of 2242×691 grid points. Secondly, the results of filtered aerodynamic properties such as vorticity and lift coefficient by various filter schemes on a coarser mesh which consists of 1181 × 259 grid points will be presented. Finally, a comparison of computational cost will be considered.

3.1.1 Problem and simulation description

In order to compare results, the same NACA-0012 configuration as Jones (2007) is utilized in this study. The sharp trailing edge of the NACA-0012 airfoil was obtained by extending the blunt trailing edge and rescaling the airfoil to c = 1. The C-mesh, geometry parameters and coordinate system are depicted in Figure 3.1. Here W is the wake length (W =5), R is the domain radius (R = 7.3) and ξ and η are the coordinate directions. An integral characteristic boundary condition (Sandhu and Sandham, 1994) is applied at the freestream boundary (η^+), while a zonal characteristic boundary condition (Sandberg and Sandham, 2006) is applied at the downstream exit boundary ($\xi^{\pm}$). An adiabatic, no-slip condition is applied at the airfoil surface and a spanwise-periodic boundary condition is applied to the simulation every subtep of the Runge-Kutta time stepping. Statistics are obtained by averaging in time and for three-dimensional calculations also in the homogeneous spanwise direction. The Reynolds number (Re), Mach number (M), Prandtl number (Pr) and incidence angle (α) are kept the same as in

Jones (2007) but the number of grid points is smaller. The Reynolds number of the flow is set to be 50,000. The angle of incidence is set as $\alpha = 0^o$, the Mach number M = 0.6, the Prandtl number Pr = 0.72 and the ratio of specific heats $\gamma = 1.4$. The main grid parameters of the two-dimensional filtered Navier-Stokes and two-dimensional DNS simulations are summarized in Table 3.1. The columns W, R, and 'Total Length' correspond to the wake length, radius and total domain length, respectively, in chord units of the airfoil, whereas N_ξ and N_η represent the numbers of grid points in curvilinear directions ξ and η, respectively. The columns PS, SS, NW, and 'Total Points' correspond to the numbers of cells on the pressure side, suction side, wake and total cells, respectively. Figure 3.2 shows the employed mesh.

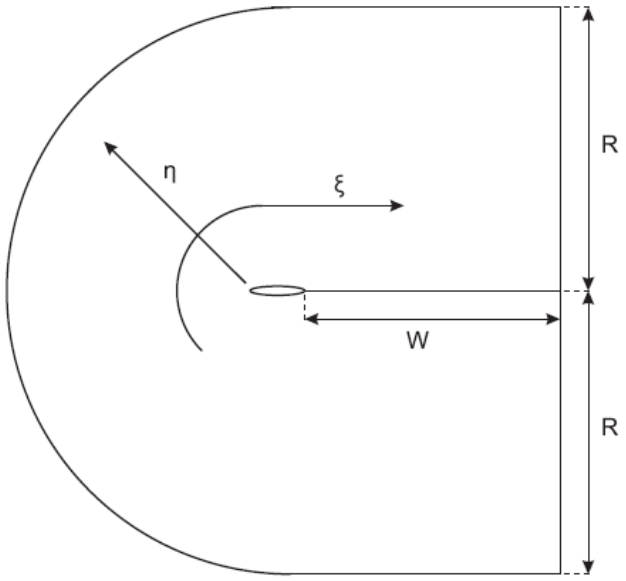

Figure 3.1 Domain boundaries and coordinate system around NACA0012 (sharp) airfoil (Jones 2007).

Table 3.1 Comparison of grid parameters for validation study (Re = 50,000 and $\alpha = 0°$)

Simulation	W	R	Total Length	N_ξ	N_η	N_z	L_z/c	PS	SS	NW	Total points
2D filtered N-S	5	5.3	12.2	1181	259	-	-	100	100	491	305879
DNS	5	7.3	14.2	2243	692	-	-	368	368	753	1552156

3.1.2 Calculation of aerodynamic coefficients

Aerodynamic coefficients such as lift, drag, skin-friction and pressure coefficient are calculated by integration of the associated force over the airfoil surface. For example, the lift coefficient is obtained using the following equation

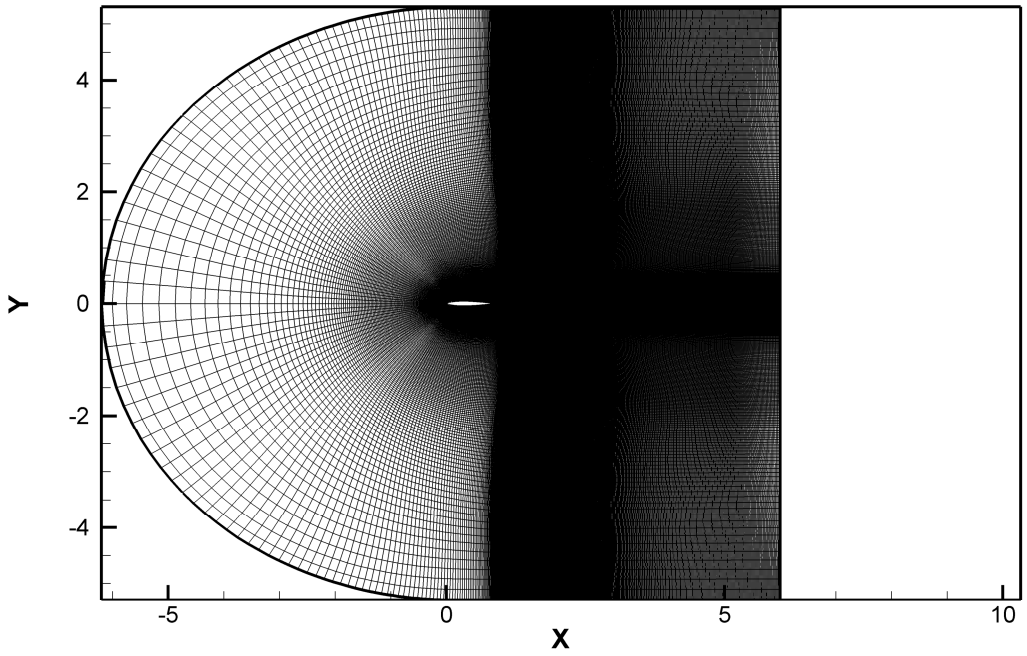

Figure 3.2 Grid for the 2D filtered Navier-Stokes simulation (1181×259).

$$C_L = \frac{-1}{\frac{1}{2}\rho_\infty u_\infty^2} \int_{s=0}^{s=s_{total}} S(p_{\eta=0} - p_\infty)\left|\sin\theta\right| ds, \tag{3.1}$$

where ρ_∞, u_∞ and p_∞ refer to the free-stream density, velocity, and pressure, respectively. The term $p_{\eta=0}$ represents the pressure at the airfoil surface, and θ refers to the local surface angle, which is defined as

$$\theta = \tan^{-1}\left(\frac{dy}{dx}\right)_{\eta=0}. \tag{3.2}$$

In order to ensure that the lift coefficient has the correct sign, the function S is imposed during the calculation so that it has a value of -1 or +1, based on whether the contribution is for the upper or lower airfoil surface, using the following expressions

$$\begin{aligned} &\text{If } \frac{dx}{d\xi} > 0, \quad \text{then} \quad S = 1 \\ &\text{If } \frac{dx}{d\xi} < 0, \quad \text{then} \quad S = -1 \end{aligned} \tag{3.3}$$

The pressure drag coefficient is calculated by integrating the pressure over the airfoil surface, according to the following equation

$$C_{dp} = \frac{1}{\frac{1}{2}\rho_\infty u_\infty^2} \int_{s=0}^{s=s_{total}} p_{\eta=0} \sin\theta ds \quad . \tag{3.4}$$

The shear stress is integrated over the airfoil surface to produce the skin-friction drag coefficient as follows

$$C_{df} = \frac{1}{\frac{1}{2}\rho_\infty u_\infty^2} \int_{s=0}^{s=s_{total}} \mu \left[\frac{du}{dy}_{\eta=0} \cos\theta - S \frac{dv}{dx}_{\eta=0} |\sin\theta| \right] ds. \tag{3.5}$$

The total drag coefficient is the sum on of the skin-friction and pressure coefficients, i.e.

$$C_D = C_{dp} + C_{df} \tag{3.6}$$

The moment coefficient is obtained using the following equation

$$C_m = \frac{1}{\frac{1}{2}\rho_\infty u_\infty^2} \int_{s=0}^{s=s_{total}} \left((p_{\eta=0} - p_\infty) \sin\tilde{\alpha} - S\mu \left[\frac{du}{dy}_{\eta=0} \cos\theta - S \frac{dv}{dx}_{\eta=0} |\sin\theta| \right] \cos\tilde{\alpha} \right) l_m \, ds \tag{3.7}$$

where

$$l_m = \sqrt{(x - x_{mom})^2 + (y - y_{mom})^2}, \tag{3.8}$$

$\tilde{\alpha}$ is the angle between the airfoil surface and the tangent line to the circle about the moment centre intersecting the x and y locations, x_{mom} and y_{mom} are located at the quarter-chord point.

3.1.3 Governing equations of the periodic forcing

Periodic forcing is applied within the curvilinear coordinate system (ξ, η and z) presented in Figure 3.1. The forcing is mathematically described as follows

$$F_\eta = \frac{A\sin(2\pi ft+\phi)(1-\cos(2\pi\xi_{\text{force}}))(\eta_{\text{force}} - \frac{1}{2\pi}\sin(2\pi\eta_{\text{force}}))}{2} \tag{3.8}$$

and

$$F_\xi = \frac{A\sin(2\pi ft+\phi)(1-\cos(2\pi\eta_{\text{force}}))(\xi_{\text{force}} - \frac{1}{2\pi}\sin(2\pi\xi_{\text{force}}))}{2}, \tag{3.9}$$

where A is the amplitude of the function, f is the frequency, t is the non-dimensional time, ϕ is the phase angle and ξ_{force} and η_{force} give the locations where forcing is applied in the ξ and η directions, respectively. The value of both ξ_{force} and η_{force} vary between 0 and 1, which are corresponded to the start and end of forcing, respectively. Equations (3.8) and (3.9) are defined in the region $0<\xi_{\text{force}}<1$ and $0<\eta_{\text{force}}<1$, respectively. F_ξ and F_η are set to zero outside the region $0<\eta_{\text{force}}<1$ and $0<\xi_{\text{force}}<1$, respectively. The differentiation of F_ξ and F_η with respect to ξ for the former and η for the latter provides a smooth cosine functions as follows (Jones, 2007)

$$\frac{dF_\xi}{d\xi} = \frac{dF_\eta}{d\eta} = \frac{A\sin(2\pi ft+\phi)(1-\cos(2\pi\eta_{\text{force}}))(1-\cos(2\pi\xi_{\text{force}}))}{2}. \tag{3.10}$$

This type of forcing is used in the present study because it provides a divergence-free body force and hence is expected to be quieter (generate less noise) than alternatives. To convert from the curvilinear system to the Cartesian coordinate metric terms should be used according to the following inverse transformations

$$\frac{dF}{dy} = \frac{dF_\eta}{d\eta}\frac{dx}{d\xi} - \frac{dF_\xi}{d\xi}\frac{dx}{d\eta}, \tag{3.11}$$

$$\frac{dF}{dx} = \frac{dF_\xi}{d\xi}\frac{dy}{d\eta} - \frac{dF_\eta}{d\eta}\frac{dy}{d\xi}. \tag{3.12}$$

Finally, the forcing derivatives $\frac{dF}{dy}$ and $\frac{dF}{dx}$ are added to the right hand side of the x momentum equation for the former and subtracted from the right hand side of the y momentum equation for the latter, while the following cosine function multiplies equations (3.11) and (3.12) to create variations in the spanwise direction.

$$\cos\left(2\pi\frac{k-1}{N_z}\right), \tag{3.13}$$

where k is the grid point in the spanwise direction and N_z is the total number of grid points in the spanwise direction.

3.1.4 Unfiltered solutions

Fine-scale numerical instabilities arise while attempting to solve the flow using a relatively coarse mesh. Figures 3.3a, with a coarse mesh (1180×258), and Figure 3.3b, with a fine mesh (2242×691), demonstrate the influence of the numerical oscillations on the solution. Figure 3.3a presents vorticity contours after 800,000 time steps with time step Δt = 0.00018 which is the maximum time step that can be used in this case to maintain numerical stability which allows the simulation to resolve a frequency of up to f = 2778, showing clear numerical oscillations and irregular wake vortices. In contrast, Figure 3.3b shows reduced oscillations and a more regular solution. Therefore, the presence of the oscillations has a significant effect on the accuracy of the solution. The main reason for the appearance of these oscillations is the inability of the finite difference scheme to represent steep gradients on a coarse mesh.

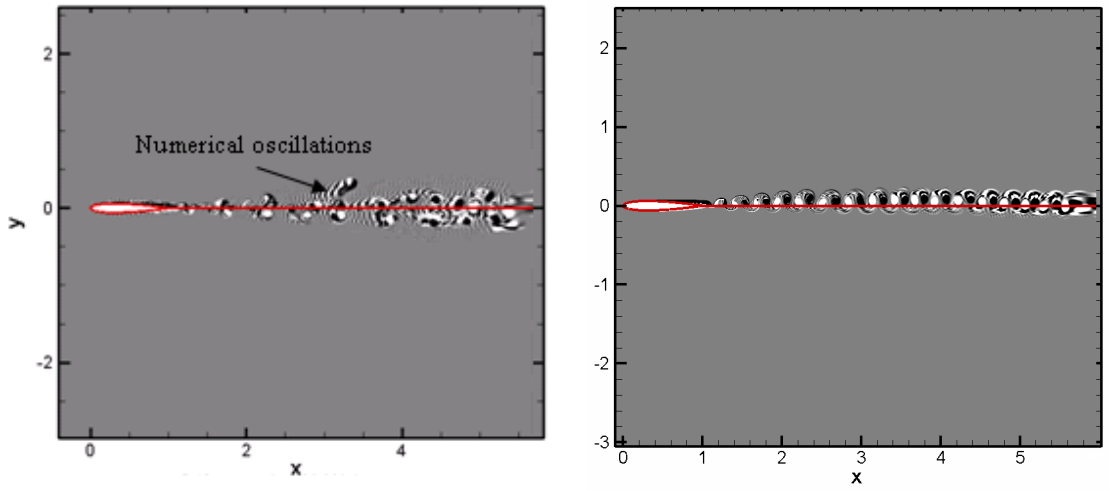

a) b)

Figure 3.3 Vorticity contours obtained from DNS for a flow around an NACA-0012 airfoil at Re = 50,000 and M = 0.6 over a) coarse mesh and b) fine mesh.

Jones (2007) noted the occurrence of a 2D low-frequency flow phenomenon called "flapping" at zero degrees incidence, where the airfoil boundary layer switches between stalled and non-stalled conditions. He performed a DNS study at different Reynolds number and Mach numbers and specified the region where flapping is observed. Figure 3.4 shows a DNS lift coefficient which shows the range of lift over ±0.2. This flow case will be revisited in Chapter 7 where the effectiveness of flow control is studied, whereas here it is used as a numerical test case. Figure 3.5 shows the lift coefficient obtained from the simulation on the coarse grid, where it is clear that the lift coefficient exhibits an irregular oscillation with too high a frequency and the solution is completely wrong compared to the solution from the fine grid. The mean values of the lift coefficient shown in Figures 3.4 and 3.5 are 0.003 and -0.005, respectively.

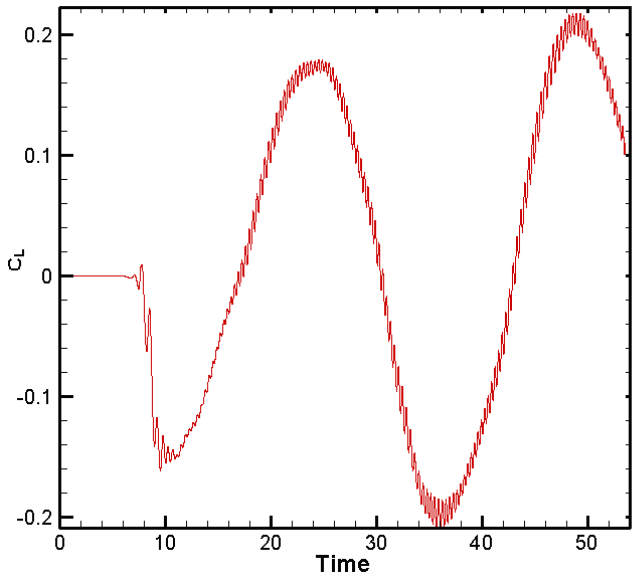

Figure 3.4 Lift coefficient for fine grid DNS at Re = 50,000.

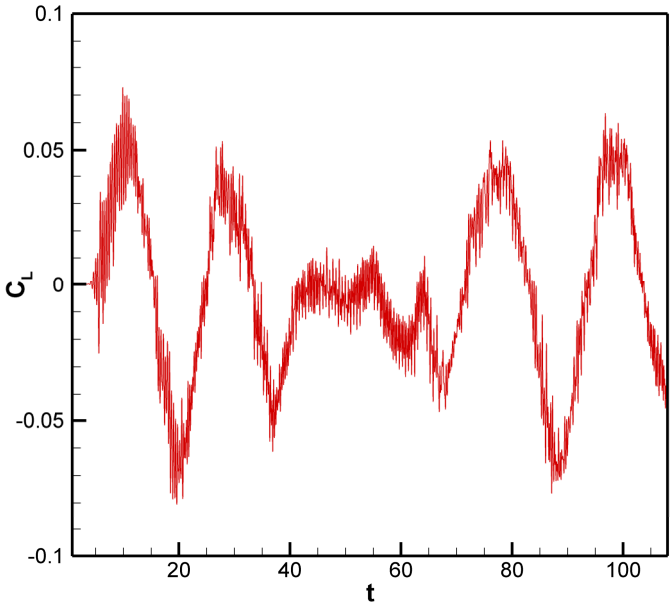

Figure 3.5 Lift coefficient for coarse grid at Re = 50,000.

3.1.5 Filtered DNS results

In this section, results of calculations using the six selected filter schemes (top hat filter A , top hat filter B, 4^{th} order explicit filter, 6^{th} order explicit filter, 4^{th} order tridiagonal and 4^{th} order pentadiagonal) will be compared.

3.1.5.1 Results for top-hat filters

Figure 3.6 displays the results after 7.2 time units (40,000 timesteps) for the top-hat filter (types A and B give nearly the same vorticity field). From this figure, it is clear that the filter has a very strong effect and causes too much removal of not only the numerical oscillations but also the physical wake vortices. In fact, the flow field has changed to become partly steady. The value of σ (equation (2.63) in section 2.8.2) used to carry out the simulation was 0.01. If this value is increased then the flow is completely steady, as shown in Figure 3.7. The filtered lift coefficient by the top-hat filter also gives poor results for the amplitude of the lift coefficient (Figure 3.8), which decreased dramatically because of the excessive removed of the numerical oscillations. In conclusion, using the top-hat filter is not a sensible choice.

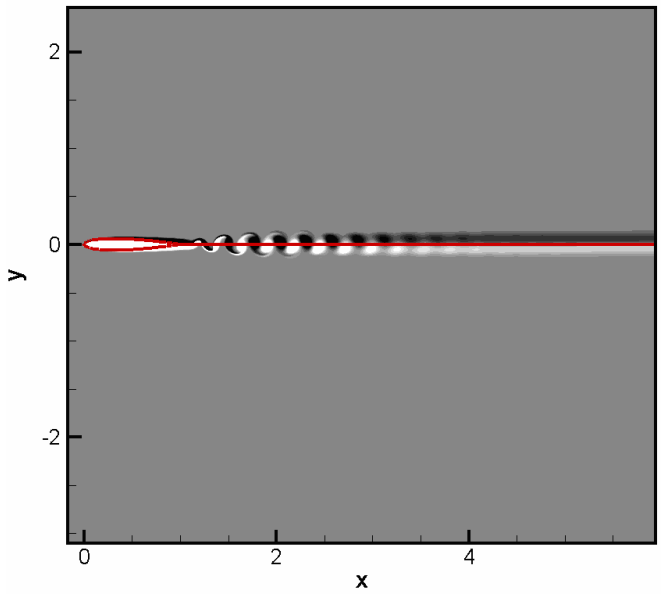

Figure 3.6 Vorticity contours using top-hat filter A (7.2 time units, σ = 0.01).

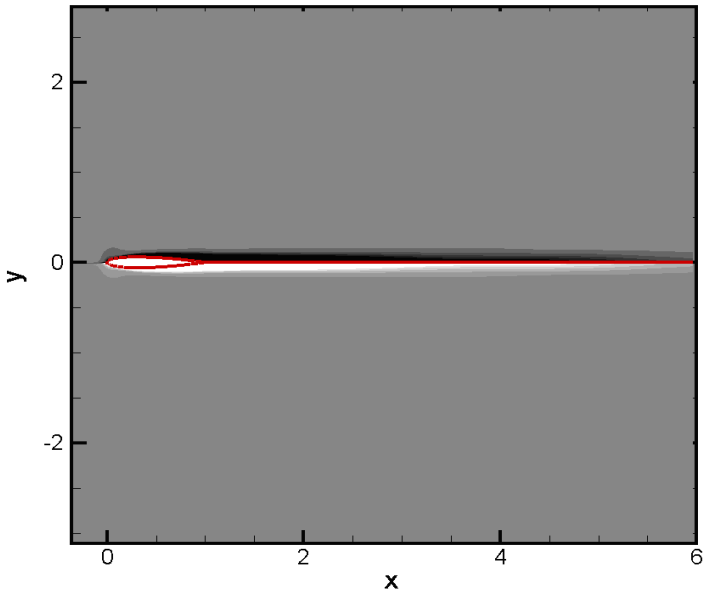

Figure 3.7 Vorticity contours using top-hat filter A (3.6 time units, $\sigma = 1$).

3.1.5.2 Results for the 4th order explicit filter

With σ = 0.1 (or larger), the solution for the 4th order explicit filter is very poor as demonstrated in Figure 3.9. The solution is improved by decreasing the value of σ to 0.01 where the vorticity exhibits a much more realistic solution as shown in Figure 3.10, which displays the solution at different times. It can also be noticed from Figure 3.10 that the wake vortices are not captured well at the end of the computational domain which is presumably due to the effect of the boundary condition that is applied at the downstream exit boundary which is applied to the last 31 points before the exit boundary layer. Flapping is also observed, which agrees with the DNS solution (Jones 2007) at this Reynolds number and Mach number ($Re = 50 \times 10^3$, M = 0.6). In addition, the filtered lift coefficient also gives a reasonable range of lift coefficient variation, between -0.2 and 0.2 (Figure 3.11), which compares well with the DNS. It is important to mention that the high frequency content of the lift coefficient observed in Figure 3.11 is due to the unsteady wake with vortex shedding which is also observed in the study of Jones (2007). Figure 3.12 shows a comparison of lift coefficient between the DNS and filtered lift coefficient where it can be clearly seen that the filtered lift coefficient has similar peak-to-peak amplitude to the DNS but with a significant difference in frequency.

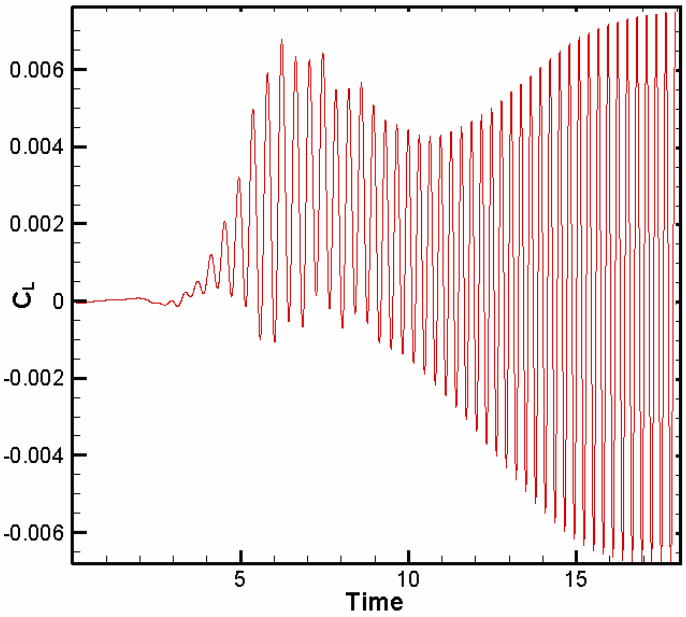

Figure 3.8 Lift coefficient using (top-hat filter A) (σ = 0.01).

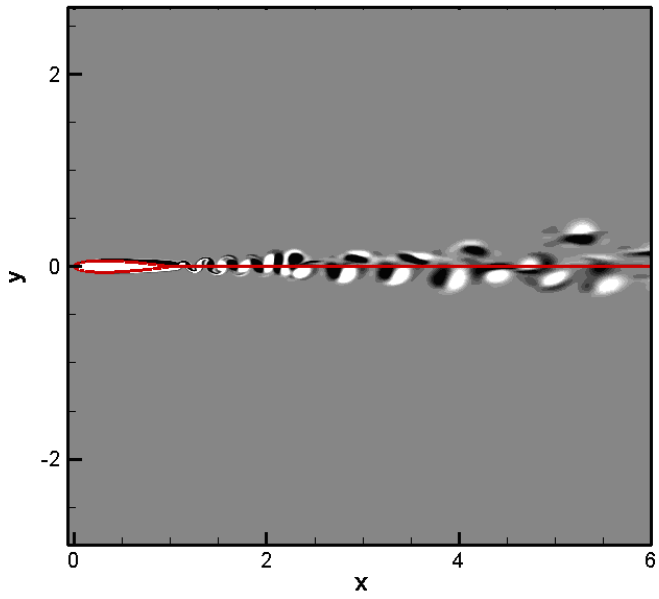

Figure 3.9 Vorticity contours using the 4th order explicit filtering with σ = 0.1.

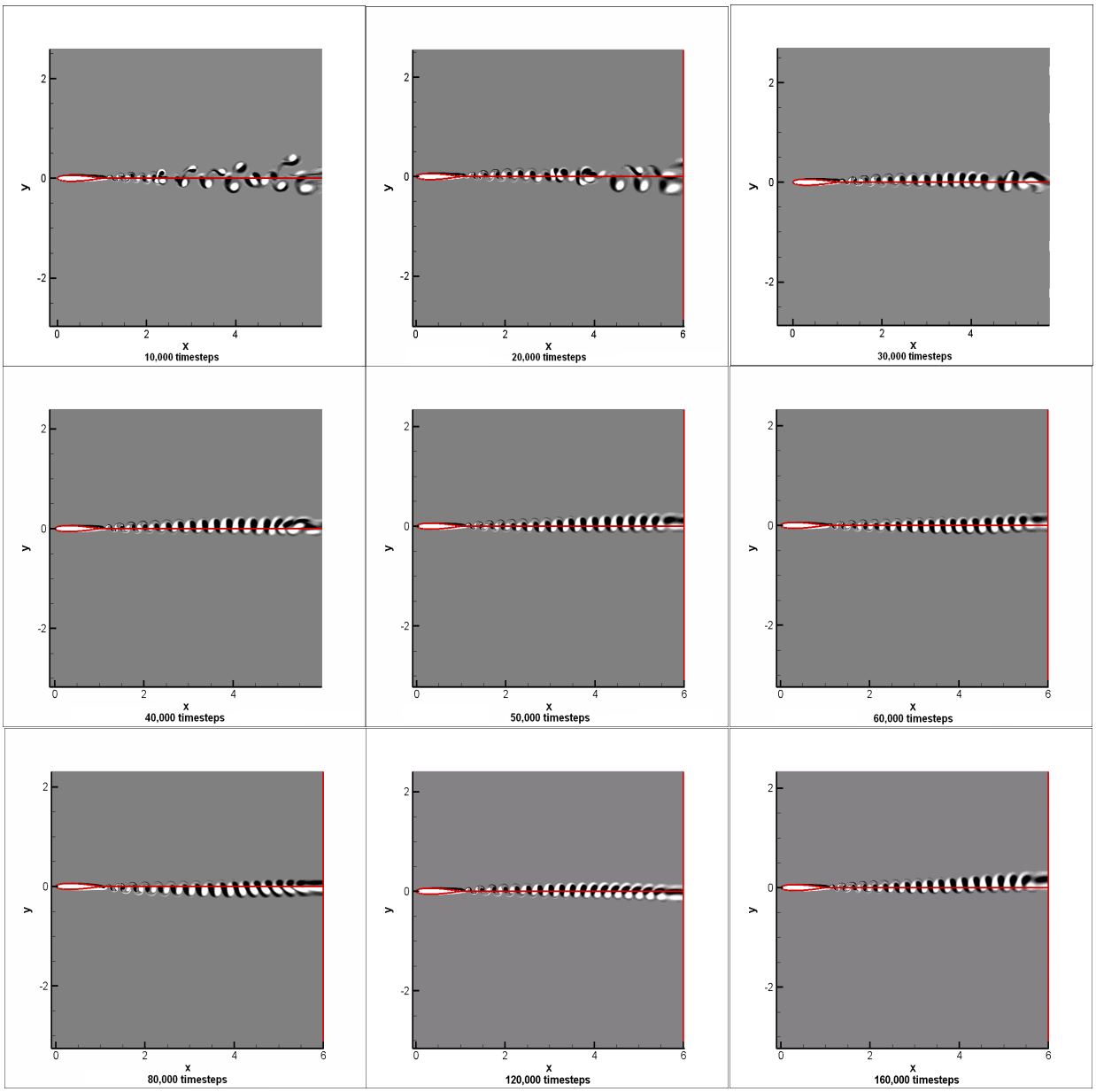

Figure 3.10 Vorticity contours using the 4th order explicit filtering at several timesteps with σ = 0.01 (Δt = 0.00018).

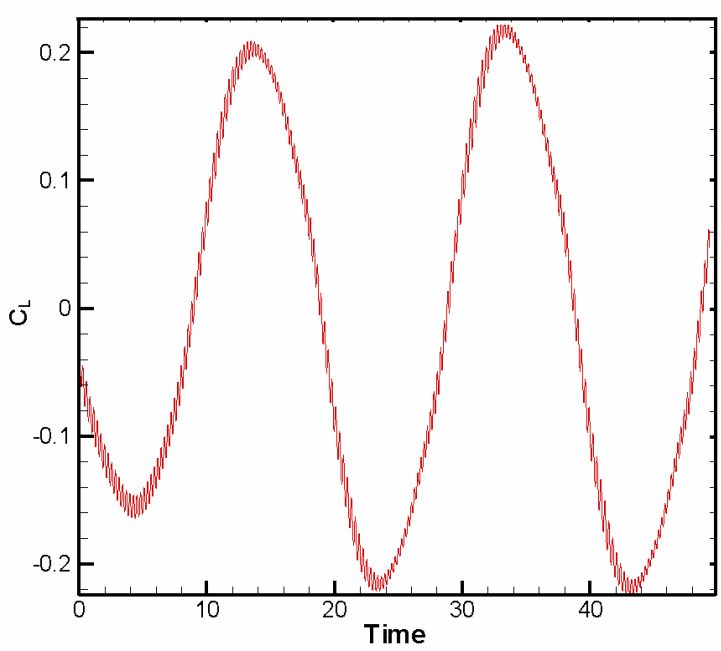

Figure 3.11 Lift coefficient using the 4th order explicit filtering with σ = 0.01.

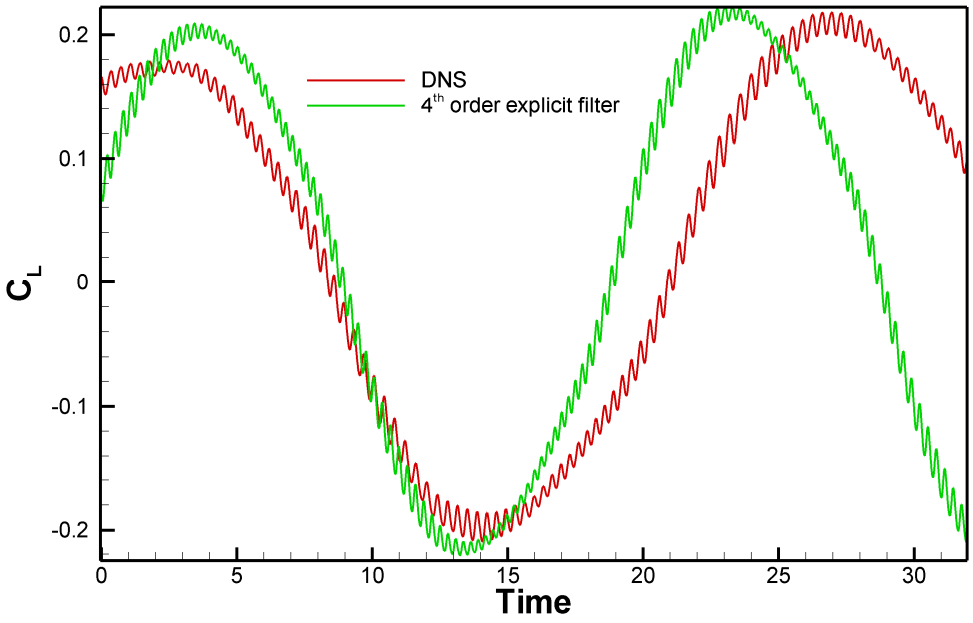

Figure 3.12 comparison of lift coefficient between the DNS and 2D filtered Navier-Stokes simulation using 4th order explicit filtering with σ = 0.01.

3.1.5.3 Results for the 6th order explicit filter

As seen earlier, the coefficient σ is very important in the filtering operation and should be chosen carefully to obtain good results. To do that, two values of σ have been investigated, namely σ = 0.01 and 0.1. Some numerical oscillations occurred when using σ = 0.01 as shown in Figure 3.13. On the other hand, Figure 3.14 illustrates the solution for σ = 0.1 where the oscillations are completely removed. It is noticeable that wake is slightly up the y = 0 plane which may be attributed to the effect of flapping. The filtered lift coefficient is depicted in Figure 3.15 where the range of lift coefficient is -0.2 to 0.2 in good agreement with the fine grid case.

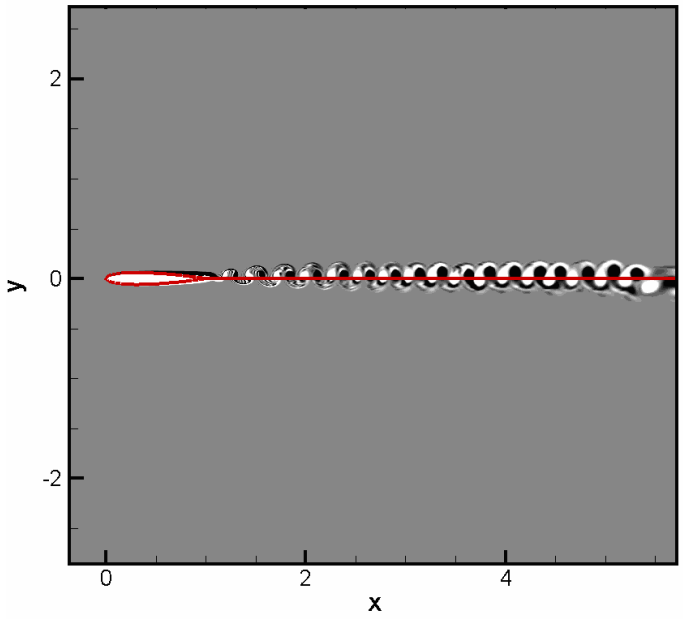

Figure 3.13 Vorticity contours using the 6th order explicit filtering with σ = 0.01.

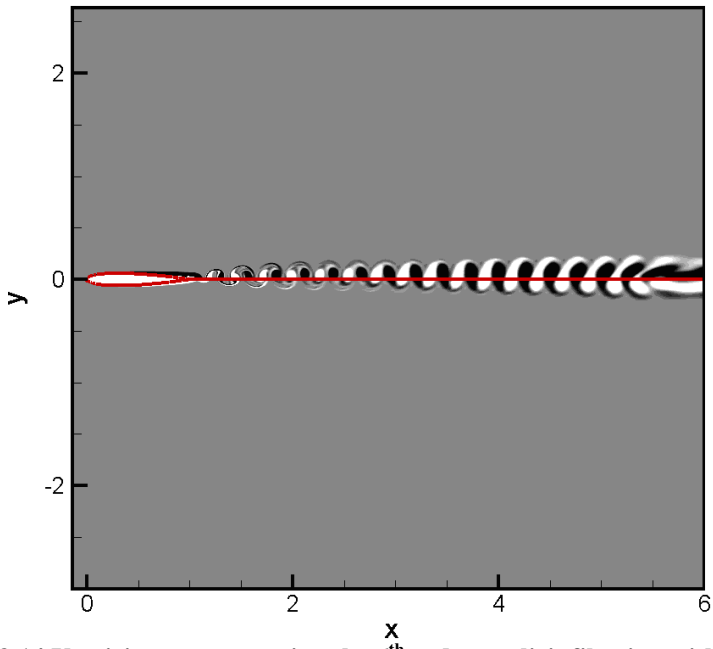

Figure 3.14 Vorticity contours using the 6th order explicit filtering with σ = 0.1.

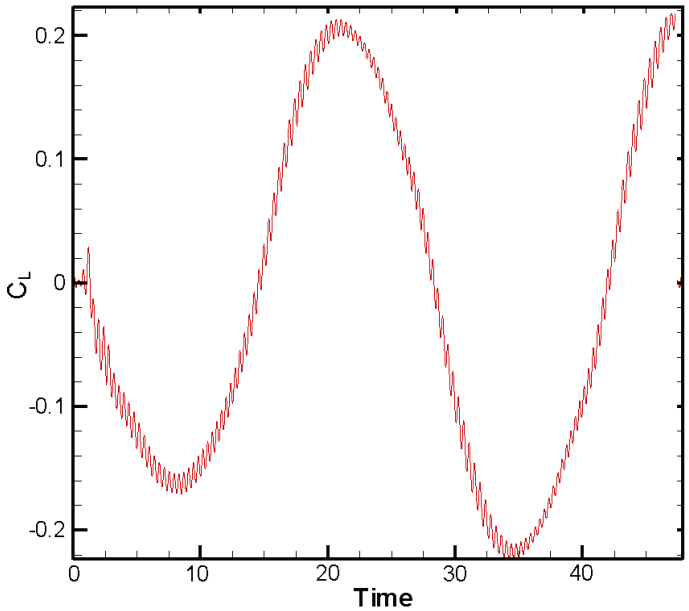

Figure 3.15 Lift coefficient using the 6th order explicit filtering with σ = 0.01.

3.1.5.4 Results for the 4th order tridiagonal filter

Figure 3.16 demonstrates the results of the filtered simulation using a 4th order tridiagonal filter scheme. The oscillations are removed completely, which means the filter

is working properly. The value of σ used to obtain the solution was 1.0, which means that whole filtered field has been used. When attempting to solve the flow with $\sigma = 0.1$ the solution gives some oscillations as shown in Figure 3.17. The solution for the lift coefficient is depicted in Figure 3.18 where a similar observation can be made regarding the good agreement with the DNS as for the 4th order explicit and 6th order explicit filters.

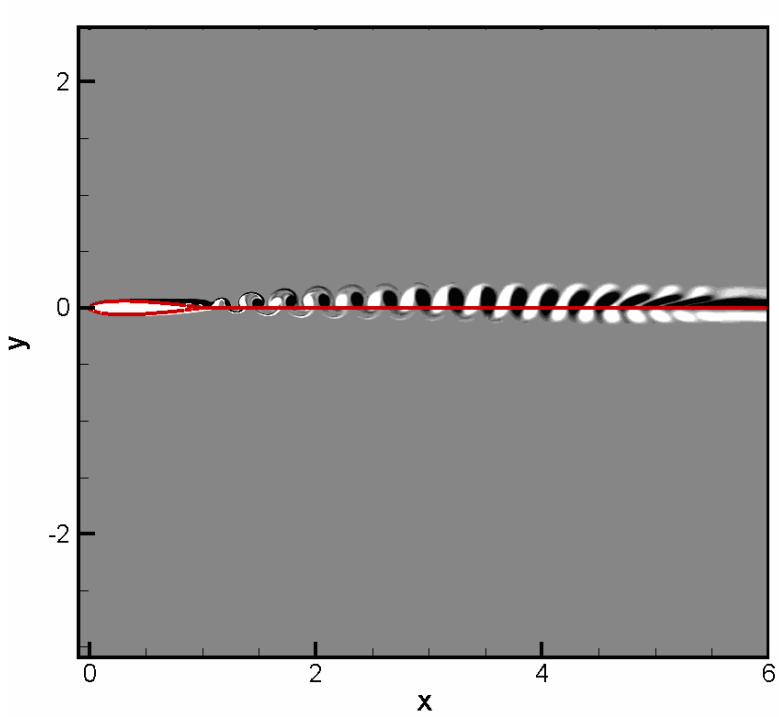

Figure 3.16 Vorticity contours using the 4th order tridiagonal filtering with $\sigma = 1.0$.

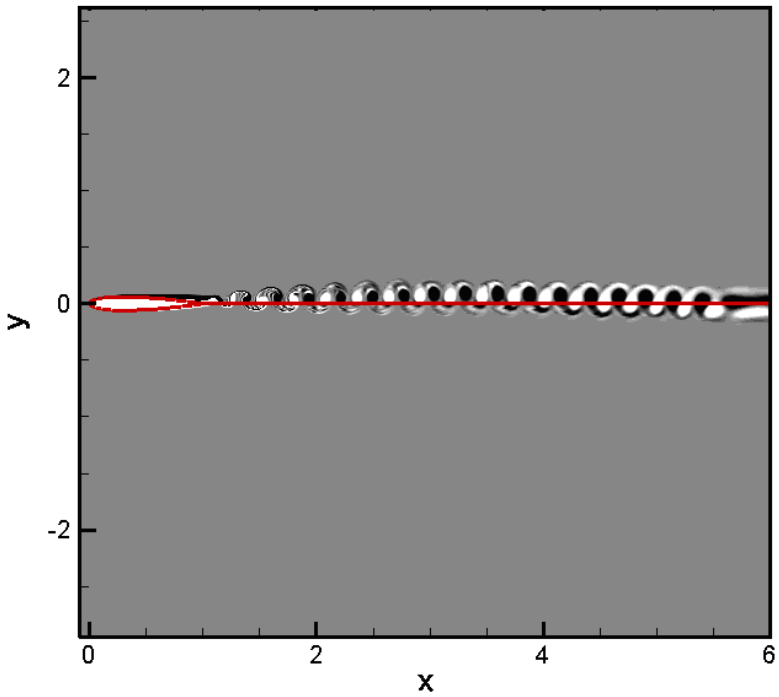

Figure 3.17 Vorticity contours using the 4th order tridiagonal filtering with σ = 0. 1.

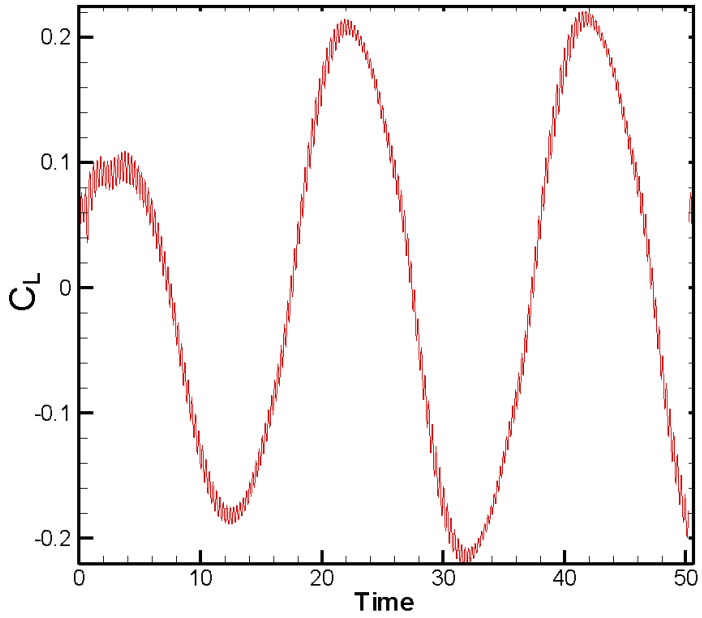

Figure 3.18 Lift coefficient using the 4th order tridiagonal filtering with σ = 0.1.

3.1.5.5 Results for the 4th order pentadiagonal filter

Although the transfer function of the 4th order pentadiagonal filter exhibits a good shape with respect to the exact function as shown in Figure 2.1, the result with σ = 1.0 is

not acceptable because many of the numerical oscillations are not removed, as shown in Figure 3.19, especially in the wake region. On the other hand, Figure 3.20 shown that the filtered lift coefficient is reasonable.

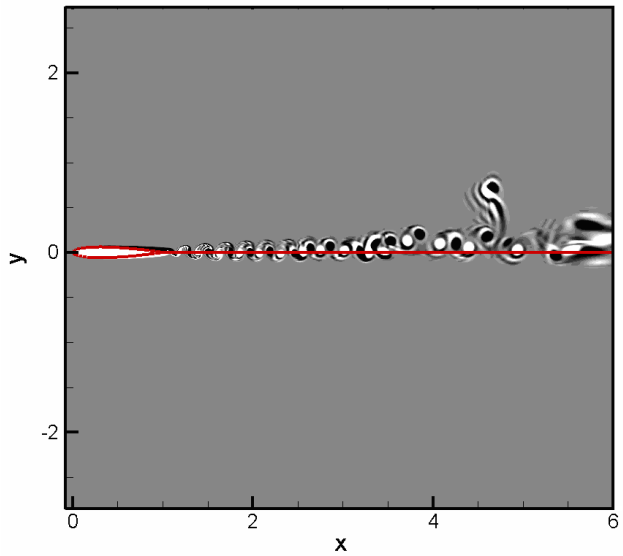

Figure 3.19 Vorticity contours using 4th order pentadiagonal filtering, using σ = 1.0.

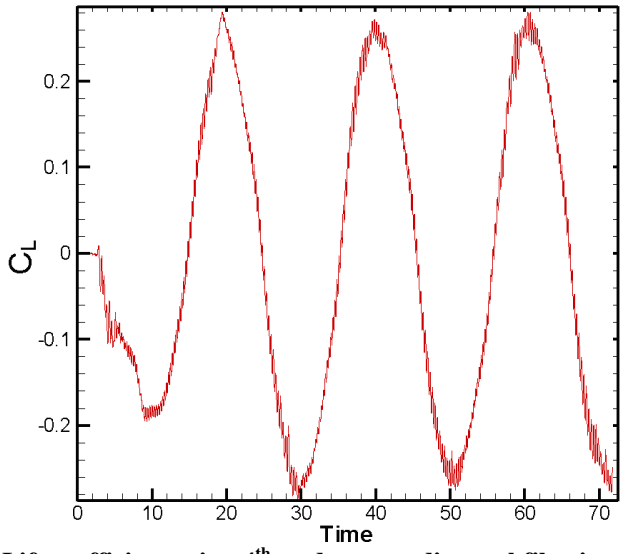

Figure 3.20 Lift coefficient using 4th order pentadiagonal filtering, using σ = 1.0.

3.1.6 Comparison of the time averaged pressure coefficient

As seen from section 3.1.5, all filter schemes can provide good agreement with the fine grid case except the top-hat filters, which have too strong an effect, and the 4th order

pentadiagonal filter where a solution with numerical oscillations is obtained. In order to make a decision about which filter is the best, a comparison based on the time averaged pressure coefficient is shown in Figure 3.21. For a clearer picture, part of Figure 3.21 is exaggerated and depicted in Figure 3.22. When examining this figure, it can be seen that the closest time averaged pressure coefficient profile to the DNS (fine grid) solution is the 4^{th} order tridiagonal scheme while the other schemes have either a large gap between the lift force of the upper and lower airfoil surfaces, such as the 4^{th} order explicit, the 6^{th} order explicit and the 4^{th} order pentadiagonal, or an inaccurate solution at the end of the airfoil, such as the top-hat filter B. The stagnation pressure coefficient obtained from the 4^{th} order explicit and top-hat filter schemes are 1.1037 and 1.1150, respectively. While the stagnation pressure obtained by the DNS and from the isentropic relation are 1.1141 and 1.0933, respectively.

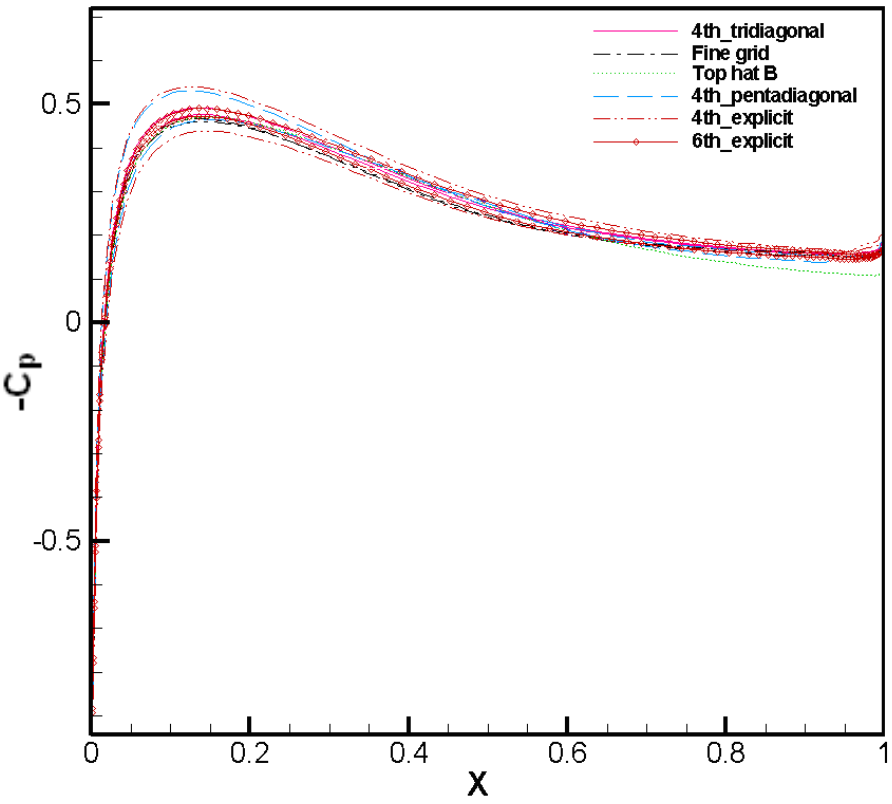

Figure 3.21 Comparison among filtered pressure coefficient by selected filter schemes and DNS solution.

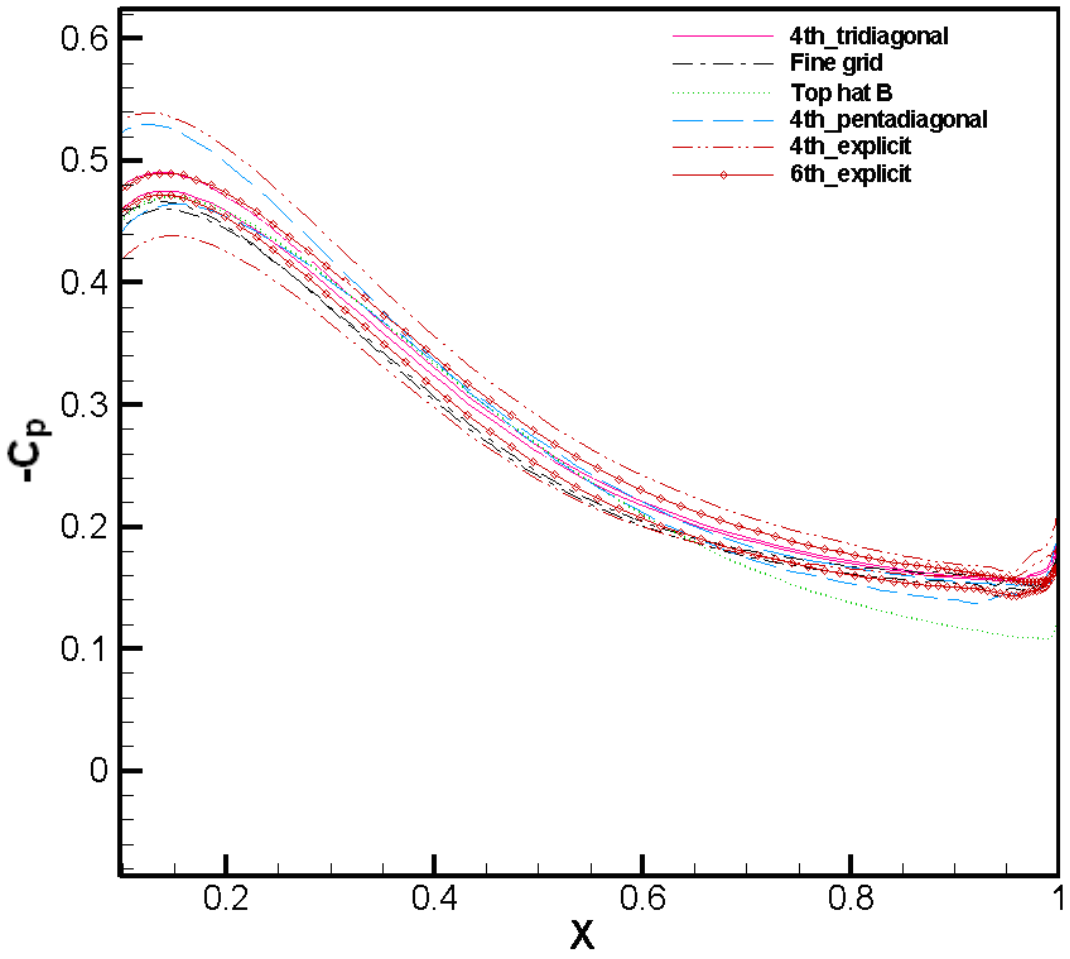

Figure 3.22 Comparison among filtered pressure coefficient by selected filter schemes and DNS solution (exaggerated view).

3.1.7 Comparison of cost between filtered and DNS results:

Using the filtering approach dramatically reduces the computational time by reducing the number of grid points needed to solve the problem numerically. In this case, the grid points are 1180 × 258 and the computational time to solve the Navier-Stokes equations over this mesh for one timestep was 0.536s. On the other hand, the time needed to complete one timestep on the fine grid was 1.563s which means a reduction of around a factor of three, which is already a significant saving. A further reduction in grid points will be attempted in the next section to find the optimum resolution.

3.2 Validation of 2D filtered Navier-Stokes simulation and 3D LES against DNS (Re = 50,000 and $\alpha = 5°$)

This section presents comparisons of two-dimensional filtered Navier-Stokes simulation and three-dimensional large-eddy simulations (LES) with direct numerical simulation in order to validate the LES code. All simulations have been applied to a flow around an NACA-0012 airfoil with a Mach number of 0.4, an angle of incidence of 5°, and a Reynolds number of 50,000.

For the two-dimensional simulation case, a 637×375 grid was generated, and calculations without a subgrid scale (SGS) model were performed. Aerodynamic data were compared with the DNS data from Jones *et al.* (2008) with a mesh size of 2570 × 692, which is clearly much more expensive. A common approach is to filter DNS data before comparing with LES, but in the present study this was not done, since the intention was to assess the accuracy of the aerodynamic data. The two-dimensional simulation was then extended to a three-dimensional simulation by distributing 32 grid points in the spanwise direction along 0.2 chord length and comparing the results with DNS on a 2570×692×96 grid. The main grid parameters of both two- and three-dimensional simulations are summarized in Table 3.2. The columns W, R, and 'Total Length' correspond to the wake length, radius and total domain length, respectively, in chord units of the airfoil, whereas N_ξ and N_η represent the numbers of grid points in curvilinear directions ξ and η, respectively. The columns PS, SS, NW, and 'Total Points' correspond to the numbers of cells on the pressure side, suction side, wake and total cells, respectively.

Grids were refined by an iterative process. For the chosen filter coefficient σ the simulation was run for a short time and under-resolved regions (revealed by grid-to-grid point oscillations) were identified. The grid was refined in these regions and the run continued. The process was repeated until a good grid was found. For the initial validations we consider 2D filtered Navier-Stokes simulations and 3D LES compared to reference DNS in 2D and 3D, respectively.

The three-dimensional simulations were conducted in two ways: first, by applying the LES without using any subgrid-scale model, i.e. relying on filtering alone and, second, by adding the mixed-time-scale (MTS) model (see section 2.5.3). It should be mentioned here that perturbation terms [equations (3.10-3.12)] were added to the three-dimensional simulation in order to trigger transition to turbulence. Low-amplitude forcing was applied inside the separated shear layer and then removed after it has triggered the transition to turbulence.

Table 3.2 Comparison of grid parameters for validation study (Re = 50,000 and $\alpha = 5°$)

Simulation	W	R	Total Length	N_ξ	N_η	N_z	L_z/c	PS	SS	NW	Total points
2D filtered N-S	5	7.3	14.2	637	375	-	-	78	190	185	238875
LES(3D)	5	7.3	14.2	637	375	32	0.2	78	190	85	7644000
DNS(3D)	5	7.3	14.2	2570	692	96	0.2	292	792	753	170730240

3.2.1 Comparison of results for two-dimensional simulations:

The numerical results from the two-dimensional case were obtained by applying filtering to every time step. In order to obtain a result that was as accurate as possible, a parametric study was performed (not shown here), using different values of the filtering coefficient (σ) to find the best solution compared with the DNS; $\sigma = 0.14$ was found to be the optimum value. The simulation was performed using a time step of 1.55×10^{-4}, which was also used for both the forced and unforced stages in 3D LES. This was the maximum allowable time step in both stages. Statistical data describing the aerodynamics of the simulation, such as pressure coefficient and skin friction, were computed after the flow had reached a time-periodic state, while the time-dependent lift coefficient (C_L) and drag coefficient (C_D) were plotted from the first time step.

The lift coefficient is depicted in Figure 3.23, which shows that the initial transient is complete after the flow has developed for 60 non-dimensional units of time. It is also apparent that the time-dependent lift coefficient (C_L) oscillates periodically around a mean of 0.495 as illustrated in Figure 3.24, which agrees with the DNS results (Jones 2007). It is noticeable that the lift coefficient exhibits more regularity than the DNS lift coefficient, which is also shown in Figure 3.24. This regularity is presumably due to the decrease in degrees of freedom associated with the coarser mesh. The frequency of the

oscillatory lift coefficient, f = 3.371 is obtained after applying a Fast Fourier Transformation (FFT) (Figures 3.25), which matches the DNS, where f = 3.375 was obtained. From the Fourier analysis, the DNS signal has an additional lower frequency (f = 1.98) present, with a fifth of the amplitude of the dominant shedding mode as shown in Figure 3.26.

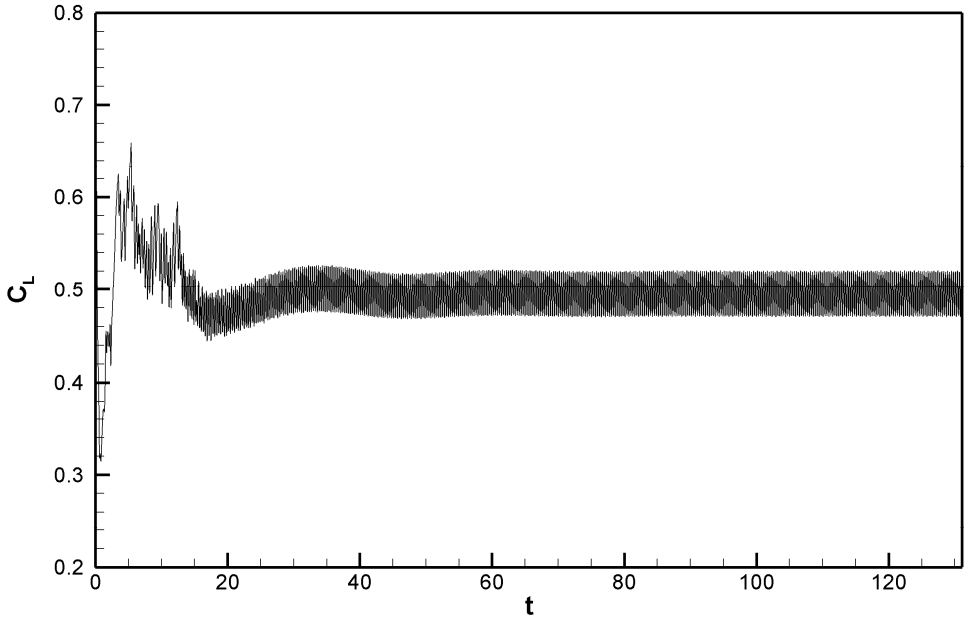

Figure 3.23 Time dependent lift coefficient (C_L) obtained by 2D filtered Navier-Stokes simulation at Re = 50,000 with 5° angle of incidence.

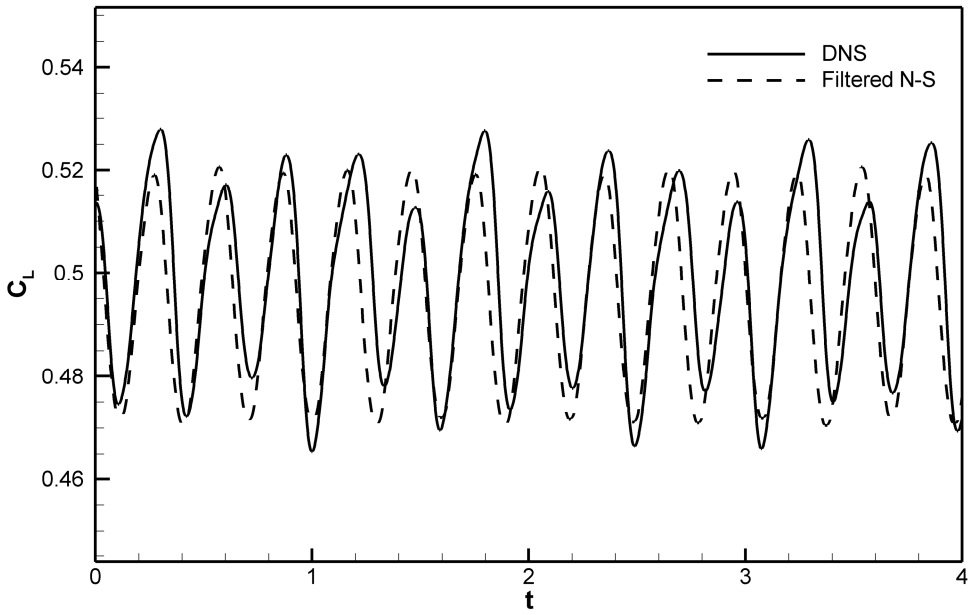

Figure 3.24 Comparison of time-dependent lift coefficient between DNS and 2D filtered Navier-Stokes simulation (Re = 50,000 and $\alpha = 5^o$).

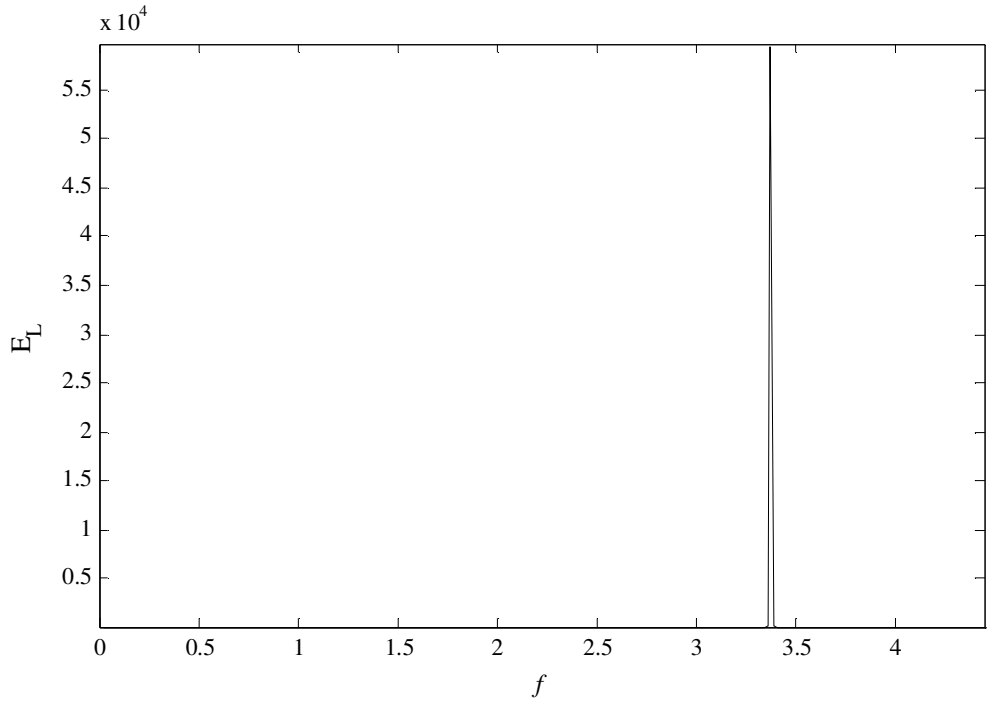

Figure 3.25 Frequency-response of the time-dependent lift coefficient obtained from FFT (2D filtered Navier-Stokes simulation).

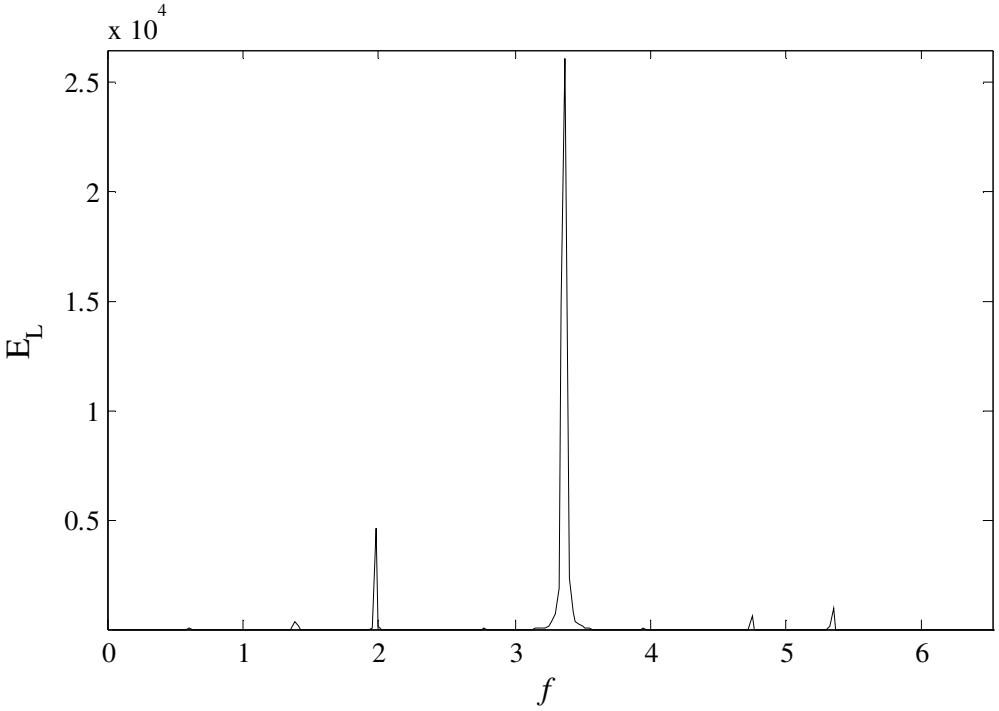

Figure 3.26 Frequency-response of the time-dependent lift coefficient obtained from FFT (DNS).

The drag coefficient (C_D) obtained by the 2D filtered Navier-Stokes equations is shown in Figures 3.27 and 3.28, where the oscillation is around a mean of 0.0225. Table 3.3 summarises the comparison between the two-dimensional solution of DNS and 2D filtered Navier-Stokes simulation based on aerodynamic forces.

Table 3.3 Time-averaged lift and drag coefficients for two-dimensional simulations.

Simulation	C_L	C_D
2D filtered N-S	0.495	0.022
DNS	0.499	0.022
Percentage error (%)	0.74	0.0

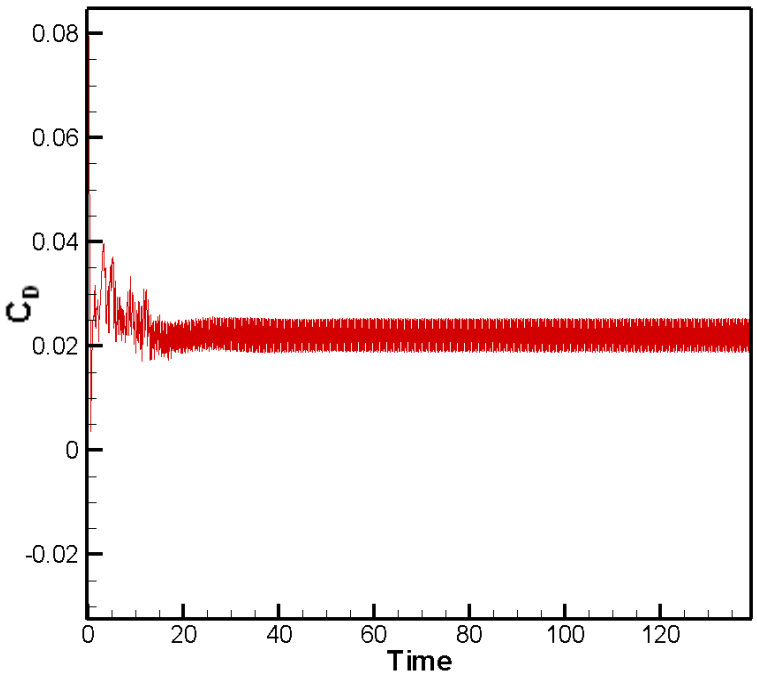

Figure 3.27 time-dependent drag coefficient obtained from 2D filtered Navier-Stokes simulation at Re = 50,000 and angle of incidence of 5°.

The pressure coefficient distribution along the airfoil that was obtained from the 2D filtered Navier-Stokes simulation is plotted together with the distribution from DNS in Figure 3.29, where it can be seen that the 2D filtered Navier-Stokes pressure coefficient matches the DNS very well. Figure 3.29 also shows the strong adverse pressure gradient near the leading edge that causes separation, followed by a pressure plateau that indicates the dead-air region in the LSB. The Reynolds number based on the momentum thickness and velocity of the boundary layer at the separation point (R_{θ_s}) is found to be 101.7 which is less than the critical Reynolds number from Gaster (1966) which is $R_{\theta_s} = 125$ (as mentioned in Chapter 1 section 1.2.1). Inspection of Figure 3.29 confirms the observation of Ripley and Pauley (1993) about the existence of a "spike" at the end of the pressure plateau for 2D simulations, as discussed in section 1.2. The rapid increase in the pressure that occurs after the pressure plateau is a result of the roll-up of vortices at the back of the bubble, prior to vortex shedding.

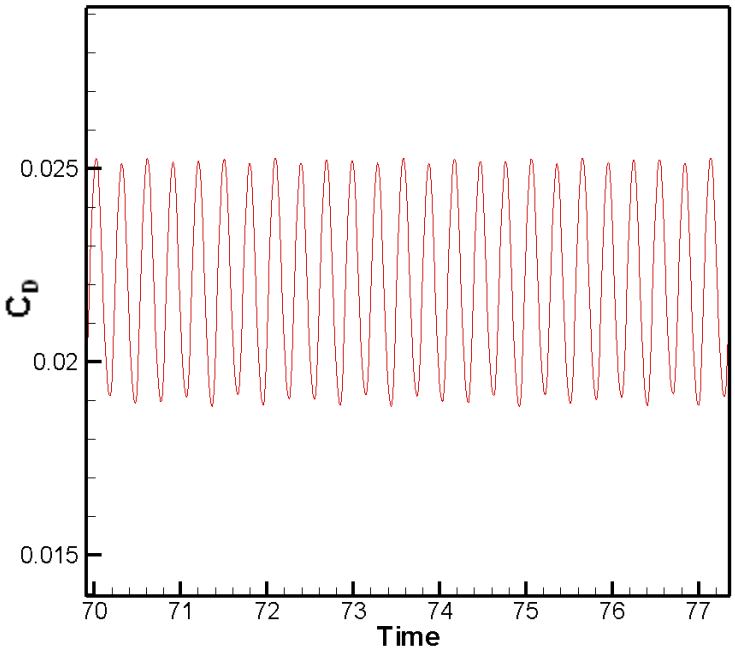

Figure 3.28 Close view for time-dependent drag coefficient obtained from the 2D filtered Navier-Stokes simulation at Re = 50,000 with 5° incidence.

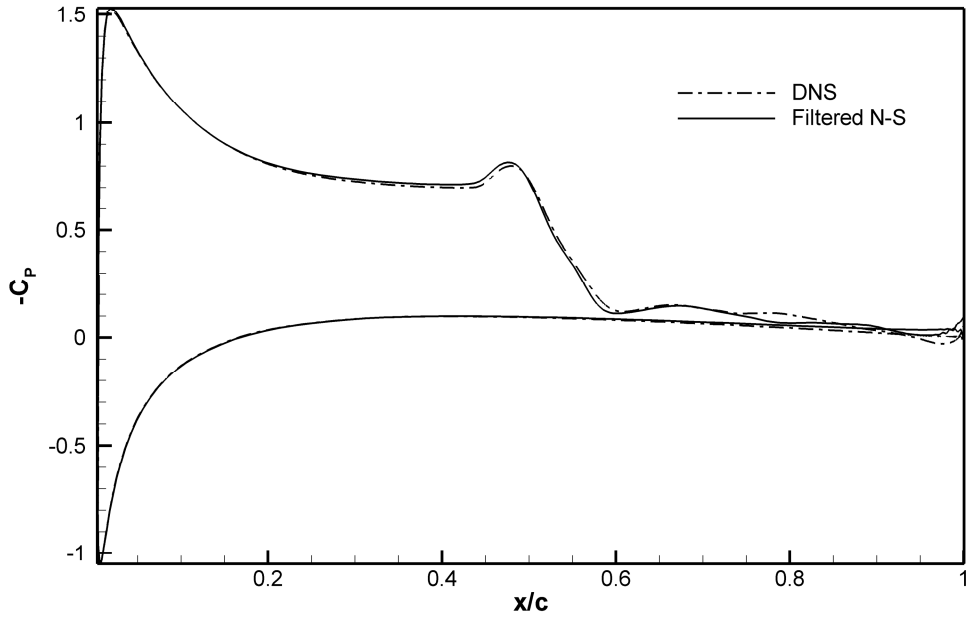

Figure 3.29 Comparison of pressure coefficient between DNS and 2D filtered Navier-Stokes simulation.

The separation and reattachment of the flow can be calculated by studying the skin-friction coefficient and finding the location of zero crossings, where a positive to

negative crossing indicates separation while a negative to positive crossing corresponds to reattachment. Figure 3.30 shows a comparison of skin friction coefficients between the DNS and 2D filtered Navier-Stokes simulation. The results of the 2D filtered Navier-Stokes simulation solution are very close to the DNS results. To be more precise, the 2D filtered Navier-Stokes simulation separation location is at x_{sep}/c = 0.144 compared to x_{sep}/c = 0.151 for the DNS solution, while the reattachment of the flow is at x_{reatt}/c = 0.5805 for 2D filtered Navier-Stokes simulation and x_{reatt}/c = 0.5820 for DNS. There is a noticeable difference between DNS and the 2D filtered Navier-Stokes simulation past the location of the laminar separation bubble which presumably due to differences in the resolution of the vortex shedding. It can also be noticed from Figure 3.30 that there is a small region where the skin-friction suddenly becomes positive before it decreases once again. This region was found to correspond to a thin layer of secondary separation located underneath the reverse flow, as shown in Figure 3.31, where the vectors of averaged streamwise velocity near to this particular region are depicted. This region was also found in the study of Shan *et al.* (2005). The existence of relatively large oscillation of C_f near the trailing edge limited the choice of grid, because any further decrease of resolution causes these oscillations to grow excessively in amplitude.

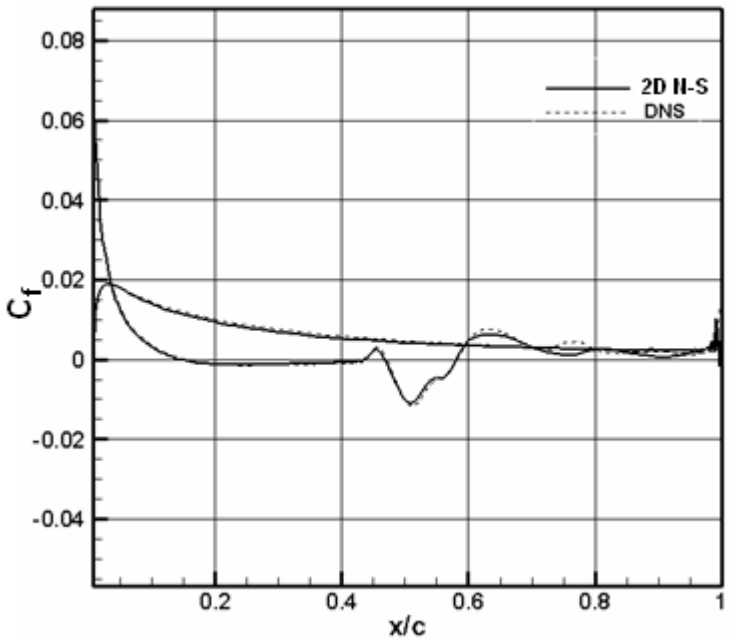

Figure 3.30 Comparison of skin friction coefficients between DNS and 2D filtered Navier-Stokes simulation.

The laminar separation bubble can be clearly seen when averaged data, such as the streamwise velocity, are produced by 2D filtered Navier-Stokes simulation, as shown in Figure 3.32.

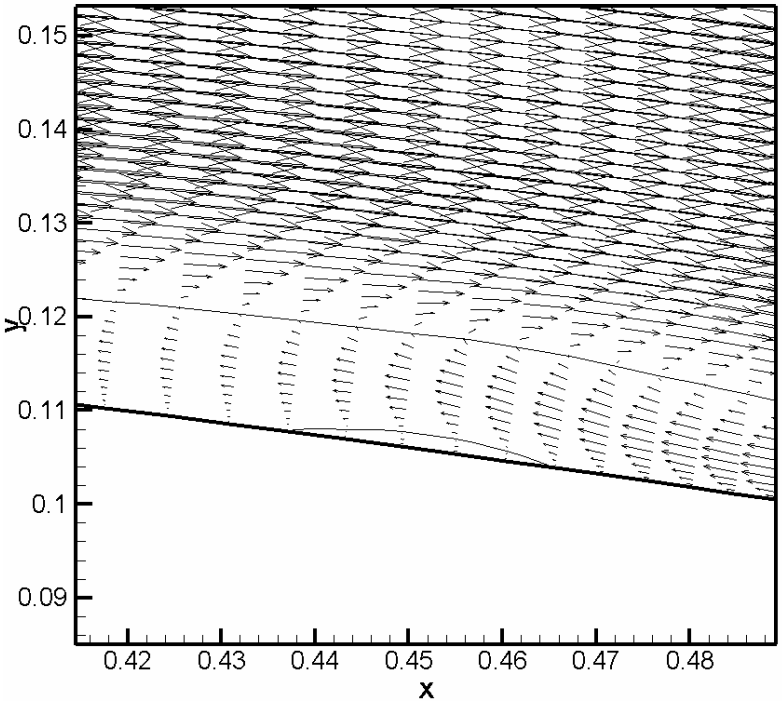

Figure 3.31 Vectors of averaged streamwise velocities showing the thin layer of secondry separation within the separation bubble.

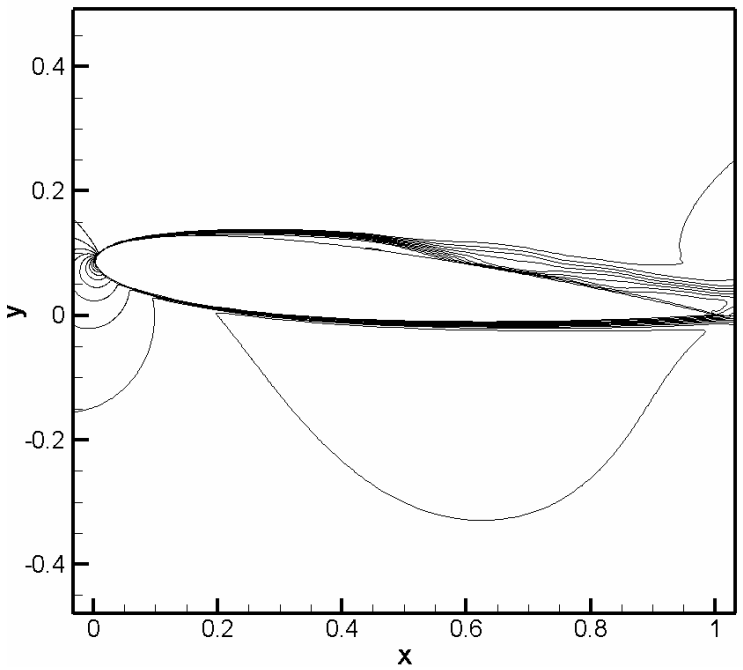

Figure 3.32 Averaged streamwise velocity using ten contour levels in the range from 0 to 1 obtained from 2D filtered Navier-Stokes simulation at Re = 50,000 and incidence of 5°.

Contours of instantaneous vorticity obtained from 2D filtered Navier-Stokes simulation are shown in Figure 3.33, where it can be observed that the separated shear layer on the suction side of the airfoil becomes unstable near the middle of the airfoil chord. Large-scale vortices are generated and convect downstream, leading to the development of vortex shedding. This growth of vortices occurs as a result of the propagation and growth of disturbances within the separated shear layer by the Kelvin-Helmholtz instability mechanism.

The successful 2D filtered Navier-Stokes calculation of flow behaviour can be confirmed when comparing Figure 3.33 with the DNS vorticity shown on Figure 3.34. From these Figures, it is obvious that the vorticity obtained by 2D filtered Navier-Stokes simulation is similar to the DNS, with very small numerical oscillations observed near the reattachment point ($x/c \approx 0.75$) due to the existence of under resolution in this region, which, however, is not harmful to the solution.

The acoustic waves obtained by the 2D filtered Navier-Stokes simulation shown in Figure 3.35 were found to be in good agreement with the DNS (Figure 3.36). Figure 3.35 illustrates the benefit of filtering since the small numerical oscillations in Figure 3.36 are removed. However, it should be noted that some of the acoustic waves in Figure 3.35 disappeared or are highly damped compared to the DNS, which is due to the damping by filtering and this implies that in order to resolve the acoustic waves by 2D filtered Navier-Stokes simulation, relatively high resolution is needed to overcome the filtering damping.

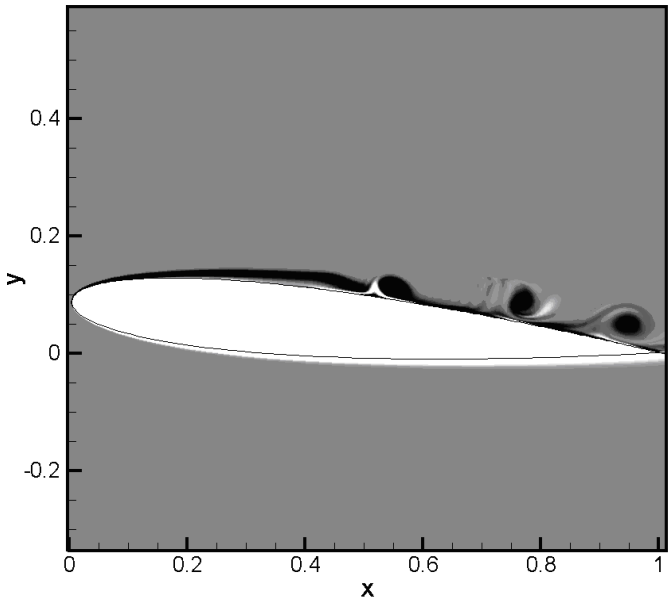

Figure 3.33 Vorticity contours for the 2D filtered Navier-Stokes simulation using 10 contour levels in the range from -50 to 50.

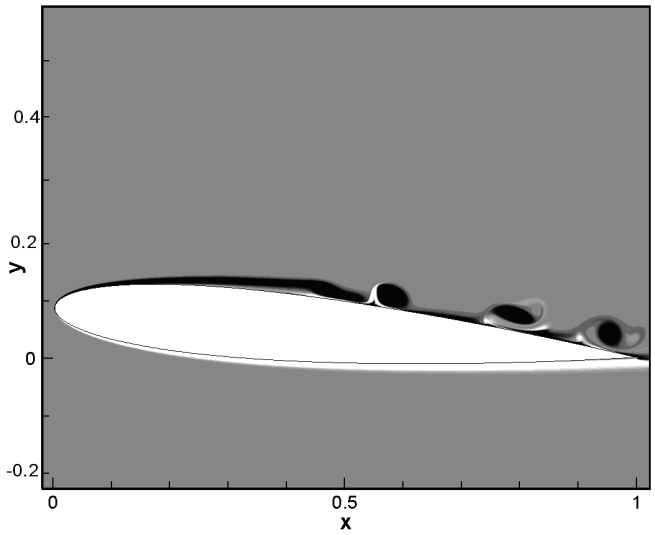

Figure 3.34 DNS vorticity contour for 2D simulation at Re = 50,000 with 5° incidence using 10 contour levels in the range from -50 to 50 (taken from Jones 2007).

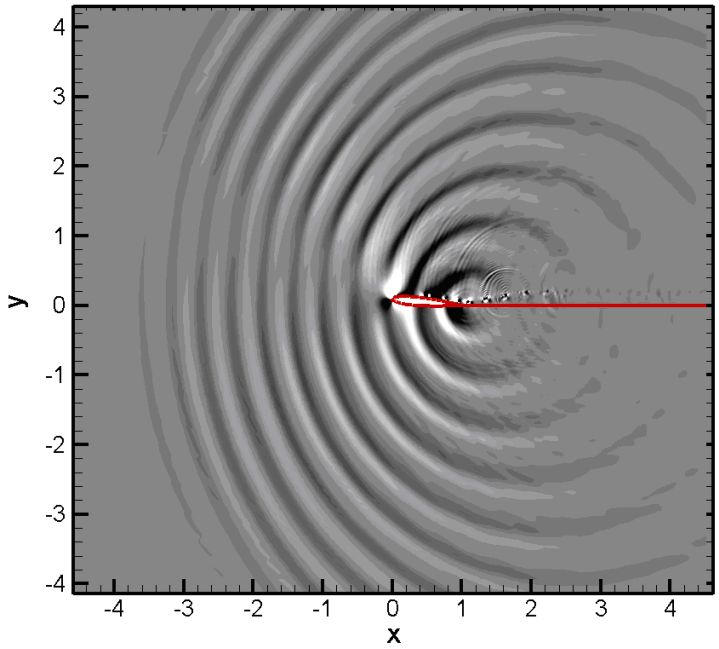

Figure 3.35 ∇.u contours for 2D filtered Navier-Stokes simulation using ten contour levels in the range from -0.1 to 0.1.

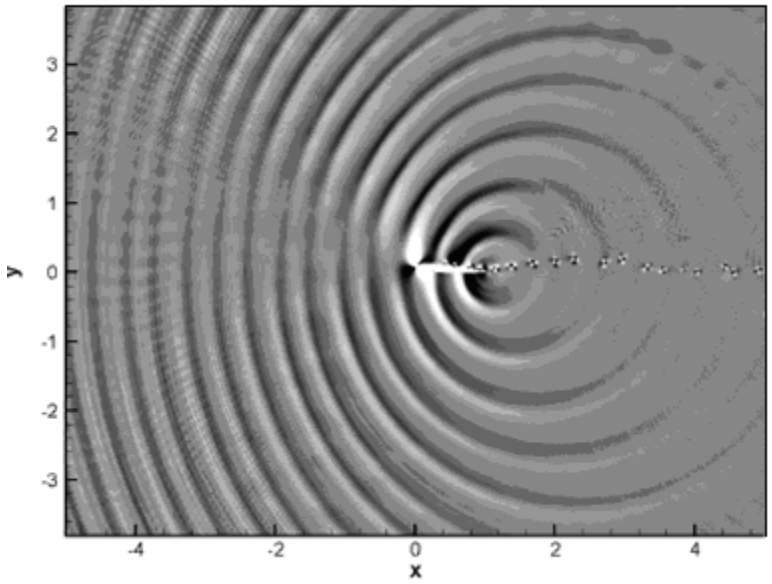

Figure 3.36 DNS ∇.u contours for 2D simulation using ten contour levels in the range from -0.1 to 0.1.

3.2.2 Comparison of results for 3D simulations

The results presented in section 3.2.1 were for two-dimensional simulations, in which large scales dominate the flow. However, in most practical applications involving turbulent flows, three-dimensional phenomena and breakdown to small scales play a

crucial role. For example, the stalling and bursting phenomena of flow around an airfoil cannot be accurately captured by a two-dimensional simulation, as will be seen in Chapter 4 where the results of simulations at higher incidence are shown.

The three-dimensional simulation needs more processors compared to the two-dimensional simulation, therefore 64 processors were used to do the calculations compared to 16 processors for the two-dimensional simulation. The two-dimensional solution is taken as an initial condition for the three-dimensional simulation. Forcing is applied at the early stages of the three-dimensional simulation to trigger transition to turbulence. Then, the forcing is removed, and the simulation is run further. The statistical data are dumped after every 10,000 time steps, where the time step is set to 1.55×10^{-4} and the level of free-stream turbulence is zero.

Figure 3.37 shows a three-dimensional isosurfaces of the second invariant of the velocity gradient tensor

$$Q = -\frac{1}{2}\frac{\partial u_i}{\partial x_j}\frac{\partial u_j}{\partial x_i} = -\frac{1}{2}(S_{ij}S_{ij} - \Omega_{ij}\Omega_{ij}) \tag{3.12}$$

over the upper surface of the airfoil. Positives values of the Q-criterion locate regions in which rotation dominates over strain rate. From this figure, it is clear that the process of breakdown to turbulence is captured in the LES, in qualitative agreement with the DNS of Jones *et al.* (2008). Starting from the leading edge, the shear layer is detached from the wall with laminar two-dimensional behaviour. Transition becomes visible as a small distortion of the shear layer and the three-dimensionality of the flow starts to grow. Large-scale structures form and then break down into small structures followed by fully three-dimensional turbulent flow.

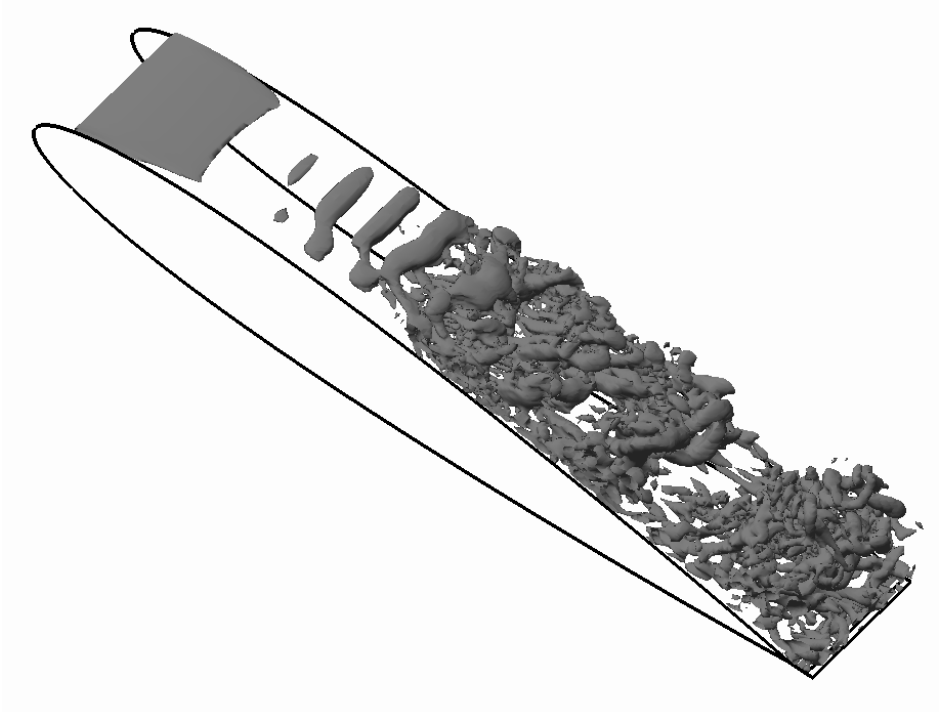

Figure 3.37 LES solution for three-dimensional isosurface of second invariant of the velocity gradient at Q =100.

Adequate mesh resolution is important to obtain an accurate solution and to ensure that the large eddies in the flow are resolved. Wall units y^+, Δx^+, and Δz^+, are normally used to check the mesh resolution for a particular grid. The friction velocity u_τ is used to calculate y^+ as shown in equation (2.34) and u_τ is obtained by using the wall shear stress τ_w and the kinematic viscosity ν:

$$u_\tau = \sqrt{\frac{|\tau_w|}{\rho}} \tag{3.13}$$

Consequently, Δx^+ and Δz^+ are calculated as:

$$\Delta x^+ = \frac{\Delta x \, u_\tau}{\nu} \tag{3.14}$$

and

$$\Delta z^+ = \frac{\Delta z \, u_\tau}{\nu} \tag{3.15}$$

respectively. LES usually needs streamwise and spanwise mesh resolutions based on wall units of approximately $\Delta x^+ \le 50$ and $\Delta z^+ \le 20$, respectively. Also, the mesh should be designed to give 3 or 4 points in $y^+ < 10$, and $y_1^+ < 1$ where y_1^+ is the maximum value of

y^+ for the first grid point from the surface. These requirements have been met in the present three-dimensional simulation as illustrated in Figures 3.38 and 3.39. Figure 3.38 shows the variation of the streamwise and spanwise resolutions on the suction side. In each case, the mesh resolutions in the transitional and turbulent regions satisfy the LES resolution requirements (we have $\Delta x^+ < 15$ and $\Delta z^+ < 21$). Figure 3.39 shows that the first grid point from the surface in the LES has $y_1^+ = 0.849$, which is the worst value in the turbulent region (at x/c = 0.7), and with five grid points in $y^+ < 10$, which satisfies the LES requirements. Table 3.4 shows a comparison of mesh resolutions between the DNS and LES.

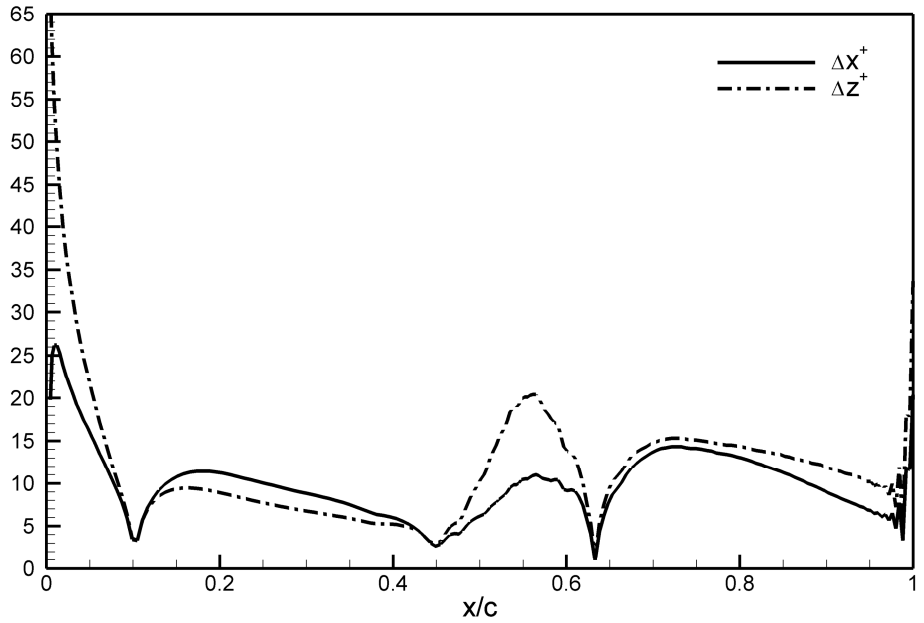

Figure 3.38 Streamwise and spanwise mesh resolutions on the suction side in the wall unit obtained from 3D LES ($\alpha = 5°$, without SGS).

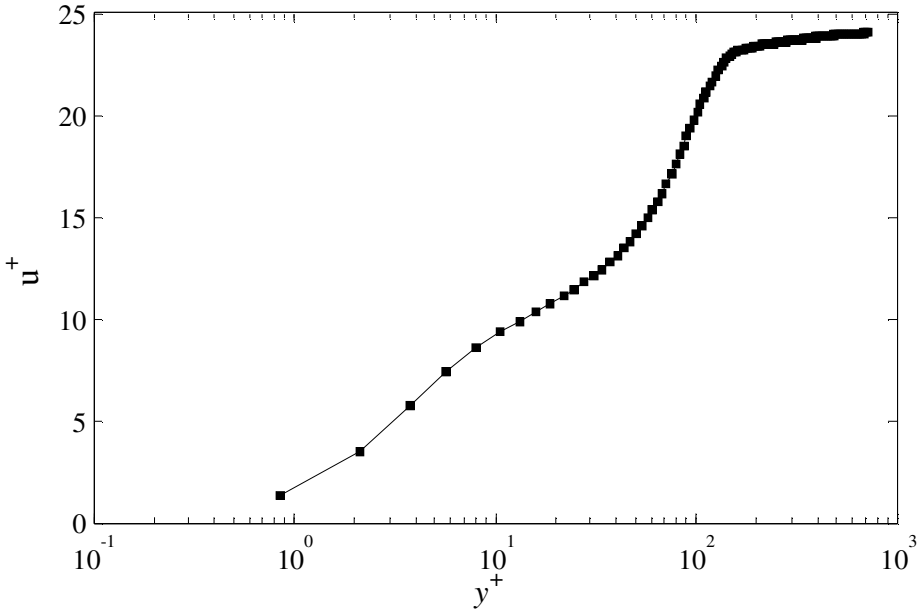

Figure 3.39 Time-averaged boundary layer at *x/c* = 0.7 showing the near wall grid points.

Table 3.4 Comparison of grid resolution in the wall unit between DNS and LES results at *x/c* = 0.7 (Re = 50,000 and α = 5°).

Simulation	Δx^+	Δz^+	No. of points at $y^+ < 10$
LES	14.3	15.3	5
DNS	3.36	6.49	9

Figure 3.40 shows the time-dependent lift coefficient obtained from the LES without an SGS model. The solution with forcing exhibits slight oscillations at the beginning of the simulation up to $t = 2$, which corresponds to the two-dimensional vortex shedding and is exactly the same as found by Jones (2007). After that, the lift increases until it reaches approximately 0.58 at $t = 10$, which is slightly lower than the DNS results (~ 0.61).

The drag coefficient is shown in Figure 3.41. The peak of the drag in this figure at a time of approximately 13 indicates the influence of removing the explicitly-added forcing at $t = 12$. Before this time, the drag exhibits fluctuations around a mean value of 0.016, which is lower than the drag obtained from the forced DNS, which was 0.0294. The drag coefficient was found to fluctuate around 0.028-0.029 for the unforced LES while it was 0.0358 in the DNS. Table 3.5 compares the time-averaged lift and drag

coefficients for forced and unforced LES over a time period of $8 \leq t \leq 11$ for the forced case and $23 \leq t \leq 27$ for the unforced case, and DNS simulations. Table 3.5 also compares the LES data with the Xfoil results for the forced case where it is clear that the drag coefficient obtained by the DNS is similar to the Xfoil drag while the lift coefficient of the Xfoil is larger than the DNS and LES lift coefficient.

Table 3.5 Time-averaged lift and drag coefficients for three-dimensional simulations.

Simulation	forced				unforced			
	C_L	C_D	C_{df}	C_{dp}	C_L	C_D	C_{df}	C_{dp}
LES	0.58	0.0160	0.0103	0.0057	0.60	0.0285	0.0073	0.0212
DNS	0.61	0.0294	0.0095	0.0199	0.62	0.0358	0.0081	0.0278
Xfoil	0.66	0.0285	0.0097	0.0188	-	-	-	-

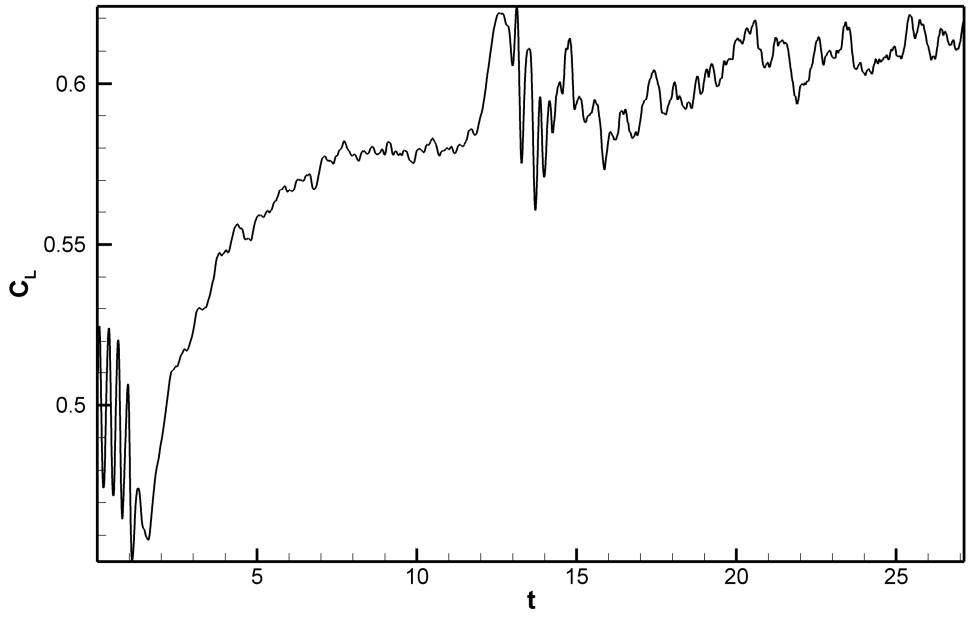

Figure 3.40 Time-dependent lift coefficient obtained by LES at Re = 50,000 with 5° incidence (3D case).

Comparisons between the LES and DNS have also been made based on the momentum and displacement thickness in Figure 3.42, in which it can be clearly seen that the LES solution matches the DNS solution very well.

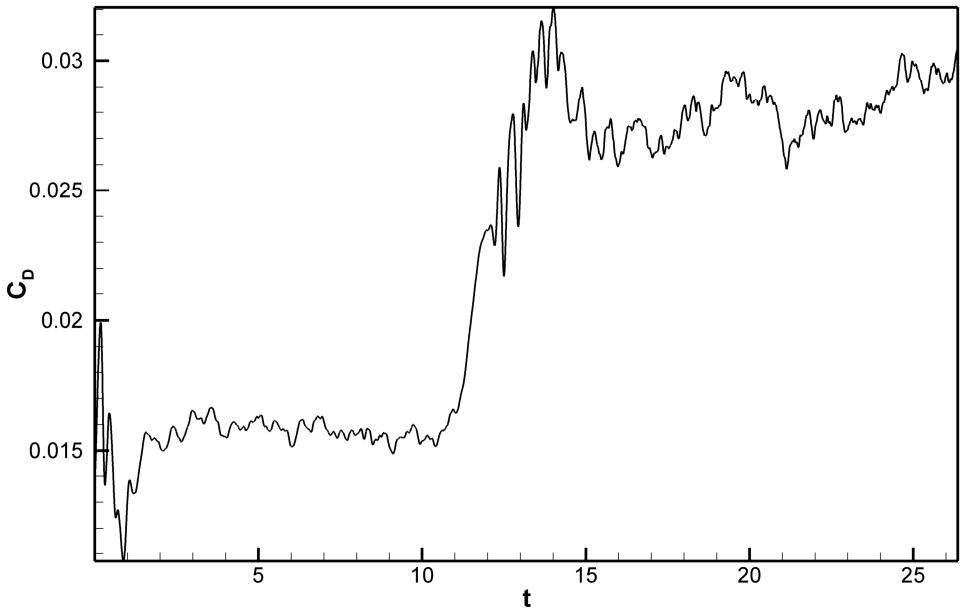

Figure 3.41 Time-dependent drag coefficient obtained by LES at Re = 50,000 with 5° incidence (3D case).

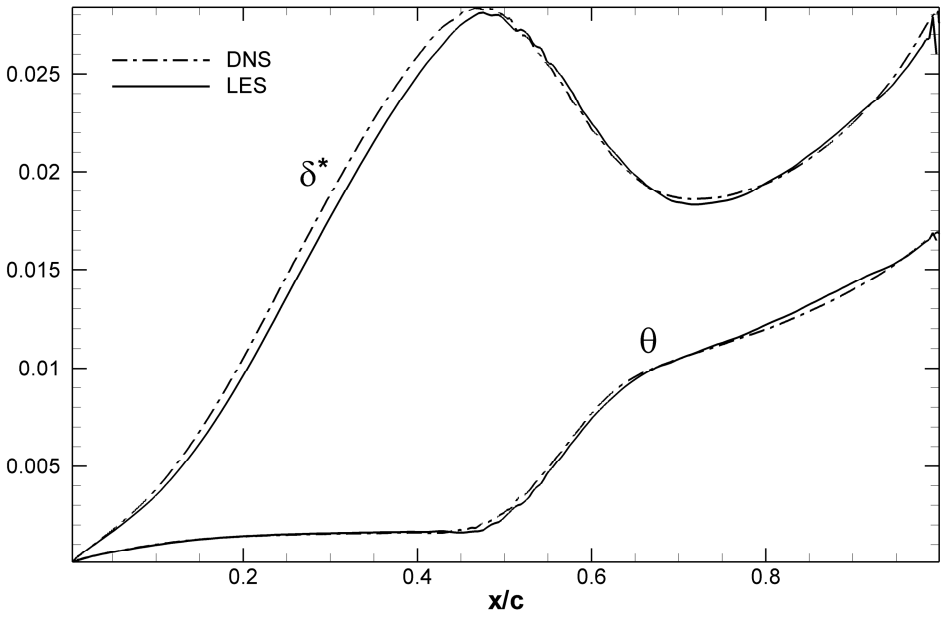

Figure 3.42 Comparison of displacement and momentum thickness between DNS and LES for the case of 5° incidence at Re = 50,000 (without SGS model).

3.2.3 Effect of Subgrid Scale Model

In order to assess the effect of the SGS model on the LES solution, the mixed-time scale model has been added to the same code that was used for the filtered three-dimensional LES without SGS (in section 3.2.2), and the simulation was run for the same grid. The aim is to reproduce statistical data of the three-dimensional simulation and compare the results with the LES solution without an SGS model, and with the DNS. The LES code always includes filtering in the present study. The procedure of performing the simulation was the same for both cases. Results obtained from this simulation exhibit the benefits of using the SGS model. For example, the pressure distributions over the airfoil obtained by both LES simulations clearly match the DNS without any significant error, as illustrated in Figure 3.43. The skin-friction profile, which is depicted in Figure 3.44, is more sensitive. It is clear that the LES with the SGS model is closer to the DNS than the LES without the SGS model, specifically under the recirculation vortex at the back of the bubble an in the region near reattachment. It is also seen that the solution on the pressure side is improved with the SGS model, even though that boundary layer is laminar. This is presumably an indirect effect due to the improved modelling of the bubble, which is transmitted to the pressure side by the change in the potential flow. It is concluded that the incorporation of the SGS model is beneficial in the present configuration and this formulation is applied for the remaining LES in this study. It is important to mention here that the dynamic Smagorinsky model was found to be impractical to use in the present study since was it found to require about two and half times more computational time compared to the MTS model.

It can be concluded from sections 3.2.1, 3.2.2 and 3.2.3 that the statistical results, such as pressure coefficient and skin friction, as well as the flow behaviour, such as vorticity, exhibit good agreement with the DNS of Jones *et al.* (2008). Numerical results of Inagaki *et al.* (2005) have shown that there is an improvement when the MTS model and filtering are included compared to the case of filtering alone, particularly for skin friction. The simulation required 15 hours for every 10,000 iterations (which is equivalent to 1.55 non-dimensional time units) using 64 processors (Intel 1.0 GHz). The

computational cost associated with LES was a factor of 22 less than the computational cost associated with DNS.

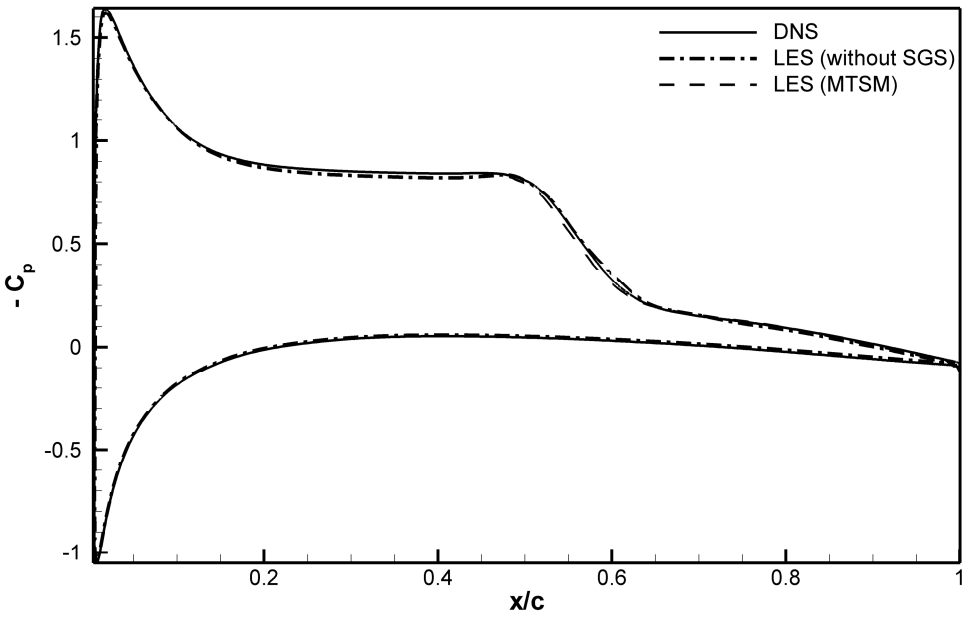

Figure 3.43 Comparison of pressure coefficients between DNS and LES without SGS and between DNS and LES using the MTS model .

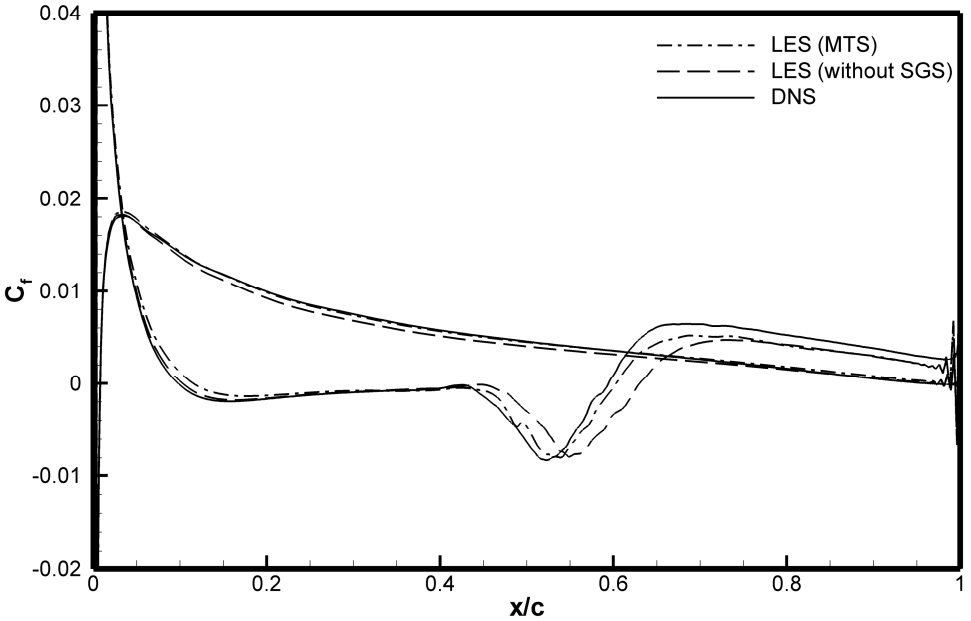

Figure 3.44 Comparison of skin-friction coefficients between DNS and LES without SGS and between DNS and LES using the MTS model.

3.3 Chapter summary

The LES code has been validated by comparing the results with the DNS of Jones (2007) for flow around a NACA 0012 airfoil at incidences of 0° and 5°. The 4^{th} order tridiagonal filter scheme has been found as the optimum filter scheme that gives the best solution among the tested filter schemes. The results of the two-dimensional filtered Navier-Stokes simulation showed the ability of the simulation to accurately reproduce the flapping phenomenon which was observed in the DNS. For the three-dimensional test case it was found that the LES code, with and without a subgrid scale model, provides comparable results with the DNS, with a small improvement when the mixed-time scale model is incorporated with the LES. Additionally, it has been shown that the computational cost associated with LES was a factor of 22 less than the computational cost associated with DNS. The computational time and space saving of the present LES code compared with the DNS for flow at a Reynolds number of 50,000 encourages application of the LES code at higher Reynolds but with more grid points, as it is necessary in order to resolve smaller turbulence scales at higher Reynolds number. This will be seen in next chapter where a LES for flow at a Reynolds number of 130,000 is performed.

The developed LES code will be used in the remaining thesis, to study flow phenomena associated with the low-Reynolds number airfoils such as the low-frequency flow oscillation (Chapter 4) and dynamic stall (Chapter 5). The LES code will also be used to investigate the effect of flow control with periodic forcing (Chapter 7).

4 Large eddy simulation of flow around an airfoil near stall

In this chapter the LES method from the previous chapters is used to study the phenomenon of low-frequency flow oscillation near stall. The chapter will be organized as follows: Firstly, the incidence range for which the low-frequency flow oscillation occurs will be sought for a NACA 0012 airfoil at a Reynolds number of 50,000. Secondly, the effect of increasing the Reynolds number will be investigated by performing another large eddy simulation around the same airfoil at a Reynolds number of 130,000 where experimental results of Rinoie and Takemura (2004) show a low-frequency flow oscillation. Finally, the influence of the computational domain width on the accuracy of predicting the phenomenon will be examined

4.1 LES results for an airfoil near stall at Re = 50,000

The objective of this section is to find the incidence at which the onset of stalling occurs for a NACA-0012 airfoil at a Mach number of 0.4 and a Reynolds number of 50,000. To accomplish this, a grid with 637×320×32 points was generated for an airfoil at incidences of 8.5°, 8.9°, 9.25°, 10°, and 11°. The grid was rotated for each case to obtain the required airfoil incidence. The main grid parameters are summarized in Table 4.1. The LES calculations were performed with the MTS subgrid model and explicit filtering. The spanwise width was set to be 0.2 of the chord.

Table 4.1 Grid parameters for LES (Re = 50,000 and α = 8.5°, 8.9°, 9.25°, 10° and 11°)

Simulation	W	R	Total Length	N_ξ	N_η	N_z	L_z/c	PS	SS	NW	Total points
LES (3D)	5	7.3	14.2	637	320	32	0.2	130	170	170	6522880

Each case is examined to determine whether the flow on the upper surface of the airfoil (suction side) exhibited a steady laminar separation bubble, low-frequency oscillation with an unsteady laminar separation bubble, or fully stalled flow. If the flow shows an indication of the presence of low-frequency oscillation, the three-dimensional LES simulation is continued for a longer period of time. Section 4.1.1 presents the differences between the two- and three-dimensional simulations based on their capabilities of capturing the stalling phenomenon. The attempts at finding the onset of stalling and the low frequency oscillations are discussed in section 4.1.2.

4.1.1 Difference between two- and three-dimensional simulations for flow near stall

As noted in section 3.2.2 of Chapter 3, it is generally accepted that the stalling and bursting phenomena of a flow around an airfoil cannot be properly captured by a two-dimensional simulation. This is supported by the study of Jones (2007) who demonstrated that the averaged results of the 2D simulation revealed a laminar separation bubble that shrinks as the incidence is increased. This is in contrast to the thin airfoil stall phenomenon where the reattachment point moves downstream as the incidence is increased. Jones (2007) also did not observe airfoil stall in 2D simulations. Gao e*t al.* (2008) concluded that 2D simulation for low Reynolds number airfoils, where the flow is characterized by laminar separation bubbles, is not recommended at high incidence and that 3D simulations are necessary to accurately predict the flow under stall conditions. The drawbacks of two-dimensional simulations are evident in Figure 4.1, where the pressure coefficient (C_p) over the surface of the airfoil is depicted at a range of incidence from 5° to 11°. As can be observed in the figure, when the incidence increases, the magnitude of the suction pressure coefficient also increases, which means that no stalling occurs. This is in contrast to the three-dimensional LES simulation, in which stalled flow can be observed at incidences of 10° and 11°, as shown in Figure 4.2. When examining this figure, it is apparent that there is an abrupt reduction of the maximum suction pressure coefficient from 2.4 to 1.9 when the incidence is increased from 8.5° to 10°, i.e. a 21% reduction, compared to an increase in suction pressure coefficient from 2.09 to 2.25 that is found in the two-dimensional simulation (Figure 4.1). Figure 4.2 indicates that the onset of bursting of the short laminar separation bubble (which is always formed at any incidence below 8.9°) occurred between 8.5° and 10° incidence. This bursting can lead to a fully separated flow that can be observed from changes in the pressure coefficient: the high suction pressure located near the leading edge in a short laminar bubble drops drastically to form a relatively flatter pressure distribution over the surface of the airfoil (for example, see the 11° case in Figure 4.2). Figure 4.3 shows the lift, drag and moment coefficients as a function of incidence which supports that the onset of stall is between 8.5° and 10°.

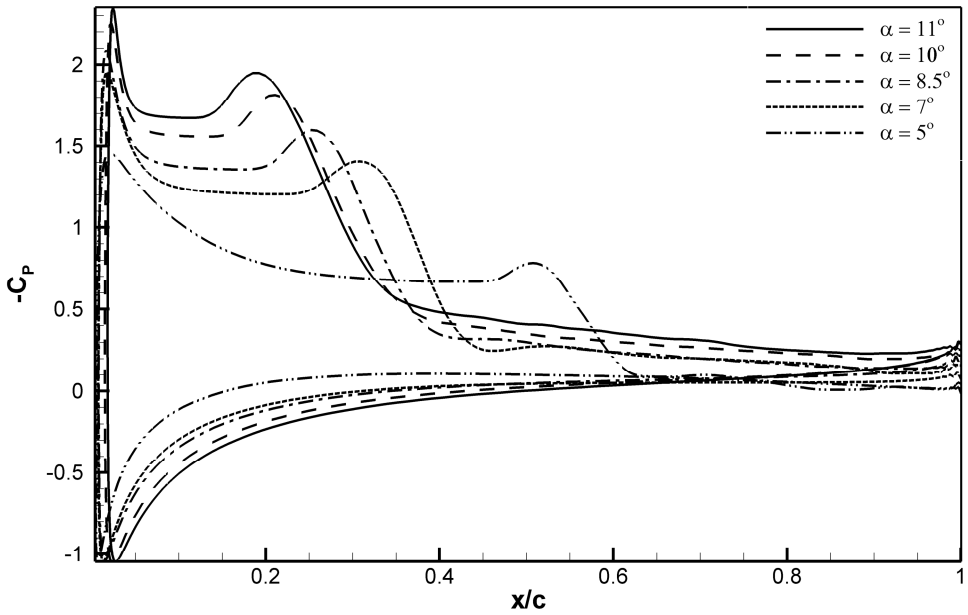

Figure 4.1 Pressure coefficients for several incidences obtained from 2D simulations.

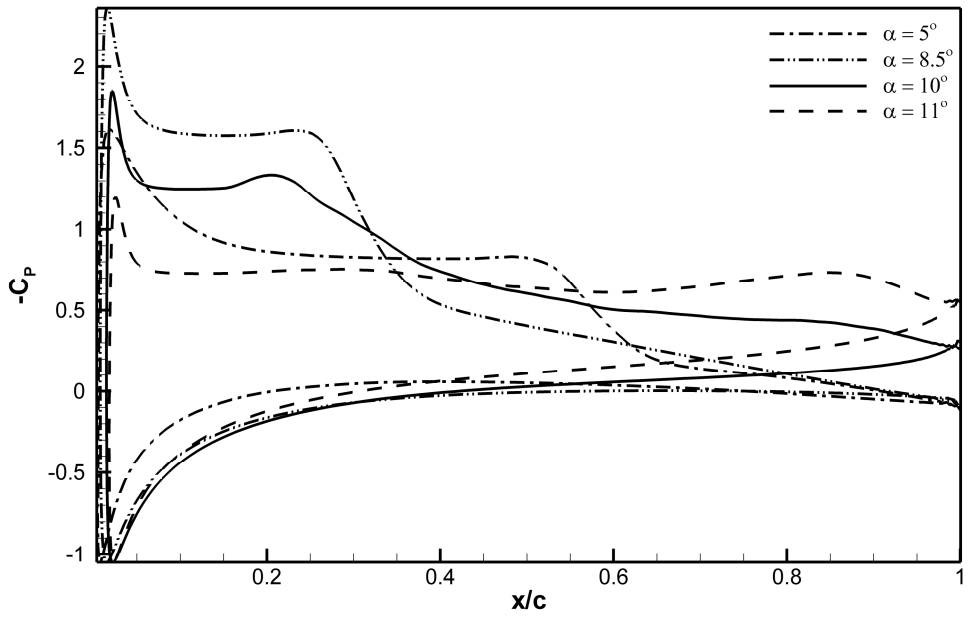

Figure 4.2 Pressure coefficient for several incidences obtained from 3D LES.

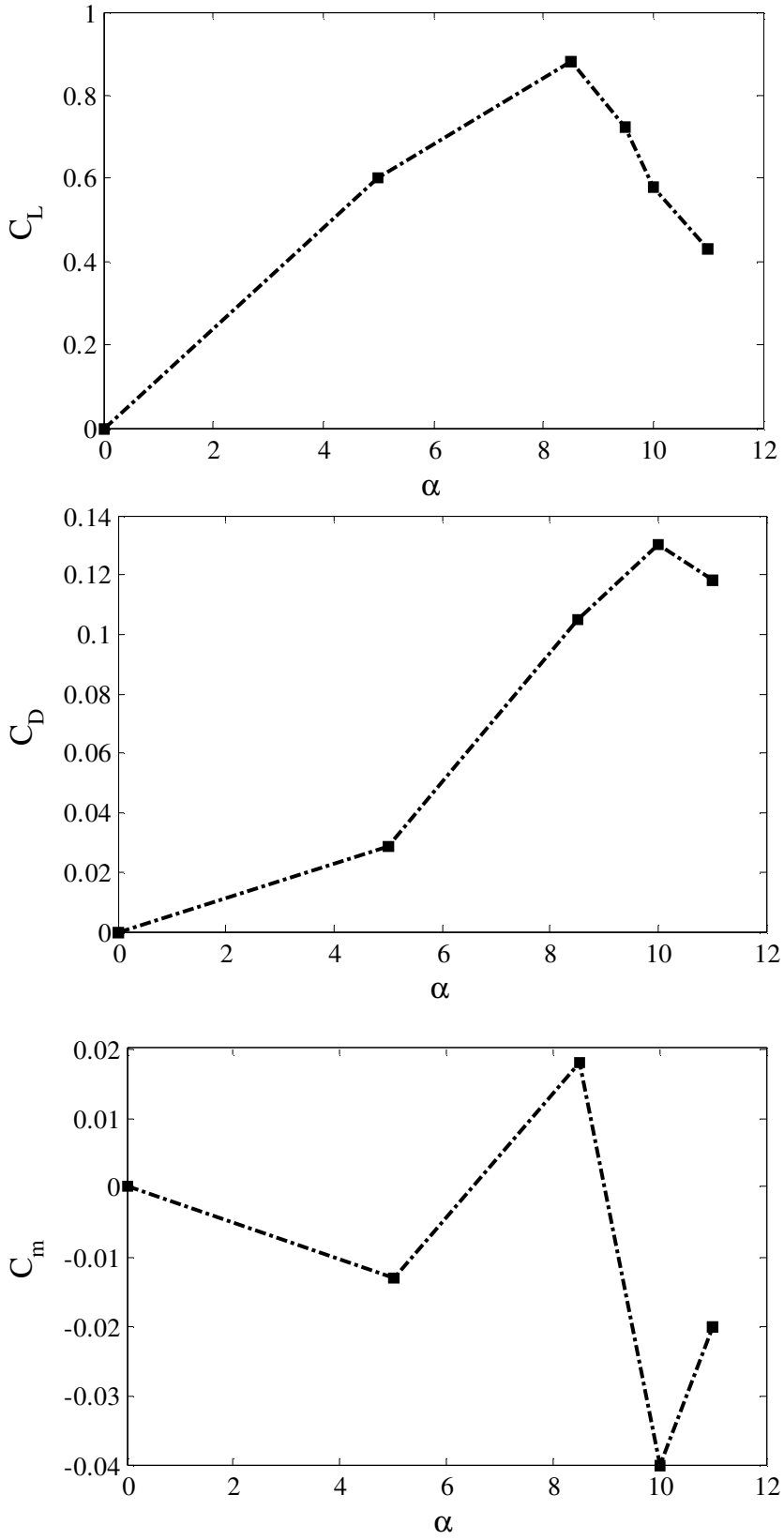

Figure 4.3 Lift, drag and moment coefficient versus the incidence for a Reynolds number of 50,000 and Mach number of 0.4 obtained from LES.

4.1.2 Low-frequency flow oscillations near stall

Trials to capture the low-frequency oscillations started from an incidence of 11°, where the flow is fully separated (Figure 4.3) and no large scale low-frequency oscillations are observed. Similarly, when the incidence was decreased to 10° a fully separated flow was formed. In contrast to the 11° and 10° cases, simulations at 8.5° and 8.9° exhibit unstalled flow without bursting of the LSB, as shown in Figures 4.4 and 4.5, respectively. Therefore, the expected incidence where the low-frequency oscillation may occur falls in the range of 8.9° to 10°. The airfoil is observed to switch initially between stalling and non-stalling conditions at an incidence of 9.25°. As discussed later, whether the cycle is maintained depends on the spanwise domain width.

Figure 4.6 shows the short time-averaged streamwise velocity over the first interval of flow oscillation for $11.2 \leq t \leq 60.0$ at $\alpha = 9.25°$. This interval is chosen because it contains a clear switching between bursting and reattachment of the laminar separation bubble. The interval was divided into six time subintervals, where each subinterval contains statistical data averaged over 50,000 time steps (eight non-dimensional time units). The bursting of the laminar separation bubble is clearly seen from $t = 11.2$ to $t = 19.2$, with the bubble reforming from $t = 43.2$ to $t = 60.0$.

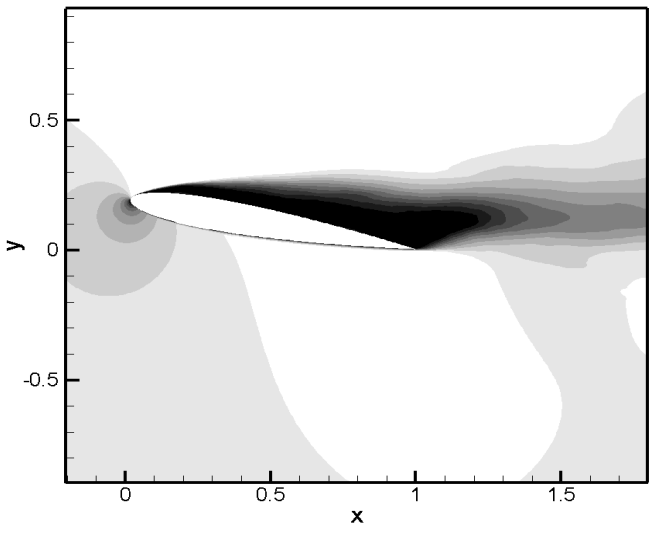

Figure 4.4 Averaged streamwise velocity contours at an incidence of 11° obtained from LES, using 10 contour levels in the range from 0 to 1.

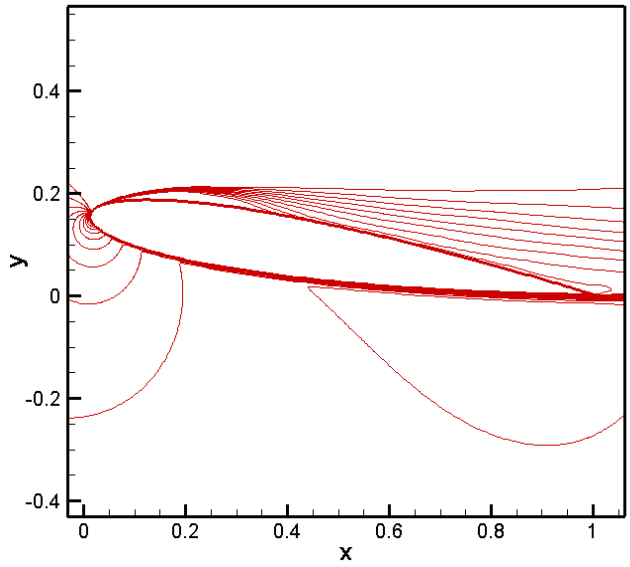

Figure 4.5 Averaged streamwise velocity contours for an incidence of 8.9° obtained from LES simulation using using 10 contour levels in the range from 0 to 1.

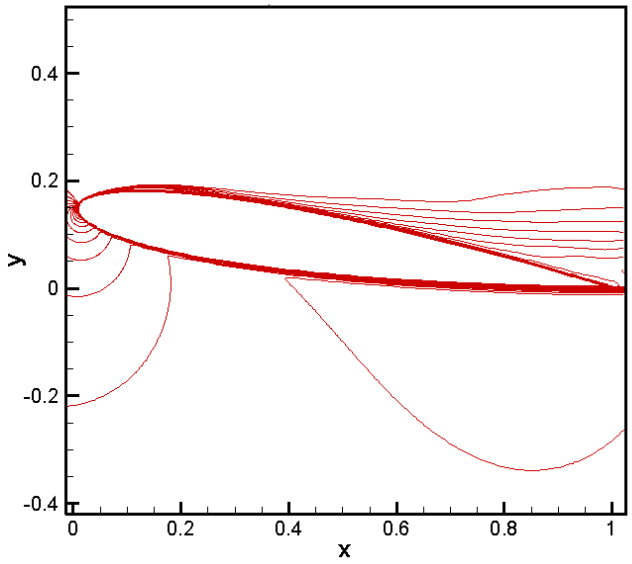

Figure 4.6 Averaged streamwise velocity contours for an incidence of 8.5° obtained from LES simulation using using 10 contour levels in the range from 0 to 1.

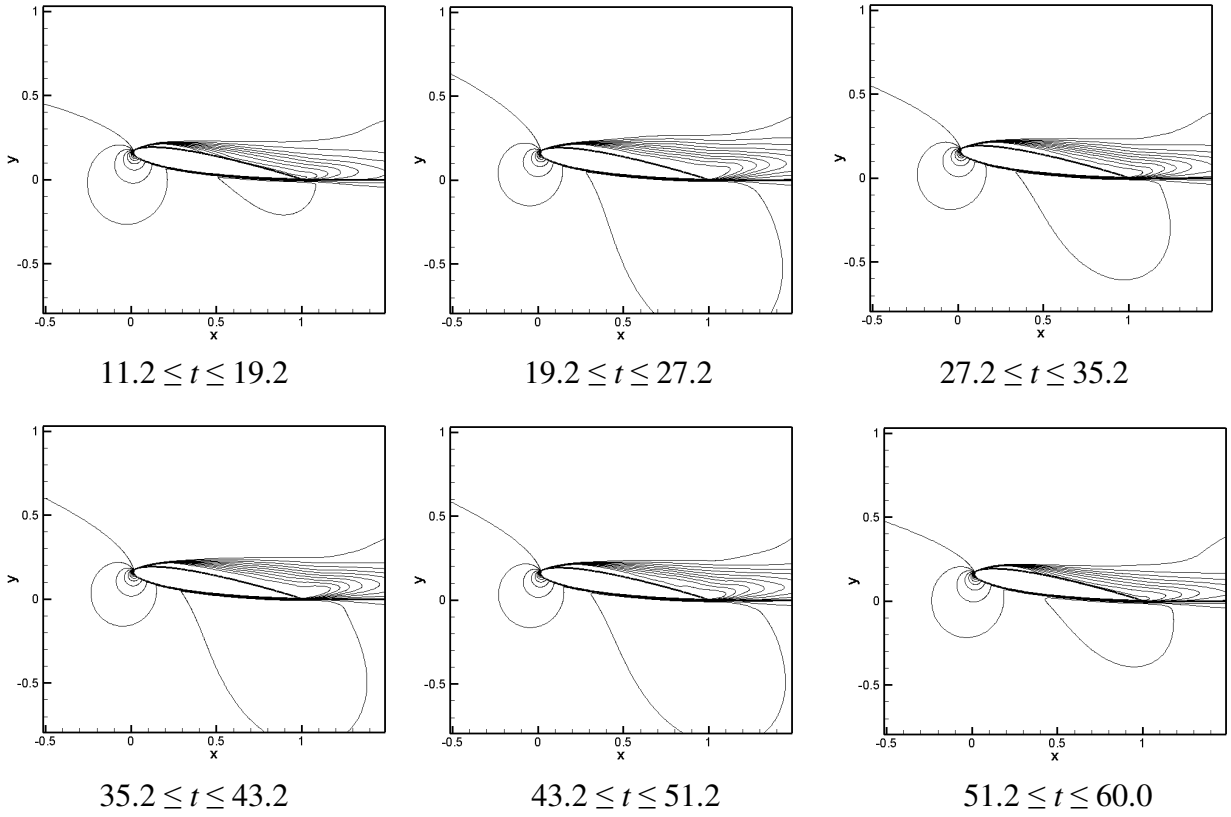

Figure 4.7 Averaged streamwise velocity contours for the low-frequency flow oscillation at Re = 50,000 and incidence of 9.25°, using 10 contour levels in the range from 0 to 1 for each subinterval.

A laminar separation bubble of approximately 42% chord length located near the leading edge is observed in the interval of $11.2 \leq t \leq 19.2$. Between $t = 19.2$ and $t = 43.2$, the airfoil is stalled, with a large area of separated flow on the upper surface of the airfoil. The time history for the lift coefficient shows the airfoil stall as an abrupt reduction of lift coefficient after nine time units, as shown in Figure 4.7. It is noticeable from Figure 4.7 that the lift coefficient drops dramatically from its maximum value of 0.895 at $t = 4$ to 0.405 at $t = 17$, which is about a 54.7% reduction of lift. This stalling is more abrupt than the stalling found by Rinoie and Takemura (2004) in their study on the oscillating behaviour of the laminar separation bubble for NACA 0012 airfoil at Re = 130,000 and incidence of 11.5°. Nevertheless, this result is in general agreement with results found in the literature concerning the low-frequency flow oscillation phenomenon, such as Zaman *et al*. (1989) and Sandham (2008). Although, there is a noticeable spike in the lift coefficient at $t = 25$, the flow at this time does not reattach to the surface. The lift coefficient begins to increase at $t = 44$, which indicates the beginning of flow reattachment until it reaches a local maximum value of 0.815 at $t = 62.5$. In the

subsequent flow development, the lift coefficient fails to increase strongly enough, and the flow oscillation ends without flow reattachment.

The Strouhal number is calculated from the equation mentioned in Chapter 1 ($S_t = fc\sin\alpha / U_\infty$), where the frequency f is obtained by performing the Fast Fourier Transformation (FFT) on the time-dependent lift coefficient. Although the time series is too short for quantitative conclusions we can see two peaks at $St = 0.0026$ and $St = 0.0065$ (see Figure 4.8), which can be compared with Rinoie and Takemura (2004), who found $St = 0.008$ at a Reynolds number of 130,000. A much larger time sample would be needed in order to make a more definitive comparison. Surface pressure distributions for the six time subintervals (shown in Figure 4.6) are depicted in Figure 4.9, where the rapid stalling is apparent from the observation of the big gap between the first and second subinterval, with suction pressure gradually increasing until it approaches the first subinterval at $51.2 \leq t \leq 60.0$, where flow reattachment occurs.

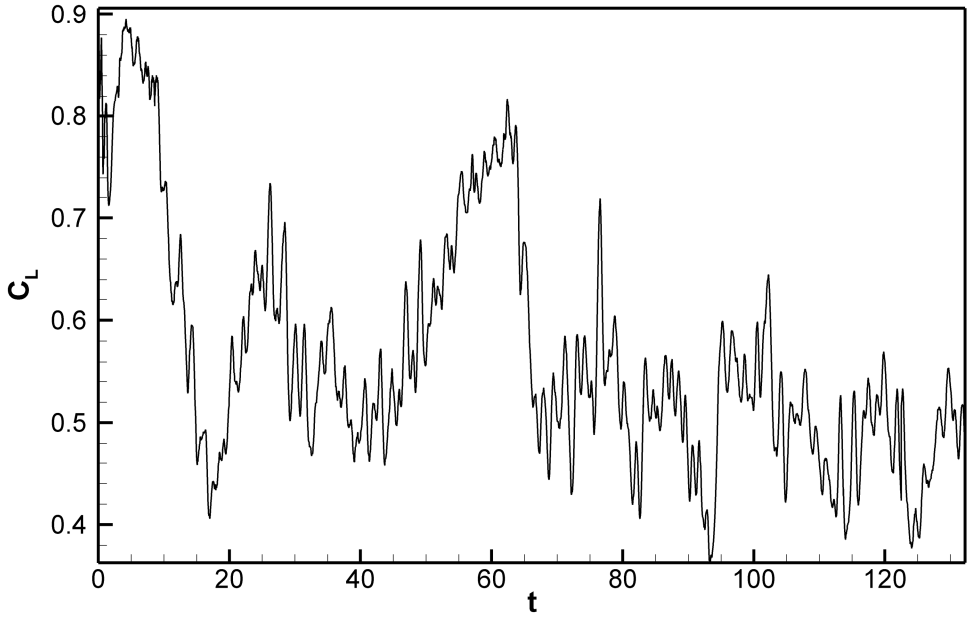

Figure 4.8 Time dependence of lift coefficient for an incidence of 9.25°.

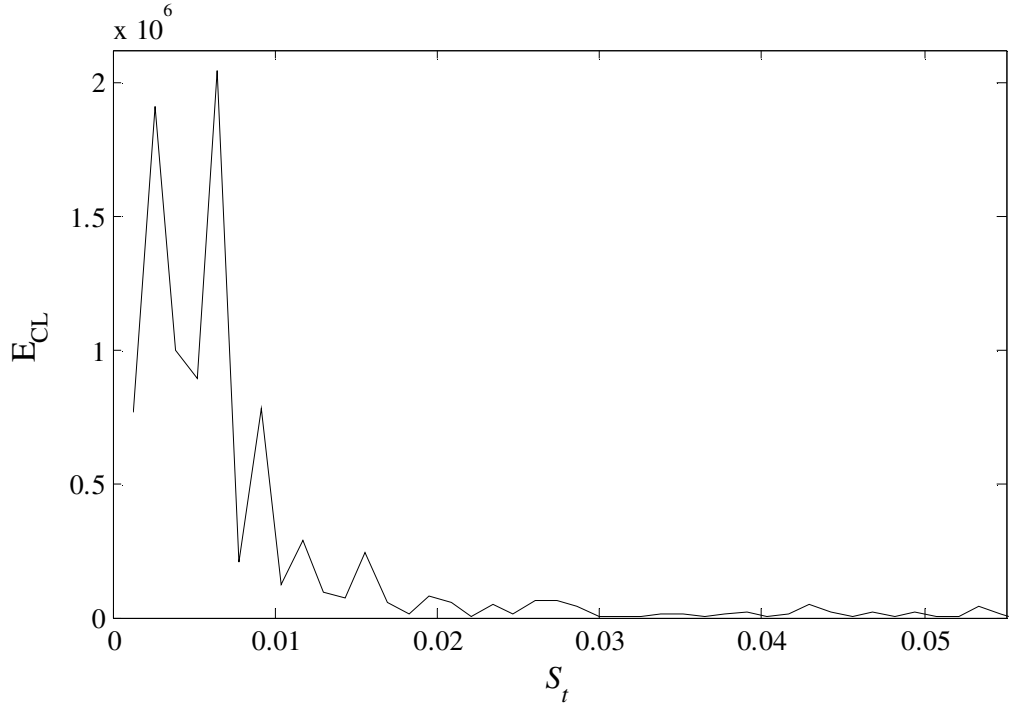

Figure 4.9 Energy spectrum for lift coefficient, plotted as a function of Strouhal number S_t for an incidence of 9.25°.

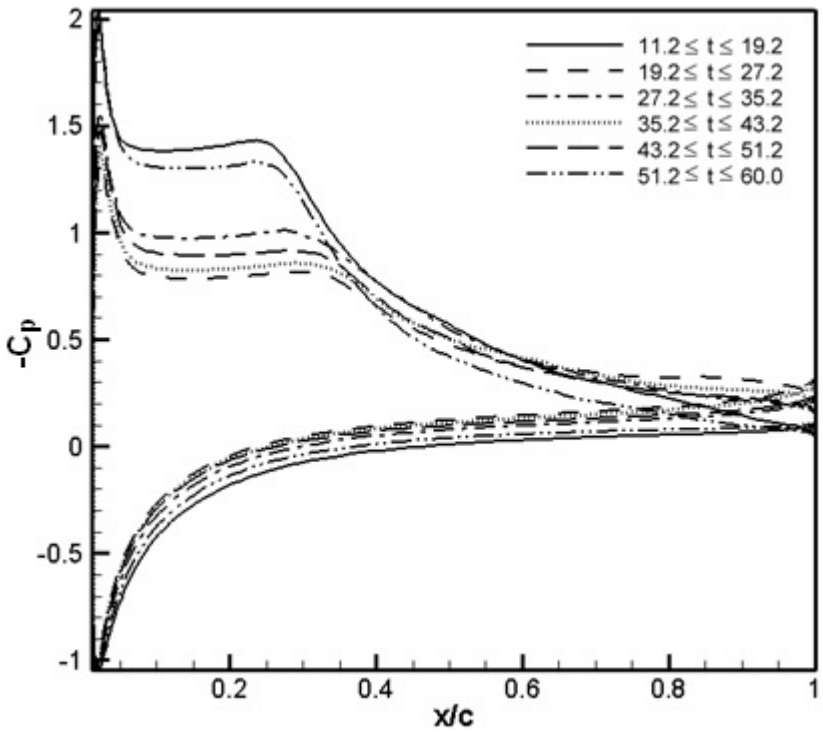

Figure 4.10 Pressure coefficients for the transient low-frequency flow oscillation for an incidence of 9.25°.

Figure 4.10 shows the skin-friction distributions at each stage of the first cycle of flow oscillation. Transition is taken to occur in the region where the skin friction

decreases steeply to the point at which it reaches its negative peak. After this point, recovery occurs, and the skin friction increases until it becomes positive, which indicates that reattachment has taken place. Maximum values of skin-friction coefficients for all subintervals are found in the laminar boundary layer near the leading edge. After this, the skin-friction coefficients reduce to the first negative peak located at $0.034 \leq x/c \leq 0.0534$. These negative values represent the recirculating fluid in the dead air region of separated flow, which is slower than the second region of re-circulating fluid.

Table 4.2 shows the locations and the corresponding skin-friction coefficients of the minimum negative values for the two recirculation regions for each time interval. It is clear that the skin-friction coefficient for the second recirculation region for subintervals $11.2 \leq t \leq 19.2$ and $51.2 \leq t \leq 60.0$ has a much lower minimum than the other subintervals. This means that the fluid in the second recirculation region becomes faster and strong enough to cause a flow reattachment downstream of the second recirculation region.

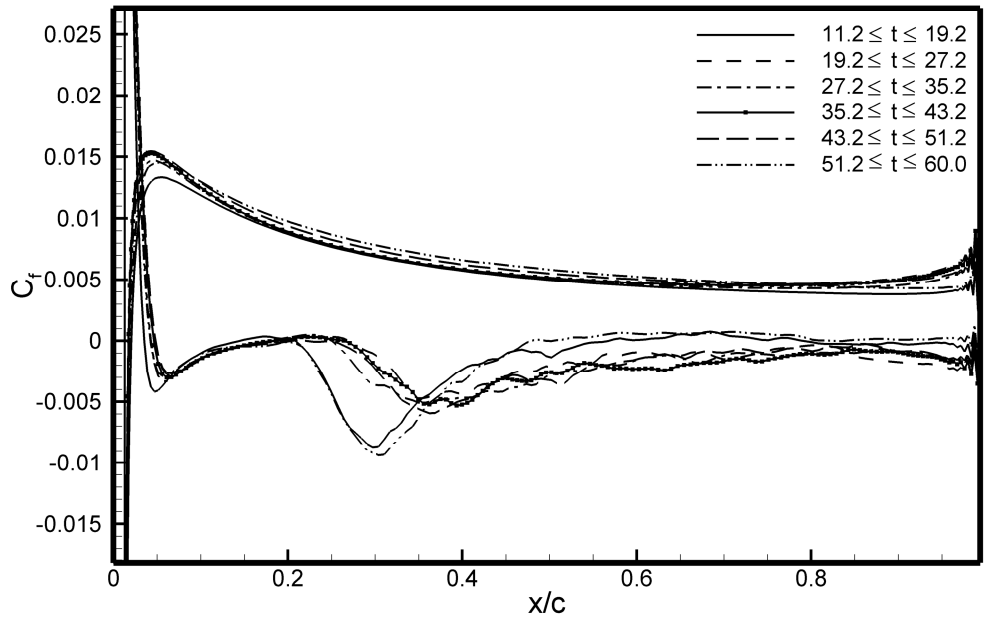

Figure 4.11 Skin-friction coefficients over the six time subinterval quantities for the transient low-frequency flow oscillation at an incidence of 9.25°.

Separation points, reattachment points (if they exist) and the bubble length for each subinterval time are tabulated in Table 4.3. The locations of laminar boundary layer

separation over the six subintervals are variable. In the range $19.2 \leq t \leq 27.2$ after bursting has occurred the separation point moves significantly downstream compared to the previous time subinterval ($11.2 \leq t \leq 19.2$). When the flow is fully separated, the location of the separation point moves upstream (at $27.2 \leq t \leq 35.2$) then downstream (at $35.2 \leq t \leq 43.2$ and $43.2 \leq t \leq 51.2$) before returning upstream at $51.2 \leq t \leq 60.0$ where the flow is reattached. It can also be seen from Table 4.2 that the laminar separation bubble at the end of the first cycle is about 18.19% smaller than at the beginning, and after the next bubble burst the flow remains fully stalled as shown on Figure 4.11.

Table 4.2 Locations of the minimum values for the two recirculation regions for each subinterval measured from the skin-friction (Figure 4.11)

Time interval	Circulation region (1) (at negative peak)		Circulation region (2) (at negative peak)	
	x/c	C_f	x/c	C_f
$11.2 \leq t \leq 19.2$	0.0340	–0.00418	0.2846	–0.00871
$19.2 \leq t \leq 27.2$	0.0524	–0.00287	0.3367	–0.00474
$27.2 \leq t \leq 35.2$	0.0452	–0.00332	0.3432	–0.00512
$35.2 \leq t \leq 43.2$	0.0492	–0.00301	0.3808	–0.00533
$43.2 \leq t \leq 51.2$	0.0534	–0.00268	0.3496	–0.00596
$51.2 \leq t \leq 60.0$	0.0433	–0.00290	0.2912	–0.00934

Table 4.3 Locations of separation and reattachment measured from the skin-friction (Figure 4.11)

Time interval	Separation point (x/c_{sep})	Reattachment point(x/c_{reatt})	Bubble Length (based on chord length)
$11.2 \leq t \leq 19.2$	0.0224	0.5558	0.5404
$19.2 \leq t \leq 27.2$	0.0354	Fully separated flow	
$27.2 \leq t \leq 35.2$	0.0300	Fully separated flow	
$35.2 \leq t \leq 43.2$	0.0335	Fully separated flow	
$43.2 \leq t \leq 51.2$	0.0354	Fully separated flow	
$51.2 \leq t \leq 60.0$	0.0296	0.4660	0.4421

The question is now raised: why does the flow with a low-frequency oscillation become fully separated after completing the first cycle? There are three possible reasons that could cause this kind of flow behaviour. First, that the Reynolds number is too low to have an extended range where the low-frequency is observable. Low Reynolds number

effects are known, for example Laitone (1997) found that there is a discontinuity of lift coefficient versus the increase of the angle of attack when a flow around NACA-0012 airfoil was studied at a Reynolds number below 70,000. Here we have a steady LSB at 8.9° and stalled flow at 9.25° indicating only a narrow range where the low-frequency flow oscillation may exist compared to higher Reynolds numbers. Second, the spanwise length for the airfoil model might not be enough to simulate the flow properly. This issue was discussed by Eisenbach and Friedrich (2008), who found in their study of an incompressible flow around an NACA-4415 airfoil at Re = 10,000 and incidence of 18°, that the lengths of the largest turbulent flow structures near the trailing edge are approximately 66% of the chord length. This suggests a need to study the effect of extending the spanwise computational domain on the simulation of low-frequency flow oscillation phenomenon. Third, the quasi-periodicity of flow oscillation could in fact be present in the narrow range of incidence between 8.9° and 9.25°. In the next sections the effect of Reynolds number and spanwise domain size are considered.

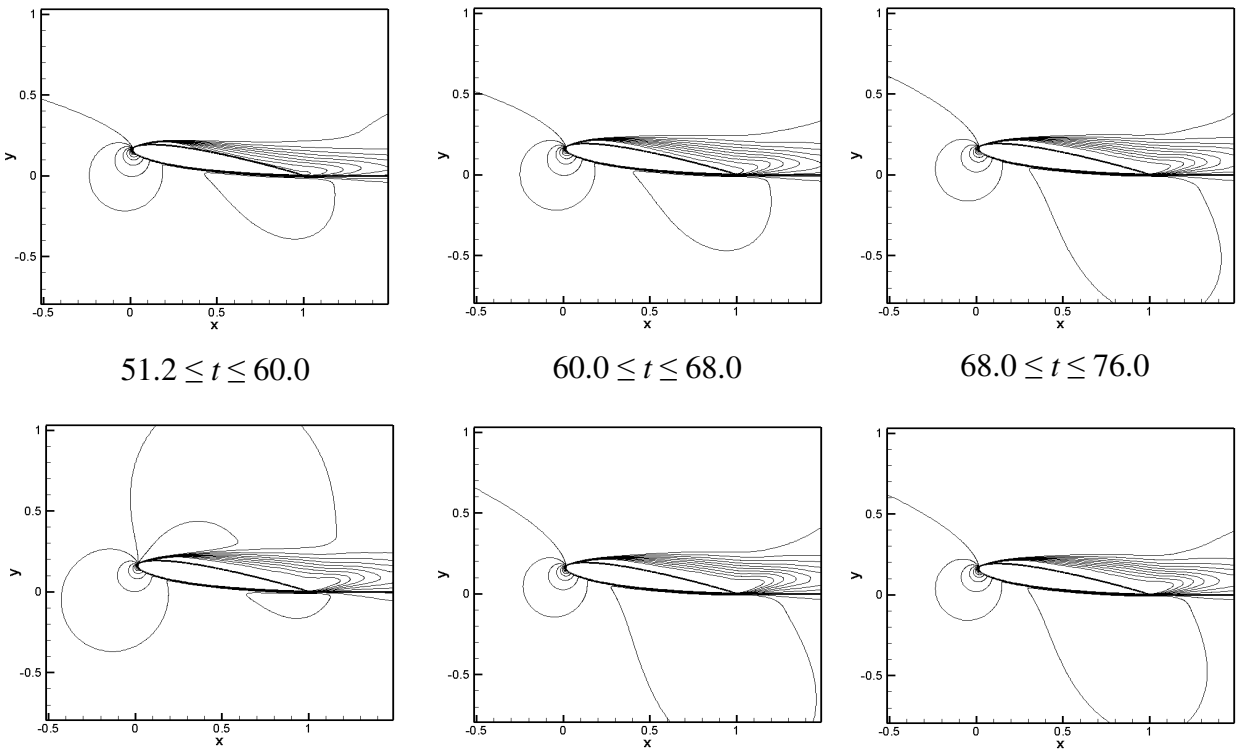

Figure 4.12 Averaged streamwise velocity contours after transient low-frequency oscillation at Re = 50,000 and incidence of 9.25°, using 10 contour levels in the range from 0 to 1 for each subinterval.

4.2 Results for a large eddy simulation of flow at a Reynolds number of 130,000 and incidence of 11.5°

To study the effect of Reynolds number, a simulation at Reynolds number of 130,000 around a NACA-0012 airfoil has been chosen because, at this condition, experimental results are available from Rinoie and Takemura (2004), who found the low-frequency flow oscillation at an incidence of 11.5°. They used a wing with 200 mm in both streamwise and spanwise directions. In the present study, the spanwise length of the numerical domain is kept 20% of the airfoil chord length. The main grid parameters of the large eddy simulation are presented in Table 4.4 and the computations are carried out with a time step of $\Delta t = 0.00012$ which is the maximum time step that can be used in this case to maintain numerical stability.

In the beginning of the calculation (up to 25 non-dimensional time units), the lift coefficient clearly oscillates between ($C_{Lmax} \approx 0.94$) ($C_{Lmin} \approx 0.40$) which is about 40.3% of the mean, with the time variation displayed in Figure 4.12. After that, the lift coefficient has a low amplitude with a mean of ($C_L \approx 0.6$) and without large oscillations as shown in Figure 4.13. This indicates fully stalled flow. Again, we have observed a transient low-frequency mode that eventually becomes fully stalled. This flow behaviour can also be examined by plotting contours of the span- and time-averaged velocity over six segments of the initial oscillation as shown in Figure 4.14. The development and bursting of the laminar separation bubble can be clearly seen. A short laminar separation bubble (about 29% of the airfoil chord) is observed in the early stage of the time interval ($0 \leq t \leq 2.4$), then the bubble length increases in the second segment before it bursts to produce a fully stalled flow in the third, fourth and fifth segments. After that, the bubble reforms near the leading edge as seen in the final segment of the selected time interval but with a larger bubble compared to the bubble in the first segment (about 39% of the airfoil chord). The smallest laminar separation observed here is clearly large in comparison with the bubble observed by Rinoie and Takemura (2004) who found a bubble that occupied 10% of the airfoil near the leading edge. This difference may be attributed to the effect of the insufficient spanwise domain length as will be seen in the next section. It is appropriate to plot the streamline patterns for span- and time-averaged velocity as

illustrated in Figure 4.15, in order to give more detail about the flow behaviour during the initial transient. The growth and bursting of the laminar separation bubble can also be seen in Figure 4.15. Figure 4.15 also reveals a turbulent separation near the trailing edge in the last stage of the transient development. It is clear that the recirculation flow in the separation zones, especially above the trailing edge, is stronger and bigger after bursting, while it shrinks as the flow reattaches to the airfoil surface.

Table 4.4 Grid parameters for LES (Re = 130,000 and $\alpha = 11.5°$)

Simulation	W	R	Total Length	N_ξ	N_η	N_z	L_z/c	PS	SS	NW	Total points
LES(3D)	5	7.3	14.2	1485	301	32	0.2	150	335	500	14303520

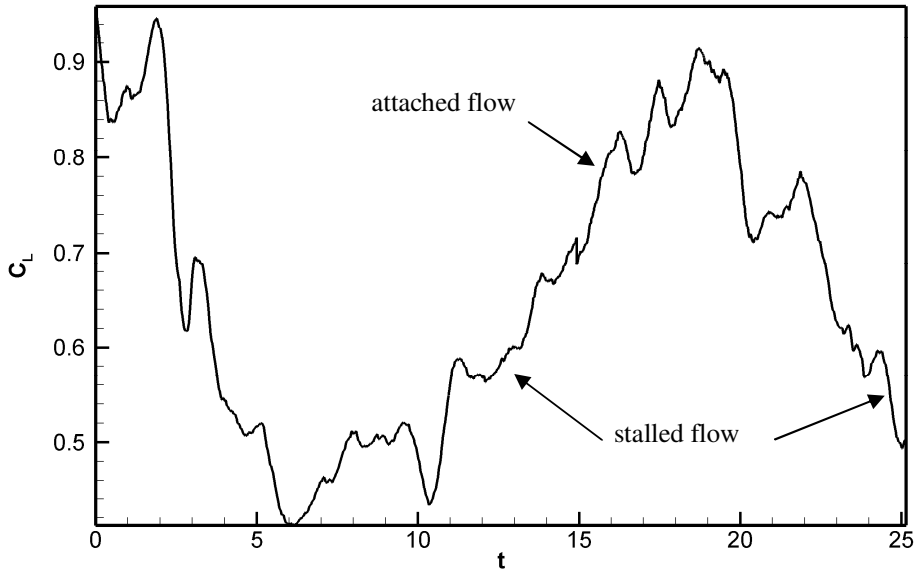

Figure 4.13 Time variation of lift coefficient obtained from LES (Re = 130,000 and $\alpha = 11.5°$), showing the flow is initially switching between stalled and unstalled states.

Figure 4.16 shows the span and time-averaged surface pressure coefficient distributions for six time segments over the time interval ($0 \leq t \leq 25.2$). The switching between stalling and non-stalling during the transient cycle can be seen clearly from the large variation of the surface pressure distributions for each time segment. The highest value of the suction peak ($-C_p$) is found in the first time interval where the short laminar separation bubble was observed near the leading edge as shown in Figures 4.14 and 4.15. As the time increases, the suction peak dramatically decreases and a flatter surface pressure distribution is observed during the intervals $7.2 \leq t \leq 8.4$ and $13.2 \leq t \leq 14.4$, which is characteristic of the fully stalled flow. Further increasing in time leads to an

increase of the suction peak ($-C_p$) and a surface pressure distribution similar to that one observed in the first stage ($0 \leq t \leq 1.2$) of the cycle, but with a lower amplitude which indicates that the bubble formed here ($19.2 \leq t \leq 20.4$) is longer than that in the first stage, as also illustrated in Figures 4.14 and 4.15. Figure 4.18 shows the surface pressure coefficient obtained experimentally by Rinoie and Takemura (2004). When comparing Figure 4.18 with the LES pressure coefficients in Figure 4.17, it is clear to see that there is a difference of pressure coefficient in terms of the bubble size and the Cp_{min} at incidence 11.5°.

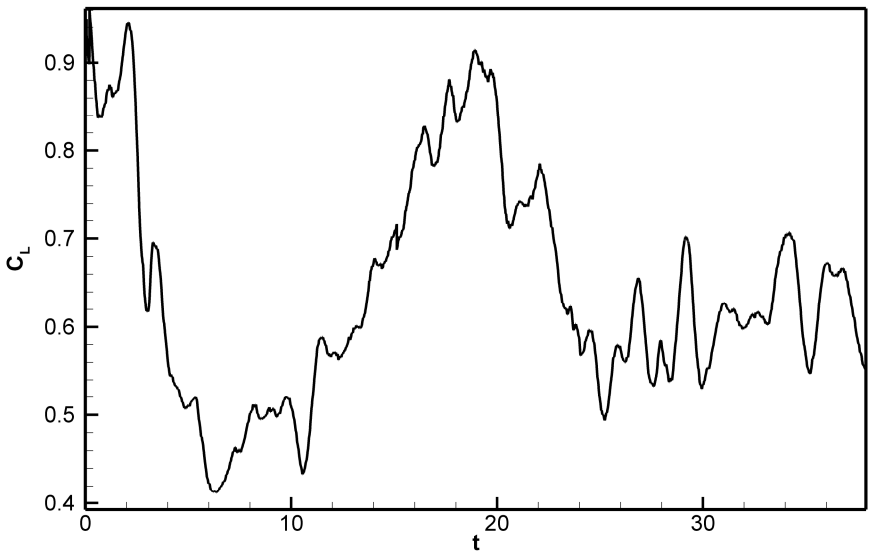

Figure 4.14 Time dependence of lift coefficient obtained by LES (Re = 130,000 and α = 11.5°), showing fully stalled flow after the transient low frequency flow oscillation.

In order to see the low frequency, the Strouhal number (S_t) is calculated from the lift coefficient (Figure 4.12) where the frequency is calculated based on the period of the first oscillation, leading to a Strouhal number of 0.0117. This value is comparable with Rinoie and Takemura (2004) who found a value of $S_t = 0.008$ and is close to the viscous inviscid interaction results of Sandham (2008) who $S_t = 0.0129$. It should be noted that this value is obtained based on the single available cycle of the low-frequency flow oscillation, and the flow continues without exhibiting this low-frequency mode. The simulation still needs to be improved in order to get a periodic or quasi-periodic low frequency flow oscillation phenomenon. The improvement can be obtained by increasing the spanwise domain length which has a significant influence on capturing the low frequency flow oscillation, as we will see in the next section.

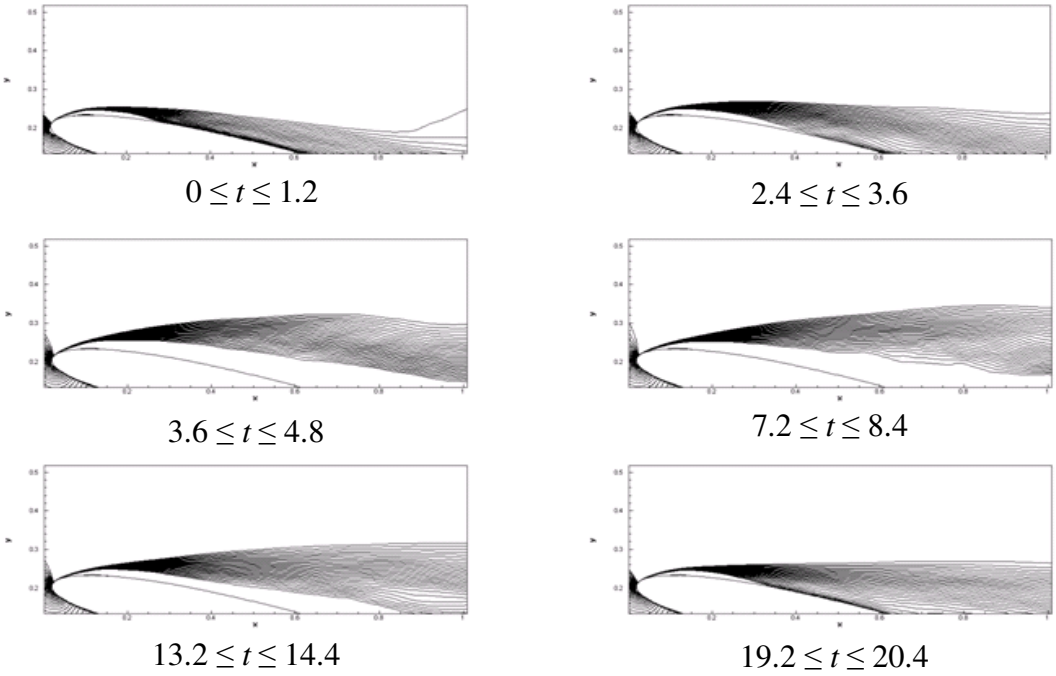

Figure 4.15 Averaged streamwise velocity contours for the initial transient at Re=130,000 and incidence of 11.5°, using 20 levels {0 to 1} for each subinterval.

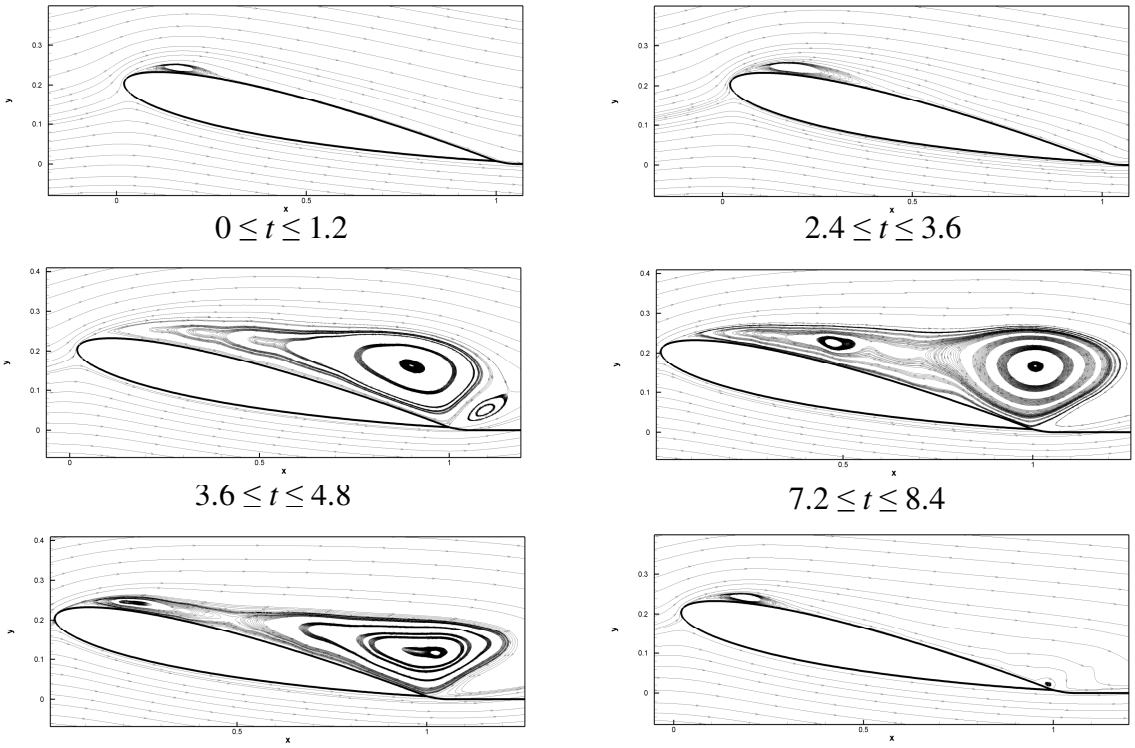

Figure 4.16 Streamline patterns for span- and short-time-averaged velocity around a NACA 0012 at $\alpha = 11.5°$, obtained by LES over the initial transient, showing the develpment of separation zones.

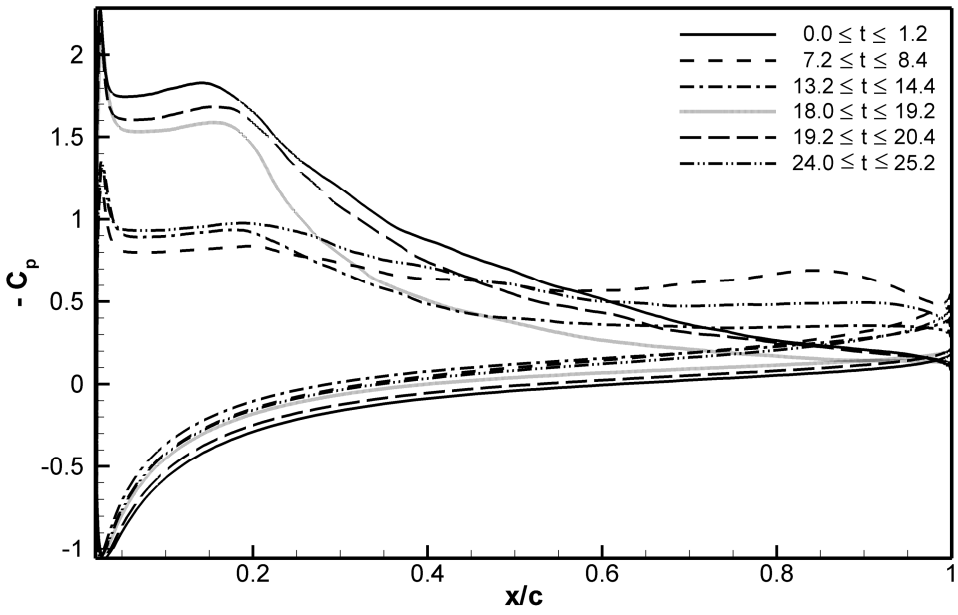

Figure 4.17 Pressure coefficients for low-frequency flow oscillation at incidence of 11.5° and Re = 130,000.

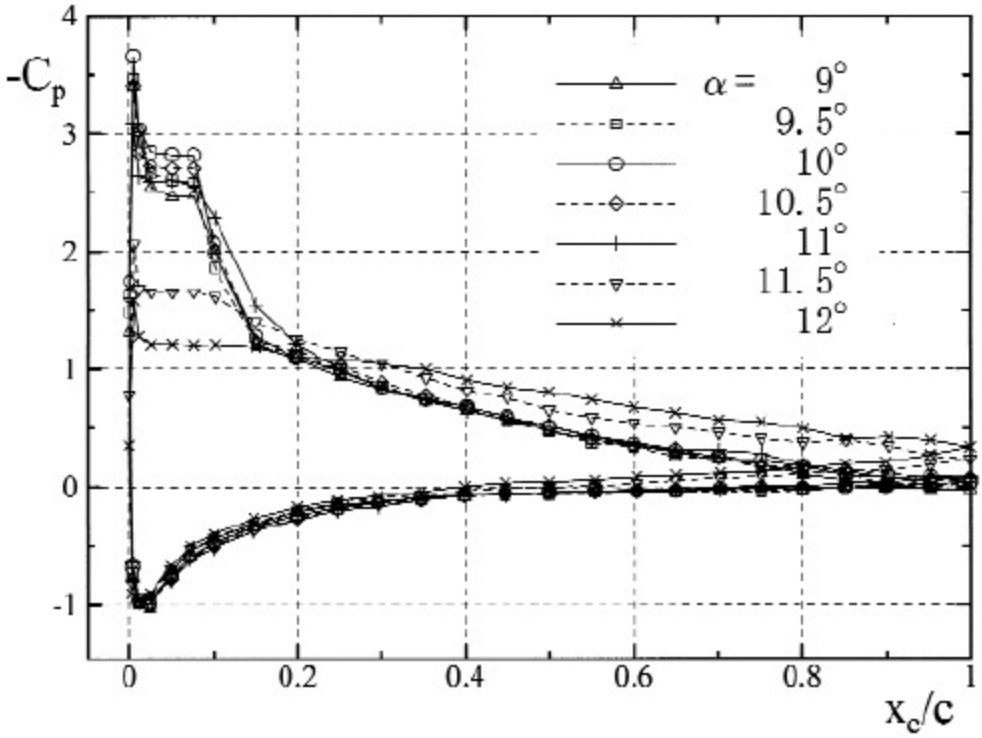

Figure 4.18 Pressure coefficients for the NACA0012 airfoil at Re = 130,000 obtained experimentally Rinoie and Takemura (2004).

4.3 Effect of the computational domain width on an airfoil near stall.

The objective of this section is to study the effect of the computational domain width on the results of LES and to give a more accurate prediction of flow around an airfoil near stall than that in section 4.2. The computational domain width is extended to 50% chord for the NACA-0012 airfoil at M_∞ = 0.4, Re = 50,000 and α = 9.25°. To accomplish this, a comparison between simulations with narrow and wide computational width is made based on lift coefficient, time-averaged streamwise velocities and two-point velocity correlations. The flow behaviour of the wider domain is then presented to show the usefulness of increasing the computational domain width to capture the low frequency flow oscillation phenomenon. The primary grid parameters of the three-dimensional simulation are summarized in Table 4.5, where "LES_narrow" refers to the large eddy simulation with a narrow computational domain L_z = 0.2c (20%), and "LES_wide" to a large eddy simulation with wide domain L_z = 0.5c (50%).

Table 4.5 Grid parameters for LES at Re = 50,000 and α = 9.25°

Simulation	W	R	Total Length	N_ξ	N_η	N_z	L_z/c	PS	SS	NW	Total points
LES_narrow	5	7.3	14.2	637	320	32	0.2	130	170	170	6522880
LES_wide	5	7.3	14.2	637	320	80	0.5	130	170	170	16307200

It should be noted that the domain widths provided here are already large compared with previous LES. For example, Mary and Sagaut (2002) conducted an LES with very small spanwise extents ($L_z/c \leq 0.005$, 0.012 and 0.03) and different resolutions, to simulate a flow past an airfoil at a Reynolds number of 2.1×10^6 and an incidence of 13.3°. They found that there was a great improvement in the results compared with the experiment results when the width of the computational domain and the numerical resolution were increased.

Figures 4.18 and 4.19 show the 3D isosurface of the second invariant of the velocity gradient Q (defined in 3.12) when the flow is stalled obtained from LES_wide and LES_narrow, respectively. It can noticed from these figures that there are spanwise variations of the flow structures in the wider domain case which could not be captured by the LES over the narrower domain. For example, in the wider domain case there are

clearly two oblique flow structures in the transition region which are extended over a large distance on the spanwise direction, these flow structures could not captured in the narrower domain case

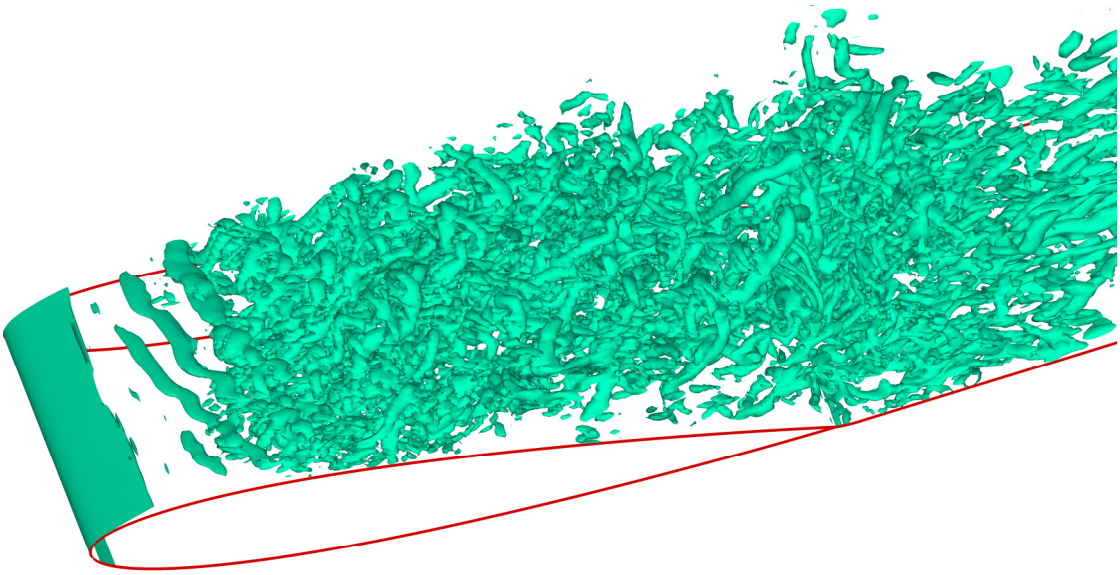

Figure 4.19 Three-dimensional view for the isosurface of the second invariant of the velocity gradient obtained by 3D LES_wide (Q = 300).

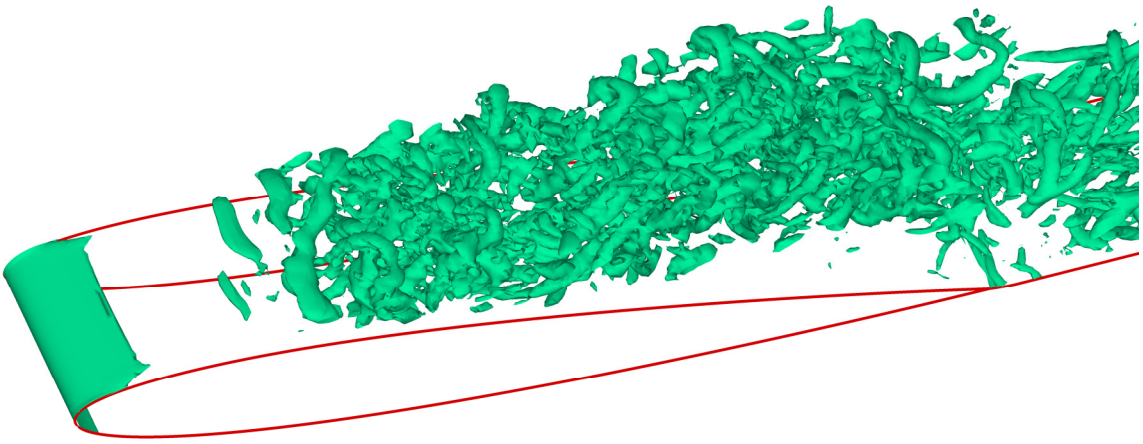

Figure 4.20 Three-dimensional view for the isosurface of the second invariant of the velocity gradient obtained by 3D LES_narrow (Q = 200).

From the variation of the lift coefficient in Figure 4.20, it can be seen that the flow behaviour changed when the domain width was increased and the flow in the wider domain case exhibits an irregular low frequency oscillation. A comparison between the span- and time-averaged streamlines over a long time period ($64 \leq t \leq 128$) is illustrated in Figure 4.21, in which the formation of a long separation bubble of about 60% chord is clearly seen for the LES_wide simulation, whereas the flow fails to reattach with LES_narrow. The differences imply that the domain width should be at least 50% of the chord length, and possibly more. It is noted that the long bubble observed in the LES_wide (which has a length of 60% chord) is longer than the 35% chord reported by Rinoie and Takemura (2004) which is attributed to the higher Reynolds number (Re = 130,000) used in their experiments. The difference between the wide and narrow domain widths can also be demonstrated by examining the pressure distribution over the same period of Figure 4.21 as shown in Figure 4.22, where it is verified that the LES_wide simulation produced a long laminar separation bubble with bigger suction pressure ($-C_p$) than LES_narrow, which has a flatter pressure distribution shape that indicates the flow is fully stalled. It is concluded that the laminar separation bubble is very sensitive to incidence, Reynolds number and L_z.

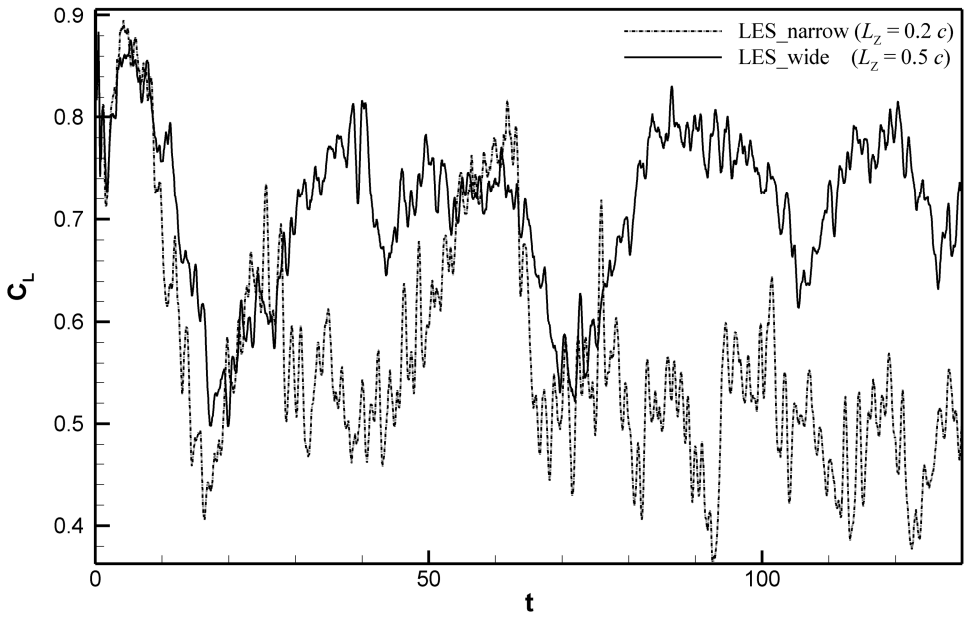

Figure 4.21 Effect of increasing the spanwise length of the computational domain on the LES time dependence lift coefficient (Re = 50,000 and α = 9.25°).

The effect of L_z can be studied in more detail using the two-point velocity correlation function:

$$R_{uu}(z_1) = \langle u'(z)u'(z+z_1)\rangle / \langle u'(z)u'(z)\rangle \qquad (4.1)$$

where $\langle\ \rangle$ denotes averaging over z, u' is the streamwise velocity fluctuation and z_1 denotes the correlation distance. Figures 4.23a and 4.23b show the two-point velocity correlations at seven different locations on the suction side of the airfoil, obtained from the LES_narrow and LES_wide simulations respectively. It is noticeable that there are negative correlations which are also observed by Kaltenabach and Choi (1995) who performed a large eddy simulation for a flow at a Reynolds number of 1.64×10^6 around a NACA 4412 airfoil near stall. They also observed that worst correlation was located near the trailing edge and they suggested that the negative correlations were due to the insufficient resolutions in the near wall region but this is not the case in the current study, where the negative correlations are probably due to the organized flow structures in the near wall region. The worst correlation value ($R_{uu} \approx$ -0.56) was observed in the trailing edge of the narrower domain, compared with $R_{uu} \approx$ -0.28 in the trailing edge of the wider domain. This means that a significant improvement was achieved by extending the width of the computational domain. The present simulation requires a wider computation domain compared with Mellen *et al.* (2003), who applied LES to simulate flow around an Aerospatiale A-airfoil with Reynolds number $\mathrm{Re} = 2.1 \times 10^6$ and $\alpha = 13.3°$. They recommended a minimum $L_z = 0.12c$ for a case at higher Reynolds number with small trailing edge separation. The presence of a large region of separation in the present configuration compared to Mellen *et al.* (2003), which only had a small trailing edge separation, is almost certainly the reason for the difference. The present results indicate that LES of airfoil flows (e.g. You *et al.* (2008), which used $L_z = 0.2c$) needs careful attention to spanwise domain width near stall.

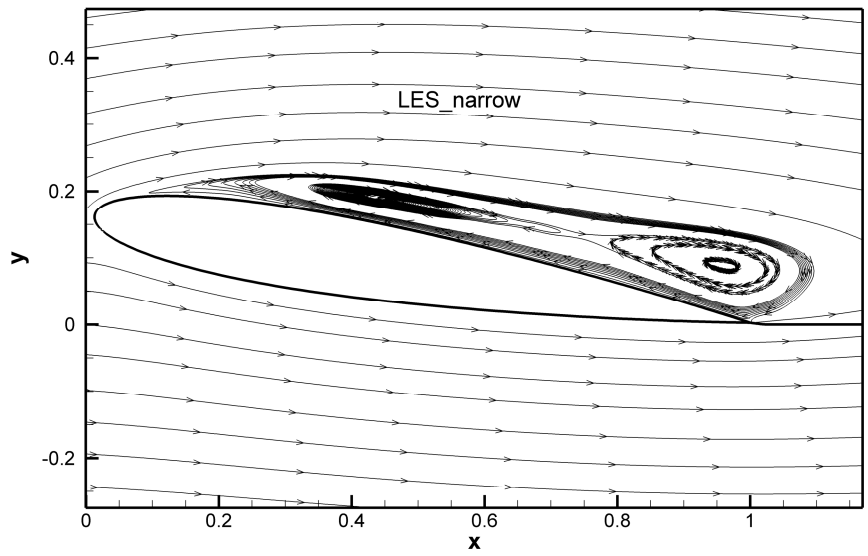

a)

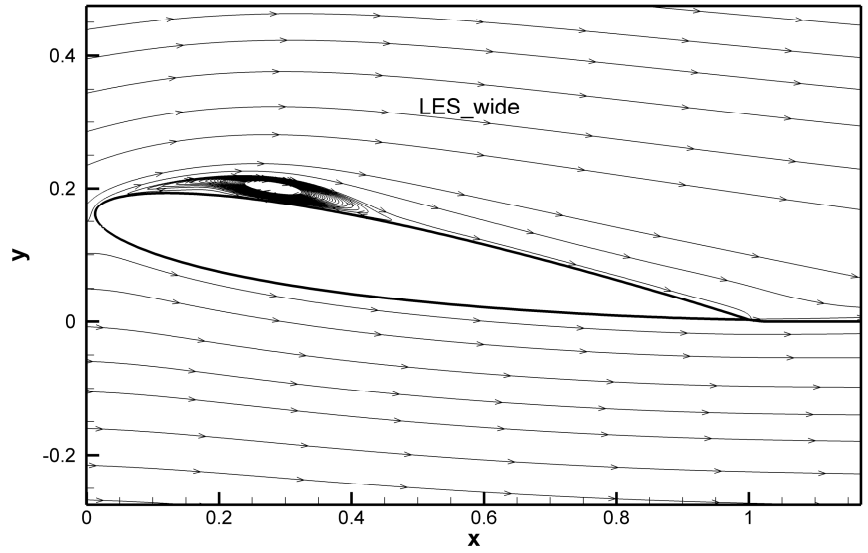

b)

Figure 4.22 Streamlines patterns for time- and span-averaged velocity over a long time interval ($64 \leq t \leq 128$) for $\alpha = 9.25°$, obtained from the a) narrow and b) wide domains simulations.

Previous studies of low frequency flow oscillation (Rinoie and Takemura, 2004; Sandham, 2008) showed regular oscillations, whereas the laminar separation bubble here is more irregular, with intermittent bursting to form either a long bubble or a fully separated flow. For example, the streamline patterns for time- and span-averaged velocity between $t = 4.8$ and $t = 6.4$ revealed a laminar separation bubble of approximately 25% of the chord located near the leading edge (Figure 4.24a). This then bursts to create a fully stalled flow at $t = 20.8$, as shown in Figure 4.24b. This process was repeated between $t \approx 58.0$ and $t \approx 70.0$.

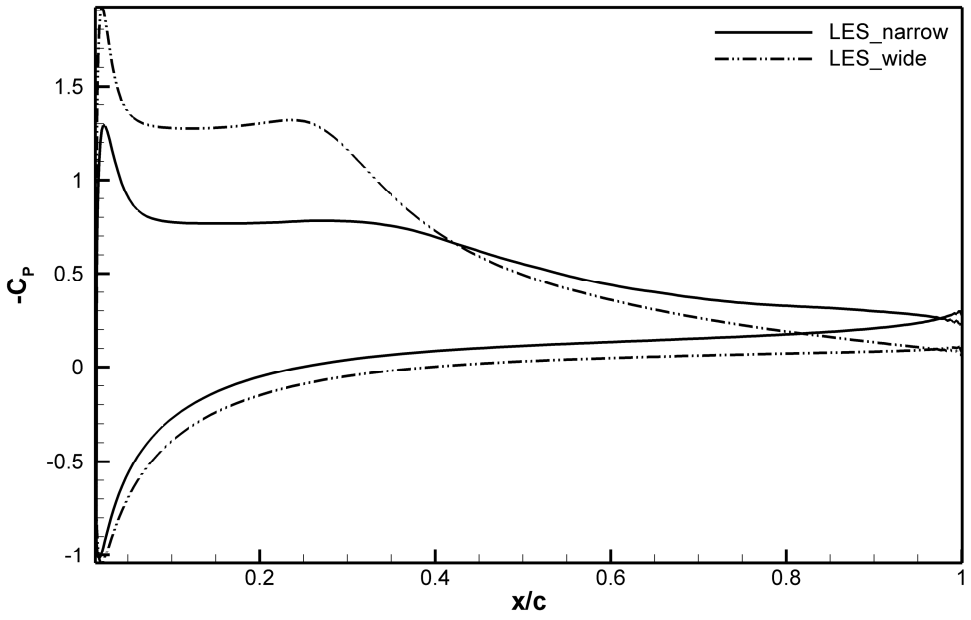

Figure 4.23 Comparison of pressure coefficient over a long averaged interval ($64 \leq t \leq 128$) for $\alpha = 9.25°$, between LES of narrow and wide computational domain widths.

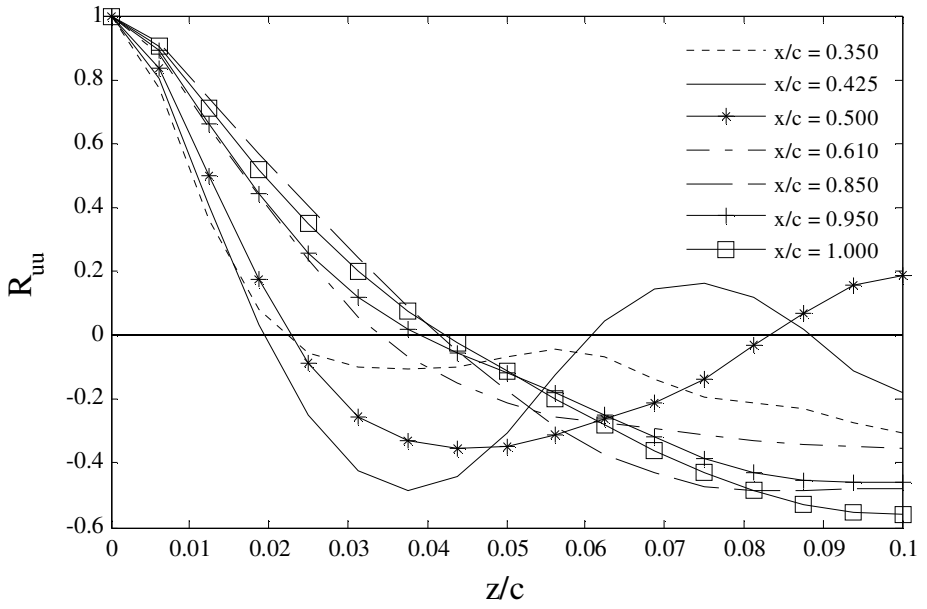

a)

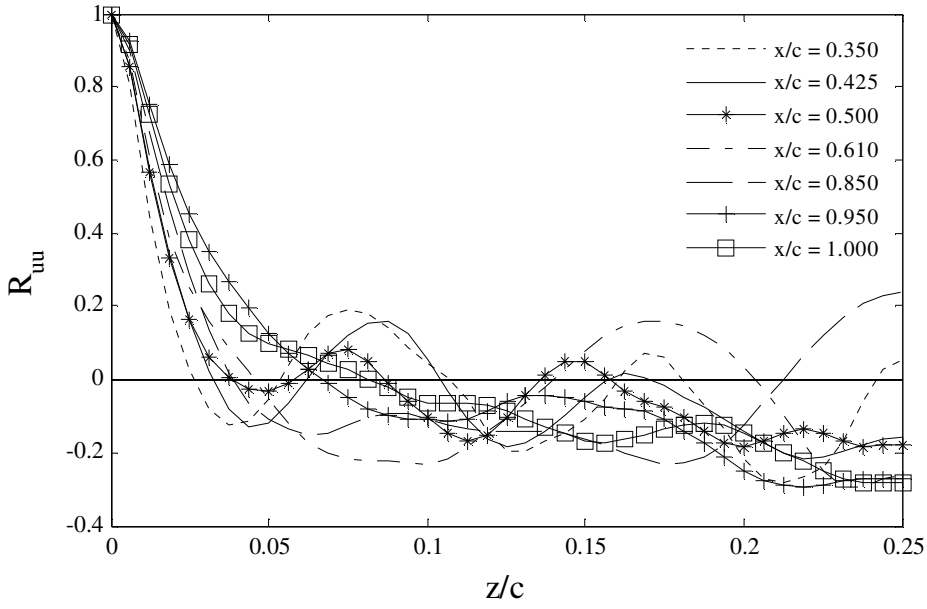

b)

Figure 4.24 Two-point velocity correlations based on the streamwise velocity obtained by a) LES_narrow and b) LES_wide for $\alpha = 9.25°$.

Continued irregular behaviour of laminar separation bubbles was observed between t = 74.9 and t = 108.8 (Figure 4.25). The formation of a laminar separation bubble of approximately 35% of the chord length was clearly seen from t = 74.9 to t = 88. After that, bursting occurred to form a long separation bubble of approximately 65% of the chord length, in conjunction with a low lift coefficient ($C_L \approx 0.615$). The length of the

shortest laminar separation bubble (25% chord) is longer than the short bubble reported by Rinoie and Takemura (2004) which was 10% of chord. In addition, it is noticeable from Figure 4.25 that the flow exhibits a trailing edge separation at the end of the oscillation cycle. This was also observed by Broeren and Bragg (1999) for the flow around the LRN-1007 airfoil, where the leading edge separation bubble and trailing edge separation both grew until they merged. The difference here is that the trailing edge separation does not always lead to a fully stalled flow. On the other hand, Rinoie and Takemura (2004) did not mention this type of turbulent boundary layer separation. Figure 4.26 shows a time-history of the spanwise averaged separation and reattachment locations from t = 43 to t = 133, where the irregular unsteady laminar separation bubble and the fully separated flow are clearly seen.

Surface pressure distributions, averaged over selected intervals, are depicted in Figure 4.27, where significant unsteadiness of the pressure can be observed. The reattachment of the flow and the formation of the laminar separation bubble occurred while the suction peak ($-C_p$) was increasing from the first interval $74.9 \leq t \leq 76.5$, until it reached a maximum value for the interval $86.4 \leq t \leq 88.0$. Subsequently, the bubble burst caused a drop in the suction peak, but never reached the same level as in the first interval, where the flow was fully stalled.

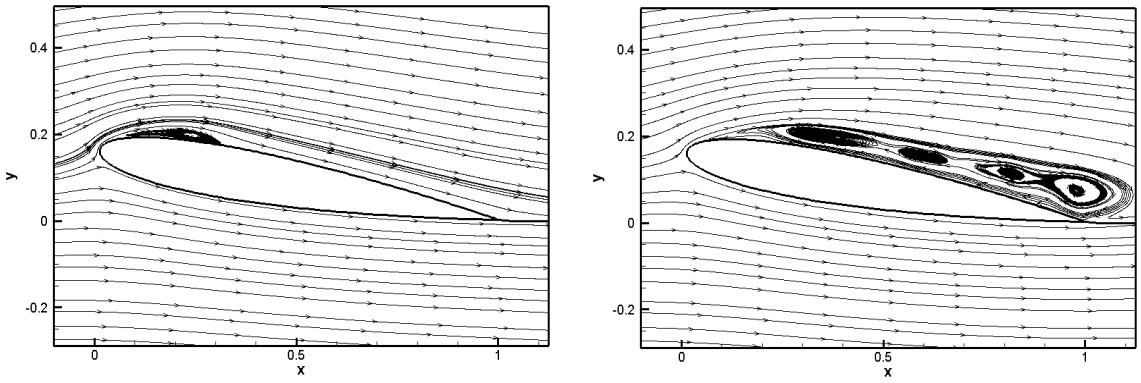

a) b)

Figure 4.25 Streamline patterns for time and span averaged flow around a NACA 0012 at a = 9.25°, obtained from LES_wide over the intervals a) $4.8 \leq t \leq 6.4$ and b) $19.2 \leq t \leq 20.8$

The Strouhal number based on the cycle $74.9 \leq t \leq 108.8$ is 0.00466 (Re = 50,000 and $\alpha = 9.25°$), compared to 0.008, as reported by Rinoie and Takemura (2004), (at $\alpha = 11.5°$, Re = 130,000) where a higher incidence and Reynolds number were employed.

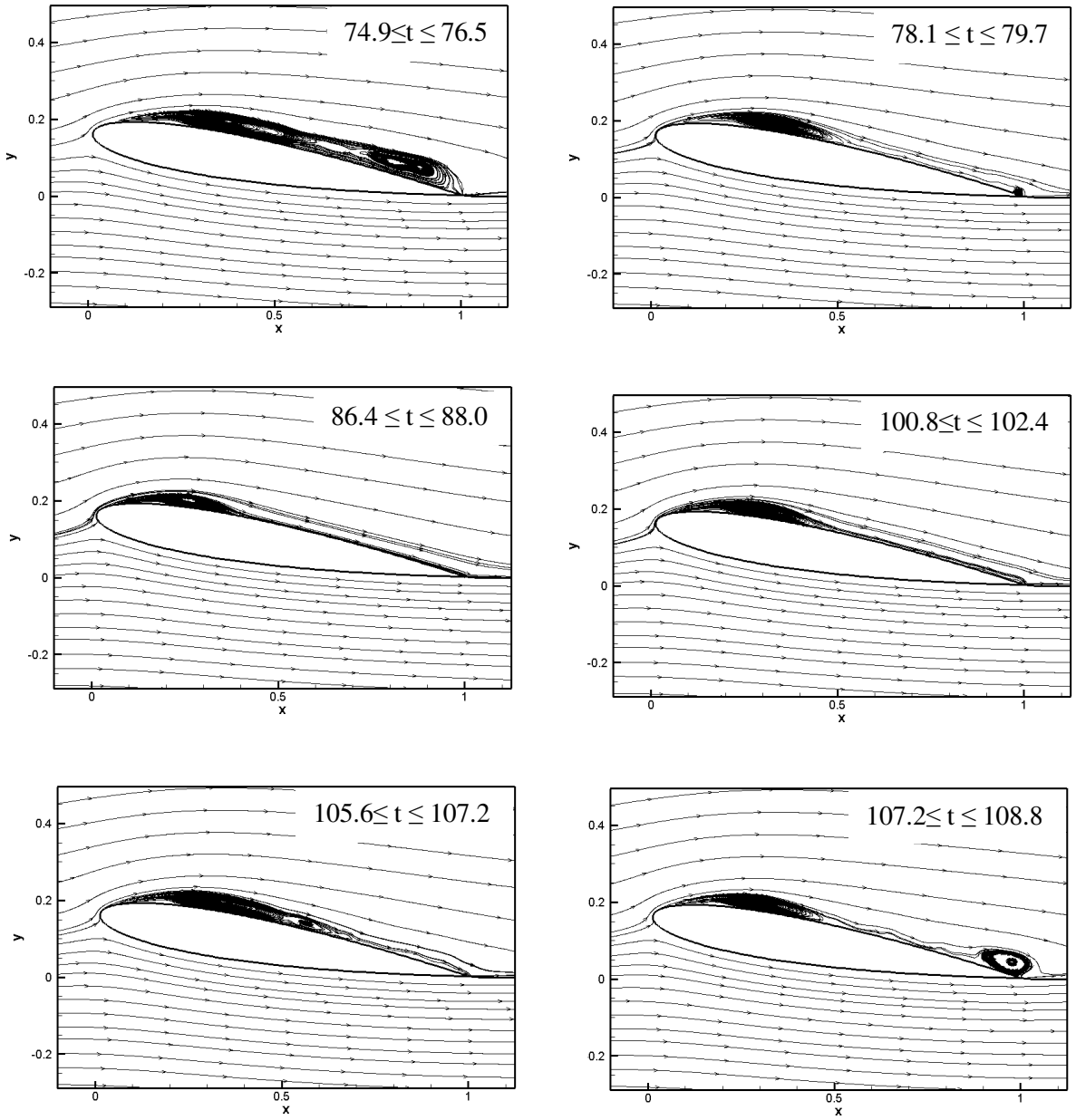

Figure 4.26 Streamline patterns for span- and short-time-averaged flow around a NACA 0012 at α = 9.25°, obtained by LES_wide over the selected intervals from *t* = 74.9 to *t* = 108.8, showing the formation of separation zones.

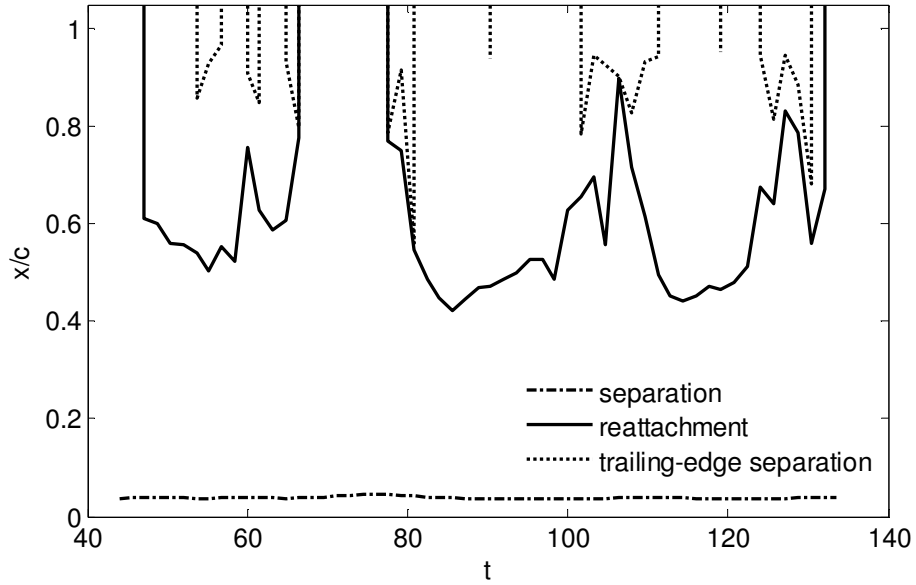

Figure 4.27 Separation and reattachment locations for the laminar sepration bubble during the low-frequency flow oscillation.

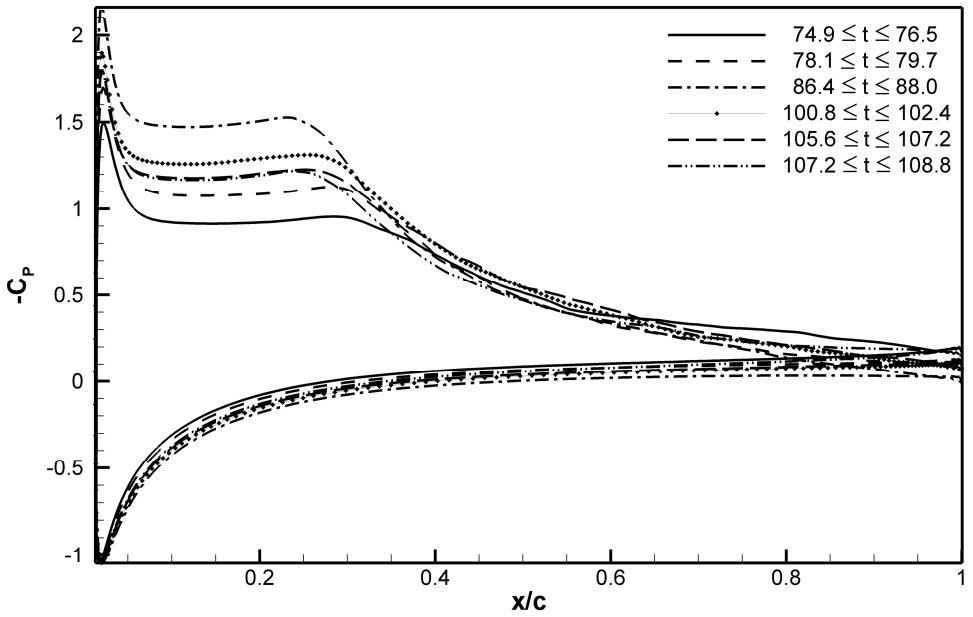

Figure 4.28 Pressure coeffficients for the captured cycle of low-frequency oscillation for an incidence of 9.25° obtained by the LES_wide.

4.4 Chapter summary

The flow around an NACA-0012 airfoil at low Reynolds number near stall has been investigated by LES. A series of tests were performed to find the incidence range in which the low-frequency flow oscillation phenomenon may be present at a Reynolds number of 50,000 with a computational domain of width $L_z = 0.2c$. It was observed that the airfoil was switching initially between stalling and non-stalling conditions at an incidence of $\alpha = 9.25°$. LES was also carried out on the same computational domain width but at higher Reynolds number (Re = 130,000), where experimental results of Rinoie and Takemura (2004) showed a low-frequency flow oscillation at an incidence of $\alpha = 11.5°$. The LES results showed transient low-frequency flow behaviour similar to that observed at Re = 50,000. The effect of the computational domain width was studied by increasing the spanwise length of the LES from 20% to 50% chord, where an irregular low-frequency flow oscillation was captured with an intermittent bursting of the laminar separation bubble (this result has been published in Almutairi *et al.*, 2010). This implies that a significant improvement was achieved by increasing the computational domain width of the LES, which was also supported by comparing two point velocity correlations for the wider domain width $L_z = 0.5c$ with those for the narrower domain width $L_z = 0.2c$.

5 Large eddy simulation of dynamic stall

In Chapter 4, LES was found to be capable of capturing a natural low-frequency flow oscillation of the NACA-0012 airfoil near the static stall condition. The main objective of this chapter is to investigate the dynamic stall of a NACA-0012 airfoil at a low Reynolds number (Re = 50,000), where the incident flow is given a low frequency oscillation. In the present study, the dynamic stall phenomenon is investigated using LES for the first time, providing more details than previous numerical studies. For computational convenience the simulations are run for variable freestream conditions rather than the more used experimental configuration of a pitching airfoil. The present study provides a description of three-dimensional vortical structures which were found by Martinat *et al.* (2008) to be essential to improve the numerical results compared to two-dimensional simulations. Martinat *et al.* (2008) found that dynamic stall has a two-dimensional flow behaviour during the upstroke and three-dimensional vortical structures and fully stalled flow during the downstroke. Those authors studied the flow behaviour around a NACA-0012 airfoil at Reynolds numbers 10^5 and 10^6 using the unsteady Reynolds-averaged Navier-Stokes (URANS) equations. The three dimensional results in the present study were obtained by LES. The other objective of this chapter is to examine the difference between the flow behaviour of the natural low-frequency oscillation and the behaviour of forced flow oscillation from the dynamic stall simulation.

5.1 Numerical configuration and boundary conditions

Dynamic stall usually refers to an oscillating airfoil configuration for which the main parameters are the mean angle of incidence, the amplitude of oscillation, the reduced frequency, the pitch axis location and the Reynolds number. The literature cited in Section 1.6 reviewed the effects of these parameters on the behaviour of airfoil dynamic stall. It was found that any combination of the parameters produced different variations of lift and drag forces and pitching moment, with reduced frequency having the major effect. The mean angle in the present configuration was set at 9.25°, which is the incidence where the NACA-0012 airfoil at a Reynolds number of 50,000 and Mach number 0.4 exhibited transient low-frequency flow oscillations, as discussed in Chapter 4. The simulation was carried out for the same grid and domain width that was used in the

wider domain simulation (LES_wide) of natural low-frequency flow oscillation (see Chapter 4, for grid details). The numerical results for the present dynamic stall simulation were obtained by solving the unsteady compressible Navier-Stokes equations on a static grid with a variable free stream instead of a moving grid around a pitching airfoil in a uniform stream. The moving grid has been used in previous dynamic stall studies, such as Shida *et al.* (1987), Visbal and Shang (1989) and Choudhuri and Knight (1996). In the present dynamic stall simulation, the grid was constructed around a fixed NACA-0012 airfoil at an angle of 9.25°, and the freestream outer boundary conditions were modified to enforce the gust of the upstream air to hit the stagnation point of the airfoil nose with a periodic instantaneous angle of attack $\alpha(t)$ according to the following equation

$$\alpha(t) = \bar{\alpha} + \Delta\alpha \sin(\omega t), \tag{5.1}$$

where t is the non-dimensional time, $\bar{\alpha}$ is the mean angle (which is 9.25° in this case), $\Delta\alpha$ is the amplitude of the oscillation and ω is the circular frequency of flow oscillation. In the present configuration, the reduced frequency ($k = \omega c / 2U_{\infty}$) was set as 0.25, giving a circular velocity ω = 0.5, while the amplitude of the oscillation was set at $\Delta\alpha$ = 3°. Figure 5.1 shows the variation in pitching oscillation incidence with normalised non-dimensional time (t/T), where T is the time period corresponding to k = 0.25 (T = 4π).

5.2 Results of the LES prediction for the dynamic stall phenomenon

The oscillating flow was set at the inflow boundary condition and the solution needs sufficient non-dimensional time to reach the airfoil. Because it is important to specify the exact incidence of flow hitting the leading edge, results start to be analysed at maximum incidence by specifying the simulation time where the direction of flow hits the stagnation point of the airfoil with maximum incidence ($\alpha(t)$ = 12.25°). This was achieved by plotting the streamline patterns of the velocity during the transient time of the first oscillation cycle.

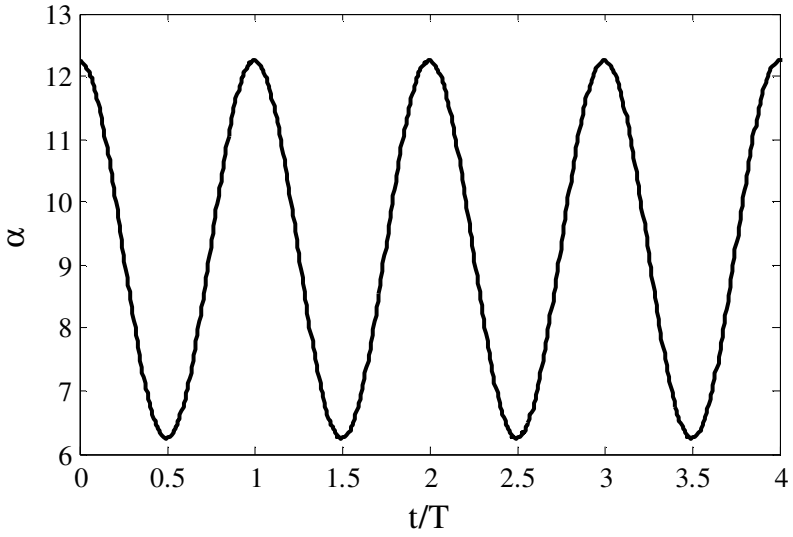

Figure 5.1 The variation of incidence with normalised non-dimensional time.

5.2.1 Dynamic stall hysteresis loops

Figure 5.2 shows the lift (C_L), drag (C_D) and pitching moment (C_m) coefficients over four oscillation cycles of the airfoil after the solution has become independent of the initial condition. By comparing the lift coefficient of Figure 5.2 with the lift coefficient of the natural low-frequency flow oscillation, it is seen that the maximum lift coefficient in the dynamic stall simulation is $C_{Lmax} = 0.98$ and the minimum is $C_{Lmin} = 0.25$, while the maximum and minimum lift coefficient obtained by the natural low-frequency flow oscillation simulation (after the transient solution) are respectively $C_{Lmax} = 0.83$ and $C_{Lmin} = 0.52$. It can also be clearly observed from Figure 5.2 that the oscillation of the lift coefficient for the dynamic stall is regular, whereas it is irregular in the natural low-frequency flow oscillation (see Figure 4.17, LES_wide line).

Figure 5.3 displays the lift, drag and pitching moment coefficients over the same four oscillation cycles of Figure 5.2, but with respect to incidence. It can be seen that there are cycle-to-cycle variations in the hysteresis loops for all of the flow characteristics. These variations were observed by Akbari and Price (2003), but with much lower magnitude than in the present study. They suggested that the reason for these cycle-to-cycle variations is the nature of the unsteady flow. Raffel *et al.* (1995) also found in their experimental study that there is a periodicity of flow structure during the downstroke motion of the NACA-0012 airfoil oscillating in pitch at a low Reynolds

number from cycle to cycle. The common observation during all cycles is that lift increases at the end of each upstroke, followed by stalling, which indicates that dynamic vortex shedding may occur at this stage. It is clear that the lift coefficient increases beyond the static stall incidence in the dynamic stall simulation, compared with the mean lift coefficient ($C_{Lmean} = 0.71$) calculated from the LES of Section 4.3.

Figure 5.4 shows the hysteresis loops of lift, drag and pitching moment coefficients versus incidence, averaged over the four oscillation cycles of Figure 5.3. A high lift coefficient is maintained after maximum incidence ($\alpha = 12.25°$) followed by stalling. While lift increases, the pitching moment dramatically decreases. It is interesting to note that similar behaviour in the hysteresis loops was found by McCroskey *et al.* (1976), especially for the lift coefficient loop, when they set the same reduced frequency as in the present study ($k = 0.25$) as shown in Figure 5.5 which plots normal force coefficient rather than lift, but the two are expected to be similar. It can be also seen from Figure 5.4 that the drag coefficient increases slightly during the upstroke (α increasing) until the airfoil reaches an incidence of $\alpha = 11.70°$, when it starts to increase dramatically towards the end of the upstroke and then decreases almost linearly and more quickly than the upstroke. The behaviour of the averaged hysteresis loops is favourably comparable to the experimental and numerical results as shown in Figure 5.6.

5.2.2 Time-dependent behaviour and averaged results for dynamic stall flow

Figure 5.7 shows instantaneous streamwise vorticity contours during the upstroke part of the dynamic stall cycle. It is noted that the flow is still fully separated at an incidence of $\alpha = 6.37°$, which is just above the minimum incidence. A noticeable reduction of the boundary layer thickness occurs at $\alpha = 7.44°$, which indicates the onset of flow reattachment. The boundary layer thickness continues to decrease until the airfoil is at $\alpha = 11.37°$, where the formation of a laminar separation bubble near the leading edge becomes more obvious. The formation of this laminar separation bubble will be clearly shown when the time and span averaged results are examined in the next section. At $\alpha = 12.12°$ the flow becomes fully separated, which indicates that the dynamic stall vortex occurs somewhere between $\alpha = 12.12°$ and $11.37°$. Figure 5.8 shows the instantaneous

streamwise vorticity during the downstroke, in which the flow is fully detached from the airfoil surface at all downstroke incidences, with a pronounced increase in boundary layer thickness, compared to that in the upstroke motion.

The dynamic stall phenomenon for the NACA-0012 airfoil can be seen more clearly by averaging the instantaneous results. Short-time and span-averaged pressure and skin-friction coefficients and streamwise velocity around the airfoil were generated over the upstroke and downstroke motions of the dynamic stall cycles. The results are averaged every 1,000 time steps (which corresponds to 0.14 non-dimensional time units which may be compared with the period of the dynamic stall of $T = 4\pi$). The labels in the figures are based on the corresponding ranges of incidence.

The time- and span-averaged pressure coefficient ($-C_P$) distributions during the upstroke are plotted in Figure 5.9. It can be seen from this figure that in the incidence range $6.273° \leq \alpha \leq 6.311°$, the pressure coefficient distribution is flat, with very small values compared to the other pressure coefficient distributions and a large pressure plateau extending to $x/c = 0.5$. This type of pressure distribution normally indicates that the airfoil is stalled (Section 4.3). It is clear that this plateau in the pressure distribution has a value which is about half of that in the natural low-frequency flow oscillation at minimum lift coefficient with a larger extension over the airfoil, as in Figure 4.24, and this indicates that the stalling from the pitching airfoil is much stronger than that in the natural low-frequency flow oscillation. This observation is consistent with the minimum lift coefficient for the low-frequency flow oscillation, which is about double that in the dynamic stall case. Figure 5.9 also shows that the suction pressure over the upper surface is increased, with a shrinking of the pressure plateau, as the incidence increases. It is also noticeable from Figure 5.9 that, when the incidence increases beyond $\alpha = 11.02°$, the suction pressure coefficient in the upper surface of the airfoil is increased after the pressure plateau has slightly decreased, and this behaviour differs compared to that at lower incidences. This pressure behaviour may indicate dynamic vortex shedding, as will be shown later in this section. The presence of the dynamic stall vortex can also be inferred from the behaviour of the pressure coefficient where it is clear that there is sudden increase of the suction pressure on the upper surface and in the incidence range

$11.02° \leq \alpha \leq 11.21°$. This feature is also present in successive pressure coefficient curves indicating that the dynamic stall vortex is formed and shed at the end of the upstroke in the incidence range $11.02° \leq \alpha \leq 12.22°$.

Figure 5.10 shows the time- and span-averaged skin-friction coefficient (C_f) distribution during the upstroke of the dynamic stall cycle. It can be observed that the flow reattaches to the upper surface in the presence of a laminar separation bubble near the leading edge, between $\alpha = 8.059°$ and $11.21°$, with a pronounced spike at the back of the bubble between $\alpha = 11.01°$ and $11.21°$, which may indicate dynamic vortex shedding. Figures 5.11 and 5.12 show the time- and span-averaged pressure and skin-friction coefficient distributions during the downstroke motion of the dynamic stall cycle, respectively. It is clear that the pressure coefficients have a completely different behaviour than seen during the upstroke with little variation along the chord. Figure 5.12 shows that the flow is mostly separated over all downstroke incidences.

Figure 5.13 shows a sequence of streamline patterns for time- and span-averaged velocity during the upstroke motion of the dynamic stall cycle. The figure clearly shows that the flow has reattached to the surface for $8.059° \leq \alpha \leq 8.283°$ while a long laminar separation bubble, with a length of approximately 60% chord forms near the leading edge for $8.985° \leq \alpha \leq 9.225°$. A short secondary bubble emerges behind the long laminar separation bubble, which in turn shrinks to less than 50% of the airfoil chord for $9.939° \leq \alpha \leq 10.17°$. The length of the short bubble slightly increases and moves upstream for $11.02° \leq \alpha \leq 11.21°$. The airfoil is apparently fully stalled, with no sign of bubble bursting for $12.18° \leq \alpha \leq 12.22°$, which indicates that the dynamic vortex originates somewhere between $11.21°$ and $12.18°$.

To search for evidence of the dynamic stall vortex, the instantaneous streamwise vorticity is re-examined over a narrow range of incidences between $\alpha = 10.92°$ and $11.94°$. As seen in Figure 5.14, the most likely candidate for the dynamic vortex (located in the figure by a black circle) emanates in the transition area of the laminar separation bubble at $x/c \approx 0.36$ and $\alpha = 10.92°$ and moves downstream at a speed of about $0.77U_\infty$. This is about double the convection speed of the dynamic vortex shedding of McCroskey

et al. (1976), perhaps because different features are tracked in the experiment, or perhaps due to a Reynolds number effect. Sankar and Tassa (1981) found an increased convection speed in dynamic vortex shedding for flow around an NACA-0012 airfoil from $0.24U_\infty$ to $0.32U_\infty$, when the Mach number was increased from 0.2 to 0.4, so a compressibility effect cannot be ruled out. Figure 5.15 shows that the variation of the dynamic vortex location with non-dimensional time (starting from the fourth point) is certainly linear, which means that convection speed of the dynamic vortex is constant which agrees the previous studies in dynamic stall phenomenon. A slower flow structure of another candidate for the dynamic vortex is found on the streamwise vorticity, which moves downstream at speed of $0.58U_\infty$, which is apparently still higher than that in previous studies.

Figure 5.16 shows a sequence of streamline patterns for time- and span-averaged velocity during the downstroke motion of the dynamic stall cycle, where the flow is clearly fully separated. A large vortex is observed near the trailing-edge between α = 11.46° and 8.392°. This large vortex starts to break down into smaller vortices as the incidence decreases below α = 7.53°.

5.2.3 3D structures during dynamic stall

In order to provide more details about the flow around the NACA-0012 airfoil under the dynamic stall condition, Figure 5.17 shows a 3D isosurface of the second invariant of the velocity gradient Q (defined in 3.12) during the downstroke at α = 8.97°. Strong irregular vortical structures with intermittent hairpin shapes appear in the flow after separation. The presence of the hairpin-like vortices has not been mentioned in previous dynamic stall studies. Figure 5.18 shows a 3D isosurface Q during the upstroke at α = 9.70°, where boundary layer thickness is smaller, especially near the trailing edge (compared with Figure 5.17). In contrast to the study of Martinat *et al.* (2008), the flow has a fully three dimensional behaviour during the upstroke motion.

Another comparison between the flow behaviour at α = 8.97° (downstroke) and 11.02° (upstroke) using an isosurface of spanwise vorticity ω_z on the surface of the

airfoil, is shown in Figures 5.19 and 5.20, where the positive vorticity in the red areas represents strong separation, while the negative vorticity in the blue areas represents attached flow. Figure 5.19 shows large areas of separation in the middle of the airfoil and towards the trailing edge, with high correlation across the span, while the attached areas are very small. Figure 5.20 predicts the reattached flow areas, which are distributed over a large area of the airfoil surface, and confirms the presence of primary and secondary separation bubbles revealed by the averaged velocity (Figure 5.13).

5.3 Chapter summary

LES was used to study the dynamic stall phenomenon around a NACA-0012 airfoil at a low Reynolds number (Re = 50,000) and Mach number M = 0.4. The averaged hysteresis loops of the lift, drag and moment coefficients were predicted well compared to previous studies. Cycle-to-cycle variations were observed in the hysteresis loops, which may be attributed to the unsteady nature of the flow. The time- and span-averaged pressure and skin-friction coefficients and streamline patterns for velocity were identified. It was noted that the averaged pressure coefficient after $\alpha = 11.02°$ during the upstroke increased in a fundamentally different way from that at lower incidences, indicating dynamic vortex shedding near this incidence. The averaged flow results revealed a fully separated flow during the whole downstroke, even at small incidences, while the flow is attached during the upstroke motion (from around $\alpha = 8.059°$). As expected from the averaged pressure coefficient, some evidence for a dynamic vortex was found at the end of the upstroke motion (between $\alpha = 10.92°$ and $11.94°$). The vortex was shed downstream at an approximate speed of $0.766U_{\infty}$. The three-dimensional flow structures for the dynamic stall of the NACA-0012 airfoil were captured well by the LES, which showed also that the behaviour of the flow is indeed fully three-dimensional during both upstroke and downstroke motions, which is in contrast to the URANS study of Martinat *et al.* (2008) who concluded that the flow behaviour is two-dimensional during the upstroke.

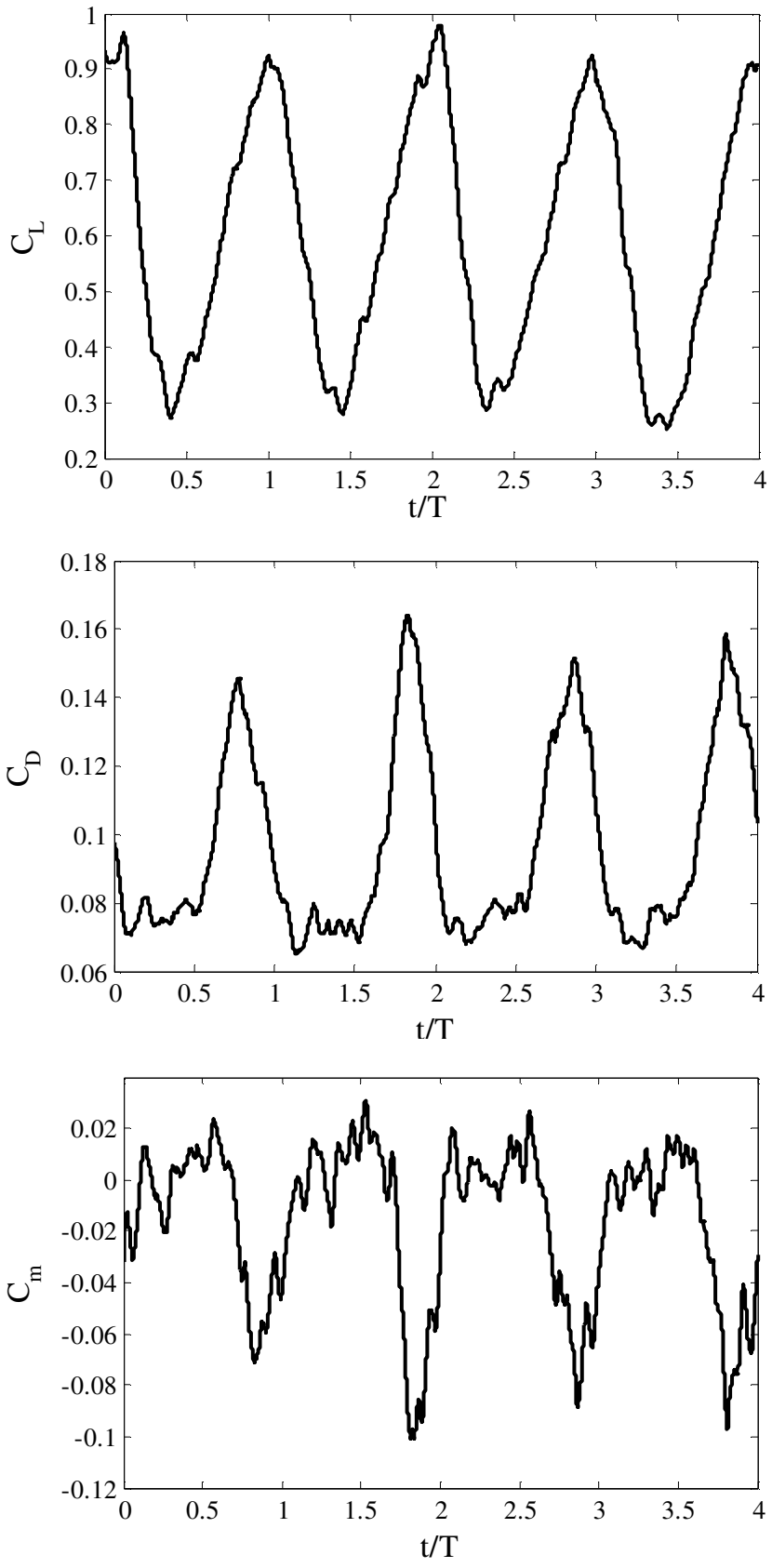

Figure 5.2 Lift, drag and moment coefficients obtained from LES for an oscillating flow around the NACA-0012 airfoil with $\alpha(t) = 9.25^{\circ} + 3^{\circ}\sin(0.5t)$ and Reynolds number of 50,000.

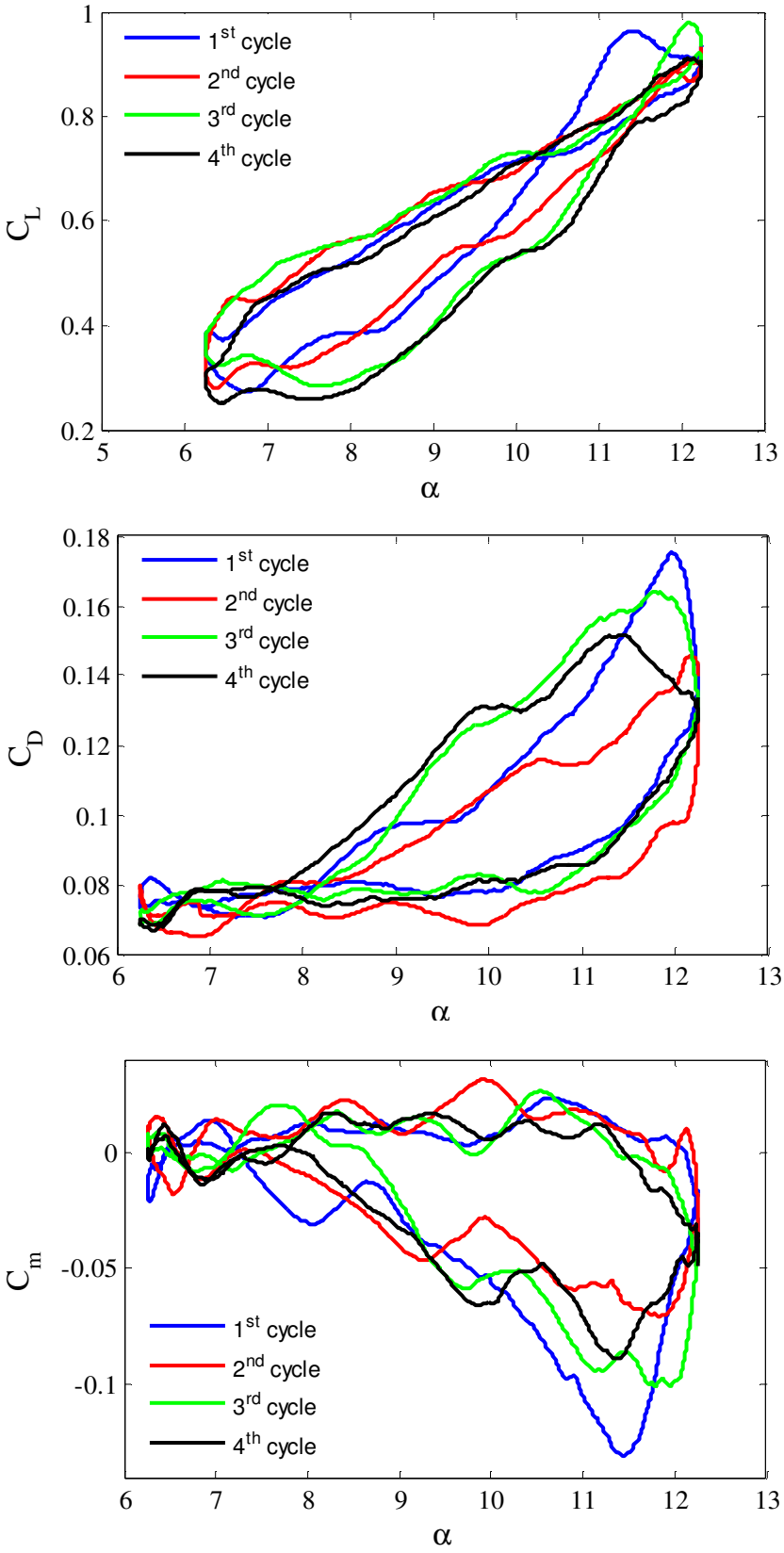

Figure 5.3 Lift, drag and moment coefficients versus incidence during four oscillation cycles obtained from 3D LES for oscillating flow around a NACA-0012 airfoil.

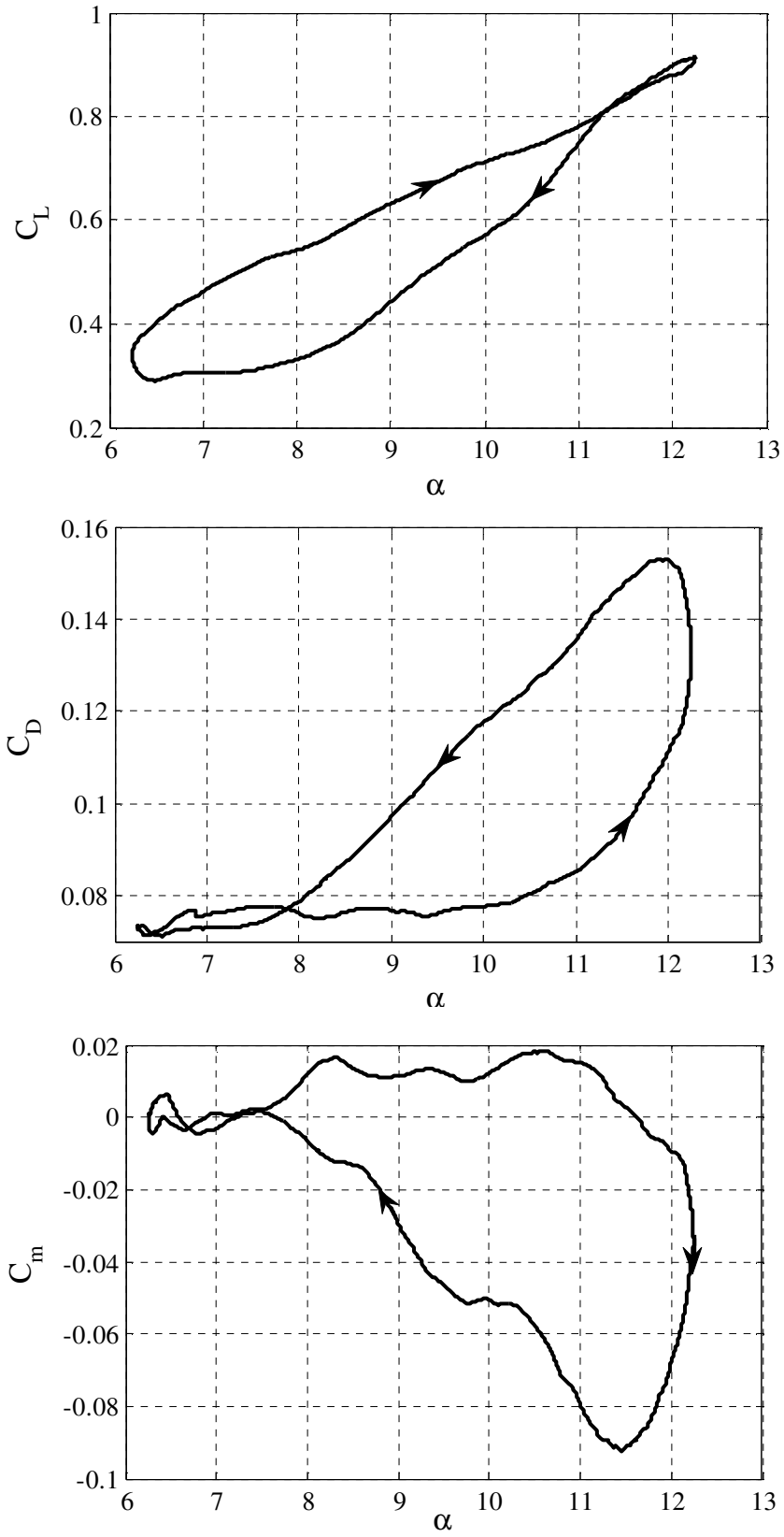

Figure 5.4 Averaged dynamic stall hysteresis loops of lift, drag and moment coefficients obtained from 3D LES for oscillating flow around an NACA-0012 airfoil at a Reynolds number of 50,000 and Mach number 0.4.

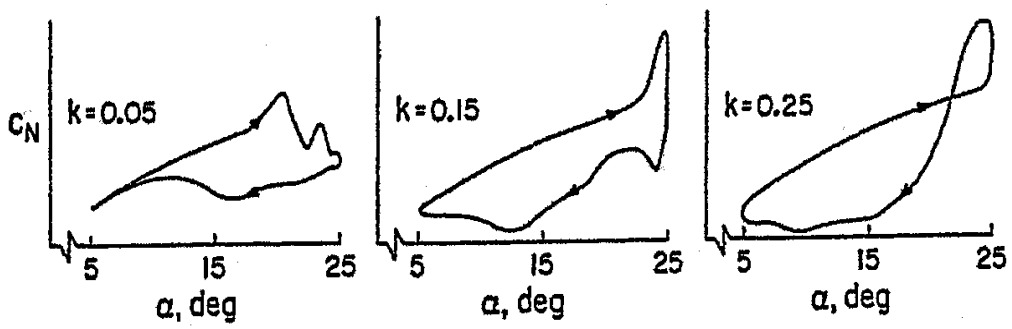

Figure 5.5 Effect of reduced frequency on the variation of lift coefficient for NACA-0012 airfoil at Re = 2.5×10^6 (McCroskey, 1976).

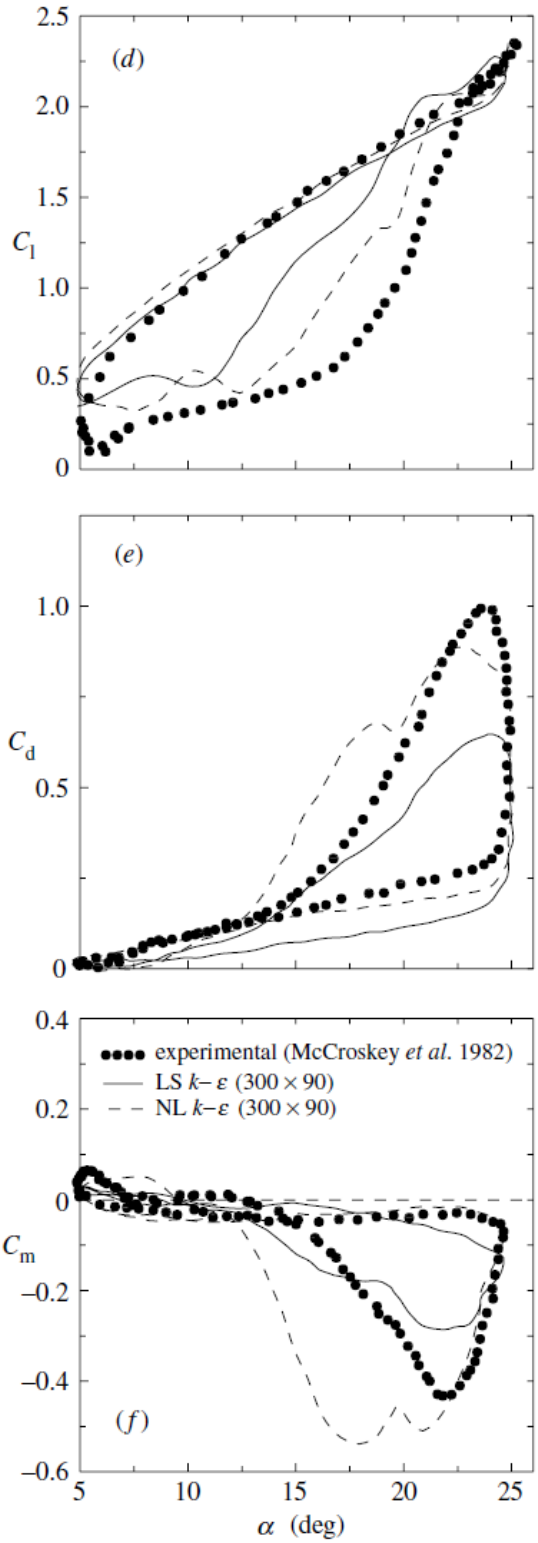

Figure 5.6 Experimental and numerical results for the hysteresis loops of lift, drag and moment coefficient for an NACA0012 airfoil at Reynolds number of 1.95×10^6 and Mach number of 0.29 (taken from Barakos and Drikakis, 2000) .

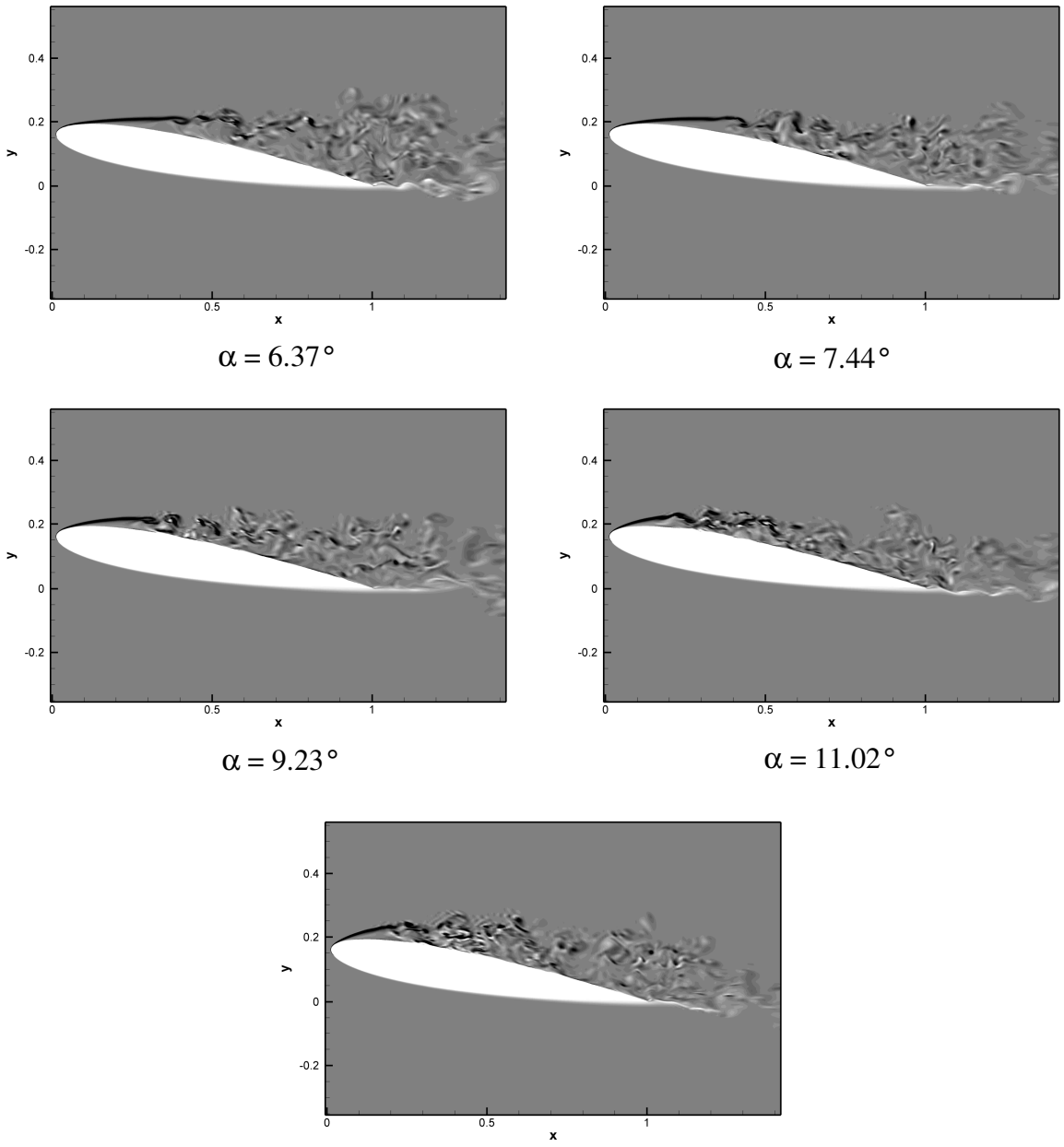

Figure 5.7 Snapshots of instantaneous spanwise vorticity during the upstroke of the dynamic stall cycle for oscillating flow around an NACA-0012 airfoil at a Reynolds number of 50,000 and Mach number 0.4, using 20 contour levels in a range from -100 to 100.

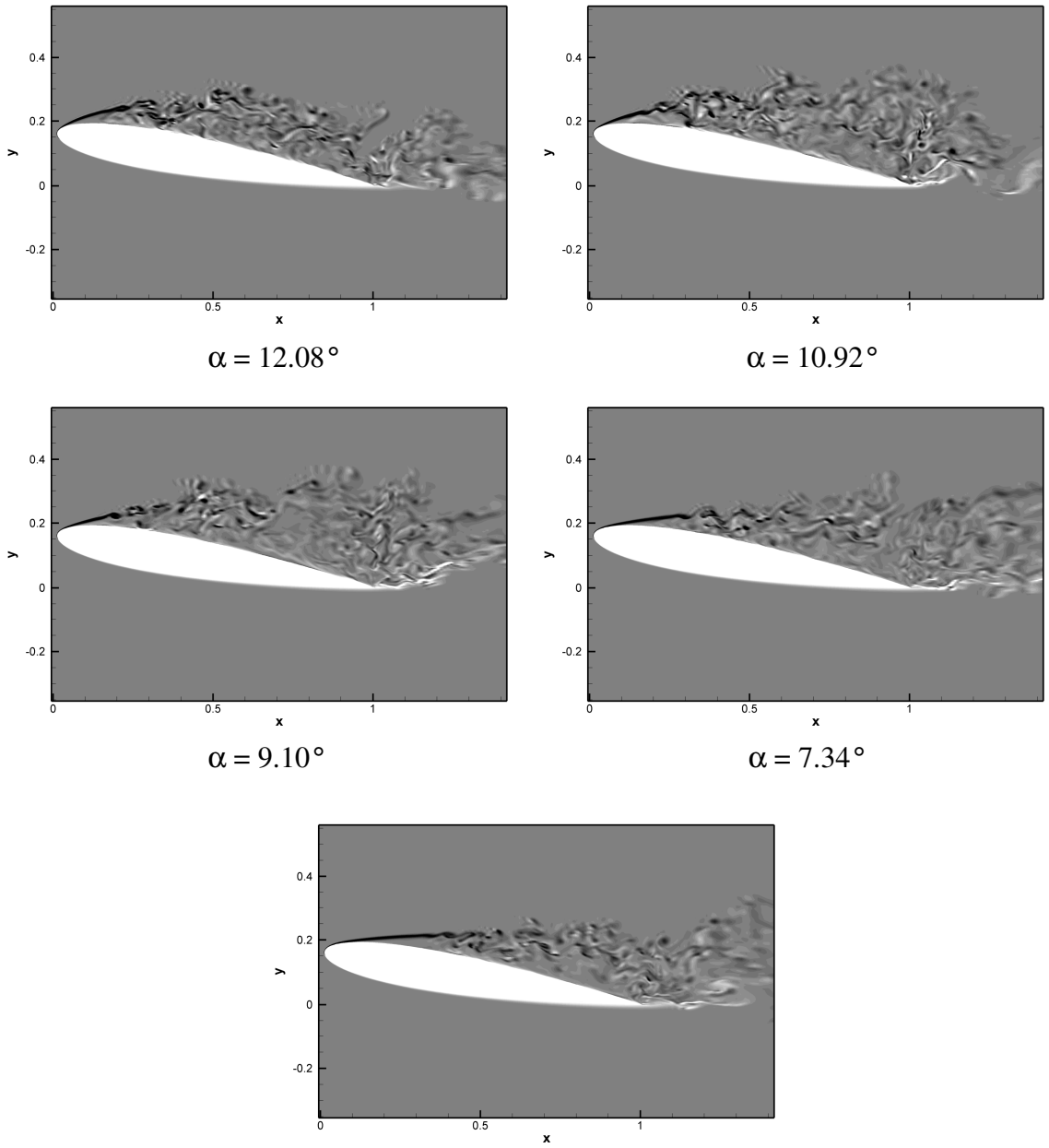

Figure 5.8 Snapshots of instantaneous spanwise vorticity during the downstroke of the dynamic stall cycle for oscillating flow around an NACA-0012 airfoil at a Reynolds number of 50,000 and Mach number 0.4, using 20 contour levels in a range from -100 to 100.

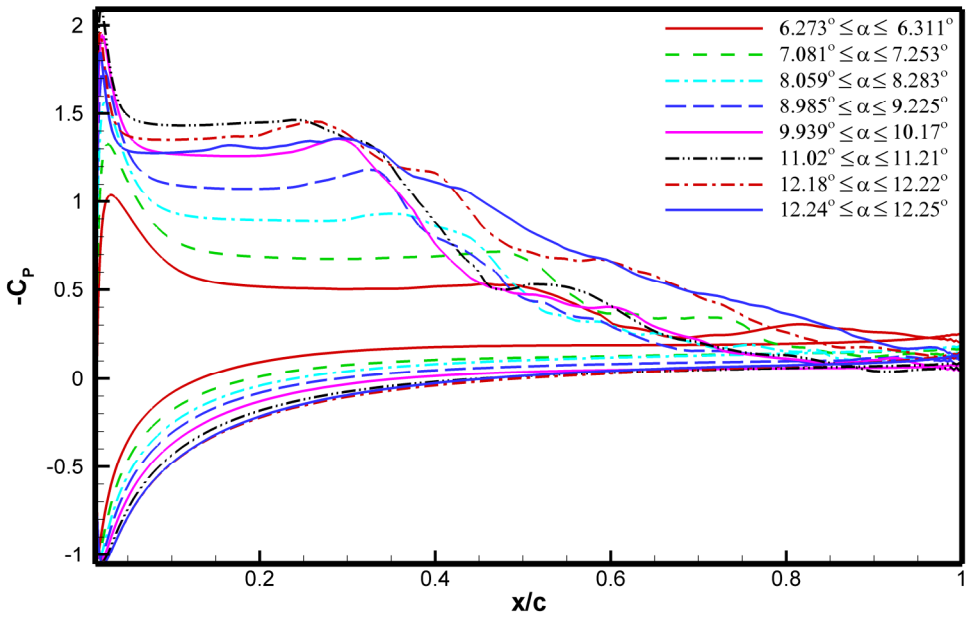

Figure 5.9 Pressure coefficients obtained from 3D LES during the upstroke motion of the dynamic stall for oscillating flow around an NACA-0012 airfoil at a Reynolds number of 50,000 and Mach number 0.4.

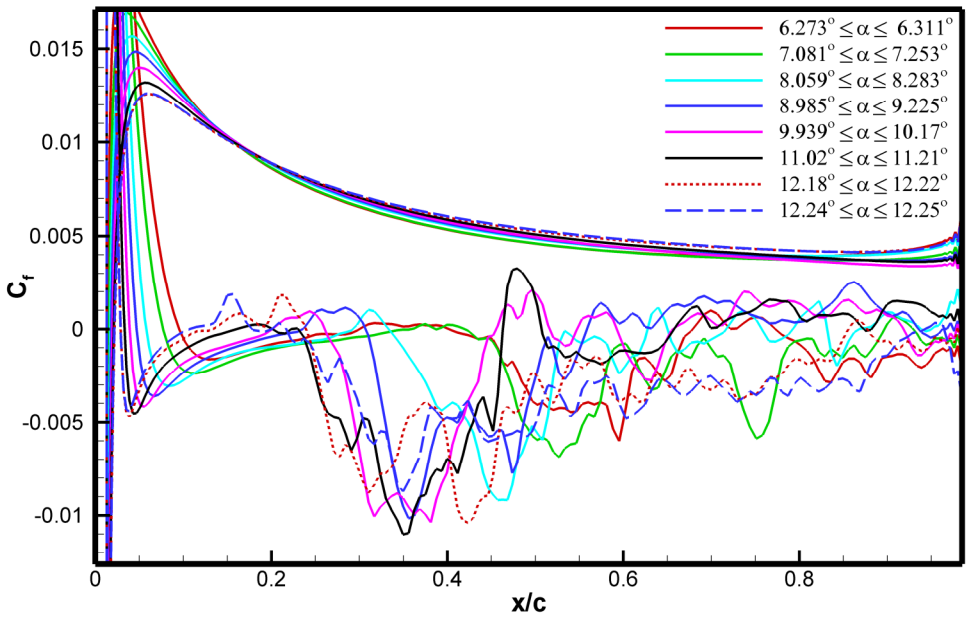

Figure 5.10 Skin-friction coefficients obtained from 3D LES during the upstroke motion of the dynamic tall for oscillating flow around an NACA-0012 airfoil at a Reynolds number of 50,000 and Mach number 0.4.

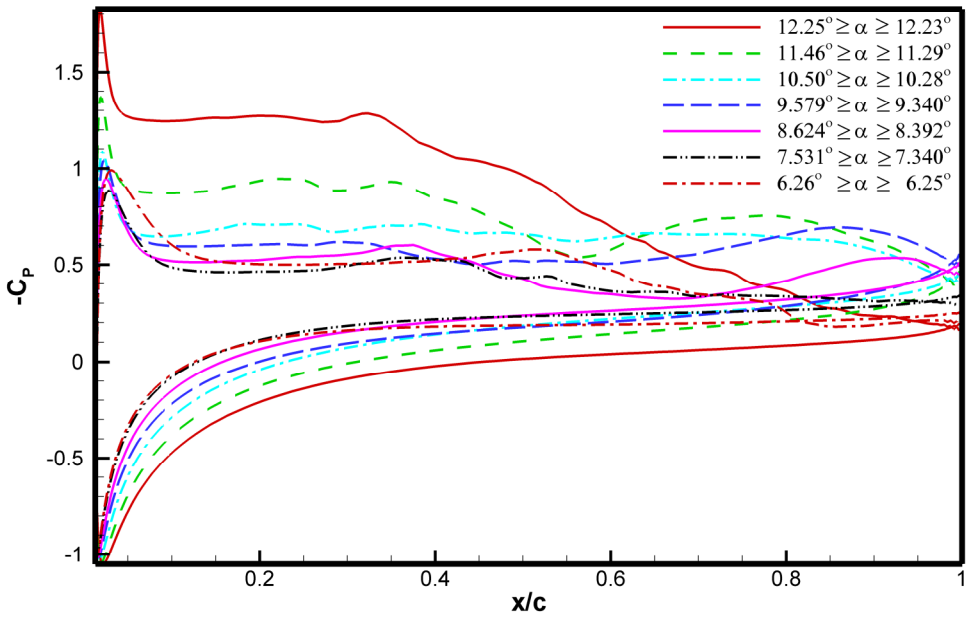

Figure 5.11 Pressure coefficients obtained from 3D LES during the downstroke motion of the dynamic stall for oscillating flow around an NACA-0012 airfoil at a Reynolds number of 50,000 and Mach number 0.4.

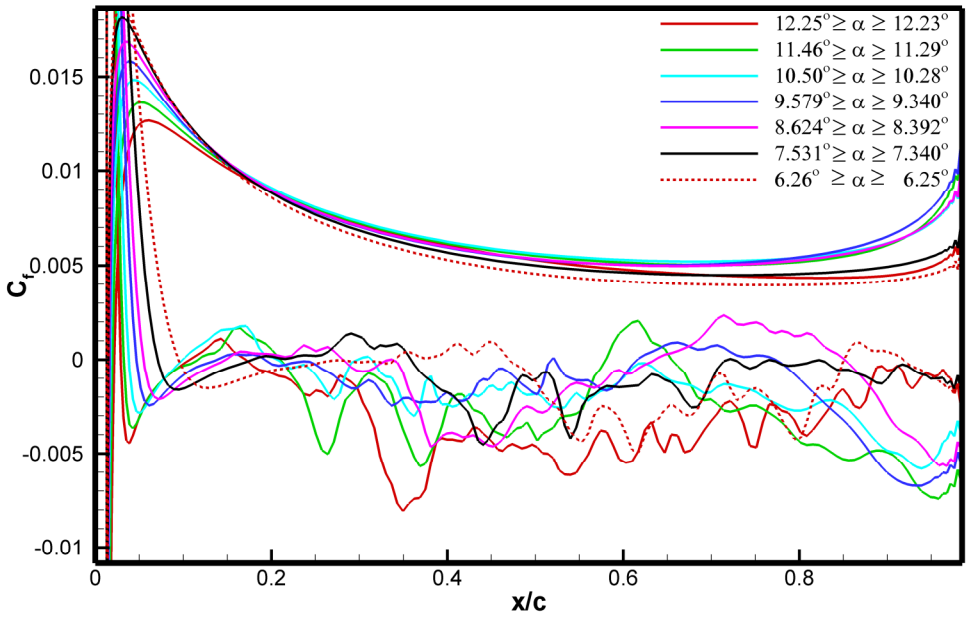

Figure 5.12 Skin-friction coefficients obtained from 3D LES during the downstroke motion of the dynamic stall for oscillating flow around an NACA-0012 airfoil at a Reynolds number of 50,000 and Mach number 0.4.

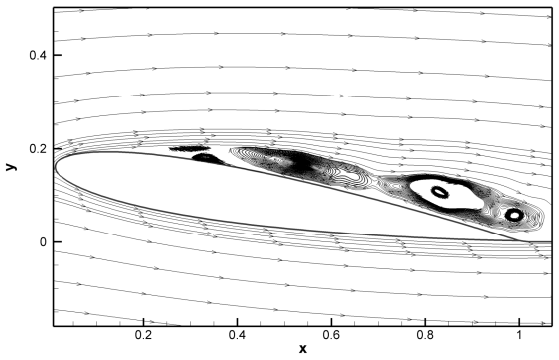

$6.273° \leq \alpha \leq 6.311°$

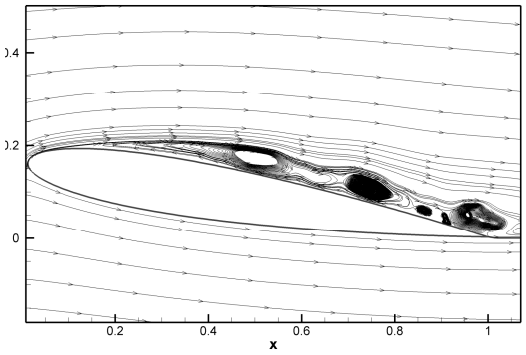

$7.081° \leq \alpha \leq 7.253°$

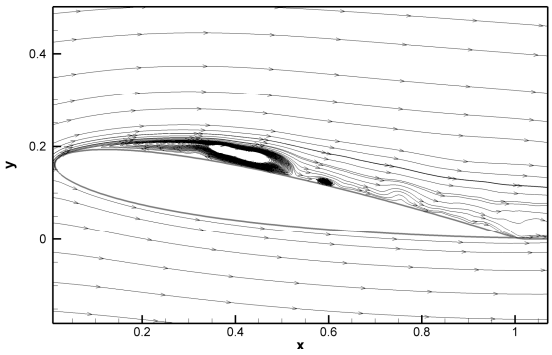

$8.059° \leq \alpha \leq 8.283°$

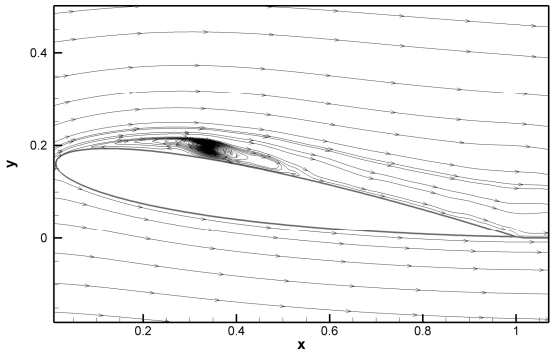

$8.985° \leq \alpha \leq 9.225°$

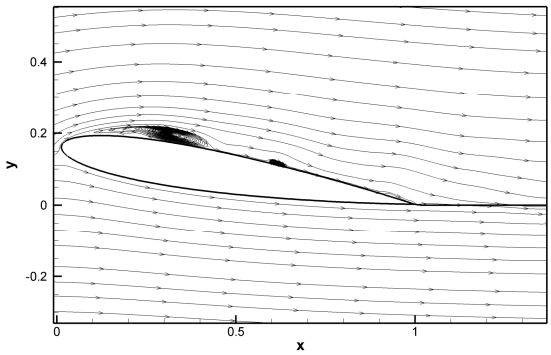

$9.939° \leq \alpha \leq 10.17°$

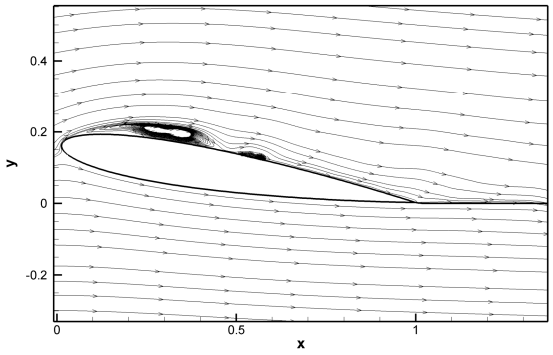

$11.02° \leq \alpha \leq 11.21°$

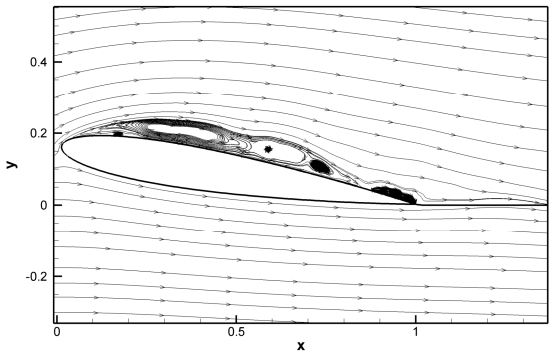

$12.18° \leq \alpha \leq 12.22°$

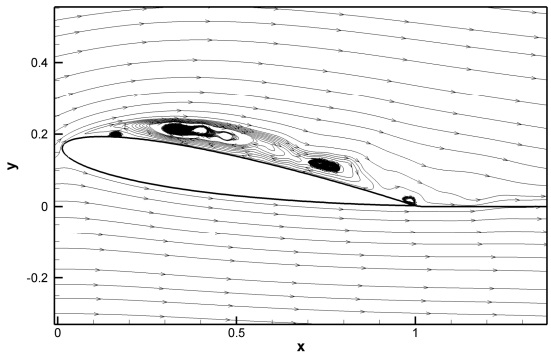

$12.24° \leq \alpha \leq 12.25°$

Figure 5.13 Sequence of streamline patterns obtained from LES for span- and short-time-averaged flow during the upstroke of the dynamic stall cycle for oscillating flow around an NACA 0012 airfoil at a Reynolds number of 50,000 and Mach number 0.4, showing the flow reattachment and subsequent abrupt separation.

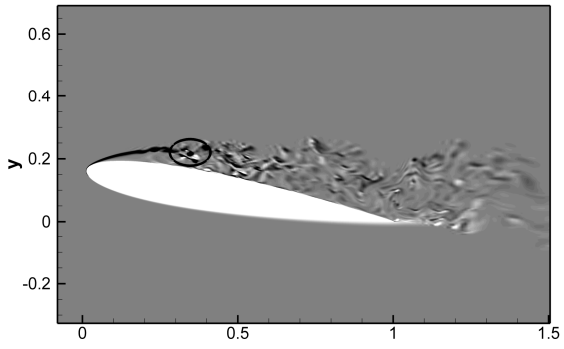

t/T = 6.844, α = 10.92°

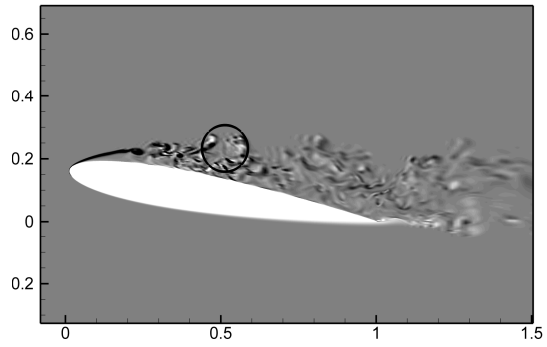

t/T = 6.850, α = 11.01°

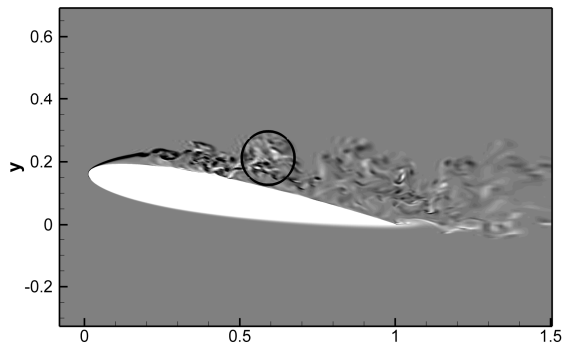

t/T = 6.856, α = 11.11°

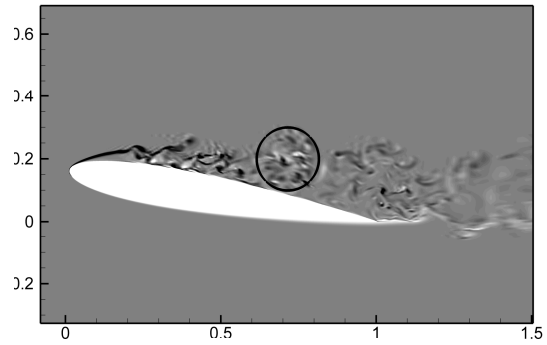

t/T = 6.863, α = 11.20°

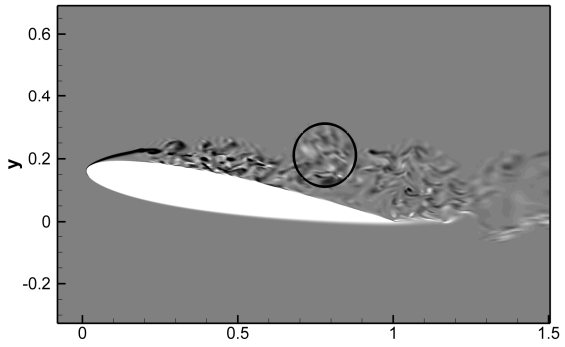

t/T = 6.869, α = 11.29°

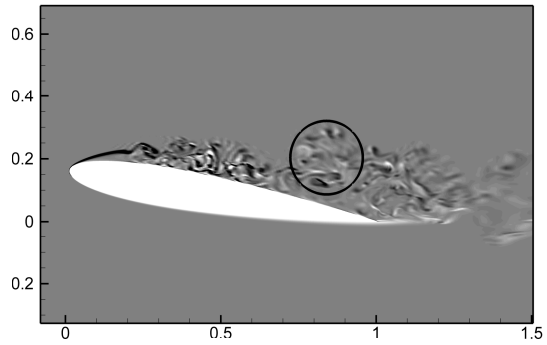

t/T = 6.876, α = 11.38°

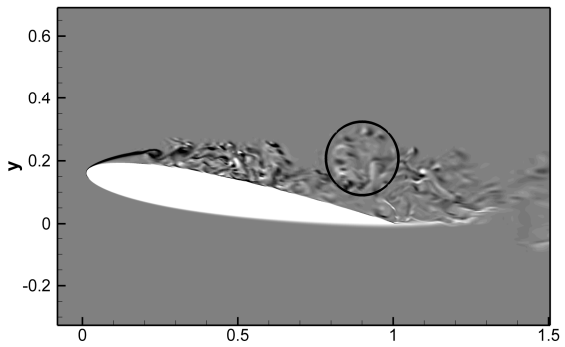

t/T = 6.882, α = 11.46°

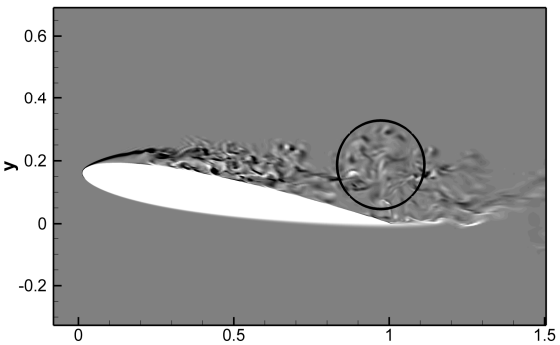

t/T = 6.888, α = 11.54°

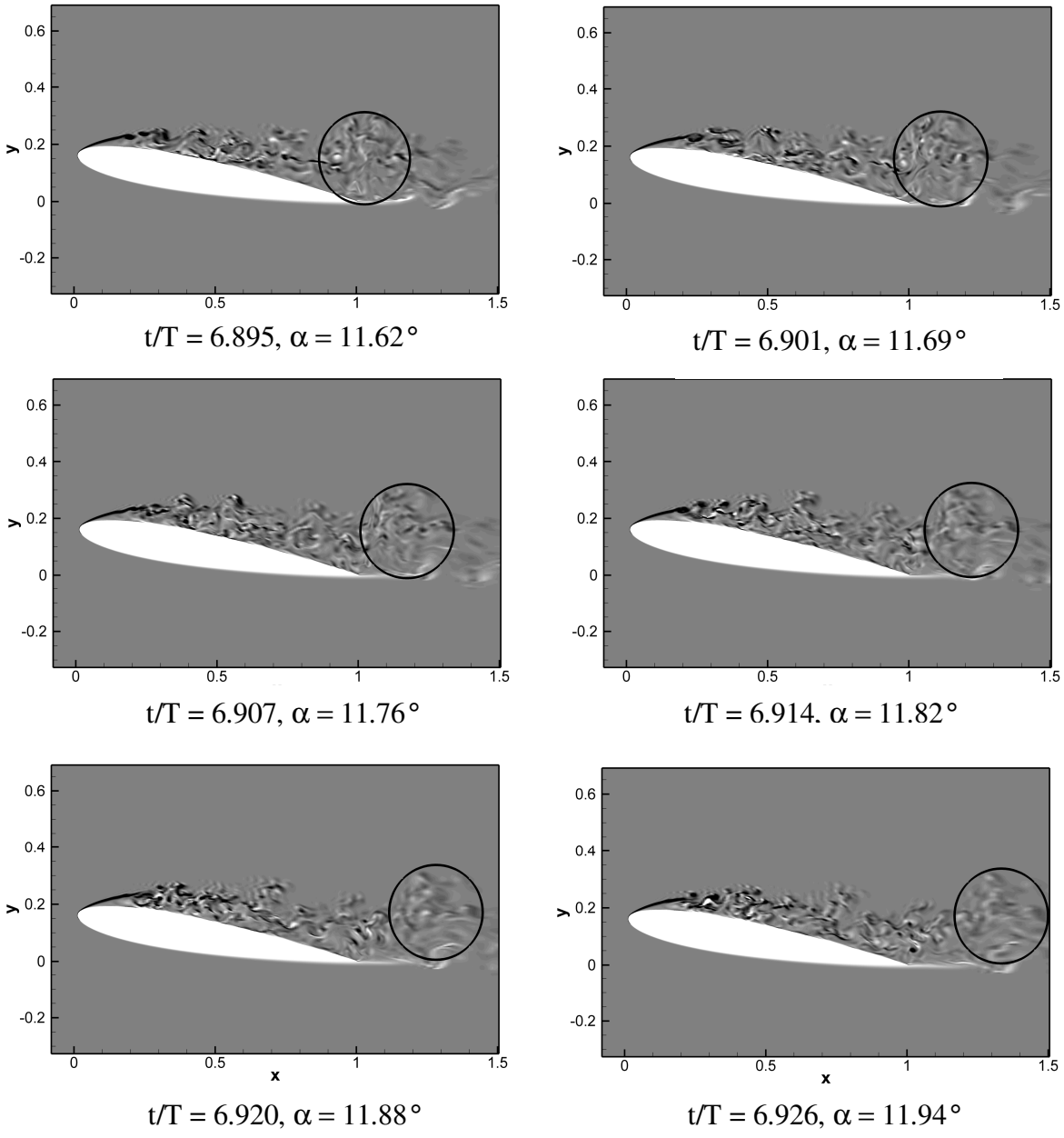

Figure 5.14 Snapshots of instantaneous spanwise vorticity at the end of the upstroke motion of the dynamic stall cycle for the oscillating flow around an NACA-0012 airfoil at a Reynolds number of 50,000 and Mach number of 0.4, using 30 contour levels in the range from -100 to 100 and showing the formation and the shedding of the candidate of the dynmaic vortex.

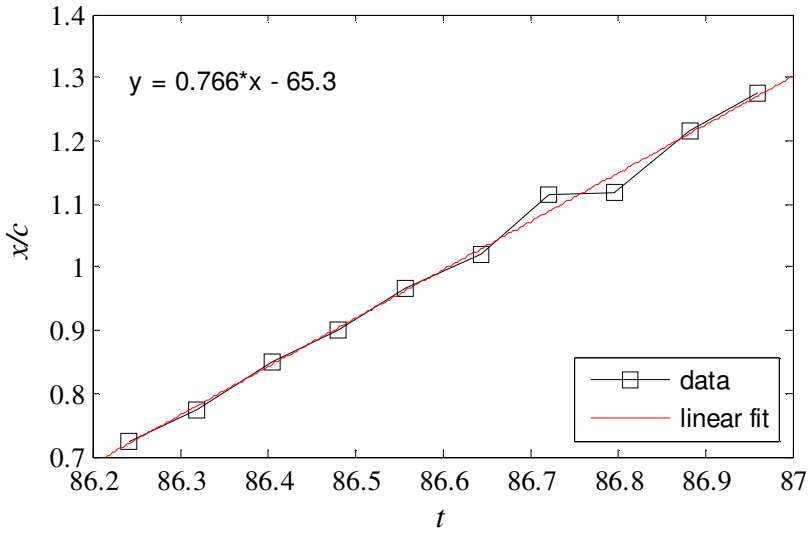

Figure 5.15 Variation of candidate dynamic vortex location with non-dimensional time.

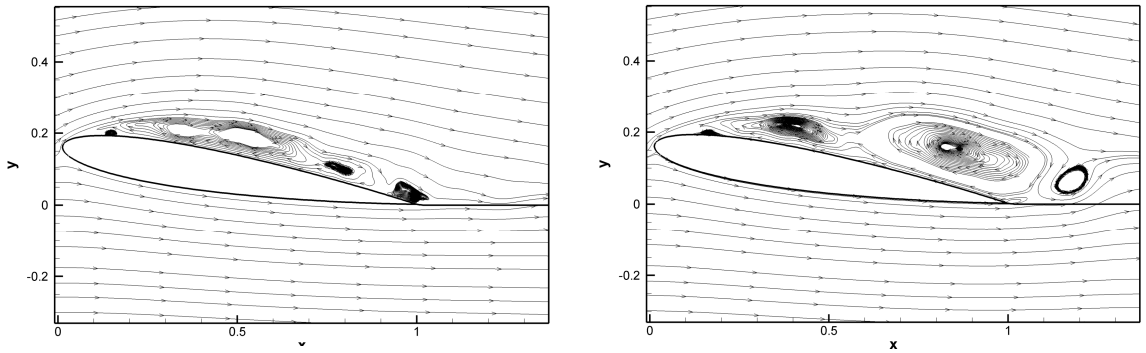

12.25° ≥ α ≥ 12.23°

11.46° ≥ α ≥ 11.29°

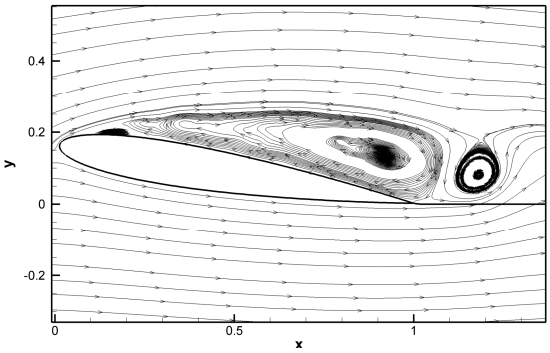

10.50° ≥ α ≥ 10.28°

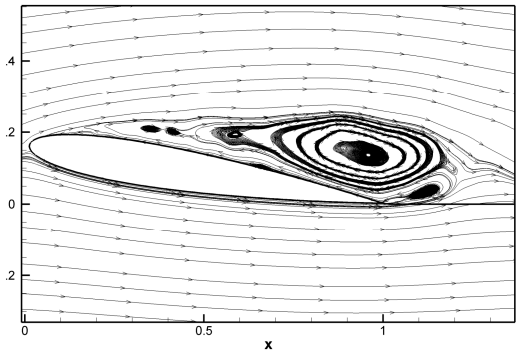

9.579° ≥ α ≥ 9.340°

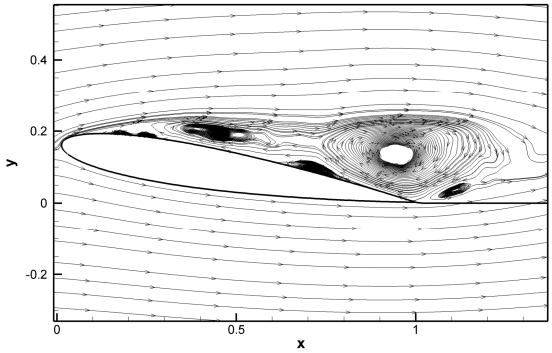

8.624° ≥ α ≥ 8.392°

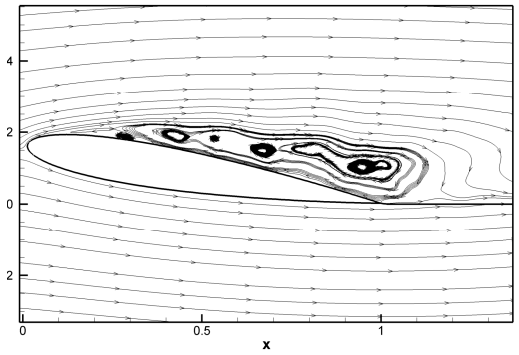

7.531° ≥ α ≥ 7.340°

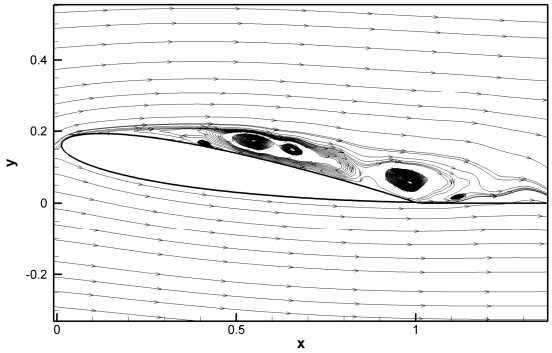

6.260° ≥ α ≥ 6.250°

Figure 5.16 Sequence of streamlines patterns obtained from LES for span- and short-time-averaged flow during the downstroke of the dynamic stall cycle for the oscillating flow around an NACA 0012 airfoil at a Reynolds number of 50,000 and Mach number of 0.4.

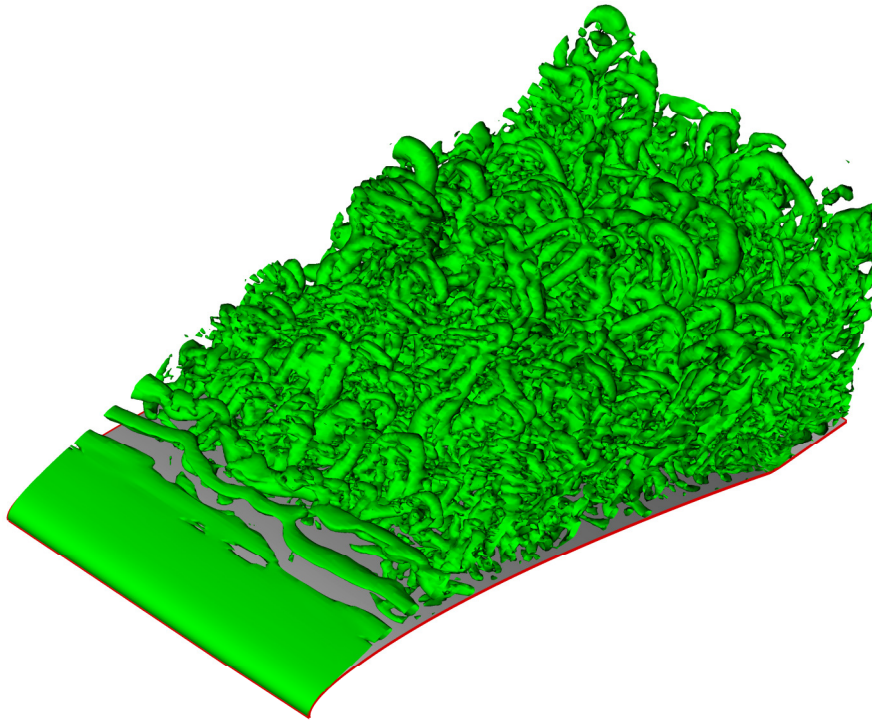

Figure 5.17 Three-dimensional view for the isosurface of the second invariant of the velocity gradient at $\alpha = 8.97°$ during the downstroke motion of the dynamic stall cycle obtained by 3D LES ($Q = 200$).

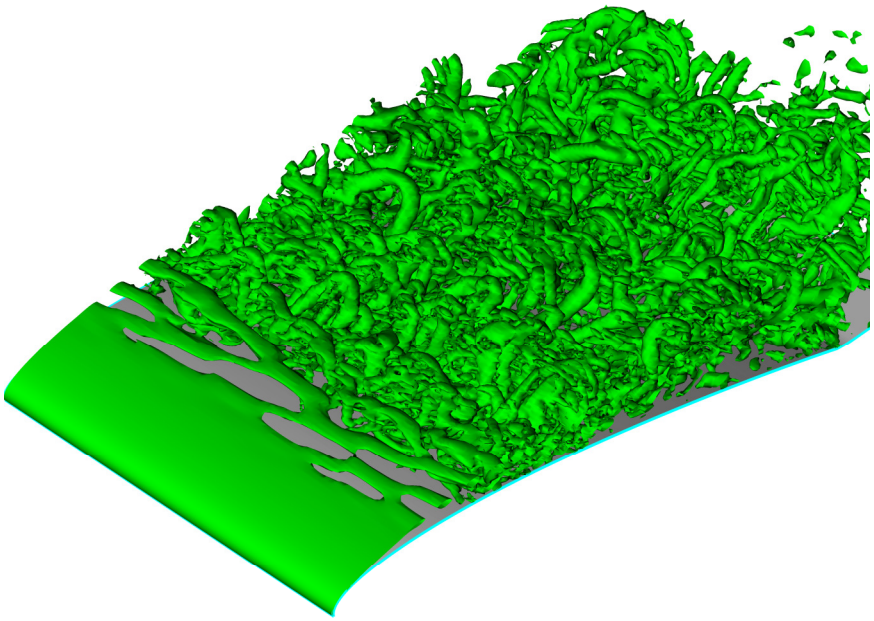

Figure 5.18 Three-dimensional view for the isosurface of the second invariant of the velocity gradient at $\alpha = 9.70°$ during the upstroke motion of the dynamic stall cycle obtained by 3D LES ($Q = 200$).

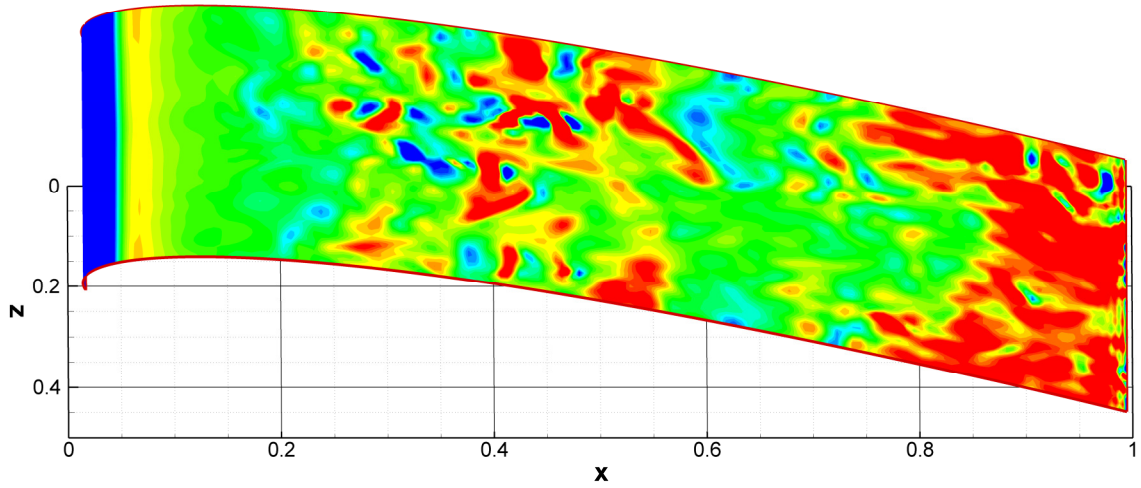

Figure 5.19 Isosurface of spanwise vorticity ω_z on the surface of the airfoil at $\alpha = 8.97°$ during the downstroke motion of the dynamic stall cycle, using 20 contours levels in the range from -100 to 100.

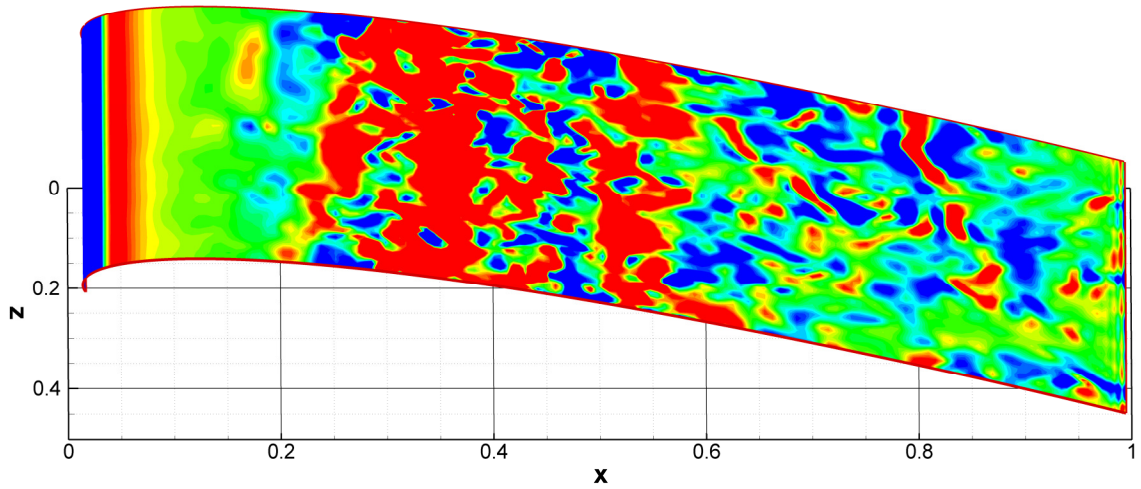

Figure 5.20 Isosurface of spanwise vorticity ω_z on the surface of the airfoil at $\alpha = 11.02°$ during the upstroke motion of the dynamic stall cycle, using 20 contours levels in the range from -100 to 100.

6 Unsteady Viscous-Inviscid Interaction calculations

The principle of the present unsteady viscous-inviscid interaction method is to couple the potential flow solution, which can be obtained by a panel method, with the viscous solution of the integral boundary-layer equations, which contains models of laminar flow, turbulent flow and transition. Viscous inviscid interaction is very cheap compared with numerical methods that solve the full Navier-Stokes equations. Usually this numerical technique was implemented only for steady flow (Drela and Giles, 1987). Sandham (2008) made a modification to the viscous-inviscid interaction method to solve an unsteady formulation of the momentum integral equation. This allows study of the unsteadiness of airfoil flows.

The aim of this chapter is to study the low-frequency flow oscillation and dynamic stall phenomena using the viscous-inviscid interaction approach. Therefore, this chapter is organised as follows: section 6.1 presents the governing equations of the viscous-inviscid interaction. Section 6.2 discusses the results of the viscous-inviscid interaction method for the low-frequency flow oscillation phenomenon on the NACA-0012 airfoil over a wide range of Reynolds numbers and incidences. Results from the viscous-inviscid interaction method for a NACA-0012 airfoil under dynamic stall condition are presented in section 6.3.

6.1 Governing Equations of the viscous inviscid interaction method

The main governing equation is the unsteady form of the momentum integral equation

$$\frac{\partial U\delta^*}{\partial t}+\frac{\partial U^2\theta}{\partial s}+U\delta^*\frac{\partial U}{\partial s}=\frac{\tau_w}{\rho} \tag{6.1}$$

where s is the airfoil surface tangent coordinate. The interaction condition for Eq. (6.1) is the surface transpiration velocity

$$v_s=\mathrm{d}(U\delta^*)/\mathrm{d}s\,, \tag{6.2}$$

which can be solved and imposed as a boundary condition for the potential flow. The viscous flow calculations are applied by modelling the shape factor $H=\delta^*/\theta$, the

entrainment E (Green *et al.*, 1977) and the amplification factor n (Drela and Giles, 1987) according to the following transport equations

$$\frac{\partial H}{\partial t} + U_H \frac{\partial H}{\partial s} = B_H \tag{6.3}$$

$$\frac{\partial E}{\partial t} + U_E \frac{\partial E}{\partial s} = B_E \tag{6.4}$$

$$\frac{\partial n}{\partial t} + U_n \frac{\partial n}{\partial s} = B_n \tag{6.5}$$

where U_H, U_E and U_n are convective velocities and B_H, B_E and B_n include laminar and turbulent boundary layer models and a laminar-turbulent transition model based on the growth of the amplification factor n via boundary-layer instability (see Sandham (2008) for more modelling details). When the amplification factor goes beyond a critical value n_{crit} the flow becomes fully turbulent. The present results were obtained with $n_{crit} = 9$ and 120 panels. The free-stream turbulence level can be calculated from the following equation (Mack, 1977)

$$n_{crit} = -8.43 - 2.4\ln(Tu) \tag{6.6}$$

where Tu is the free-stream turbulence and it is about 0.07% in the present case.

The calculations were run for 40 time units to ensure that the solution passed the transient flow region. The viscous-inviscid interaction lift coefficients revealed low frequency oscillations from which the peak-to-peak amplitude and Strouhal number were extracted.

6.2 Unsteady viscous inviscid interaction results for the low-frequency flow oscillation near stall

To determine the relationships between incidence, Reynolds number and Strouhal number that govern the behaviour of the laminar separation bubble near stall, the unsteady viscous-inviscid modelling method was employed over a wide range of Reynolds numbers. At each Re, the incidence was increased through the stall regime. Low-frequency modes were only detected between Re = 50,000 and Re = 420,000; beyond this range, the airfoil stalled suddenly. Figure 6.1 shows the Strouhal number as a

function of incidence for all the cases where the low-frequency flow oscillation phenomenon was observed. For comparison, the results of LES and experiments (Rinoie and Takemura, 2004) are included. It can be seen from this figure that the magnitude of the Strouhal number obtained by the viscous-inviscid interaction method increases as the Reynolds number, and hence the stall incidence, increases. It is also clear that there is a variation of the Strouhal number at each Reynolds number, but the general trend shows an increase until it reaches a maximum Strouhal number (St = 0.015) at Re = 300,000 and α = 13.4°. A significant drop is then observed at Re = 420,000 and any further increase in the Reynolds number leads to the disappearance of the low-frequency flow oscillation phenomenon. Figure 6.1 also shows that the Strouhal numbers from LES and experiment follow similar trends with the viscous-inviscid interaction results, although their values are smaller and there is insufficient data to properly map the behaviour.

Another relationship that can be deduced from the viscous-inviscid interaction method is between the incidence and the peak-to-peak amplitude of the lift coefficient, as illustrated in Figure 6.2. The peak-to-peak amplitude increases as the incidence is increased and also as the Reynolds number is increased, as seen in Figure 6.3, which also shows that the LES amplitude is larger than that obtained by the viscous-inviscid interaction method. Figure 6.4 shows that the incidence corresponding to the maximum Strouhal number increases significantly with the Reynolds number, which is in agreement with the observation of Bragg *et al.* (1996) as discussed in section 1.3. Peak amplitudes of 0.75 are comparable to Zaman *et al*. (1989), while the Strouhal number for the NACA0012 seems to be lower than for the E374 airfoil (Bragg *et al.*, 1996; Broeren and Bragg, 1999; Broeren and Bragg, 2001). There is a clear difference between the absolute values of the viscous-inviscid interaction method and the LES and experiment which means that the viscous-inviscid interaction can only be used as a guide to the range of Reynolds number and the corresponding airfoil incidence where the low-frequency flow oscillation occurs, which is useful as a starting point for further LES study.

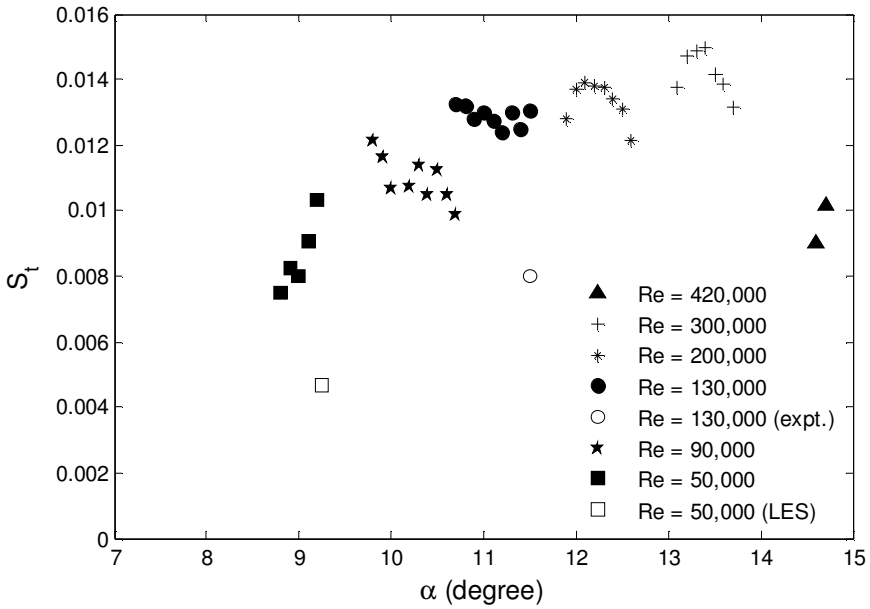

Figure 6.1 The relationship between the incidence and the Strouhal number of the low-frequency flow oscillation.

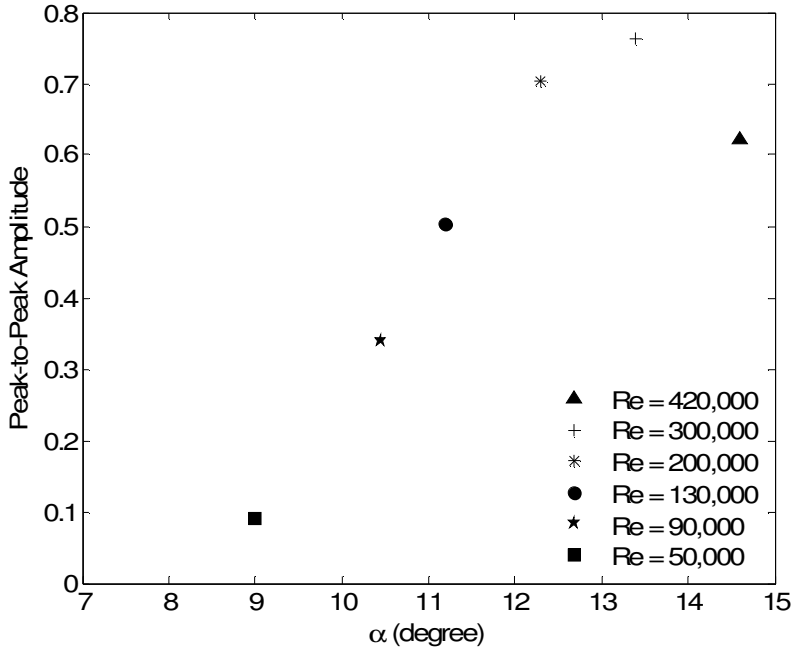

Figure 6.2 The relationship between the incidence and the peak-to-peak amplitude of the low-frequency flow oscillation.

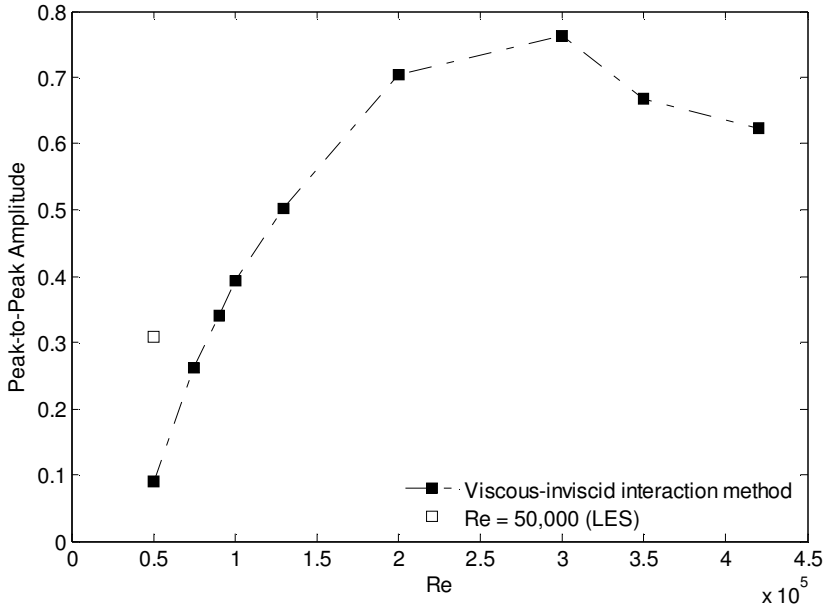

Figure 6.3 The relationship between the Rynolds number and the peak-to-peak amplitude of low-frequency flow oscillation and comparison between the LES and the viscous-inviscid interaction method results.

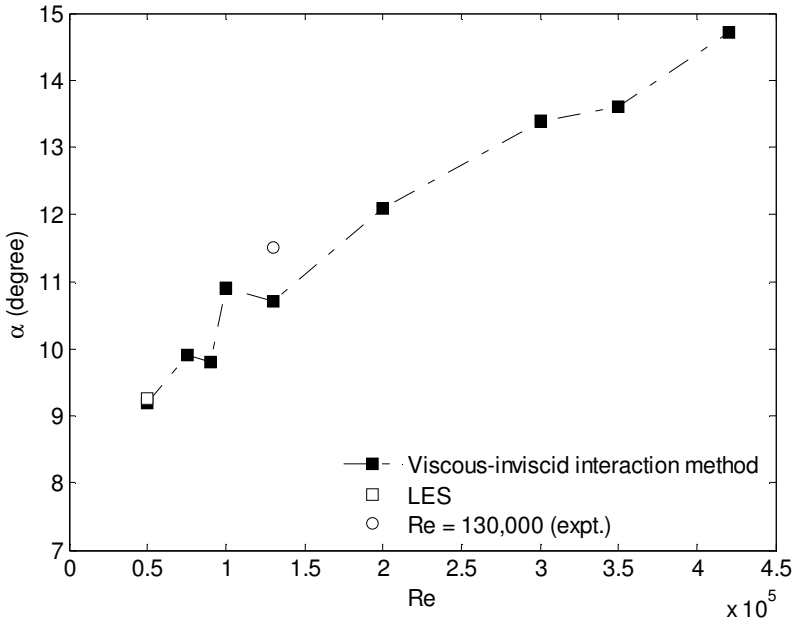

Figure 6.4 The relationship between the Reynolds number and the incidece of low-frequency flow oscillation and a comparison between the expirment, LES and the viscous-inviscid interaction method results.

6.3 Unsteady viscous inviscid interaction results for an airfoil under dynamic stall condition

A simulation of sinusoidally-varying flow around a NACA-0012 airfoil with a reduced frequency of $k = 0.25$, an amplitude of oscillation of 3° and a Reynolds number of Re = 50,000 was carried out using the unsteady viscous-inviscid interaction modelling method to compare the dynamic stall LES (Chapter 5). The mesh was fixed while the free-stream was rotated during the computations. Figure 6.5 shows a comparison of lift and drag coefficients between LES and viscous-inviscid interaction method, both showing regular oscillations. The trend and frequency of the lift coefficient cycles for both simulations are similar but the peak-to-peak amplitude in the viscous-inviscid interaction method is larger than that in the LES. There is clear difference between both simulations in terms of the peak-to-peak amplitude and the location of the minimum and maximum drag coefficient. the in the drag coefficient is Table 6.1 compares the maximum and minimum lift and drag coefficients of the viscous-inviscid interaction modelling method and LES. It can be observed from the table that the amplitude of lift oscillation obtained by the viscous-inviscid method is larger than in the LES and the maximum and minimum lift coefficients are larger and lower than the maximum and minimum lift coefficients obtained by LES, respectively. Figure 6.6 shows a comparison of the hysteresis loops of the lift and drag coefficients between the LES and viscous-inviscid interaction. A rapid increase in the lift coefficient can be seen at the end of the upstroke motion of the dynamic stall cycle in the viscous-inviscid interaction results, indicating that a dynamic vortex is formed and shed in this region, which is in agreement with Lorber and Carta's (1988) experiment, discussed in Section 1.4. The behaviour of the drag coefficient is different from the LES except small portion of the drag coefficient during the downstroke, while there is a reduction in the drag coefficient during the upstroke compared to the increasing seen in the LES. A noticeable reduction in the drag coefficient is clearly observed near the end of the upstroke ($\alpha > 11.05°$) which can also be attributed to the formation and shedding of the dynamic vortex. It is interesting to note that the cycle-to-cycle variations in the viscous-inviscid interaction results are very limited compared with the significant cycle-to-cycle variations in the LES results. The

difference between the results of the LES and viscous-inviscid interaction may be attributed to the improved representation of turbulence in LES.

Table 6.1 Comparison of maximum and minimum lift and drag coefficients for dynamic stall simulations between viscous-inviscid interaction and LES.

Simulation	C_L (max)	C_L (min)	C_D (max)	C_D (min)
Viscous-inviscid interaction	1.33	0.17	0.115	0.022
LES	0.98	0.25	0.153	0.075

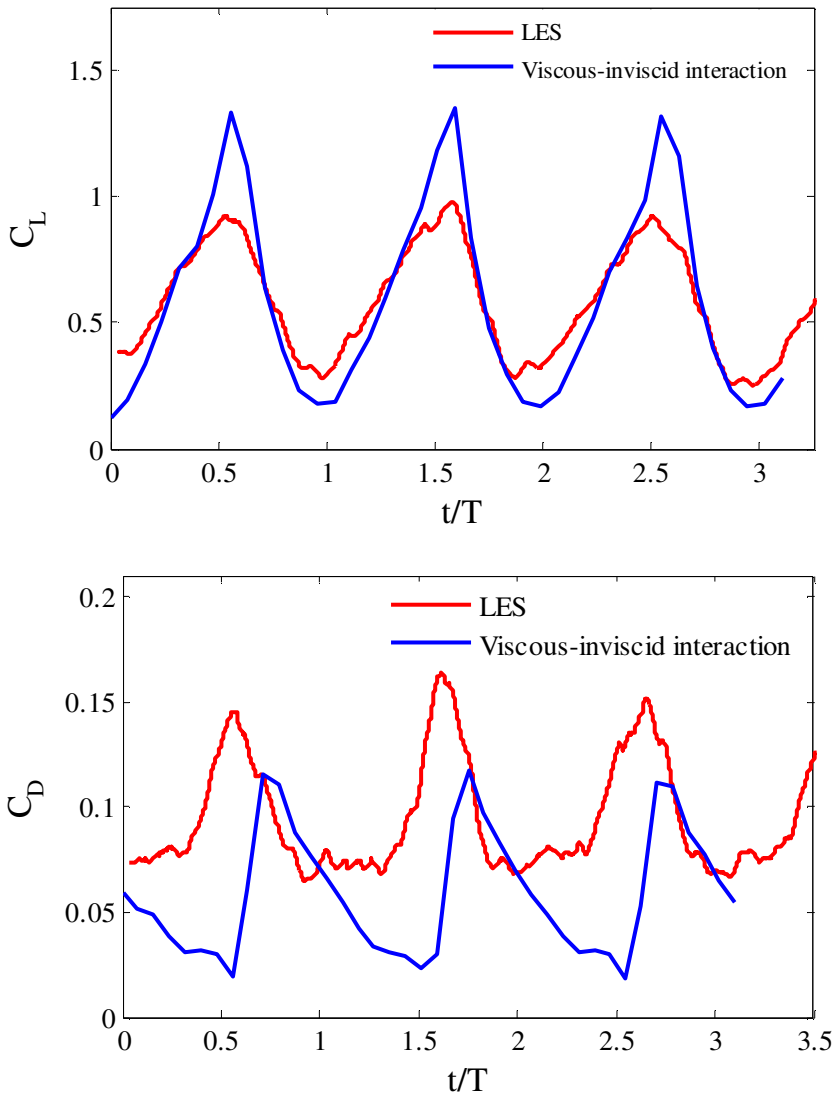

Figure 6.5 Comparison of Lift and drag coefficients between LES and viscous-inviscid interaction modelling method for oscillating NACA-0012 airfoil at a Reynolds number 50,000.

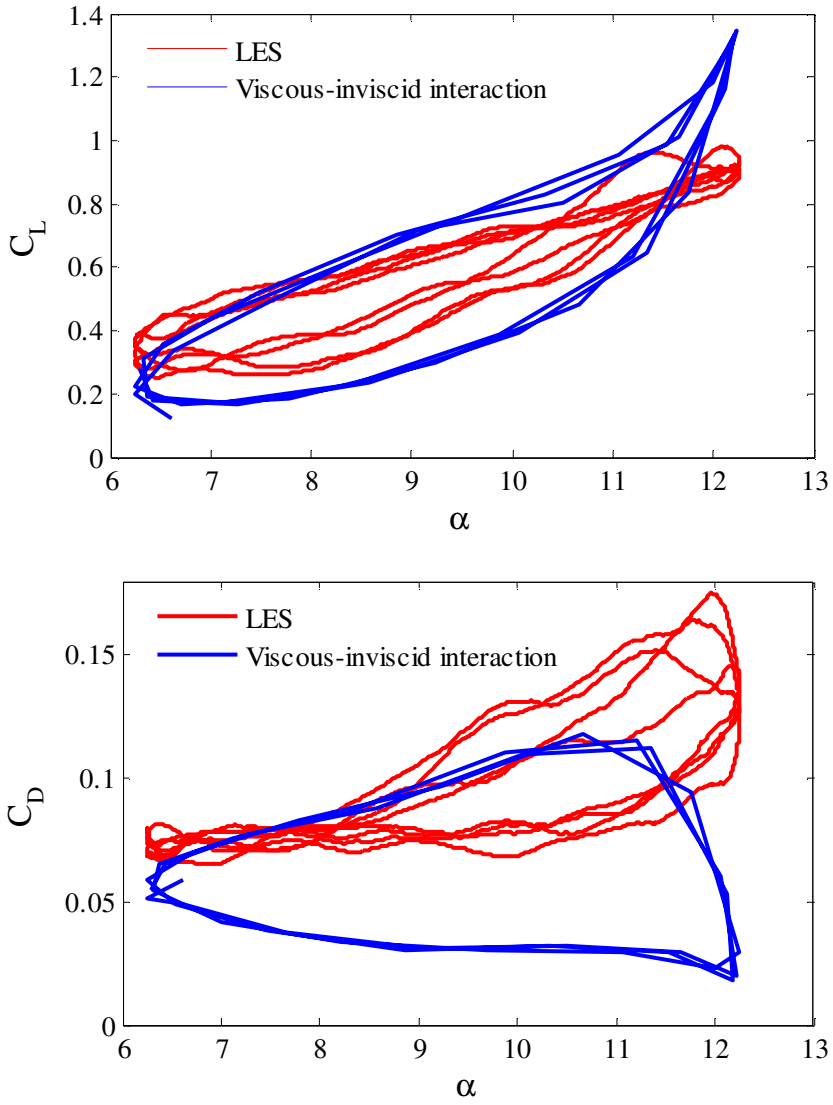

Figure 6.6 Comparison of hysteresis loops of Lift and drag coefficients between viscous-inviscid interaction method and LES for oscillating NACA-0012 airfoil at a Reynolds number 50,000.

6.4 Chapter summary

The viscous-inviscid interaction modelling methods was used to study low-frequency flow oscillation and dynamic stall phenomena for a NACA-0012 airfoil at low-Reynolds numbers. In the low-frequency flow oscillation case, it was found that the peak-to-peak amplitude and Strouhal number for the lift coefficient strongly depend on two factors: the Reynolds number and the incidence. It was found that as the Reynolds number and incidence increase, the peak-to-peak amplitude and Strouhal number tend to increase, in agreement with the experimental observations of Bragg *et al.* (1996). The lift

coefficient obtained in the viscous-inviscid interaction method had lower peak-to-peak amplitude compared with the limited data from LES and a larger Strouhal number. In the dynamic stall case, it was found that the aerodynamic characteristics are different from that obtained by the LES.

7 Flow control for low-Reynolds number airfoils

This chapter is focused on control of some of the flow phenomena that have been observed in the previous chapters. The first phenomenon is the low-frequency flow oscillation around a NACA-0012 airfoil near stall, as studied in Chapter 4. The second phenomenon, which was observed by Jones (2007) and was presented in Chapter 1, is the flapping that occurs around an NACA-0012 airfoil in two-dimensional simulations at $\alpha = 0°$, Mach number of 0.8 and Reynolds number of 50,000. Although flapping can occur on lower Mach number, it is stronger at a Mach number of 0.8 which was selected for this study. The main objectives of this chapter are to remove the low-frequency flow oscillation and to reduce or entirely eliminate the flapping, thus enhancing the performance of the airfoil. Low-amplitude periodic forcing will be exploited to achieve these objectives.

The periodic forcing is introduced into the laminar boundary layer just upstream of the natural flow separation in order to produce perturbations in the near wall region. This has been found to be an effective and successful technique in the field of separation control, as mentioned in Chapter 1 (section 1.5). The periodic forcing equation is the same as that used by Jones (2007), with a similar low amplitude (0.1% of the freestream velocity) but with additional frequencies. The forcing was applied wherever separation occurred, i.e. if the separation occurred on the suction side of the airfoil then the forcing was applied on that side only. The forcing was implemented on both sides of the airfoil to eliminate the flapping at zero incidence.

This chapter is organised as follows: Section 7.1 presents the effects of adding the periodic forcing on the low-frequency flow oscillation phenomenon, including a comparison between the uncontrolled (unforced) baseline case and the controlled (forced) case. Flow control to remove the two-dimensional flapping motion is discussed in Section 7.2. Results for a long run LES of flow around an NACA-0012 airfoil at a Reynolds number of 50,000 and Mach number of 0.4 are presented and compared with the DNS in Section 7.3.

7.1 Periodic forcing control of the low frequency flow oscillation at $\alpha = 9.25°$ and Reynolds number = 50,000

In order to assess the effect of periodic forcing on the low frequency flow oscillation the calculation with the wider computational domain from section 4.3 is restarted (at $t \approx 95$ non-dimensional time units) with the addition of periodic forcing. The amplitude of the forcing is set to be 0.1% of the freestream velocity while several different frequencies of the forcing are chosen so that equation 3.9 becomes

$$\frac{dF_\xi}{d\xi} = \frac{dF_\eta}{d\eta} = \frac{1}{2}A\left\{\sin(2\pi ft+\phi)+\sin(2\pi 4ft+\phi)+\sin(2\pi\frac{f}{4}t+\phi)\right\} (1-\cos(2\pi\eta_{\text{force}}))(1-\cos(2\pi\xi_{\text{force}})) \quad (7.1)$$

where, $f = 7.76$ is taken from Jones (2007), who performed a linear stability analysis and found that the most unstable modes are observed at this frequency. The frequencies $f/4$ and $4f$ are included to cover a wider range of possible instabilities. The low-amplitude periodic forcing is implemented just upstream of the laminar separation point at x/c = 0.0295 and y/c = 0.182. In future, this forcing could be implemented practically via flow control techniques such as placing control jets or plasma actuators upstream of the separation with a motion similar to the employed force.

The performance of the airfoil can be determined from the lift and drag coefficients and the lift-to-drag ratio. Figure 7.1 shows a comparison of time-dependent lift coefficient between the uncontrolled (unforced) case and the controlled (forced) case. The results of the forced simulation shows a transient period between $t = 95$ and $t = 102$, then the lift coefficient sustains at a level above the maximum lift coefficient obtained by the unforced case. It is clear that the low-frequency mode has disappeared in the forced case. The lift coefficient oscillates around $C_L = 0.85$ with a very small peak-to-peak amplitude ≈ 0.03, while the lift coefficient of the uncontrolled case exhibited lower values than the controlled case with a large peak-to-peak oscillation amplitude ≈ 0.20. Figure 7.2 shows the effect of periodic forcing on the drag coefficient where it is clear that the drag coefficient is dramatically decreased due to the implementation of the periodic forcing, with markedly smaller fluctuations compared to the natural drag coefficient. The friction

drag coefficients obtained by the simulation with forcing exhibited a noticeable increase compared to the unforced case, as shown in Figure 7.3.

The time-averaged force coefficients for both cases are given in Table 7.1 which shows that the lift coefficient is increased from 0.727 in the unforced case to 0.856, meaning that the periodic forcing increases the lift coefficient by about 17.7%. The performance of the airfoil is also increased due to the enormous reduction of the drag coefficient, from 0.0848 in the unforced case to about 0.0476, i.e. a drag reduction of 43.9%. This leads to a large increase in the lift-to-drag ratio of 110% and thus proves that forcing transition, by adding periodic forcing significantly enhances the performance of the present airfoil near stall. It is useful to compare the effect of periodic forcing on the flow near stall with the flow at lower incidence, for example with the DNS study of Jones (2007) at incidence of 5°, where the Reynolds number is the same as in the present study (Re = 50,000). Jones observed that the lift coefficient was not increased by adding the forcing and in fact it decreased slightly, while the drag coefficient was decreased by 17.9% and the lift-to-drag ratio was increased by about 22.7%, which is in agreement with the observation of Zaman *et al.* (1987), who found that the lift coefficient decreased while the lift-to-drag ratio increased when he applied an external acoustic excitation technique to control the separation of flow around LRN-1007 airfoil at low Reynolds number (Re = 40,000) both for a range values of pre-stall incidences (α = 4°, 6°, 8°, 10°and 12°) and near the stall incidence (α = 15°), whereas the lift coefficient increased when the incidence was above the stall (α = 18° and 22°). Similar observations were found by Bar-Server (1989), where the effectiveness of forcing starts at the onset of the stall and increases as the post-stall incidence increases, and by Wong and Rinoie (2009) who used burst control plates to delay stall.

Table 7.1 Time-averaged lift and drag coefficients for the unforced and forced LES simulations.

Simulation	C_L	C_D	C_L/C_D	C_{df}
Unforced	0.727	0.0848	8.57	0.0055
Forced	0.856	0.0476	17.98	0.0071

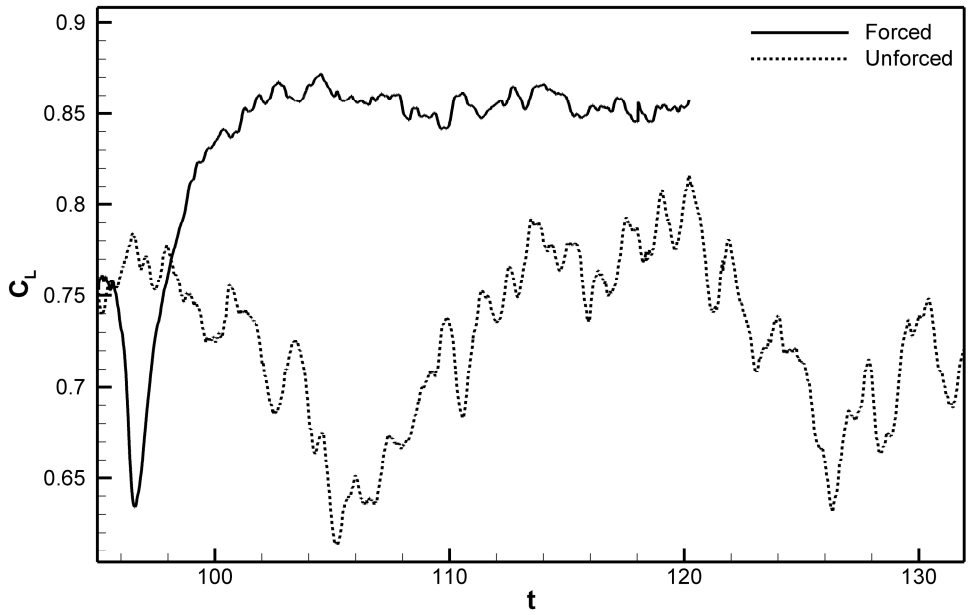

Figure 7.1 Effect of adding the low-amplitude periodic forcing on the lift coefficient.

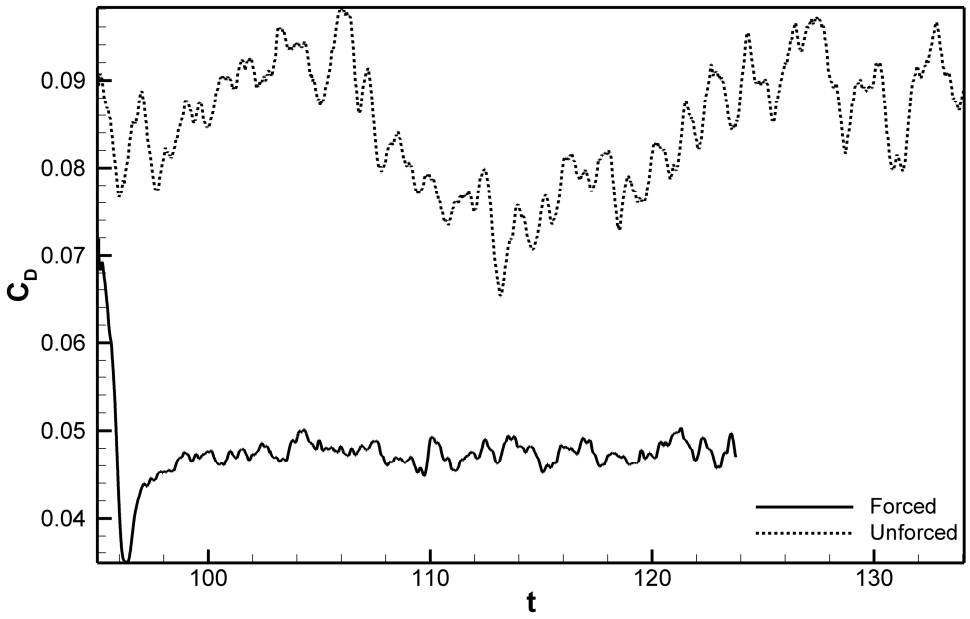

Figure 7.2 Effect of adding the low-amplitude periodic forcing on the drag coefficient.

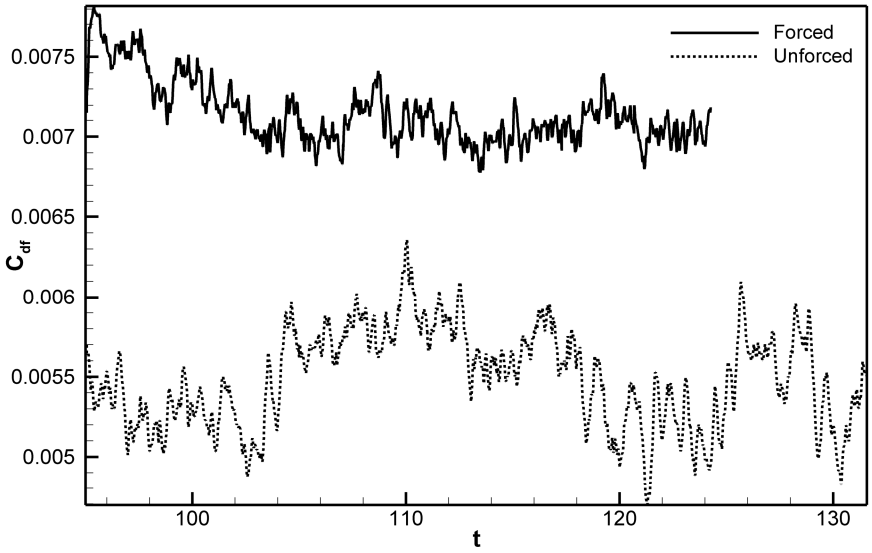

Figure 7.3 Comparison of the time variation of friction drag coefficient between the controlled (forced) case and uncontrolled (unforced) case.

The behaviour of the flow field in the unforced case was demonstrated in section 4.3, where the flow has irregular low-frequency flow oscillations and the airfoil was observed to be switching between stalled and non-stalled conditions. By contrast, the flow in the forced case is always attached to the airfoil surface with very low unsteadiness and with a short laminar separation bubble. This is clearly seen from the time- and span-averaged pressure and lift coefficients along the airfoil surface as seen in figures 7.4 and 7.5, respectively. For these figures, two cases were picked from the unforced simulation where the time-averaged flow field showed fully separated flow in the first case ($105.6 \leq t \leq 107.2$) and a laminar separation bubble near the leading edge in the second case taken in the interval of ($116.8 \leq t \leq 118.4$). In order to show the effectiveness of the periodic forcing, two more cases were picked from the forced (controlled) simulation at the same time intervals of the unforced cases. Figure 7.4 shows that the surface pressure distributions of the forced cases are almost identical, with a large increase in the suction peak near the leading edge on the upper side of the airfoil, and a noticeable shrinking of the plateau, which is due to the more rapid transition to turbulence. The maximum suction pressure ($-C_p$) increases in the first case from 1.794 to 3.090, while it increases in the second case from 2.142 to 3.110. This means that the suction pressure increased by 72.2% and 45.2% in the first and second controlled cases, respectively.

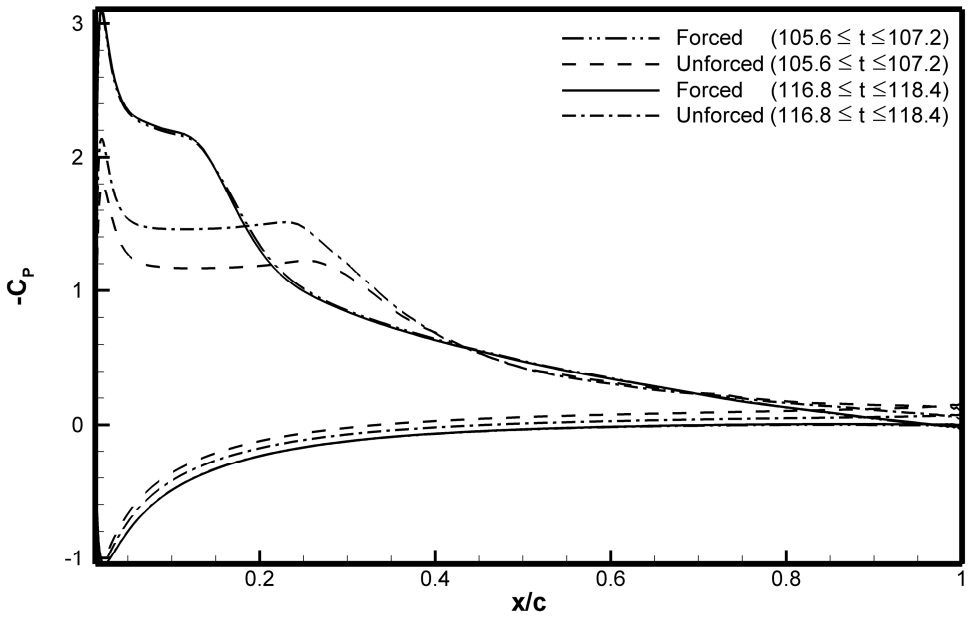

Figure 7.4 Comparison of pressure coefficient between uncontrolled (forced) and controlled (unforced) cases.

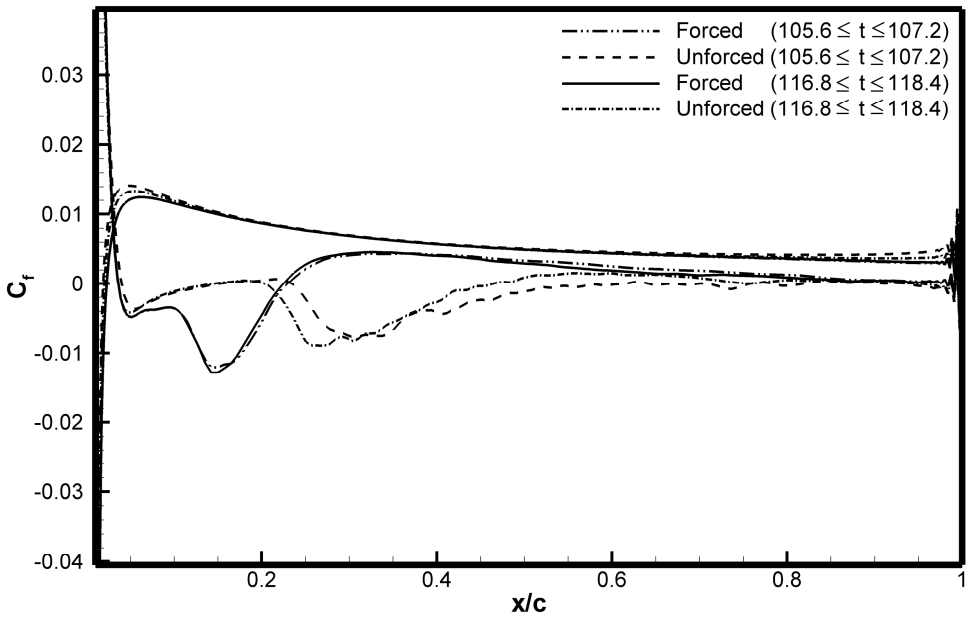

Figure 7.5 Comparison of skin-friction coefficients between uncontrolled (forced) and controlled (unforced) cases.

Figure 7.5 shows the skin-friction coefficient for the unforced and forced cases, where the influence of the periodic forcing is obvious. When examining this figure, it is

clear that the separation point remains fixed, while the large impact of the periodic forcing is seen at the reattachment points, which are shifted upstream from x/c = 0.615 to x/c = 0.23 in the first case and from x/c = 0.465 to x/c = 0.225 in the second case. This leads to a 66.3% and 56.0% reduction of the length of the laminar separation bubble in the first and second controlled cases, respectively. Figure 7.6 shows the streamwise distribution of y-maximum turbulence kinetic energy with x/c location for the two cases, where the turbulent kinetic energy is averaged along the span and it defined as $K = 0.5\left(\overline{u'u'} + \overline{v'v'} + \overline{w'w'}\right)$. The beginning of the transition area can be determined from the abrupt increase of the maximum turbulence kinetic energy distribution. It is obvious that the transition is shifted upstream in the forced case.

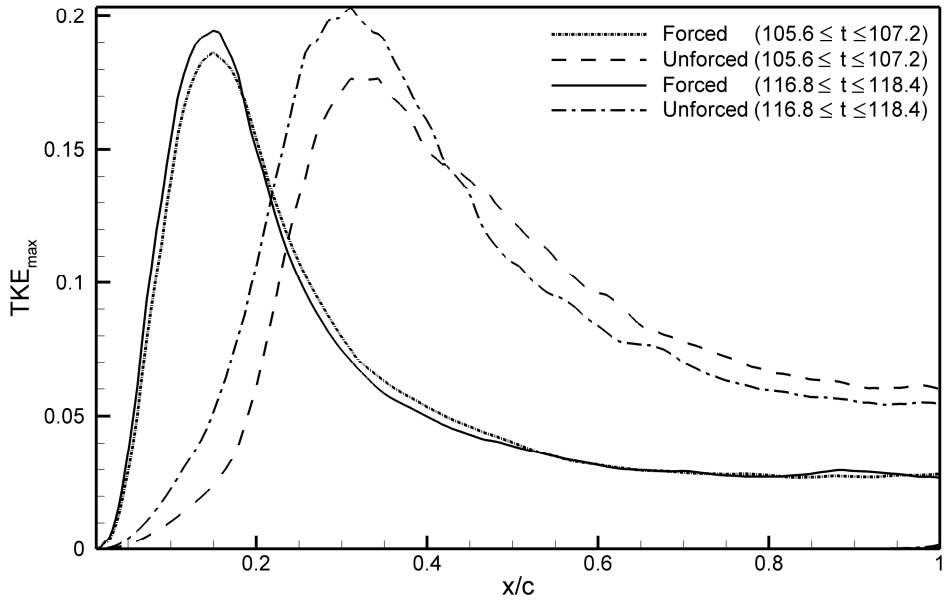

Figure 7.6 Streamwise distribution of the maximum turbulent kinetic energy for the two forced cases in comparison with the unforced cases.

Figures (7.7) and (7.8) show the streamline patterns of the span- and time-averaged streamwise velocity over the interval of $105.6 \leq t \leq 107.2$ for the unforced and forced cases, respectively. Comparing figures (7.7) and (7.8) shows the effectiveness of the periodic forcing, in which the periodic forcing completely changes the condition of the flow from a fully stalled to fully reattached flow with the formation of a short laminar separation bubble of approximately 17% chord length located near the leading edge.

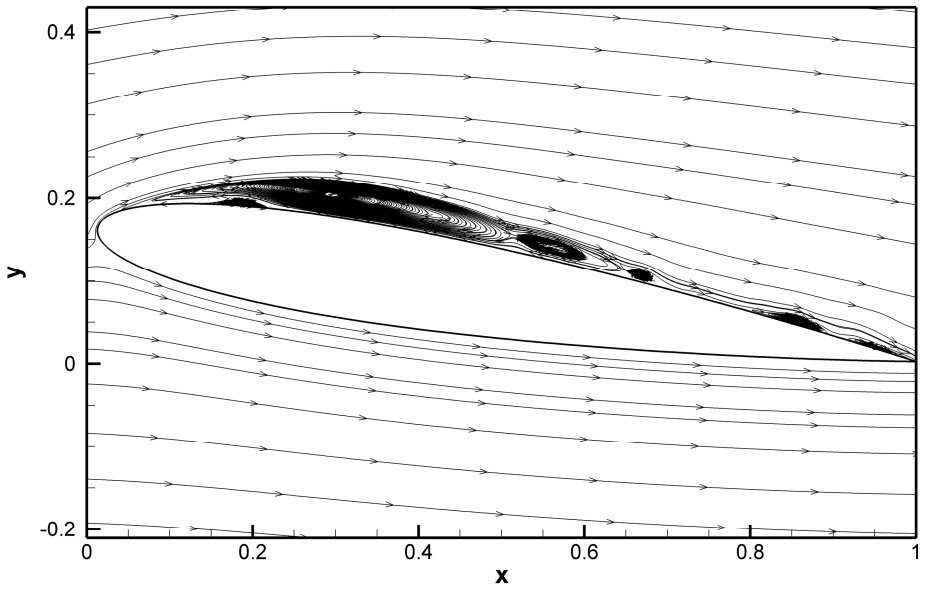

Figure 7.7 Streamline patterns of the span- and time-averaged flow without periodic forcing over the interval ($105.6 \leq t \leq 107.2$).

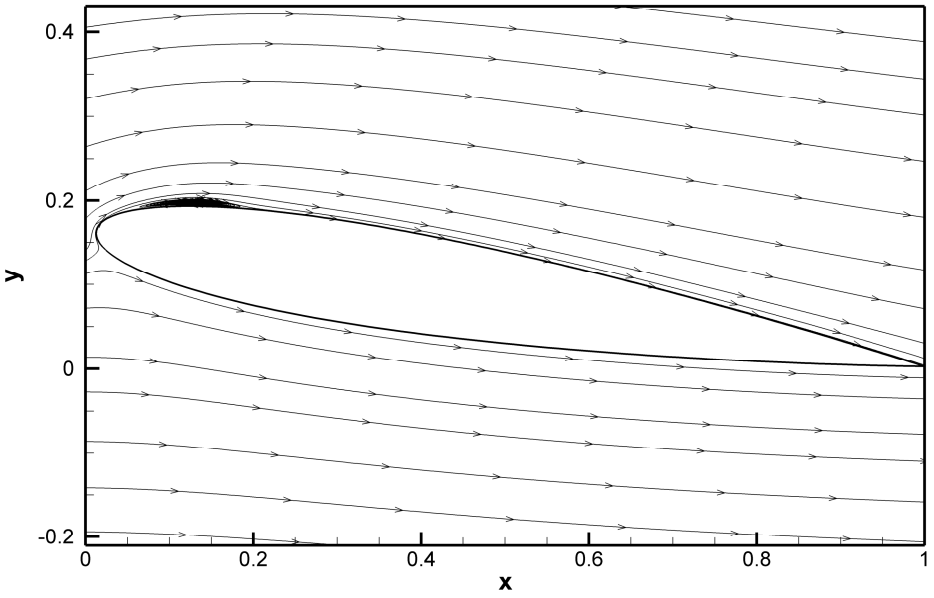

Figure 7.8 Streamline patterns of the span- and time-averaged flow with periodic forcing over the interval ($105.6 \leq t \leq 107.2$).

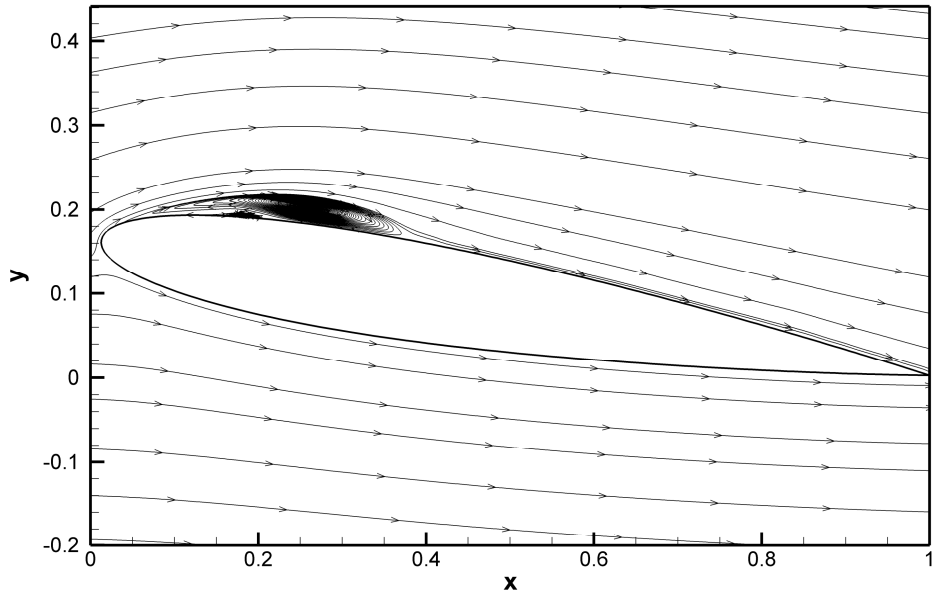

Figure 7.9 Streamline patterns of the span- and time-averaged flow without periodic forcing over the interval ($116.8 \leq t \leq 118.4$).

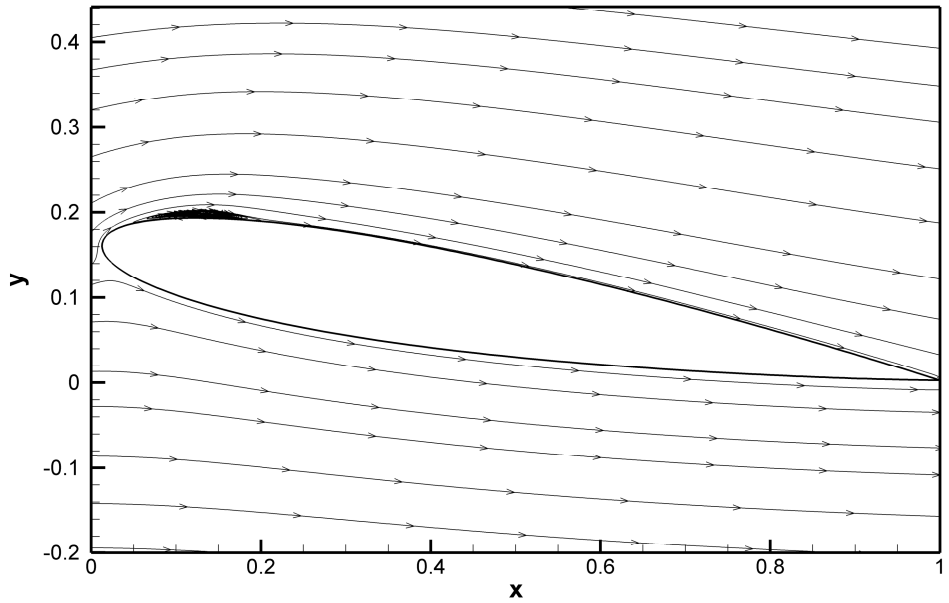

Figure 7.10 Streamline patterns of the span- and time-averaged flow with periodic forcing over the interval ($116.8 \leq t \leq 118.4$).

The shape and size of the laminar separation bubble before and after applying the periodic forcing can be investigated from the streamline patterns computed from the time- and span-averaged velocity as shown in Figure 7.9 (unforced case, over the interval $116.8 \leq t \leq 118.4$) and Figure 7.10 (forced case, over the same interval). These figures show that not only is the length of the bubble decreased, but also the thickness of the bubble is markedly decreased. Figure 7.11 shows a comparison of the displacement thickness between the forced and unforced case over the interval $116.8 \leq t \leq 118.4$, where it is clear that the displacement thickness on the upper surface of the airfoil obtained from the forced case is lower than for the unforced case, with a noticeable difference starting from the separation point. The reduced boundary layer thickness is an indication of the improvement in airfoil performance.

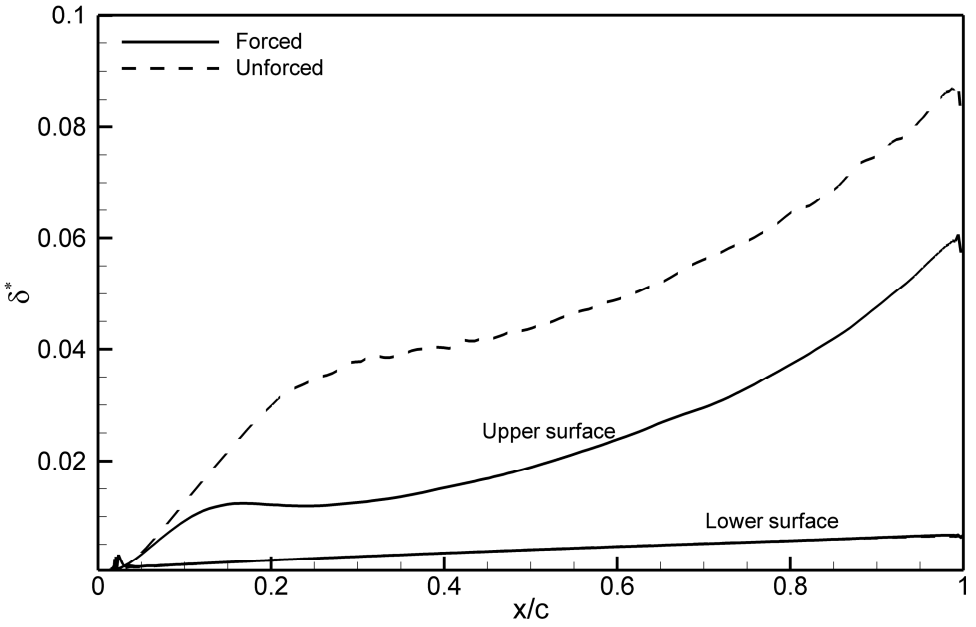

Figure 7.11 Comparison of displacement thickness between the forced and unforced cases forcing over the interval ($116.8 \leq t \leq 118.4$)

As explained earlier, flow separation is characterised by the enlargement of the thickness of the rotational flow just downstream of the separation point with an associated increase of the normal velocity component. These flow separation characteristics can be seen in the instantaneous spanwise vorticity contours and the contours of the normal velocity components which are displayed in Figures 7.12 to 7.15. The instantaneous

spanwise vorticity contours of the forced case (Figure 7.13) show a much thinner boundary layer than for the unforced case (Figure 7.12), which has an irregular boundary layer with a variable thickness on the upper surface of the airfoil and an increase of the boundary layer thickness near the trailing edge. Figures 7.14 and 7.15 show contours of the normal velocity around the airfoil at t = 123.2, using 20 levels between -0.2 and 0.2 from the unforced and forced cases respectively. When comparing these figures, it is clearly seen that the magnitude of the normal velocity in the unforced case is reduced when the forcing is activated. This is a consequence of the effective suppression of the flow separation.

Three-dimensional isosurfaces of the second invariant of the velocity gradient for the unforced and forced cases are illustrated in Figures 7.16 and 7.17. The relatively large area of the laminar flow observed in the unforced case (Figure 7.16) is dramatically decreased by the effect of the periodic forcing, as shown in Figure 7.17. Additionally, there is some evidence of two-dimensional shedding in the forced case, even though the forcing is three-dimensional.

It can be concluded from the results of this section that the benefit of periodic forcing is to remove the low-frequency flow oscillation, and as a consequence improve the aerodynamic characteristics of the low-Reynolds number airfoil. It has been seen that the enlargement of the turbulent boundary layer that usually occurs after separation and the associated increase of the normal velocity component are reduced sharply when the periodic forcing is added to force an early transition of the boundary layer and shorten the separation bubble.

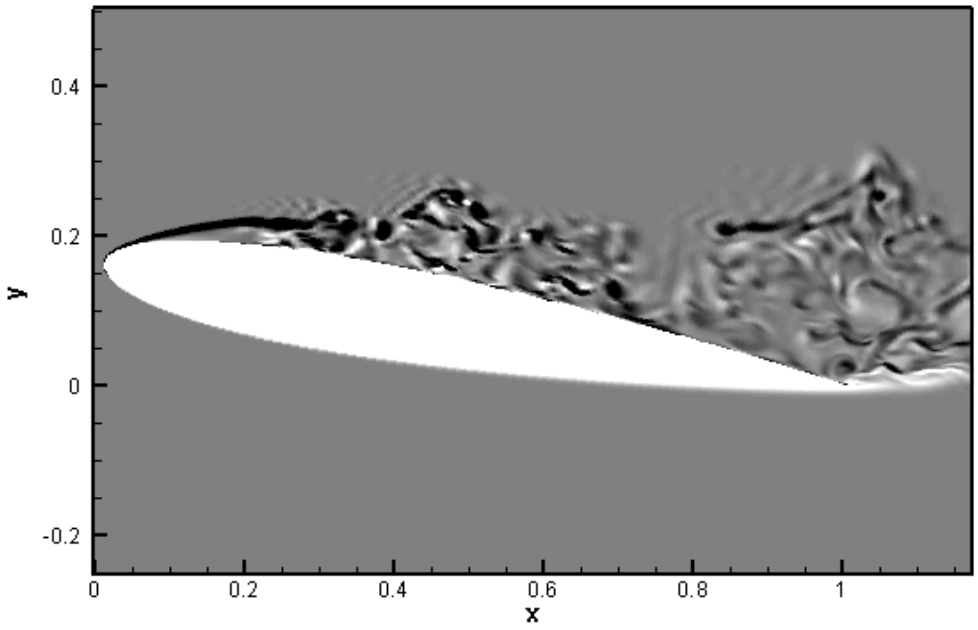

Figure 7.12 Instantaneous spanwise vorticity contours obtained from LES without forcing using 50 levels from -50 to 50 (at t = 108.5).

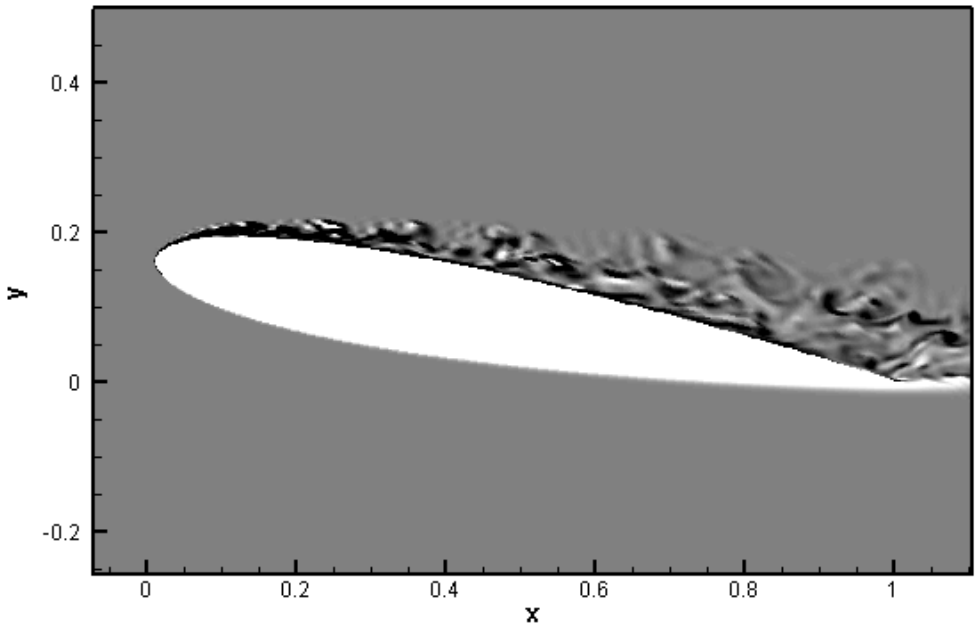

Figure 7.13 Instantaneous spanwise vorticity contours obtained from LES with forcing at t = 108.5, using 50 levels {-50 : 50}.

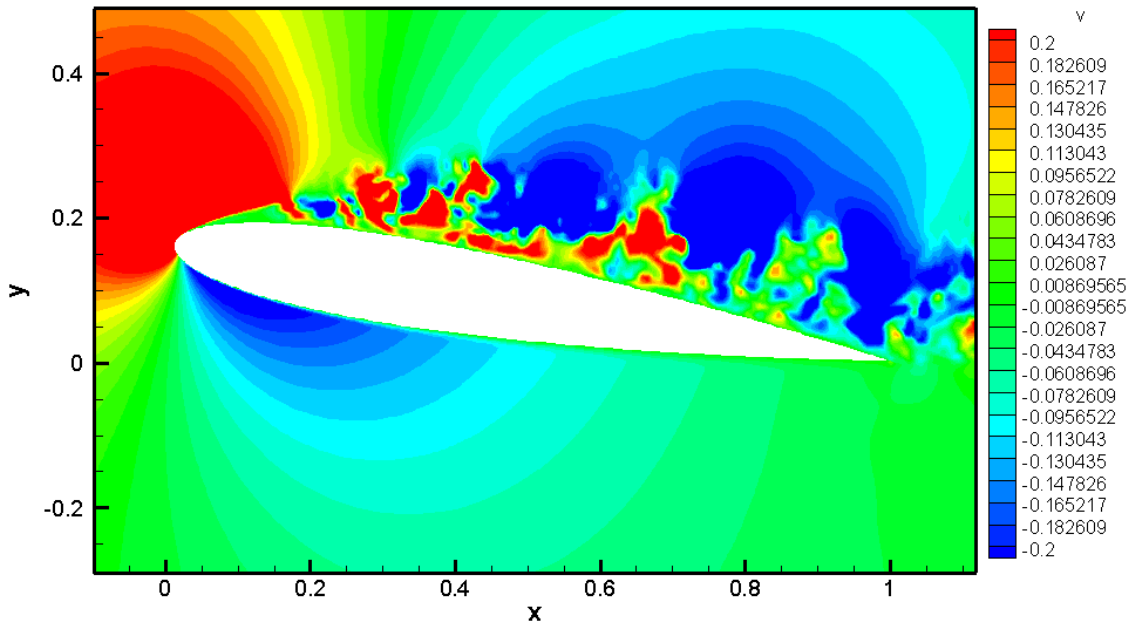

Figure 7.14 Instantaneous vertical velocity contours obtained from LES without periodic forcing at *t* = 123.2.

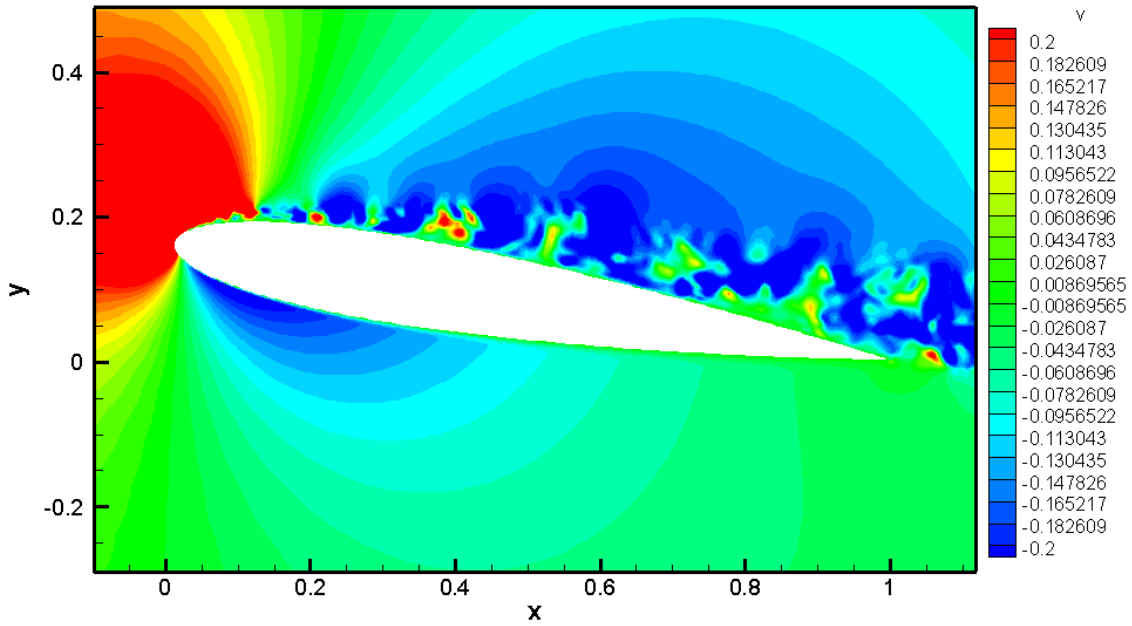

Figure 7.15 Instantaneous vertical velocity contours obtained from LES with periodic forcing at *t* = 123.2.

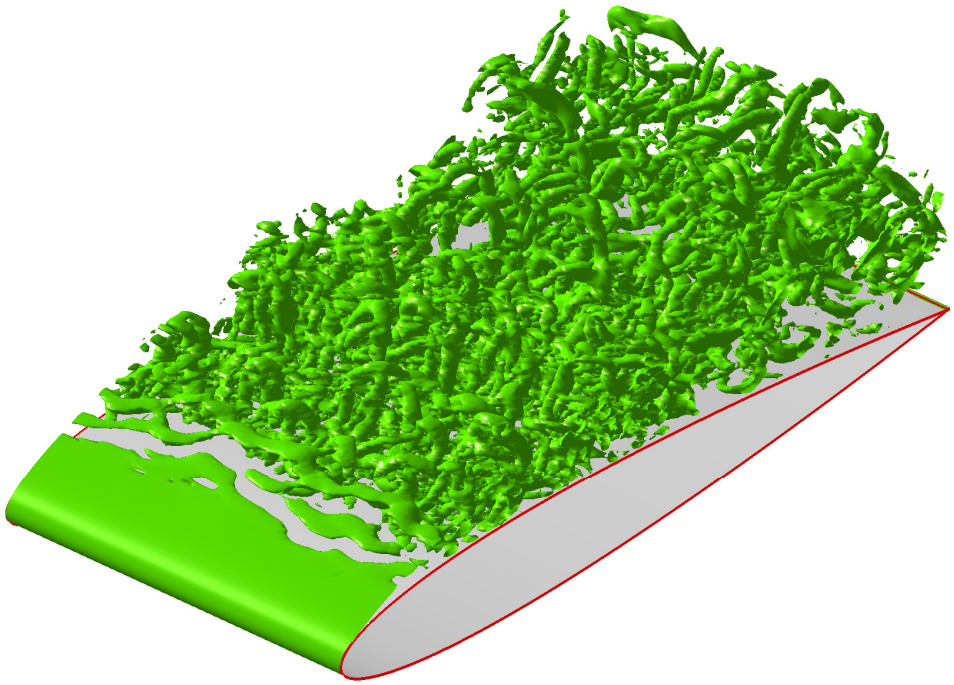

Figure 7.16 Unforced LES solution for three-dimensional isosurface of second invariant of the velocity gradient at Q = 300.

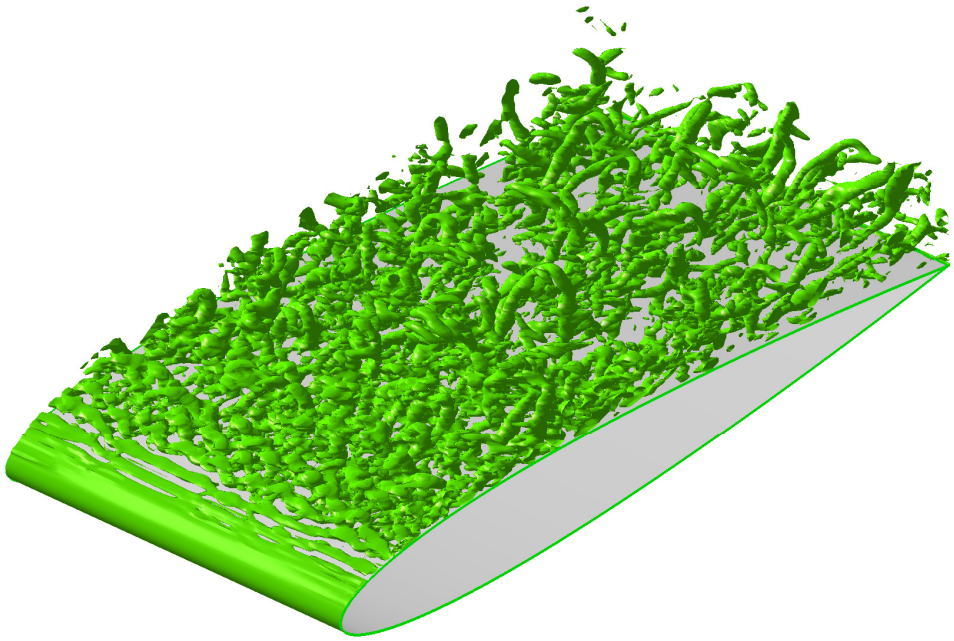

Figure 7.17 Forced LES solution for three-dimensional isosurface of second invariant of the velocity gradient at Q = 300.

7.2 Control of the flapping around low-Reynolds number airfoil with zero incidence (Re = 50,000, M = 0.8)

A flapping oscillation was observed by Jones (2007) when he performed two-dimensional DNS of a flow around an NACA-0012 airfoil at zero incidence. He found that the boundary layers switched between fully separated and fully attached conditions. This phenomenon occurs at a low-frequency and at certain Reynolds and Mach numbers. Jones determined that the range of Reynolds numbers and Mach numbers for which of flapping occurred increased as the Reynolds number decreased and as the Mach number increased.

The flapping phenomenon causes the lift coefficient to severely fluctuate around zero with high amplitude and low-frequency. The overall performance of the airfoil is also affected since drag coefficient is increased. For example, two dimensional filtered Navier-Stokes calculations of a flow at a Reynolds number of 50,000 and Mach number of 0.8 was carried out for grid of 1180 × 258. The simulation reveals a peak-to-peak variation of C_L of around 0.6 (Figure 7.18), with a low-frequency ($f \approx 0.07$), whereas the drag coefficient oscillates around a mean of 0.055 as shown in Figure 7.19.

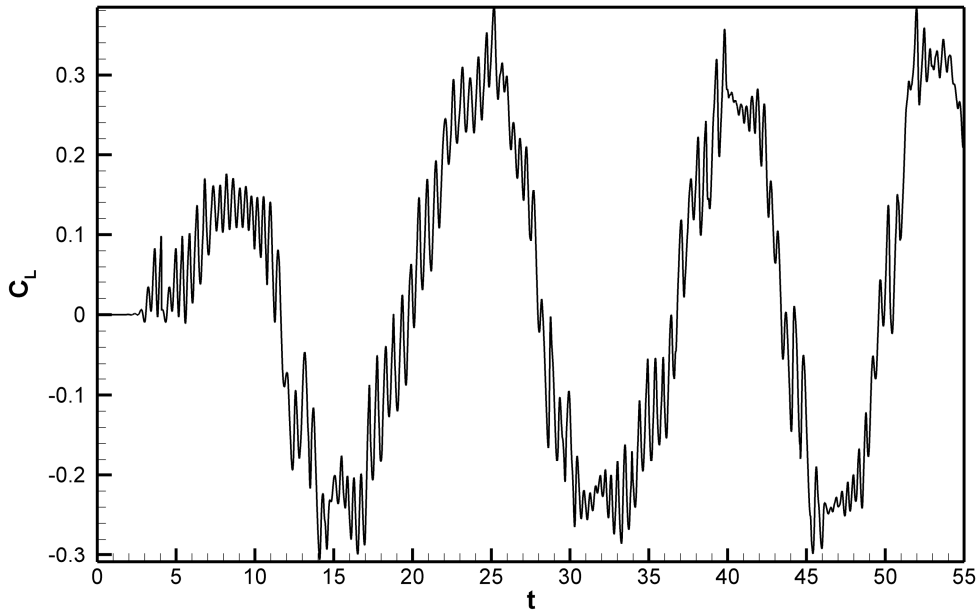

Figure 7.18 Lift coefficient of NACA-0012 airfoil at zero incidence at a Reynolds number of 50,000 and Mach number of 0.8, showing the oscillation of lift coefficient with low-frequency (flapping).

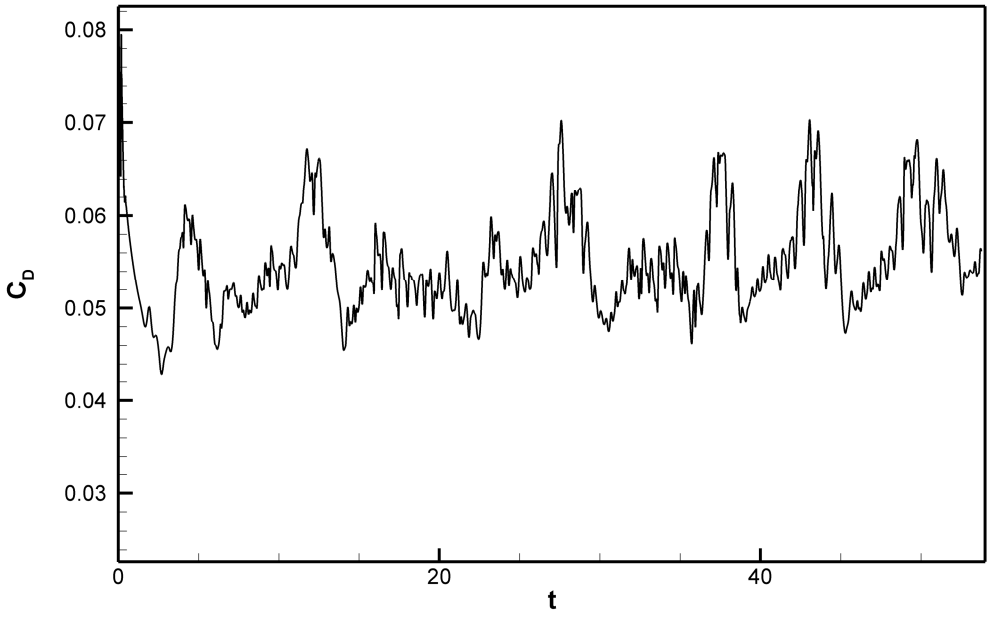

Figure 7.19 Drag coefficient of NACA-0012 airfoil at zero incidence at a Reynolds number of 50,000 and Mach number of 0.8.

Figure 7.20 shows contours of the averaged streamwise velocity at $43.4 \leq t \leq 44.8$, $46.2 \leq t \leq 47.6$ and $51.8 \leq t \leq 53.2$. This figure clearly shows the flapping phenomenon. At $43.4 \leq t \leq 44.8$ the flow is largely separated from the upper surface whereas only a small separated region is present on the lower surface. At $46.2 \leq t \leq 47.6$ the flow detaches symmetrically from the upper and lower surface of the airfoil while the flow separation moves to the lower surface at $51.8 \leq t \leq 53.2$.

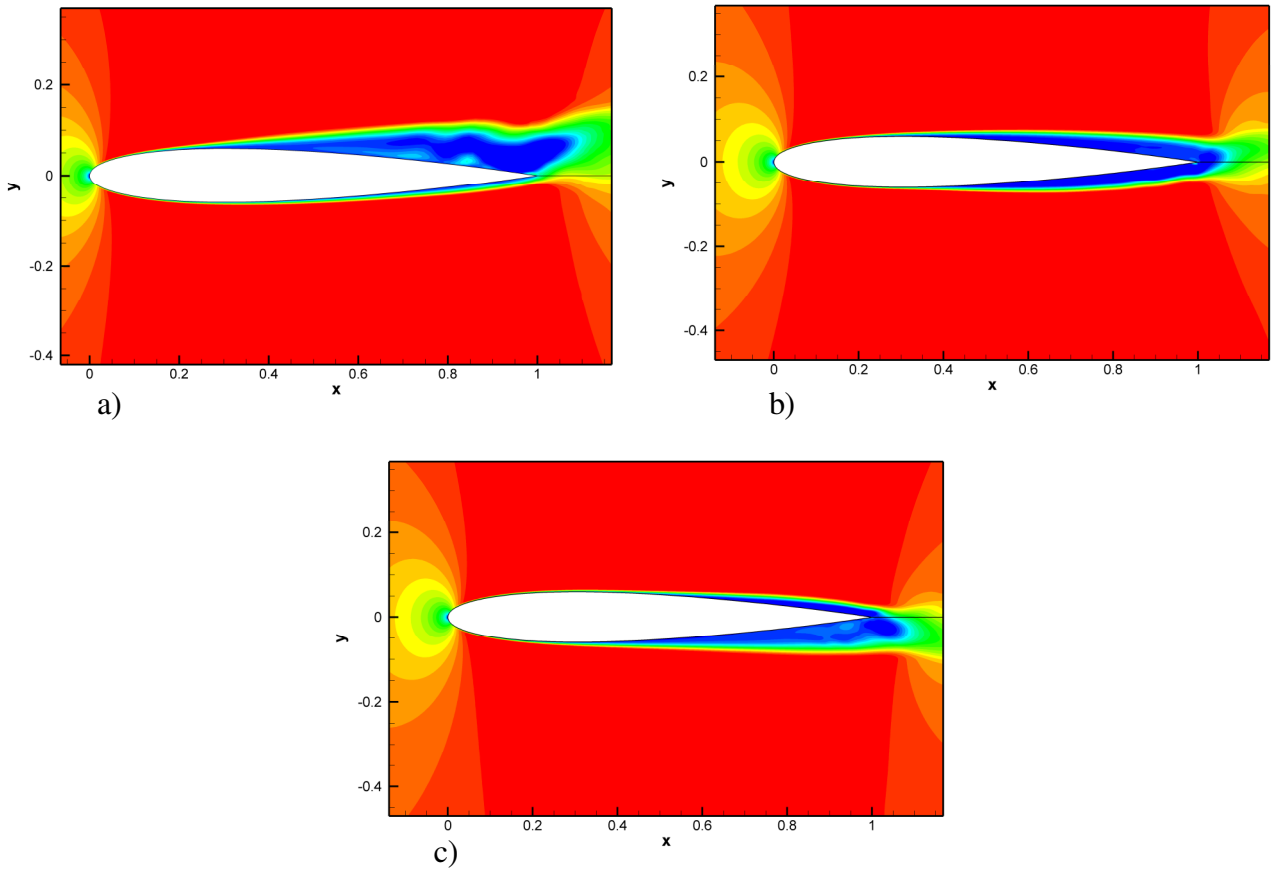

Figure 7.20 Averaged streamwise velocity contours for a flow around an NACA-0012 airfoil at Reynolds number of 50,000 and Mach number of 0.8 using 20 levels from 0 to 1 at a) $43.4 \leq t \leq 44.8$ b) $46.2 \leq t \leq 47.6$ and c) $51.8 \leq t \leq 53.2$, showing the flow behaviour of the flapping phenomenon.

The flapping phenomenon can also be seen by plotting the averaged pressure and Mach number contours at $46.2 \leq t \leq 47.6$ and $51.8 \leq t \leq 53.2$ as shown in Figures 7.21 and 7.22 which show that the flow is transonic with supersonic flow over the lower surface at $46.2 \leq t \leq 47.6$ and over the upper surface at $51.8 \leq t \leq 53.2$.

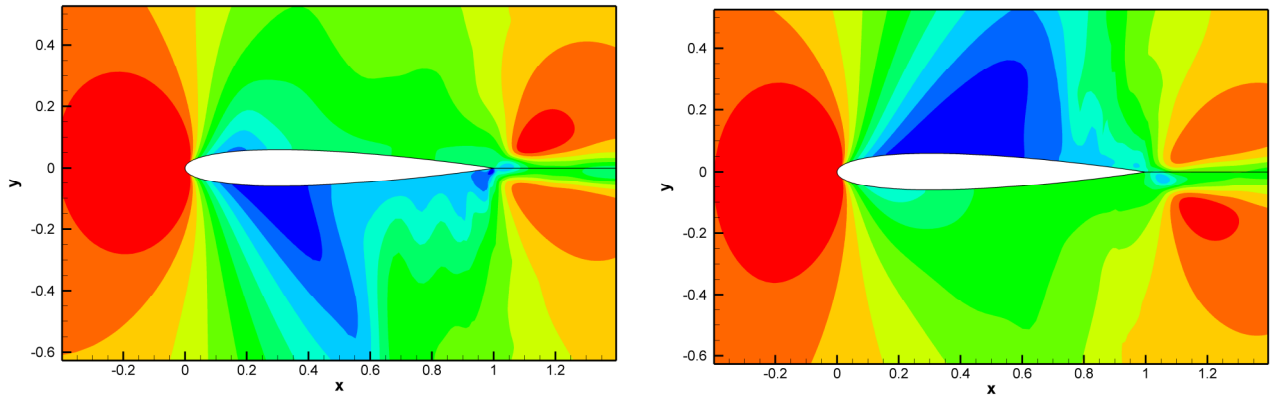

Figure 7.21 Averaged pressure contours for an NACA-0012 airfoil at a Reynolds number of 50,000 and Mach number of 0.8 using 10 levels from 0.8 to 1.2 at a) $46.2 \leq t \leq 47.6$ and b) $51.8 \leq t \leq 53.2$.

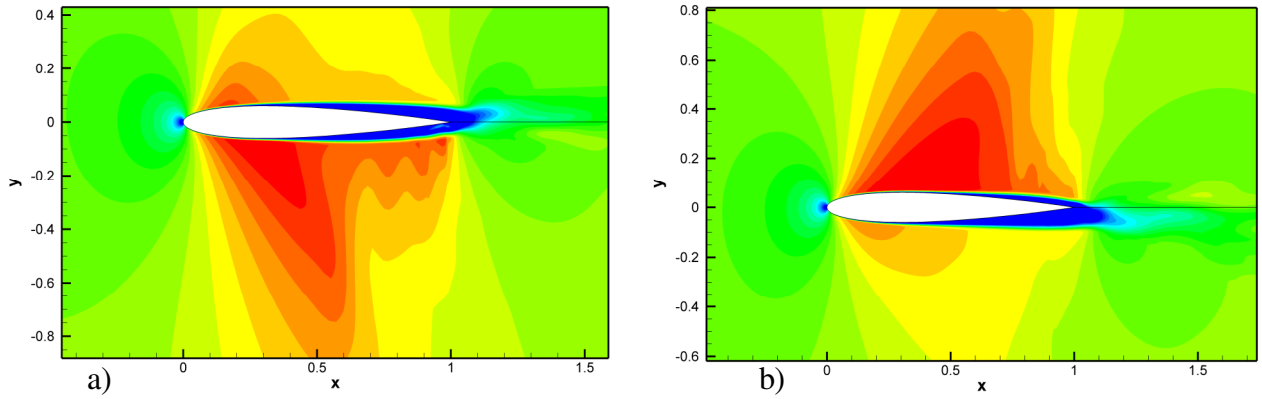

Figure 7.22 Averaged local Mach number contours for an NACA-0012 airfoil at a Reynolds number of 50,000 and Mach number of 0.8 using 20 levels from 0.4 to 1.3 at a) $46.2 \leq t \leq 47.6$ and b) $51.8 \leq t \leq 53.2$, showing the supersonic areas around the airfoil.

With the objective of reducing or entirely eliminating the flapping behaviour, different forcing frequencies were tested for a 2D grid of 1180 × 258 points around a NACA-0012 airfoil. Forcing was applied inside the boundary layer just upstream of the flow separation point on the upper and lower surfaces of the airfoil at $x/c = 0.24$ and $y/c = 0.065$ for the former and at $x/c = 0.24$ and $y/c = -0.065$ for the latter. A parametric study was performed to find the optimum forcing frequencies that give a solution without flapping. The starting point to search for suitable frequencies was the solution for the flapping (baseline) case where no forcing is added to the simulation. Figure 7.23 shows a spectrum of the lift fluctuations, in which the low-frequency oscillation is clearly found at $f \approx 0.07$, whereas there is another noticeable peak at $f \approx 1.95$, which is connected with the vortex shedding phenomenon. A series of 2-D filtered Navier-Stokes calculations were therefore performed using different frequencies. A simulation with a forcing frequency of $f = 1.95$ exhibits a solution with a different flow behaviour than the natural flow, and the

flapping is completely removed. Figure 7.24 shows a comparison between the unforced and forced short-time averaged streamwise velocity contours for two different time ranges, where it is clear that the severe separation of the boundary layer is removed by forcing. The resulting averaged boundary layer exhibits a symmetric flow separation with a noticeable shrinking in thickness compared with the unforced case.

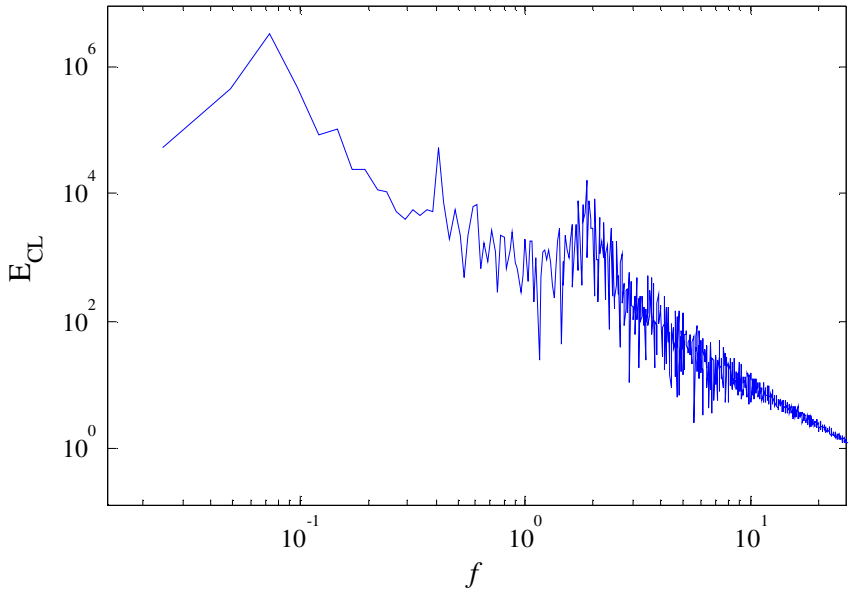

Figure 7.23 Energy spectra for unforced lift coefficient of NACA-0012 at zero incidence (Re = 50,000 and M = 0.8).

The effect of the forcing frequency on the solution was investigated by picking two more frequencies; f =1.6 and f = 2.2. For each frequency, the 2-D filtered Navier-Stokes simulation was restarted from t = 0. Figure 7.25 shows a comparison of lift coefficient between the unforced solution and the forced solutions using three forcing frequencies. At f =1.95, the lift coefficient oscillates periodically around a mean of zero with a peak-to-peak amplitude of $\Delta C_L \approx 0.075$, which is an order of magnitude lower than for the baseline case ($\Delta C_L \approx 0.6$). Also the low-frequency mode has completely vanished which indicates the disappearance of flow flapping. Figure 7.25 also shows that the high fluctuations of lift coefficient are suppressed and completely removed when the lower frequency (f =1.6) is used, however it is also observed that the mean lift coefficient has a long transient time with a mean value below zero ($C_L \approx -0.14$) which means that the flow is asymmetrically separated around the airfoil. It is also noticeable that the behaviour of the lift coefficient exhibited more irregularity than the forced case when f = 1.95 is used.

On the other hand, the higher frequency $f = 2.2$ shows an increase of the mean lift and a sustained low-frequency different to the original flapping mode. It is noticeable that the peak-to-peak amplitude of the lift coefficient obtained by the simulations with forcing is markedly decreased compared with the unforced case. It is interesting that a non-zero mean lift develops for some forcing frequencies, despite the fact that the airfoil and the forcing are symmetric. In these cases the flow seems to lock into a non-symmetric solution. Figure 7.26 shows the effect of forcing on the drag coefficient, where all the forced cases reveal a drag coefficient with a significantly lower peak-to-peak amplitude compared to the unforced case as well as a noticeable reduction in the mean ($C_{Dmean} \approx 0.026$), which can be considered an improvement of the airfoil performance. The reduction of the drag coefficient is mainly from the pressure drag coefficient component while the friction drag coefficient oscillates around the mean of the unforced case without low-frequency oscillation as shown in Figure 7.27.

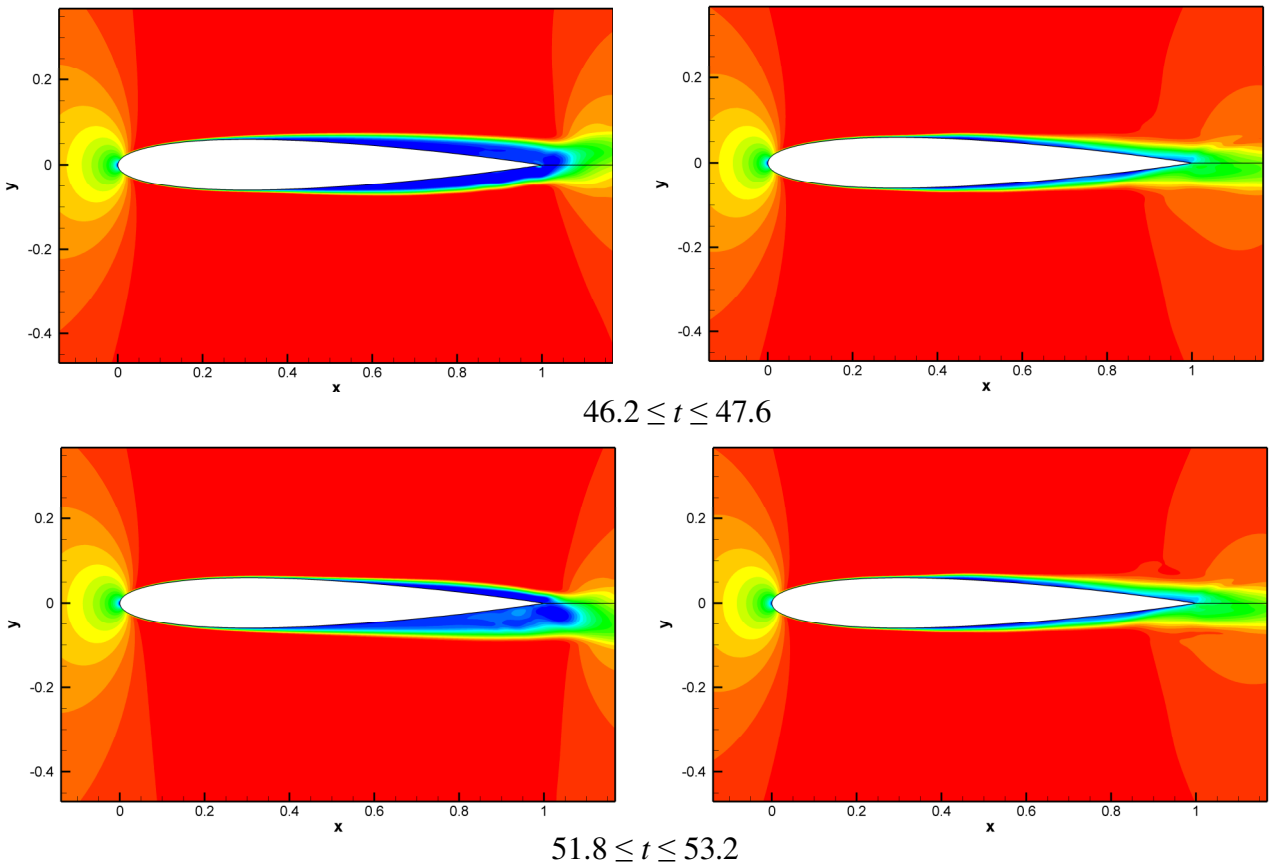

Figure 7.24 Comparison of averaged streamwise velocity contours at two different times between the unforced case (left side) and forced case with a frequency of f = 1.95 (right side) using 20 contour levels in the range from 0 to 1, showing how the flapping phenomenon is removed by forcing.

Energy spectra for the three forced cases are shown in Figure 7.28. It is clearly observed that the forcing frequencies are the dominant frequencies. There are two harmonics with equal amplitude in the lowest frequency forced case while there is only one harmonic in the forced case with f = 1.95. Figure 7.28 also shows that the highest frequency case has several frequencies and high frequency fluctuations compared with the other forced cases. It is interesting to note that the forcing frequency of the simulation with f = 2.2 is not the dominant frequency as was the case in the other forced cases. A noticeable low frequency ($f \approx 0.036$) with high amplitude is observed in the simulation with a forcing frequency of f = 2.2. However, this frequency is apparently not fully resolved which may be attributed to the insufficient sample length. In order to resolve this frequency, the simulation should be run further until the energy spectra reveal a clear spike at this frequency and this probably need another 30 to 60 time steps which will cost about 7300 to 14600 CPU time.

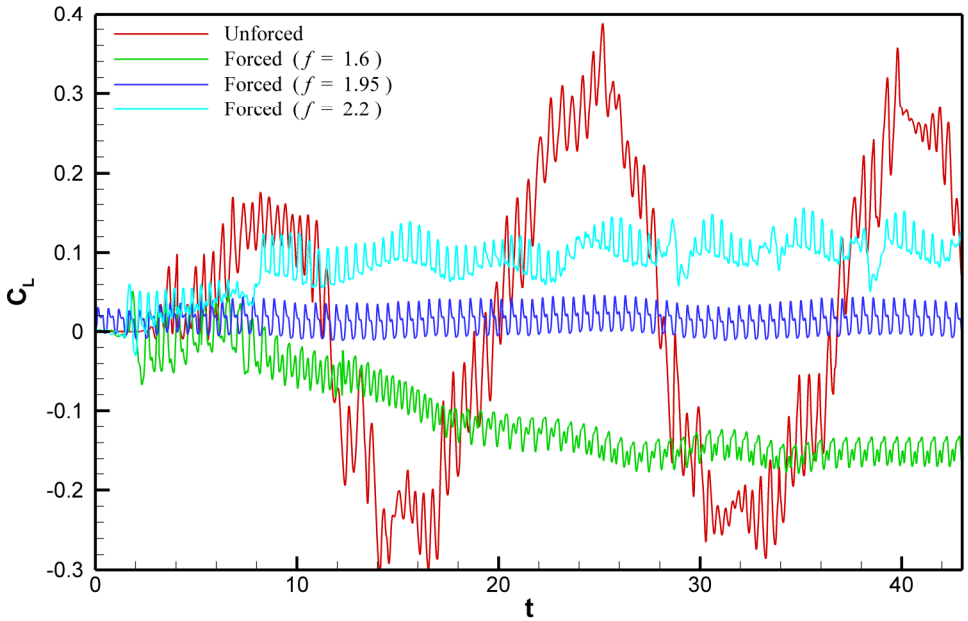

Figure 7.25 Effect of forcing frequency on the lift coefficient obtained from 2-D filtered Navier-Stokes simulations (Re = 50,000, M = 0.8 and α = 0°).

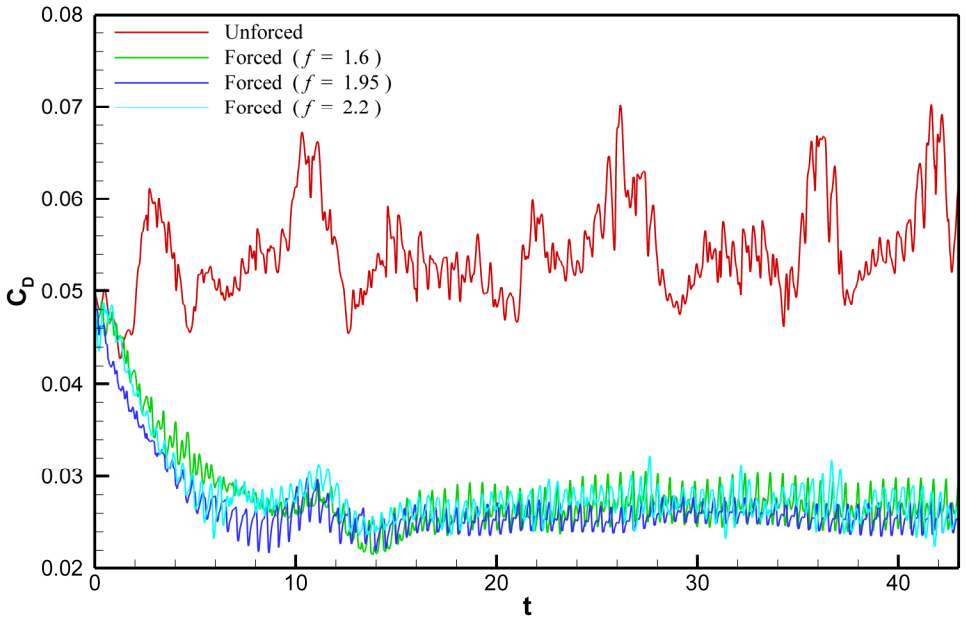

Figure 7.26 Effect of forcing frequency on the time dependence drag coefficient obtained from 2-D filtered Navier-Stokes simulations (Re = 50,000, M = 0.8 and $\alpha = 0°$).

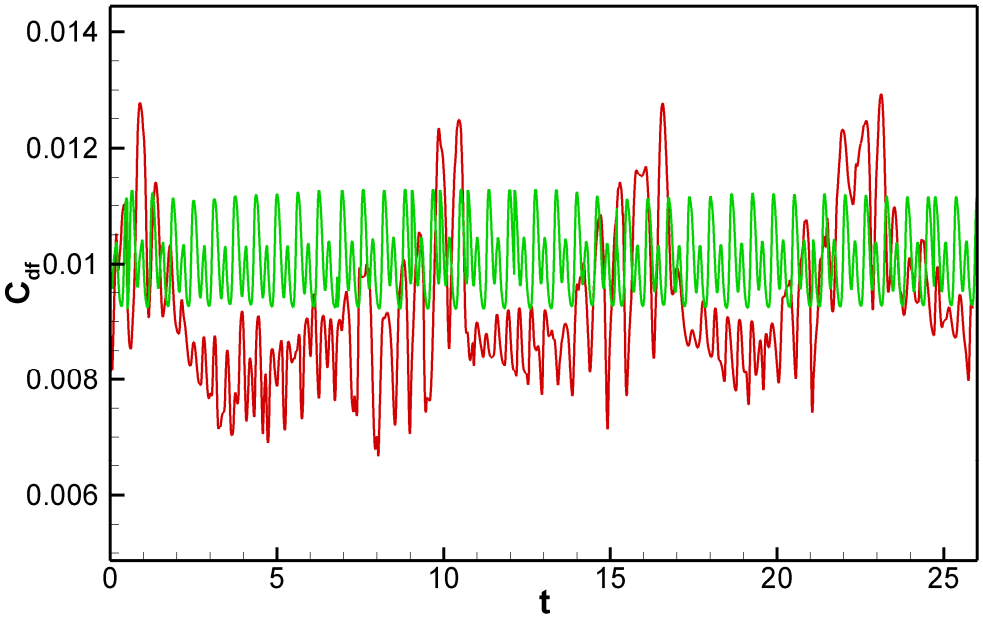

Figure 7.27 comparison of friction drag coefficient between the forced and unforced solution obtained from 2-D filtered Navier-Stokes simulations (Re = 50,000, M = 0.8 and $\alpha = 0°$).

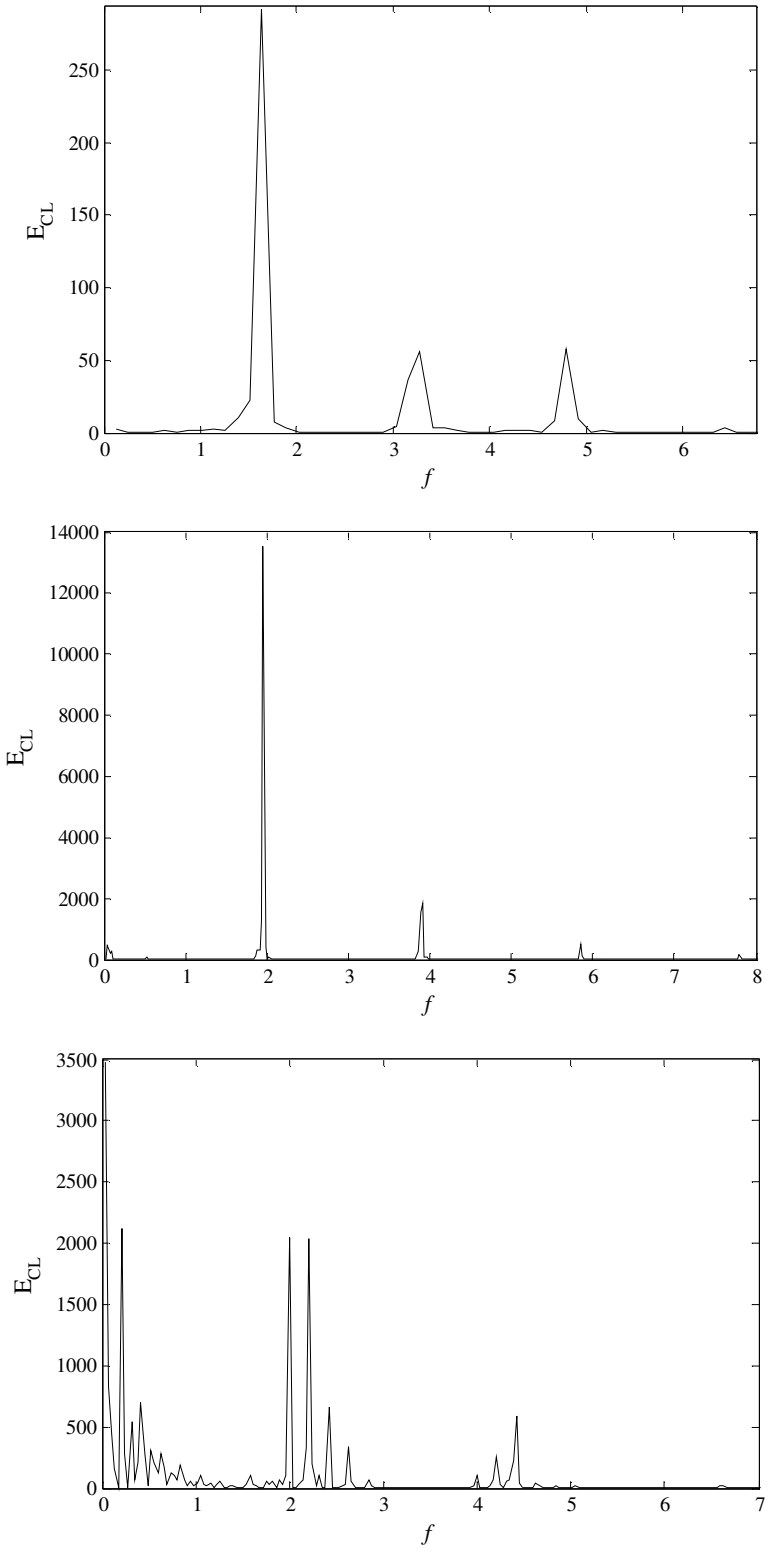

Figure 7.28 Energy spectra for the forced 2-D filtered Navier-Stokes simulations with frequencies (from top) of f = 1.6, 1.95 and 2.2.

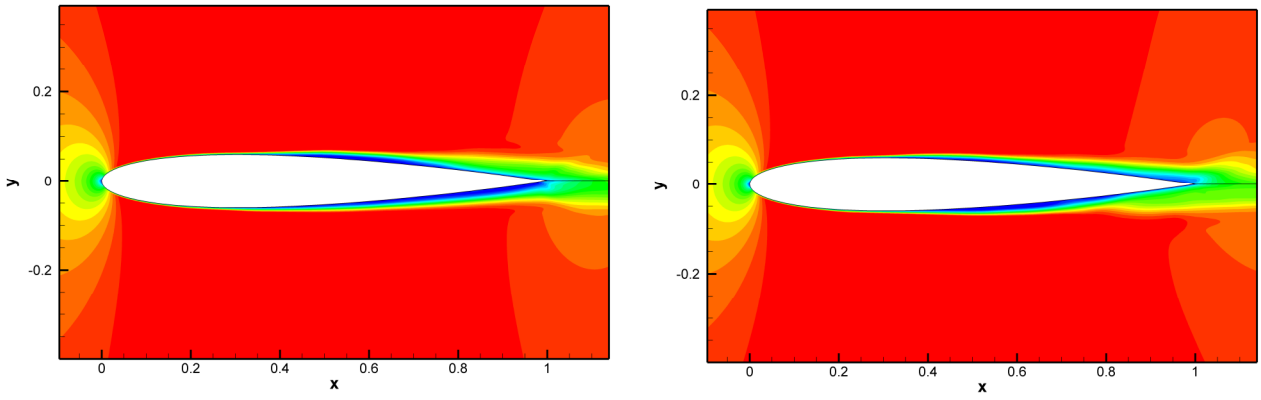

Figure 7.29 Comparison of averaged streamwise velocity between the two forced cases with a frequency of a) $f = 2.2$ and b) $f = 1.6$, using 20 contour levels in the range from 0 to 1.

The non-zero lift coefficient obtained for the NACA-0012 airfoil at $\alpha = 0°$ is surprising as it indicates that lift can be generated by periodic forcing of a symmetrical airfoil at zero incidence (It was checked that the forcing was symmetric). Figure 7.29 shows a comparison of averaged streamwise velocity between the forced cases where the lift is non-zero. It can be observed from this figure that a long LSB is located on the upper and lower surfaces of the airfoil for the forced cases with $f = 2.2$ and $f = 1.6$, respectively.

It can be concluded that low-frequency airfoil flapping can be completely eliminated by periodic forcing with a frequency of $f = 1.95$, while the periodic forcing can generate a non-zero lift when lower or higher frequencies are forced. The solutions are very sensitive to the forcing frequencies with a narrow range of forcing effectiveness. Also, it can be deduced from this section that in order to eliminate flapping from the airfoil, the procedure of the present study might usefully be followed by firstly searching for the vortex shedding frequency and then applying periodic forcing at this frequency.

7.3 Analysis of lift and pressure spectra from long run LES

Jones (2007) studied pressure spectra around the NACA-0012 airfoil from three-dimensional DNS at eight pressure probes variously located in the boundary layer and in the potential flow at a Reynolds number of 50,000 and incidence of 5°. Since the DNS simulation requires a large computational effort, the pressure spectra were computed only over 7.7 time units. Taking advantage of the enormous computational time and space saving of the present LES code compared with the DNS, a long run simulation is

performed in the present study to extend the DNS results and investigate the low-frequency mode that may be present in the pressure spectra around the airfoil.

A grid refinement study was first performed to find the grid with the fewest grid points, and hence provide the greatest saving in computational time. To accomplish this, three grids were constructed and tested; grid A (637 × 375), which is the same as used in the 2D and 3D LES code validation in Chapter 3, grid B (635 × 250) and grid C (549 × 375). The 2-D filtered Navier-Stokes simulation was then carried out for each grid. Figure 7.30 shows a comparison of lift coefficients for the three grids. It is apparent that the lift coefficients obtained from the 2D filtered Navier-Stokes simulations are almost identical which indicates that grid B could be used to perform the 3-D LES calculation. The selected grid provides enormous saving in grid points compared with the DNS simulation, since it uses 33.6 times fewer grid points than in the DNS.

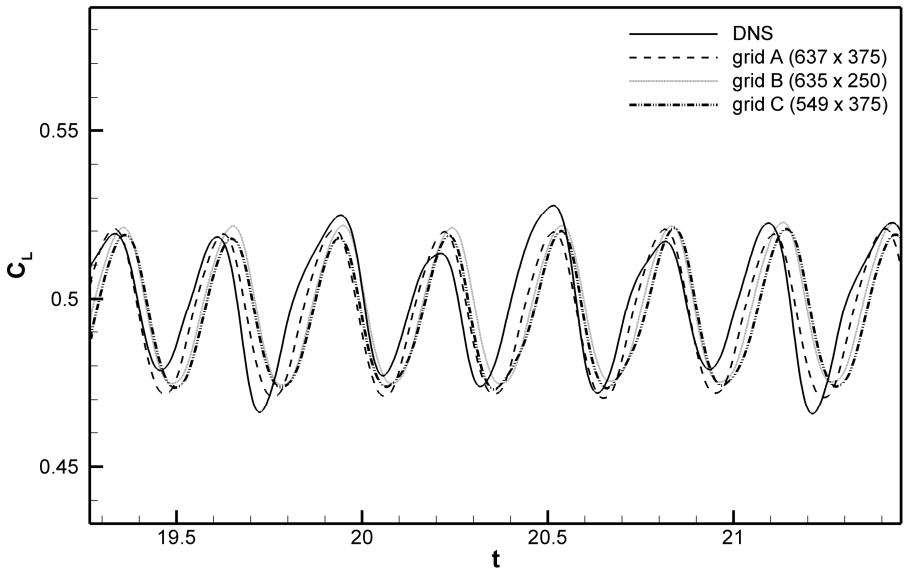

7.30 Comparison of lift coefficient between DNS and 2-D filtered N-S over several grids.

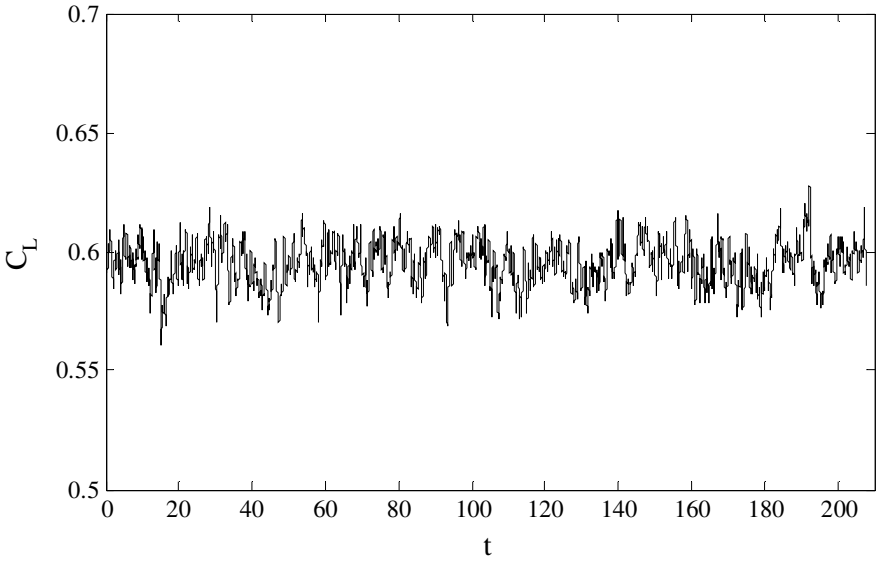

Figure 7.31 Lift coefficient obtained from the long run of LES of flow around an NACA-0012 airfoil (Re = 50,000 and α = 5°).

The two-dimensional simulation was extended to three-dimensions by evenly distributing 32 grid points in the spanwise direction. The spanwise length is set to be 20% of the chord length which is the same as the spanwise length of the DNS simulation. Figure 7.31 shows the lift coefficient obtained from the LES simulation over an interval of 208 time units, which is about 27 times larger than the DNS. Spectra were computed as follows; firstly, the whole signal was divided into seven overlapping segments with each segment 50% overlapped with the previous segment. Secondly, an FFT was computed for each segment and finally the seven segments were averaged. This technique provides smoother spectra. Figure 7.32 shows the pre-multiplied energy spectra in which it is apparent that the dominant frequency is at $f = 0.13$. This low frequency may represent a low-frequency shear layer flapping. It is interesting to mention that Hain *et al.* (2009) performed time-resolved PIV measurements for flow around an SD7003 aerofoil at a Reynolds number of 66,000, and observed low frequency mode of flow at $f \approx 0.3$ inside the water tunnel even though the aerofoil was taken out, which means that this frequency originated from the disturbances of water tunnel, while the current study has showed that a lower frequency content originates from the airfoil itself.

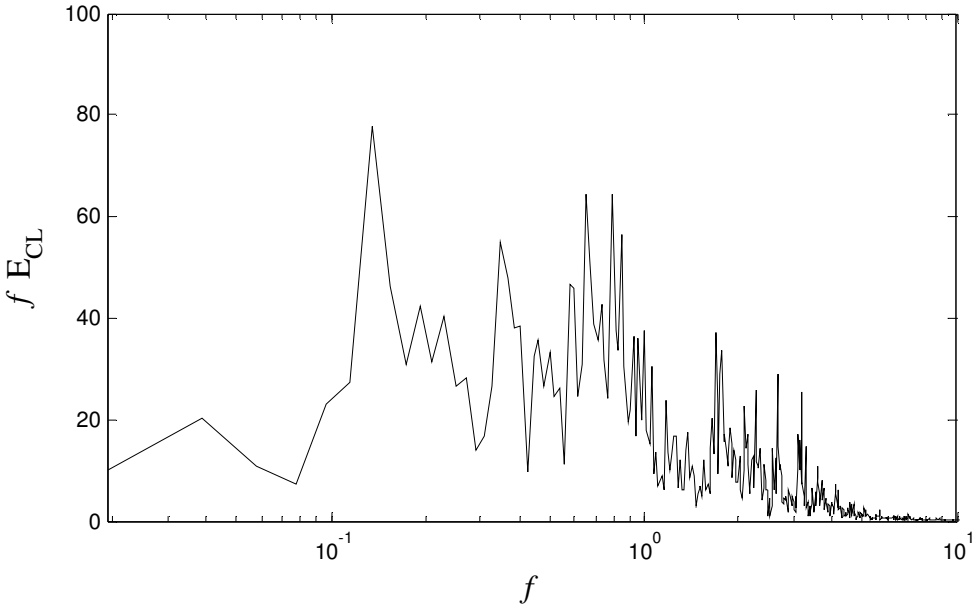

Figure 7.32 Pre-multiplied energy spectra of lift coefficient obtained from the long run LES for a flow around an NACA-0012 airfoil (Re = 50,000, M = 0.4 and α = 5°).

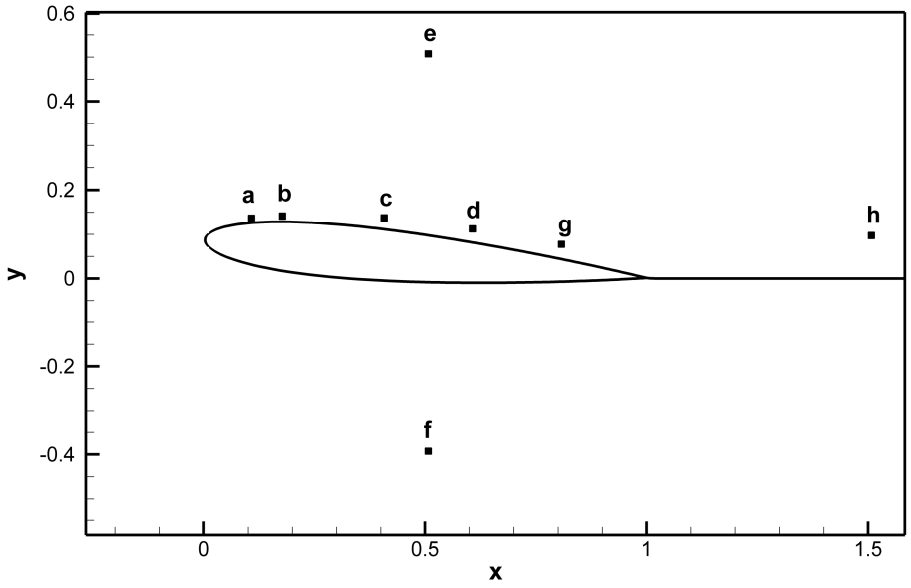

Figure 7.33 Locations of pressure probes on the upper surface and the potential flow regions.

In order to study the behaviour of the flow around the airfoil, the pressure at eight different locations is stored from the long run LES. These pressure probes are chosen to give the pressure in the boundary layer just upstream of separation (probe 1), in the separated shear layer (probes 2 and 3), near the beginning of vortex shedding in the two-dimensional simulation (probe 4), in the potential flow above and under the airfoil

(probes 5 and 6, respectively), in the turbulent boundary layer (probe 7) and in the near-wake region (probe 8). Figure 7.33 shows the pressure probe locations. Spectra for all the probes were computed using a similar procedure as for the lift coefficient, with the results shown on Figure 7.34. The first observation from this figure is the ability of the LES code to detect similar frequencies as found in the DNS of Jones (2007), which provides more validation of the LES code. The pressure spectra of the points in the laminar and transitional boundary layers (Figures 7.34a-7.34b) reveal noticeable frequency peaks at f = 11.2 , f = 22.2 and f = 33.5. These frequencies were also seen by Jones (2007) but they are clearer in the present study due to the long run time. It is interesting to mention that Zhang *et al.* (2008) found that the dominant frequency of the power spectra of streamwise and normal velocity components of the flow, in the laminar/transition region around an SD7003 airfoil at a Reynolds number of 60,000 and incidence of 4°, was at 10.7 Hz (corresponding to a dimensionless f =7.133), which is comparable to the present frequency. They suggested that this frequency is associated with the vortex shedding of the laminar separation bubble. They also found a lower frequency with high amplitude at 1.2 Hz (f = 0.8), in which they suggested that it is low frequency flapping of the laminar separation bubble.

The pressure spectrum in the upper potential flow is shown in Figure 7.34e and exhibits a peak at the same dominant frequency found for the first three pressure probes, i.e. at f = 11.2. Unlike the upper surface pressure spectra, no distinguishing frequencies are seen in the pressure spectra for the lower potential flow (Figure 7.34f) which agrees with the DNS result. A low frequency with a high amplitude at f = 0.044 becomes visible at x = 0.6 (Figure 7.34d), whereas a broadband peak is found at f = 4 which could be of interest because it is close to the vortex shedding frequency found in the two-dimensional simulation (f = 3.32). The pressure spectrum at x = 0.8 (Figure 7.34g) exhibits a similar form to that found at x = 0.6 (Figure 7.34d) except that the low frequency has disappeared. Also, it is noticeable that there is an additional frequency which becomes the highest amplitude at f = 3.62. There is no distinguishing frequency found in the near wake region (Figure 7.34h).

With the objective of eliminating or reducing the low-frequency flapping of the flow around the NACA-0012 airfoil at $\alpha = 5°$, a 2D filtered Navier-Stokes simulation with low-amplitude periodic forcing at f =7.76 was carried out for grid A which has 637 × 375 grid points. The periodic forcing was applied at x/c = 0.1 and y/c = 0.129. The simulation ran up to t = 52 which is about one fourth the length of the unforced simulation. Figure 7.35 shows a comparison of lift coefficient between the unforced and forced simulations in which is clear that the amplitudes of lift oscillations are markedly reduced in the forced case. A pre-multiplied spectrum is shown on Figure 7.36 which can be compared to the unforced case (Figure 7.33), showing that the periodic forcing apparently reduces the flapping of the laminar separation bubble.

7.4 Chapter summary

A flow control technique which uses periodic forcing just upstream of the separation has been applied to the NACA-0012 airfoil. At a Reynolds number of 50,000, incidence of 9.25° and Mach number of 0.4 the low-frequency flow oscillation was removed and the performance of the airfoil was enormously increased (110% increase in lift-to-drag ratio). The 2-D filtered Navier-Stokes calculations were also used to investigate the ability of periodic forcing to eliminate or reduce the flapping of the NACA-0012 airfoil at zero incidence with Re = 50,000 and M = 0.8. It was found that the flapping can be completely removed if the forcing frequency used is set equal to the vortex shedding frequency, while a non-zero lift coefficient is obtained if the forcing frequency is either higher or lower than the vortex shedding frequency. A long run simulation for a flow around an NACA-0012 airfoil at an incidence of 5° and Reynolds number of 50,000 detected very low frequencies. Periodic forcing reduces the amplitude of this low-frequency content.

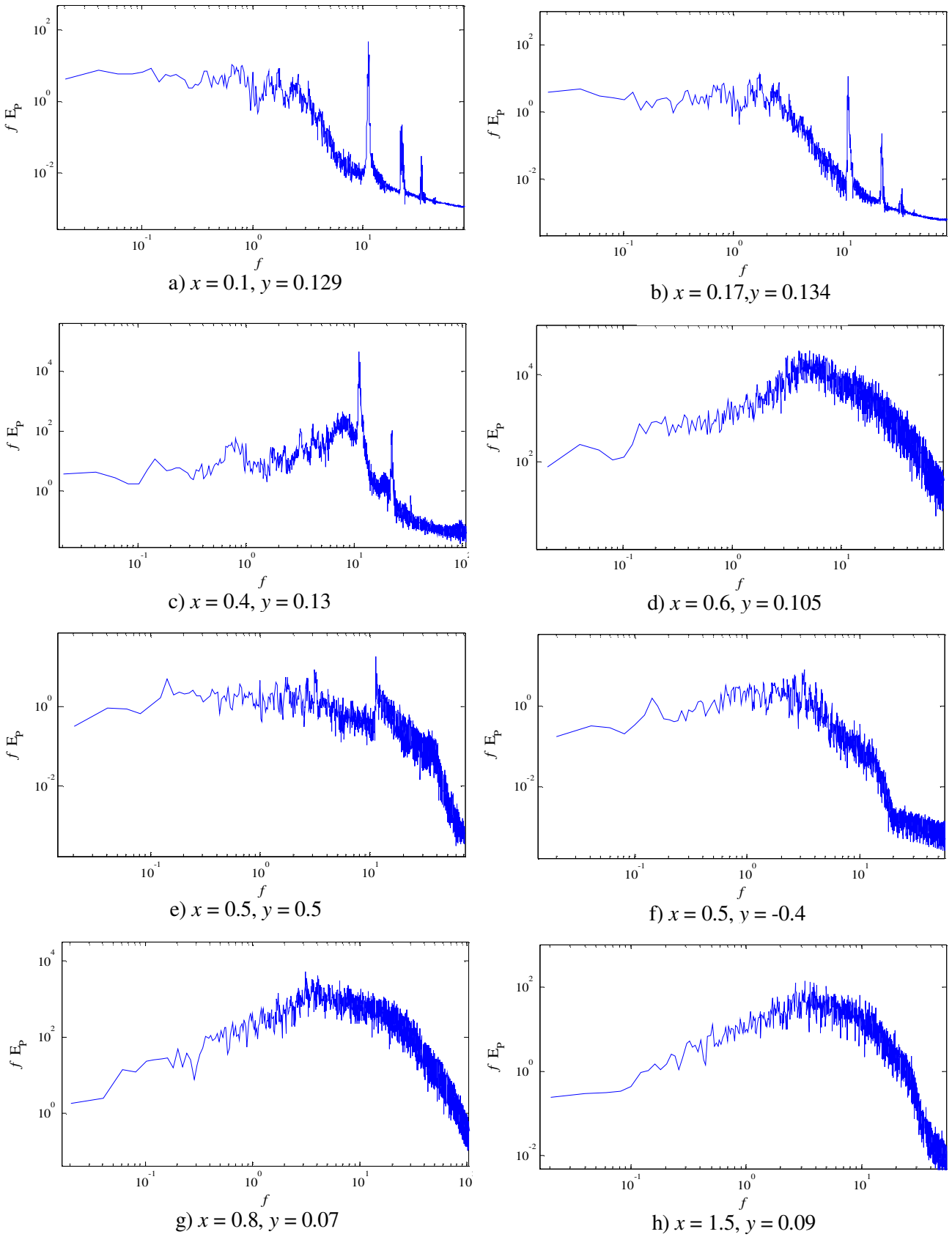

Figure 7.34 Pre-multiplied energy spectra for all pressure probes of a flow around an NACA-0012 airfoil obtained from LES and illustrated in Figure 3.44 (Re = 50,000, M = 0.4 and $\alpha = 5°$).

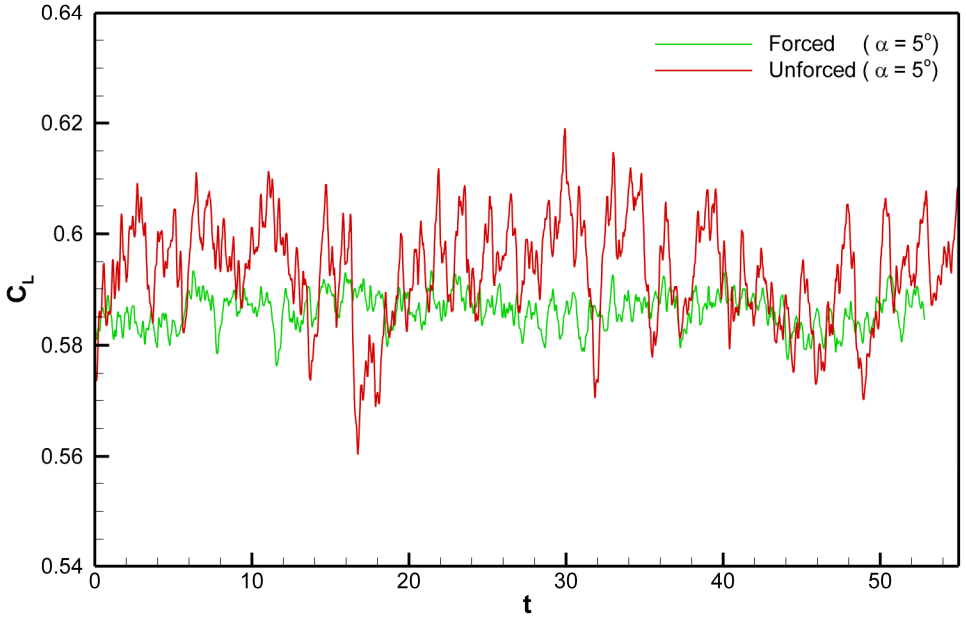

Figure 7.35 Comparison of lift coefficient between forced and unforced cases for flow around a NACA-0012 airfoil (Re = 50,000, M = 0.4 and α = 5°).

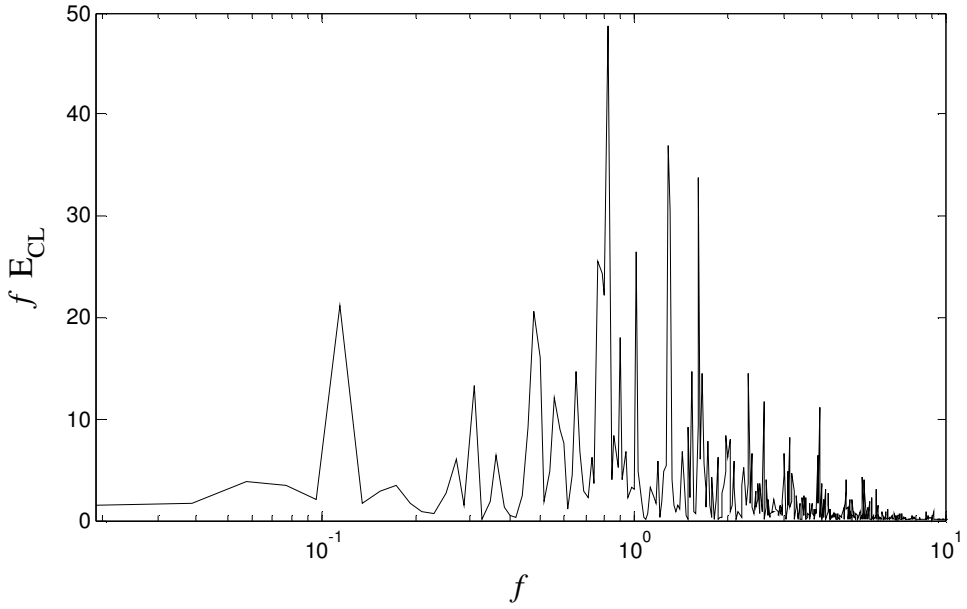

Figure 7.36 Energy spectrum of lift coefficient obtained from LES with forcing for a flow around a NACA-0012 airfoil (Re = 50,000, M = 0.4 and α = 5°).

8 Conclusions and future work

8.1 Thesis conclusions

The present thesis has dealt with several numerical issues, including development and validation of an efficient numerical tool (LES) to predict flow around an airfoil at a low Reynolds number. The low-frequency flow oscillation phenomenon that occurs near the static stall incidence of the NACA-0012 airfoil at a Reynolds number of Re = 50,000 was reproduced. Dynamic stall of a NACA-0012 airfoil was also investigated. The thesis also used a flow control technique, based on the introduction of flow disturbances inside the laminar boundary layer just upstream of the laminar separation point, to eliminate the low-frequency flow oscillation around the airfoil near stall and to remove the flapping of the airfoil on the 2D simulation at zero incidence and Reynolds number 50,000. A more detailed summary of the results as follows.

- At the beginning of the current study, numerical simulations of two-dimensional flow around NACA 0012 airfoil were developed using filtering. The code was validated by comparison with the DNS of Jones (2007) for flow around a NACA 0012 airfoil at incidences of 0° and 5°.
- Several filter schemes were studied to determine their relative performance. A fourth order tridiagonal filter scheme was found to be the optimum filter scheme to obtain the best solution, with strong evidence supporting the good performance of a fourth order tridiagonal filter scheme on a stretched grid.
- The results of the two-dimensional filtered Navier-Stokes simulation showed the ability of the simulation to accurately reproduce the flapping phenomenon observed in the DNS. In the three-dimensional test case, it was found that the LES code (which always uses filtering), with and without the subgrid scale model, provides comparable results with the DNS, with a slight improvement when a mixed time scale subgrid model is incorporated with the LES.
- It was shown that the computational cost associated with LES was reduced by a factor of 22 compared with DNS for the validation case.

- After performing the code validation, a three-dimensional large eddy simulation was conducted at $\alpha = 9.25°$, where stalling is believed to start, while the other flow conditions remained unchanged. The code was able to reveal the behaviour of a low Reynolds number flow near airfoil stall and to show its ability to capture the corresponding special physical phenomenon called "low-frequency flow oscillation", where an unusual switching between stalling and non-stalling occurs in airfoils. However, only one cycle of the oscillation was observed for the narrow grid cases and the flow failed to reattach during the second cycle.
- Increasing the spanwise length of the airfoil from 20% to 50% chord length was found to be the key to successfully capturing the low-frequency phenomenon for a flow around the NACA-0012 airfoil at a Reynolds number of 50,000 with incidence of $\alpha = 9.25°$, in which an intermittent bursting of the laminar separation bubble was observed. This conclusion was supported by comparing the two-point velocity correlations of the wider and the narrower domain, with a significant improvement in the decay of the two-point correlation in the wider domain case.
- The bubble bursting observed in the current study was more irregular than in the experimental results at higher Reynolds numbers. It was concluded that the laminar separation bubble is very sensitive to incidence, Reynolds number and L_z.
- LES was applied to study the dynamic stall phenomenon for a NACA-0012 airfoil at low Reynolds number (Re = 50,000) and Mach number (M = 0.4). The averaged hysteresis loops for the lift, drag and pitching moment coefficients were well predicted compared with previous studies.
- Cycle-to-cycle variations were observed from in the dynamic stall hysteresis loops, which may be attributed to the unsteady nature of the flow. The time- and span-averaged pressure and skin-friction coefficients and streamline patterns of velocity were identified and studied.
- Some evidence of a dynamic vortex shedding was found. The averaged flow revealed a fully separated flow during the whole downstroke, even at small incidences, while the flow reattached during the upstroke motion.
- The candidate dynamic vortex was first observed at the end of the upstroke, which was shed downstream at an approximate speed of $0.77U_\infty$.

- Three-dimensional flow structures for the dynamic stall of the NACA-0012 airfoil were captured very well by the LES, which showed also that the behaviour of the flow is indeed fully three-dimensional during both upstroke and downstroke as opposed to Martinat *et al.* (2008).
- An unsteady viscous-inviscid interaction method was used to study the low-frequency flow oscillation and dynamic stall phenomena for a NACA-0012 airfoil. Low-frequency behaviour was observed from Re = 50,000 to 420,000.
- The peak-to-peak amplitude and the Strouhal number of the lift coefficient for the low-frequency flow oscillation were found to be dependent on the Reynolds number and incidence.
- It was found that the magnitude of the Strouhal number increases as the Reynolds number increases, in agreement with the observations of Bragg *et al.* (1996). It was also found that peak-to-peak amplitude increases as incidence increases and also as the Reynolds number increases.
- A comparison between the results of the unsteady viscous-inviscid interaction method and the LES and experiment was carried out. It was found that the peak-to-peak amplitude of the lift coefficient obtained by LES was larger than that obtained by the viscous-inviscid interaction method. The comparison also revealed that the Strouhal number of LES and the experiment followed similar trends as in the viscous-inviscid interaction results, although their values were smaller. Overall the trends from the viscous-inviscid interaction method are consistent with the limited data currently available from LES (wide domain) and the experiment.
- The viscous-inviscid interaction results of the oscillating airfoil through static stall show similar aerodynamic characteristics as in the LES and experimental observations, for airfoils in dynamic stall, but there was a significant difference between the maximum and minimum lift and drag coefficients.
- A flow control technique using periodic forcing just upstream of the separation was applied to improve the aerodynamic performance. For the NACA-0012 airfoil at Re = 50,000, $\alpha = 9.25°$ and M = 0.4, the low-frequency flow oscillation was

removed and the performance of the airfoil was enormously increased (a doubling of lift-to-drag ratio).

- Navier-Stokes calculations were used to investigate the ability of periodic forcing to eliminate or reduce the flapping of the NACA-0012 airfoil at zero incidence with Re = 50,000 and M = 0.8. It was found that the flapping can be completely removed if the forcing frequency used is set as equal to the vortex shedding frequency, while a non-zero lift coefficient is obtained if the forcing frequency is either higher or lower than the vortex shedding frequency.
- The long run simulation was capable of detecting very low frequencies which could not be detected in the DNS. Periodic forcing has found to reduce the amplitude of this low-frequency content.

8.2 Future work

The present study has highlighted a number of different simulations that could not be performed because of computing time limitations but which could become feasible over the next 5-10 years (the first five items could be performed now with sufficient supercomputer time):

- The large eddy simulation of a flow around an NACA-0012 airfoil at a Reynolds number of 130,000 near stall can be repeated with a wider computational domain (L_Z = 0.5c or higher) to obtain more accurate results that can be compared quantitatively with the experiment of Rinoie and Takemura (2004).
- The effect of periodic forcing on the NACA-0012 airfoil can be investigated above stall and a maximum stall incidence can be obtained.
- The peaks of frequency found in the long-run simulation for flow around an NACA-0012 airfoil at a Reynolds number of 50,000 and an incidence of $5°$ can be identified better when using a wider domain (L_Z = 0.5 c) and even longer run time.
- Further LES over a wider range of parameters should allow the viscous-inviscid interaction method to be improved

- Dynamic stall at higher Reynolds number and different reduced frequencies can be performed by LES and compared with the experiments in order to study the feasibility of LES for predicting the dynamic stall phenomenon.
- An LES can be performed to study the wing tip vortex effect on a NACA0012 airfoil near stall using the same Reynolds number that had been used in this thesis. Hence, the effect of the low-frequency flow oscillation phenomenon in conjunction with the wing tip vortex on the performance of the airfoil can be studied.

Appendix A: Taylor series analysis and transfer function

A.1 Taylor series analysis:

In order to find the coefficients of equation 4.1 all terms in the right hand side are first transferred to the left hand side as follows:

$$\hat{q}_i + \beta(\hat{q}_{i-2} + \hat{q}_{i+2}) + \alpha(\hat{q}_{i-1} + \hat{q}_{i+1}) - aq_i - \frac{b}{2}(q_{i-1} + q_{i+1}) - \frac{c}{2}(q_{i-2} + q_{i+2}) - \frac{d}{2}(q_{i-3} + q_{i+3}) = 0 \quad \text{(A.1)}$$

Then, a Taylor series expansion is applied and each part of the equation is expanded as follows:

$$\beta\hat{q}_{i-2} = \beta\left(q_i - (2h)q_i' + \frac{(2h)^2}{2!}q_i'' - \frac{(2h)^3}{3!}q_i''' + \frac{(2h)^4}{4!}q_i^{IV} - \frac{(2h)^5}{5!}q_i^{V} + ... \right) \quad \text{(A.2)}$$

$$\beta\hat{q}_{i+2} = \beta\left(q_i + (2h)q_i' + \frac{(2h)^2}{2!}q_i'' + \frac{(2h)^3}{3!}q_i''' + \frac{(2h)^4}{4!}q_i^{IV} + \frac{(2h)^5}{5!}q_i^{V} + ... \right) \quad \text{(A.3)}$$

$$\alpha\hat{q}_{i-1} = \alpha\left(q_i - hq_i' + \frac{h^2}{2!}q_i'' - \frac{h^3}{3!}q_i''' + \frac{h^4}{4!}q_i^{IV} - \frac{h^5}{5!}q_i^{V} + ... \right) \quad \text{(A.4)}$$

$$\alpha\hat{q}_{i+1} = \alpha\left(q_i + hq_i' + \frac{h^2}{2!}q_i'' + \frac{h^3}{3!}q_i''' + \frac{h^4}{4!}q_i^{IV} + \frac{h^5}{5!}q_i^{V} + ... \right) \quad \text{(A.5)}$$

$$-\frac{b}{2}q_{i-1} = -\frac{b}{2}\left(q_i - hq_i' + \frac{h^2}{2!}q_i'' - \frac{h^3}{3!}q_i''' + \frac{h^4}{4!}q_i^{IV} - \frac{h^5}{5!}q_i^{V} + ... \right) \quad \text{(A.6)}$$

$$-\frac{b}{2}q_{i+1} = -\frac{b}{2}\left(q_i + hq_i' + \frac{h^2}{2!}q_i'' + \frac{h^3}{3!}q_i''' + \frac{h^4}{4!}q_i^{IV} + \frac{h^5}{5!}q_i^{V} + ... \right) \quad \text{(A.7)}$$

$$-\frac{c}{2}q_{i-2} = -\frac{c}{2}\left(q_i - (2h)q_i' + \frac{(2h)^2}{2!}q_i'' - \frac{(2h)^3}{3!}q_i''' + \frac{(2h)^4}{4!}q_i^{IV} - \frac{(2h)^5}{5!}q_i^{V} + ... \right) \quad \text{(A.8)}$$

$$-\frac{c}{2}q_{i+2} = -\frac{c}{2}\left(q_i + (2h)q_i' + \frac{(2h)^2}{2!}q_i'' + \frac{(2h)^3}{3!}q_i''' + \frac{(2h)^4}{4!}q_i^{IV} + \frac{(2h)^5}{5!}q_i^{V} + ... \right) \quad \text{(A.9)}$$

$$-\frac{d}{2}q_{i-3} = -\frac{d}{2}\left(q_i - (3h)q_i' + \frac{(3h)^2}{2!}q_i'' - \frac{(3h)^3}{3!}q_i''' + \frac{(3h)^4}{4!}q_i^{IV} - \frac{(3h)^5}{5!}q_i^{V} + ... \right) \quad \text{(A.10)}$$

$$-\frac{d}{2}q_{i+3} = -\frac{d}{2}\left(q_i + (3h)q_i' + \frac{(3h)^2}{2!}q_i'' + \frac{(2h)^3}{3!}q_i''' + \frac{(3h)^4}{4!}q_i^{IV} + \frac{(3h)^5}{5!}q_i^{V} + ... \right) \quad \text{(A.11)}$$

where $q_i', q_i'', q_i''', q_i^{IV}$ and q_i^V are the first, second, third, fourth and fifth derivatives, respectively. The following Taylor series table will be used to match the coefficients of equations A.2 to A.11.

Table (A.1) Taylor series coefficients

	q_i	hq_i'	$\frac{h^2}{2!}q_i''$	$\frac{h^3}{3!}q_i'''$	$\frac{h^4}{4!}q_i^{IV}$	$\frac{h^5}{5!}q_i^V$	$\frac{h^6}{6!}q_i^{VI}$
$\hat{q}_i$	1						
$\beta\hat{q}_{i-2}$	β	-2β	4β	-8β	16β	-32β	64β
$\beta\hat{q}_{i+2}$	β	2β	4β	8β	16β	32β	64β
$\alpha\hat{q}_{i-1}$	α	$-\alpha$	α	$-\alpha$	α	$-\alpha$	α
$\alpha\hat{q}_{i+1}$	α	α	α	α	α	α	α
$-aq_i$	$-a$						
$-\frac{b}{2}q_{i-1}$	$-\frac{b}{2}$	$\frac{b}{2}$	$-\frac{b}{2}$	$\frac{b}{2}$	$-\frac{b}{2}$	$\frac{b}{2}$	$-\frac{b}{2}$
$-\frac{b}{2}q_{i+1}$	$-\frac{b}{2}$	$-\frac{b}{2}$	$-\frac{b}{2}$	$-\frac{b}{2}$	$-\frac{b}{2}$	$-\frac{b}{2}$	$-\frac{b}{2}$
$-\frac{c}{2}q_{i-2}$	$-\frac{c}{2}$	c	$-2c$	$4c$	$-8c$	$16c$	$-32c$
$-\frac{c}{2}q_{i+2}$	$-\frac{c}{2}$	$-c$	$-2c$	$-4c$	$-8c$	$-16c$	$-32c$
$-\frac{d}{2}q_{i-3}$	$-\frac{d}{2}$	$\frac{3d}{2}$	$-\frac{9d}{2}$	$\frac{27d}{2}$	$-\frac{81d}{2}$	$\frac{243d}{2}$	$\frac{729d}{2}$
$-\frac{d}{2}q_{i+3}$	$-\frac{d}{2}$	$-\frac{3d}{2}$	$-\frac{9d}{2}$	$-\frac{27d}{2}$	$-\frac{81d}{2}$	$-\frac{243d}{2}$	$-\frac{729d}{2}$

By equating coefficients the following equations can be obtained from table (A.1):

$$1+2\beta+2\alpha = a+b+c+d \quad \text{(A.12)}$$

$$8\beta+2\alpha = b+4c+9d \quad \text{(A.13)}$$

$$32\beta+2\alpha = b+16c+81d \quad \text{(A.14)}$$

$$128\beta+2\alpha = b+64c+729d \quad \text{(A.15)}$$

In order to find the coefficients of any filter scheme, equations (A.12) to (A.15) should be solved with constraints as mentioned in the following section. The accuracy of the scheme depends on the truncation error which is the last equation not solved. For example, if a 4th order accurate scheme is required then only equations (A.12) and (A.13) should be solved while the imbalance in equation (A.14) is the truncation error.

A.2 Transfer function

The transfer function is derived from equation (4.1) by setting:

$$q = e^{ikx}, q_{i-1} = e^{i(x-kh)}, q_{i-2} = e^{i(x-2kh)}, \tag{A.16}$$

where k is the wavenumber and h is the space between grid points. Then, equation (4.1) becomes

$$e^{ikx} + \beta\left(e^{ik(x-2h)} + e^{ik(x+2h)}\right) + \alpha\left(e^{ik(x-h)} + e^{ik(x+h)}\right) =$$
$$ae^{ikx} + \frac{b}{2}\left(e^{ik(x-h)} + e^{ik(x+h)}\right) + \frac{c}{2}\left(e^{ik(x-2h)} + e^{ik(x+h)}\right) + \frac{d}{2}\left(e^{ik(x-3h)} + e^{ik(x+3h)}\right). \tag{A.17}$$

Dividing equation (A.17) by e^{ikx} gives

$$1 + \beta\left(e^{-2ikh)} + e^{2ikh)}\right) + \alpha\left(e^{ikh} + e^{ikh}\right) = a + \frac{b}{2}\left(e^{-ikh} + e^{ikh}\right) + \frac{c}{2}\left(e^{-2ikh} + e^{2ikh}\right) + \frac{d}{2}\left(e^{-3ikh} + e^{3ikh)}\right) \tag{A.18}$$

Recalling the trigonometric identities:

$$\cos(2kh) = \frac{\left(e^{-2ikh)} + e^{2ikh)}\right)}{2} \quad \text{and} \quad \cos(kh) = \frac{\left(e^{-ikh)} + e^{ikh)}\right)}{2},$$

equation (A.18) can be written as:

$$1 + 2\beta\cos(2kh) + 2\alpha\cos(kh) = a + b\cos(kh) + c\cos(2kh) + d\cos(3kh). \tag{A.19}$$

Then the transfer function can be written as

$$TF(kh) = \frac{a + b\cos\left(kh\right) + c\cos\left(2kh\right) + d\cos\left(3kh\right)}{1 + 2\alpha\cos(kh) + 2\beta\cos(2kh)} \tag{A.20}$$

A constraint that should be applied for all filters is:

$$TF(\pi) = 0 \tag{A.21}$$

The 4th order tridiagonal and 6th order explicit schemes are generated when (A.21) are imposed. An additional constraint is applied to obtain the 4th order explicit scheme.

$$\frac{d^2(TF)}{d(kh)^2}(\pi) = 0 \tag{A.22}$$

A.3 Example (4th order tridiagonal)

The 4th order tridiagonal scheme will be taken as example of finding the coefficients. In this case equations (A.12) and (A.13) will be used:

$$1 + 2\beta + 2\alpha = a + b + c + d \tag{A.23}$$

$$8\beta + 2\alpha = b + 4c + 9d \tag{A.24}$$

In order to get the 4th order tridiagonal scheme β should be zero and α will be a free parameter; in this case α=0.475 and for a 5 point stencil scheme d=0. Furthermore, constraint (A.21) should be used with conjunction of equations (A.12) and (A.13). Hence, the equations that should be solved are:

$$a + b + c = 1.95 \tag{A.25}$$

$$b + 4c = 0.95 \tag{A.26}$$

$$a - b + c = 0 \tag{A.27}$$

Solution of these equations give: $a = \frac{7.85}{8}$, $b = \frac{7.8}{8}$ and $c = -\frac{0.05}{8}$. The truncation error ε can be obtained when these coefficients are substituted into equation (A.14) giving

$$\varepsilon = \frac{0.05}{16} h^4 q^{IV}$$

Appendix B: Taylor analysis for non-periodic boundary points

Boundary schemes can be obtained by following the same procedure of matching coefficients using a Taylor series analysis. The first boundary point with a 4^{th} order accuracy can be obtained by starting from the following one-sided equation:

$$\hat{q}_i - aq_i - bq_{i+1} - cq_{i+2} - dq_{i+3} - eq_{i+4} = 0 \tag{B.1}$$

Then, expanding each term by Taylor series:

$$-bq_{i+1} = -b\left(q_i + hq_i' + \frac{h^2}{2!}q_i'' + \frac{h^3}{3!}q_i''' + \frac{h^4}{4!}q_i^{IV} + \frac{h^5}{5!}q_i^{V} + ... \right) \tag{B.2}$$

$$-cq_{i+2} = -c\left(q_i + (2h)q_i' + \frac{(2h)^2}{2!}q_i'' + \frac{(2h)^3}{3!}q_i''' + \frac{(2h)^4}{4!}q_i^{IV} + \frac{(2h)^5}{5!}q_i^{V} + ... \right) \tag{B.3}$$

$$-dq_{i+3} = -d\left(q_i + (3h)q_i' + \frac{(3h)^2}{2!}q_i'' + \frac{(3h)^3}{3!}q_i''' + \frac{(3h)^4}{4!}q_i^{IV} + \frac{(3h)^5}{5!}q_i^{V} + ... \right) \tag{B.4}$$

$$-eq_{i+3} = -e\left(q_i + (4h)q_i' + \frac{(4h)^2}{2!}q_i'' + \frac{(4h)^3}{3!}q_i''' + \frac{(4h)^4}{4!}q_i^{IV} + \frac{(4h)^5}{5!}q_i^{V} + ... \right) \tag{B.5}$$

The Taylor table is constructed in table B.1

Table (B.1) Taylor series coefficients

	q_i	hq_i'	$\frac{h^2}{2!}q_i''$	$\frac{h^3}{3!}q_i'''$	$\frac{h^4}{4!}q_i^{IV}$
$\hat{q}_i$	1				
$-aq_i$	$-a$				
$-bq_{i+1}$	$-b$	$-b$	$-b$	$-b$	$-b$
$-cq_{i+2}$	$-c$	$-2c$	$-4c$	$-8c$	$-16c$
$-dq_{i+3}$	$-d$	$-3d$	$-9d$	$-27d$	$-81d$
$-eq_{i+3}$	$-e$	$-4e$	$-16e$	$-64e$	$-256e$

From table (B.1), the following equations are obtained:

$$a+b+c+d+e=1 \tag{B.6}$$

$$b+2c+3d+4e=0 \tag{B.7}$$

$$b+4c+9d+16e=0 \tag{B.8}$$

$$b+8c+27d+64e=0 \tag{B.9}$$

The transfer function of (B.1) can be split into real and imaginary parts. The real part is given by:

$$TF_r(kh)=a\cos(kh)+b\cos(2kh)+c\cos(3kh)+d\cos(4kh)+e\cos(5kh), \tag{B.10}$$

while the imaginary part of the transfer function is:

$$TF_i(kh)=a\sin(kh)+b\sin(2kh)+c\sin(3kh)+d\sin(4kh)+e\sin(5kh) \tag{B.11}$$

The fifth equation that needs to be solved in conjunction with equations (B.6) to (B.9) is obtained from the constraint (A.21):

$$TF(\pi)=a\cos(\pi)+b\cos(2\pi)+c\cos(3\pi)+d\cos(4\pi)+e\cos(5\pi)=0$$

$$\Rightarrow b-a-c+d-e=0 \tag{B.12}$$

Solving equations (B.6) to (B.9) and (B.12) will given:

$$a=\frac{15}{16}\quad,\quad b=\frac{4}{16}\quad,\quad c=-\frac{6}{16}\quad,\quad d=\frac{4}{16},\quad e=-\frac{1}{16}$$

The truncation error ε of this scheme is obtained from the last column of table (B.1) which is:

$$\varepsilon=(b+16c+81d+256e)\frac{h^4}{4!}q_i^{IV}$$

$$=-\frac{3}{2\cdot 4!}h^4 q_1^{IV}$$

In a similar fashion, the second boundary point can be obtained with some modification of equation (B.1), which should be rewritten as follows:

$$\hat{q}_i-aq_{i-1}-bq_i-cq_{i+1}-dq_{i+2}-eq_{i+3}=0 \tag{B.13}$$

References

Akbari, M. H. and Price, S.J. (2003) 'Simulation of dynamic stall for a NACA 0012 airfoil using a vortex method'. *Journal of Fluids and Structures* **17** 855-874.

Alam, M. and Sandham, N.D. (2000) 'Direct numerical simulation of 'short' laminar separation bubbles with turbulent reattachment', *Journal of Fluid Mechanics* **403,** 223-250.

Almutairi, J. H., Jones, L. E., and Sandham, N. D. (2010) 'Intermittent bursting of a laminar separation bubble on an airfoil', *AIAA Journal.* **48** (2), 414-426.

Barakos, G. N. and Drikakis, D. (2000) 'Unsteady separated flows over manoeuvring lifting surfaces', *Phil. Trans. R. Soc. Lond. A.* **358**, 3279-3291

Baragona, M. (2004) 'Unsteady characteristics of laminar separation bubbles', PhD Thesis, Delft University of Technology.

Bar-Sever, A. (1989) 'Separation control on an airfoil by periodic forcing', *AIAA Journal.* **27** (6), 820-821.

Bogey, C. and Bailly, C. (2002) 'A family of low dispersive and low dissipative explicit schemes for flow and noise computational', *Journal of Computational Physics.* **194** , 194-214.

Bragg, M. B., Heinrich, D. C., Balow, F. A. and Zaman, K. B. M. Q. (1996) 'Flow oscillation over an airfoil near stall', *AIAA Journal.* **34** (1), 199-201.

Broeren, A. P. and Bragg, M. B. (1999) 'Flowfield measurements over an airfoil during natural low-frequency oscillations near stall', *AIAA Journal.* **37** (1), 130-132.

Broeren, A. P. and Bragg, M. B. (2001) 'Spanwise variation in the unsteady stalling Flowfields of two-dimensional airfoil models', *AIAA Journal.* **39** (9), 1641-1651.

Carpenter, M.H., Nordstrom, J. and Gottlieb, D. (1999) 'A stable and conservative interface treatment of arbitrary spatial accuracy', *Journal of Computational Physics* **148**, 341-365.

Choudhuri, P. G. and Knight, D. D. (1996) 'Effects of compressibility, pitch rate, and Reynolds number on unsteady incipient leading-edge boundary layer separation over a pitching airfoil', *Journal of Fluid Mechanics* **308** 195- 217.

Collins, F. G. and Zelenevitz, J. (1975) 'Influence of sound upon separated flow over wings', *AIAA Journal.* **13** (3), 408- 410.

Crabtree, L.F. (1959) 'The formation of regions of separated flow on wing surfaces', ARC R&M 3122.

Deardorff, J. W. (1970) 'A numerical study of three-dimensional turbulent channel flow at large Reynolds numbers', *Journal of Fluid Mechanics* **41** 453- 480.

Drela, M. and Giles, M. B. (1987) 'Viscous-inviscid analysis of transonic and low Reynolds number airfoils ', *AIAA Journal.* **25** (10), 1347-1355.

Ducoin, A., Astolfi, J. A., Deniset, F. and Sigrist, J. (2009) 'Computational and experimental investigation of flow over a transient pitching hydrofoil ', *European Journal of Mechanics B/Fluids.* **28**, 728-743.

Eisenbach, S. and Friedrich, R. (2008) 'Large-eddy simulation of flow separation on an airfoil at a high angle of attack and $Re = 10^5$ using Cartesian grids'. *Theoretical and Computational Fluid Dynamics* **22** 213-225.

Ericsson, L. E. and Reding, J. P. (1980) 'Dynamic stall at high frequency and large amplitude', *Journal of Aircraft* **17** 136-142.

Eriksson, L.E. (1982) 'Generation of boundary conforming grids around wing-body configurations using transfinite interpolation', *AIAA Journal*, **20** No.10, 1313-20.

Gad-el-Hak, M., (1989) 'Flow control', *Appl. Mech. Rev.* **42** 261-293.

Gad-el-Hak, M., (1990) 'Control of low-speed airfoil aerodynamics', *AIAA Journal* **28** 1537-1552.

Gad-el-Hak, M., and Bushnell, D. M. (1991) 'Separation control: review', *Journal of Fluid Engineering* **113** 5-30.

Gao, H., Hu, H., and Wang, Z. J., (2008) 'Computational Study of Unsteady Flows Around Dragonfly and Smooth Airfoils at Low Reynolds Numbers', *46th AIAA Aerospace Sciences Meeting and Exhibit*, Reno, NV, Jan. 7–10, AIAA Paper No. 2008-0385.

Gaster, M., 'The structure and behaviour of laminar separation bubbles', In Proc. Conf. AGARD, Rhode-Saint-Genese, Belgium, 10-13 May 1966, paper no. 4, pp. 813-854.

Germano, M., Piomelli, U., Moin, P., and Cobat, W. H., (1991). 'A dynamic subgrid-scale eddy viscosity model', *Phys. Fluids A* **3**(7), 1760-1765.
Ghosal, S. and Moin, P (1995) 'The basic equation of the large eddy simulation of turbulent flows in complex geometry', *Journal of Computational Physics* **118**, 24-37.

Ghosal, S., Lund, T. S., Moin, P. and Akselvoll, K. (1995) 'A dynamic localization model for large-eddy simulation of turbulent flows', *Journal of Fluid Mechanics* **286** 229-255.

Giguere, P. and Selig, M. S. (1999) 'Aerodynamic effect of leading-edge tape on aerofoils at low Reynolds numbers', *Wind Energy* **2** 125-136.

Green, J. E., Weeks, D. J. and Brooman, J. W. F. (1977) 'Prediction of turbulent boundary layers and wakes in compressible flow by a lag-entrainment method', ARC R&M 3791.

Greenblatt, D. and Wygnanski, I. J. (2000) 'The control of flow separation by periodic excitation', *Progress in Aerospace Sciences* **36** (7) 487-545.

Gross, A. and Fasel, H. F. (2009) 'Active flow control for airfoil at low Reynolds numbers'. AIAA 2009-4275.

Haggmark, C. (2000) 'Investigations of disturbances developing in a laminar separation bubble flow', Technical Report, Department of Mechanics, Royal Institute of Technology, Stockholm.

Hall, D. J. and Gibbings, J. C. (1972) 'Influence of stream turbulence and pressure gradient upon boundary layer transition', *Journal of Mechanical Engineering Science* **14** (2), 134-146.

Hain, R., Kahler, C. J. and Radespiel, R. (2009) 'Dynamic of laminar separation bubbles at low-Reynolds-number aerofoils', *Journal of Fluid Mechanics* **630** 129-153.

Hoarau, Y., Faghani, D., Braza, M., Perrin, R., Anne-Archard, D. and Ruiz, D. (2003) 'Direct numerical simulation of the three-dimensional transition to turbulence in the incompressible flow around a wing'. *Flow, turbulence and Combustion* **71** 119-132.

Horton, H. P. (1969) 'A semi-empirical theory for the growth and bursting of laminar separation bubbles'. *Aeronautical Research Council CP* 1073.

Hsiao, F.-B., Liu, C.-F. and Shyu, J.-Y. (1990) 'Control of wall-separated flow by internal acoustic excitation' *AIAA Journal.* **28** (8) 1440-1487.

Huang, J., Corke, T. C. and Thomas, F. O. (2006) 'Unsteady plasma actuators for separation control of low-pressure turbine blades', *AIAA Journal.* **44** (7) 1477-1487.

Inagaki, M., Kondoh, T. and Nagano, Y. (2005) 'A Mixed-time-scale SGS model with fixed model-parameters for practical LES', *Journal of Fluid Engineering* **127** (1) 1-13.

Jones, L. E. (2007) 'Numerical studies of the flow around an airfoil at low Reynolds number', PhD thesis Southampton University.

Jones, L. E., Sandberg, R.D. and Sandham, N.D. (2008) 'Direct numerical simulations of forced and unforced separation bubbles on an airfoil at incidence', *Journal of Fluid Mechanics* **602** 175 -207.

Jones, L. E., Sandberg, R.D. and Sandham, N.D. (2010) 'Stability and receptivity characteristics of a laminar separation bubble on an airfoil', *Journal of Fluid Mechanics* **648** 257-296.

Jones, L. E., Sandberg, R.D. and Sandham, N.D. (2006) 'Direct Numerical Simulation of an Airfoil with Unsteady Wake', European Conference on Computational Fluid Dynamics.

Johnson, W. and Ham, N. D. (1972) 'On the mechanism of dynamic stall', *Journal of t he American Helicopter Society* **17** 36-45.

Kaltenbach, H. and Choi, H. (1995) 'Large-eddy simulation of flow around an airfoil on a structured mesh', *Center for Turbulence Research* 51-60.

Katz, Y., Nishri, B. and Wygnanski, I. (1989) 'The delay of turbulent boundary layer separation by oscillatory active control', *Phys. Fluids A* **1**(2) 179-181.

Krishnan, L., Sandham, N. D. and Steelant, J. (2009) 'Shock-wave boundary-layer interactions in a model scramjet intake ', *AIAA Journal* **47** (7), 1680-1691.

Laitone, E.V. (1997) 'Wind tunnel tests of wings at Reynolds numbers below 70,000', *Experiments in Fluids* **23** 405-409.

Lele, S.K. (1992) 'Compact finite-difference schemes with spectral-like resolution'. *Journal of Computational Physics* **103**, 16-42.

Lian, Y. and Shyy, W. (2007) 'Laminar-turbulent transition of a low Reynolds number rigid or flexible airfoil', *AIAA Journal* **45** (7), 1501-1513.

Liebeck, R. H., (1978) 'Design of subsonic airfoils for high lift', *Journal of Aircraft* **15** 547-561.

Lissaman, P. B. S. (1983) 'Low-Reynolds-number airfoils', *Ann. Rev. Fluid Mech.* **15** 223-239.

Liu, S., Meneveau, C. and Kataz, J. (1994) 'On the properties of similarity subgrid-scale models as deduced from measurements in turbulent jet', *Journal of Fluid Mechanics* **275** 83-119.

Lorber, P. F. and Carta, F. O. (1988) 'Airfoil dynamic stall at constant pitch rate and high Reynolds number' *Journal of Aircraft* **25** 548-556.

Mack, L. M. (1977). *Transition prediction and linear stability theory*. AGARD CP-224, 1.1

Mack, L. M. (1977). *Transition prediction and linear stability theory*. AGARD CP-224, 1.1.

Martinat, G., Braza, M., Hoarau, Y. and Harran, G. (2008) 'Turbulence modelling of the flow past a pitching NACA0012 airfoil at 10^5 and 10^6 Reynolds numbers'. *Journal of Fluids and Structures* **24** 1294-1303.

McCroskey,B. S., Carr, L.W. and McAlister, K. W. (1976) 'Dynamic stall experiments on oscillating airfoils ', *AIAA Journal* **14** (1), 57-63.

Mary, I. and Sagaut, P. (2002) 'Large eddy simulation of flow around an airfoil near stall', *AIAA Journal.* **40** (6), 1139-1145.

Mason, P. J. and Callen, N. S. (1986) 'On the magnitude of the subgrid-scale eddy coefficient in large-eddy simulation of turbulent channel flow', *Journal of Fluid Mechanics* **162** 439- 462 .

McCullough, G. B. and Gault, D. E. (1951) 'Examples of three representative types of airfoil-section stall at low speed', NACA TN 2502.

McLachlan, B. G. (1989) 'Study of a circulation control airfoil with leading/trailing-edge blowing' *Journal of Aircraft* **26** 817-821.

Mellen, C. P., Fröhlich, J., and Rodi, W. (2003) 'Lessons from LESFOIL project on large-eddy simulation of flow around an airfoil', *AIAA Journal.* **41** (4), 573-581.

Moin, P. and Kim, J. (1982) 'Numerical investigation of turbulent channel flow', *Journal of Fluid Mechanics* **118** 341-377.

Mueller, T. J. and DeLaurier, J. D. (2003) 'Aerodynamics of Small Vehicles', *Ann. Rev. Fluid Mech*. **35** 89-111.

Nerger, D., Kähler, C. J. and Radespiel, R. 'Zeitaufgelöste PIV-messungen an einem schwingenden SD7003-profil bei Re = 60,000', Lasermethoden in der messtechnik 11th GALA Fachtagung, Braunschweig, 9-11 September 2003.

Owen, P.R. and Klanfer, L. 'On the laminar boundary-layer separation from the leading edge of a thin aerofoil'. ARC C.P. 220. October, 1953.

Pauley, L. L. (1994) 'Response of two-dimensional separation to three-dimensional disturbances'. *Journal of Fluids Engineering* **116** (3) 433-438.

Pauley, L. L., Moin, P. and Reynolds, W. C. (1990) 'The structure of two-dimensional separation'. *Journal of Fluid Mechanics* **220** 397-411.

Piomelli, U., Zang, T.A.,Speziale C.G. and Hussaini, M. Y. (1990) 'On the large-eddy simulation of transitional wall-bounded flows', *Phys. Fluids A* **2**(2), 257-265.

Pope, S. B. (2000) 'Turbulent Flows'. Cambridge University Press

Post, M. L. and Corke, T. C. (2004) 'Separation control on high angle of attack airfoil using plasma actuators', *AIAA Journal.* **42** (11) 2177-2184.

Press, H. P., Flannery, B. P., Teukolsky, S. A. and Vetterling, W. T. (1992) 'Numerical Recipes in FORTRAN 77, The Art of Scientific Computing', Cambridge University Press.

Purohit, S. C. (1987) 'Effect of vectored suction on a shock-induced separation', *AIAA Journal.* **25** 759-760.

Raffel,M., Kompenhans, J. and Wernet, P. (1995) 'Investigation of the unsteady flow velocity field above an airfoil pitching under deep dynamic stall conditions', *Experiments in Fluids* **19** 103-111.

Rinoie, K. and Takemura, N. (2004) 'Oscillating behaviour of laminar separation bubble formed on an aerofoil near stall', *The Aeronautical Journal* **108**, 153-163.

Rinoie, K., Okuno, M. and Sunada, Y. (2009) 'Airfoil stall suppression by use of a bubble burst control plate', *AAIA Journal* **47** (2) 322-330.

Ripley, M.D. and Pauley L.L. (1993) 'The unsteady structure of two-dimensional separation', *Phys. Fluids* , A5, 3099-3106.

Roberts, W. B. (1980) 'Calculation of laminar separation bubbles and their effect on airfoil performance', *AIAA Journal*, **18** 25-31.

Roos, F. W., and Kegelman, J. T. (1986) 'Control of coherent structures in reattaching laminar and turbulent shear layer', *AIAA Journal.* **24** 1956-1963.

Sandberg, R.D. and Sandham, N. D. (2006) 'Nonreflecting zonal characteristic boundary condition for direct numerical simulation of Aerodynamic sound', *AIAA Journal,* **44** 402-405.

Sandham, N. D. (2008) 'Transitional separation bubbles and unsteady aspects of aerofoil stall', *The Aeronautical Journal* **112** 395-404.

Sandhu, H. S. and Sandham, N. D. 'Boundary conditions for spatially growing compressible shear layer'. Rep. QMW-EP-1100. Faculty of Engineering, Queen Mary and Westfield College, University of London, 1994.

Sankar, N.L. and Tassa, Y. (1981) 'Compressibility effects on dynamic stall of an NACA 0012 airfoil', *AIAA Journal,* **19** 557-558.

Shan, H., Jiang, L. and Liu, C. (2005) 'Direct numerical simulation of flow separation around a NACA 0012 airfoil', *Computers & Fluids* **34** 1096-1114.

Shan, H., Jiang, L., Liu, C., Love, M. and Maines, B. (2008) 'Numerical study of passive and active flow separation control over a NACA0012 airfoil', *Computers & Fluids* **37** 975-992.

Shida, Y., Kuwahara, K., Ono, K. and Takami, H. (1987) 'Computation of dynamic stall of a NACA-0012 airfoil', *AIAA Journal* **25** (3) 408-413.

Smagorinsky, J.S. (1963) 'General circulation experiments with the primitive equations, I, the basic experiment', *Mon. Weather Rev.* **91** 99-164.

Spalart, P. R. and Strelets, M. K. (2000) 'Mechanisms of transition and heat transfer in a separation bubble', *Journal of Fluid Mechanics* **403** 329-349.

Stratford, B. S. (1959a) 'An experimental flow with zero skin friction throughout its region of pressure rise', *Journal of Fluid Mechanics* **5** 17-35.

Stratford, B. S. (1959b) 'The prediction of separation of the turbulent boundary layer ', *Journal of Fluid Mechanics* **5** 1-16.

Tuncer, I. H., Wu, J. C. and Wang, C. M. (1990) 'Theoretical and numerical studies of oscillating airfoils', *AIAA Journal* **28**(9) 1615-1624.

Van der Ven, H. (1995). 'A family of large eddy simulation (LES) filters with nonuniform filter widths', *Phys. Fluids* **2** 1171-1172.

Vasilyev, O. V., Lund, T. S. and Moin, P. (1998) 'A general class of commutative filters for LES in complex geometries', *Journal of Computational Physics* **146** 82-104.

Visbal, M. R., and Shang, J. S. (1989) 'Investigation of the flow structure around a rapidly pitching airfoil', *AIAA Journal* **27**(8) 1044-1051.

Visbal, M. R. and Rizzetta, D. P. (2002) 'Large eddy simulation on curvilinear grids using compact differencing and filtering schemes', *Journal of Fluids Engineering* **124** 836-847.

Wilson, P.G. and Pauley, L.L. (1998) 'Two-and three-dimensional large-eddy simulations of a transitional separation bubble, *Phys. Fluids* **10** (11) 2932-2940.

Windte, J., Scholz, U. and Radespiel, R. (2006) 'Validation of the RANS-simulation of laminar separation bubbles on airfoil', *Aerospace Science and t echnology* **10** (6) 484-494.

Wong, C. W. and Rinoie, K. (2009) 'Bubble burst control for stall suppression on a NACA 63_1-012 airfoil', *Journal of Aircraft* **15** 547-561.

Yang, Z. and Voke, P. R. (2001) 'Large-eddy simulation of boundary-layer separation and transition at a change of surface curvature'. *Journal of Fluid Mechanics* **439** 305-333.

Yoshizawa, A., Kobayashi, K., Kobayashi, T. and Taniguchi, N. (2000) 'A onequilibrium fixed-parameter subgrid-scale model obeying the near-wall asymptotic constraint', *Phys. Fluids* **12** (9) 2338-2344.

You, D. and Moin, P. (2008) 'Active control of flow separation over an airfoil using synthetic jets'. *Journal of Fluids and Structures* **24**(8) 1349-1357.

You, D., Ham, F. and Moin, P. (2008) 'Discrete conservation principle in large-eddy simulation with application to separation control over an airfoil'. *Phys. Fluids* **20**(10), Art No. 101515.

Young, A. D. and Horton, H.P. (1966) 'Some results of investigation of separation bubbles', AGARD CP, 4 779-811.

Yuan, W., Xu, H., Khalid, M. and Radespiel, R. (2006) 'A parametric study of LES on laminar-turbulent transitional flows past an airfoil', *International Journal of Computational Fluid Dynamics* **20** (1) 45-54.

Zaman, K. B. M. Q., Mckinzie, D. J. and Rumsey, C. L. (1989) 'A natural low-frequency oscillation of the flow over an airfoil near stalling conditions', *Journal of Fluid Mechanics* **202** 403-442.

Zaman, K. B. M. Q., Bar-Sever, A. and Mangalam, S. M. (1987) 'Effect of acoustic excitation on the flow over a low-Re airfoil', *Journal of Fluid Mechanics* **182** 127-148.

Zhang, W., Hain, R. and Kähler, C. J. (2008) 'Scanning PIV investigation of the laminar separation bubble on a SD7003 airfoil', *Experiment in Fluids* **45** 725-743.